Dissertation

submitted to the
Combined Faculties for the Natural Sciences and for Mathematics
of the Ruperto-Carola University of Heidelberg, Germany
for the degree of
Doctor of Natural Sciences

presented by
M.Sc. Arno Becker
born in Gießen

Oral examination: January 15, 2016

Imaging of Neutral Fragmentation Products from Fast Molecular Ion Beams: Paving the Way for Reaction Studies in Cryogenic Environment

Referees

Prof. Dr. Andreas Wolf

Prof. Dr. Robert Moshammer

Abstract

Imaging of Neutral Fragmentation Products from Fast Molecular Ion Beams - Paving the Way to Reaction Studies in Cryogenic Environment

The focus of this work are experimental studies on dissociative recombination in merged-beams experiments at storage rings. Dissociative recombination of the sulfur hydride cation (SH^+) has been investigated at the magnetic Test Storage Ring (TSR) in Heidelberg, Germany. Measurements of the reaction rate coefficient and momentum spectroscopy of the fragmentation products have been performed. From these, the total reaction cross section and the branching ratios of the different product states were derived. These kind of studies will be continued at the new electrostatic and Cryogenic Storage Ring (CSR) in Heidelberg. Operated at cryogenic temperatures, the vacuum conditions are improved by several orders of magnitude which enables the storage of heavy molecules in their lowest ro-vibrational quantum state. In this way, gas phase processes can be investigated under conditions similar to those found in interstellar media. A new multi-coincidence particle imaging detector was developed. For experiments on dissociative recombination in this harsh environment, the detector has been partly simulated, constructed, built and tested.

Zusammenfassung

Abbildung neutraler Fragmentationsprodukte von schnellen Molekülionenstrahlen - Wegbereitung für Reaktionsuntersuchungen in kryogener Umgebung

Der Schwerpunkt dieser Arbeit sind experimentielle Untersuchungen von Dissoziativer Rekombination in Experimenten mit überlappenden Strahlen an Speicherringen. Dissoziative Rekombination des Schwefelhydrid Kations (SH^+) ist am magnetischen Testspeicherring (TSR) in Heidelberg untersucht worden. Es wurden sowohl Messungen des Reaktionsratenkoeffizienten, als auch Impulsspektroskopie der Fragmentationsprodukte durchgeführt. Hiermit wurde der vollständige Reaktionsquerschnitt und das Verzweigungsverhältnis der verschiedenen Produktzustände bestimmt. Diese Art von Untersuchungen werden in Zukunft bei ähnlichen Experimenten an dem neuen elektrostatischen und kryogenen Speicherring CSR in Heidelberg fortgesetzt werden. Bei kryogenen Temperaturen können erheblich verbesserte Vakuumbedingungen erzielt werden, was die Speicherung von schweren Molekülen in ihren niedrigsten Rotations- und Schwingungszuständen ermöglicht. Auf diese Weise können Gasphasenprozesse unter Bedingungen ähnlich denen von interstellaren Medien untersucht werden. Ein neuer ortsauflösender Teilchendetektor wurde entwickelt. Für Experimente von Dissoziativer Rekombination in dieser widrigen Umgebung ist der Detektor teilweise simuliert, konstruiert, aufgebaut und getestet worden.

Contents

1 Introduction

Atomic and molecular gas-phase reactions play an important role in all forms of natural and artificial plasma media. On earth, plasmas can mainly be found in artificial environments such as fusion reactors, combustion engines and fluorescence lamps. Prominent natural occurrences are the outer layers of planetary atmospheres, the so-called ionospheres, exposed to ionizing stellar and cosmic radiation. In the universe, the majority of visible matter is in fact ionized [1]. Diffuse and dense interstellar clouds in the interstellar medium (ISM) exhibit a great variety of molecular ions [2].

Molecular signatures in astronomical observations are used to probe the chemical compositions and physical properties of various astronomical environments. The conditions and dynamical processes in these environments can be investigated by comprehensive modeling of the whole chemical network. This requires a detailed understanding of all involved interaction processes between atoms, molecules, both in neutral and ionic form, as well as electrons and photons. The formation of molecular systems in the interstellar media (ISM) occurs both in the gas-phase as well as on the surfaces of ice and dust particles. Gas-phase reactions can be better modeled compared to surface reactions, as the latter rely on uncertain assumptions [3]. Hence, a good understanding of gas-phase reactions can also help to constrain contributions from surface reactions.

Dissociative recombination (DR) is a key reaction in the vast chemical network of interstellar media and other plasma environments, which are governed by gas-phase reactions with ionic species [4–6]. This dissociation mechanism of molecular ions is induced by recombinations of free, low-energy electrons which leads to the formation of neutral fragments. Recombination of electrons with molecular ions exhibit very large cross sections, typically, three to five orders of magnitudes larger than atomic-ion recombinations [7]. The barrier-less nature of dissociative recombination makes it most efficient towards lower collision energies in an energy range from meV to eV. For this reason, dissociative recombination is one of the most important processes of the gas-phase chemistry, especially, in cold plasma environments such as interstellar media with typical temperatures well below 100 K [8]. Only very little energy is available in such an environment, so that practically all endothermic gas-phase reactions are inhibited. This makes DR an often dominant destruction and neutralization mechanism of molecular ions which in particular frequently marks the endpoint of a molecular formation chain. Beyond that, dissociative recombination is an exothermal reaction with energy releases of typically a few eV. This makes it also a considerable source of energy for chemical reactions especially in cold environments.

The reaction data required for atmospherical or astrochemical models can be ob-

tained in laboratory studies. However, the multitude of reactions that need to be considered exceeds by far the experimental capacities in the foreseeable future. DR is a particularly complex gas-phase reaction and despite major advances in over 60 years of DR research there are still significant discrepancies between theory and experiment even in case of fundamental systems [4]. Hence, experimental studies provide important benchmarks for the development of theoretical models both regarding molecular structure and dynamics. In context of astrochemical models, some of the assumed energy excess of DR reactions may be stored in excited product states, accompanied by a lower release of kinetic energy. In current astrophysical models, this has not been considered as of now. Yet, it might have a considerable effect on the energy dissipation of DR reactions in interstellar media.

The focus of this work are experimental studies of dissociative recombination in merged-beams experiments at cooler storage rings, which are ideal platforms for high-resolution gas-phase reaction studies under well defined conditions. Ion storage rings provide efficient means for both beam preparation and diagnostics, as well as efficient separation and detection capabilities of both charged and neutral reaction products. The ion storage helps to define the initial quantum state of the investigated ions. Electron coolers facilitate the preparation of high brilliance ion beams and enable high-resolution electron-ion interaction studies.

In this work, dissociative recombination of SH^+ was investigated in such a merged-beams experiment at the magnetic Test Storage Ring (TSR) in Heidelberg, Germany. These investigations were motivated by large discrepancies in several astrophysical studies concerning this fundamental sulfur-bearing molecular ion [9, 10]. This was one of the heaviest diatomic molecular ions investigated at TSR and was pushing the experimental technique to its limits.

Dissociative recombination experiments will be continued at the new Cryogenic Storage Ring (CSR) in Heidelberg, Germany. At the time of this work, this is the worldwide largest fully electrostatic storage ring, which can be operated at temperatures down to the cryogenic range of only a few Kelvin. With cryogenic temperatures it is possible to prepare state-selected beams down to their rotational and vibrational ground state and thus effectively mimic the conditions of interstellar media. In addition, the vacuum pressure improves by orders of magnitudes, in comparison to room-temperature storage rings, which enables significantly longer storage times of the ion beam. An electron cooler will allow both phase-space cooling and electron-ion interaction studies. Both, the electrostatic storage and the longer storage times facilitate studies of, in particular, heavier molecular species. Within the scope of this work, a detector system for neutral reaction products which is operated inside the harsh environment of CSR has been developed.

In Chapter 2, the role of molecular ions in astrophysical observations is briefly discussed, based on the specific case of SH^+. The most important molecular fragmentation processes, induced by recombination of low-energy electrons, are introduced with emphasis on dissociative recombination. The experimental techniques and instrumentations used in this work are introduced in Chapter 3. In Chapter 4, the results of the experimental investigation on dissociative recombination of SH^+

in a merged-beams experiment at TSR are reported. The merged-beams rate coefficient was measured from which the reaction cross section was extracted. From this, a thermal plasma rate coefficient was derived which can be used in astrophysical models. In addition, fragment momentum spectroscopy has been employed. The relative branching ratios of different DR product states could be determined with a new analysis procedure. This new method is also useful for future measurements at CSR. In Chapter 5, the development of a multi-coincidence imaging detector for neutral reaction products, operated in the cryogenic environment of the new CSR, is described. The results of a preceding off-line test as well as the first operations at room- and cryogenic temperature conditions are reported. Chapter 6 concludes with a summary of the results of the investigations of SH^+ and the achieved performances of the new detector system and gives an outlook to further improvements and prospects for DR investigations at CSR.

2 Molecular Fragmentation Processes

The key for a priori understanding of chemistry is the quantum dynamics of molecules. In particular, molecular ions play a central role in various chemical systems such as salt-solutions, acid-base reactions and electrolysis, not least, in the photosyntheses which forms the foundation to most of the known life [11]. Less prominent chemical systems are interstellar gas clouds, which are dominated by ionic processes. The chemical reactions in these environment proceed under almost ideal conditions: Due to the typically very low particle densities in these gas clouds only binary collision processes occur and by virtue of the low temperatures the number of quantum mechanically relevant energy levels is limited so that an a priori modeling seems feasible. Nevertheless, the chemistry in these structures, supported by astronomical observation, is quite complicated, which is important for the evolution of interstellar media.

At the beginning of this chapter, the role of molecules for astrophysical studies of the interstellar medium is shortly reviewed based on the specific case of SH^+. The experimental studies on dissociative recombination of SH^+ performed in this work (see Ch. 4) were motivated by large discrepancies in several astrophysical studies concerning this fundamental molecular ion. The most important fragmentation processes of molecular ions, induced by electron recombination, are introduced with an emphasis on the DR process.

2.1 Molecules in Interstellar Media

The *interstellar medium* refers to the tenuous gas and dust filling the void between stellar systems [12]. New stars are formed from this material by gravitational collapse in the denser regions of the interstellar medium. This material is returned back again by supernovae, enriched by new elements produced in stellar nucleosynthesis processes. These denser environments are referred to as *molecular clouds* as most of the hydrogen is present in molecular form with typical particle densities of 10^2 to 10^4 particles per cm^3 and temperatures in the range from 6 K to 50 K [8]. Other interstellar environments exhibit even lower particles densities, but in some cases, also temperatures up to 10^4 K [8].

Astronomical observations rely on the electromagnetic radiation both absorbed and emitted by atoms or molecules. Electronic transitions in atoms and molecules are typically in the order of eV corresponding to the visible range or higher. Molecules have, due to their additional degrees of freedom, vibrational transitions typically in the 0.1 eV range (infrared) and rotational transitions from about 1 meV to 10 meV (THz to radar). For molecular observations in the radio band major progress was

achieved in the recent past by earth-based telescopes such as the Atacama Large Millimeter/submillimeter Array (ALMA) [13], which went into operation in 2011, or before by its prototype the Atacama Pathfinder Experiment (APEX) [14]. The earth's atmosphere is opaque for electromagnetic radiation beyond the ultraviolet regime. Furthermore, most of the infrared spectrum is absorbed, which is most interesting for rotational transitions of molecular species. Here, observations were made with airborne observations such as the Stratospheric Observatory for Infrared Astronomy (SOFIA) [15, 16] or satellite borne telescopes like the Spitzer Space Telescope (NASA) [17] or the Herschel Space Observatory (ESA) [18]. Their spectra show signatures of a large number of both neutral and ionic molecular species in many different astronomical environments. By 2013, the Cologne Database for Molecular Spectroscopy (CDMS) [19] listed more than 170 molecular species [20] which have been identified. However, some species are difficult to observe in cold environments due to a lack of a suitable transition dipole moment, which is the case for homonuclear diatomic molecules, including the most abundant H_2 molecule. Because of their symmetry, these species have no electric dipole moment and all ro-vibrational transitions within the ground state are quadrupolar with low spontaneous emission coefficients [8, 21].

Instead of a direct spectroscopic identification, the abundance of such *invisible* species can be inferred from observable proxy species which chemically react with these molecules by modeling the corresponding astrochemical network. For this reason, even rare molecules such as the heteronuclear SH^+ are of interest, which is a focus of this work. The gas-phase chemistry in interstellar environments depends on the local physical conditions concerning the gas density, the gas temperature as well as the radiation field. These can be inferred from the observed rotational level populations and transition strengths. In cold environments, only exothermal reactions are possible and even those may have *potential barriers* or *activation barriers*, respectively, which must be overcome first. In photodissociation regions and shocks, endothermal reactions or reactions with activation barriers may become possible [22]. Their small rotational and vibrational transition energies make molecular species especially well suited as probes for cold astronomical environments, even despite their small relative abundances. More abundant molecular species can be also quite effective coolants as they can convert kinetic energy via collisions into internal excitations, which may decay via radiative transitions, whereas the emitted radiation may escape the local environment.

The chemistry in such cold and dilute environments is mostly driven by binary exothermic reactions. In the presence of ultraviolet photons, molecules can be photodissociated or photoionized, besides the ionization by cosmic ray particles. Molecules can be effectively formed by mostly barrier-less ion-molecule reactions which may be destroyed and neutralized by also barrier-less dissociative recombination (see Sect. 2.2.3). Formation can also be achieved via neutral-neutral reactions or radiative association.

In order to utilize the spectroscopical observations for model predictions any involved formation and destruction mechanisms have to be taken into account. In

current models [3,8], both gas-phase as well as surface-catalyzed reactions on ice or dust particles are considered. Especially, surface reactions are not so well understood as the grain composition, structure, and surface coverage is not well known. Gas-phase reactions can, on the other hand, be experimentally measured with high accuracy. If one turns the argument around, one can compare the model predictions from the better known gas-phase reactions in order to constrain the contributions from surface reactions. Nevertheless, such accurate experimental rate measurements are also quite involved so that most of the reactions have an unknown rate coefficient. In these models, the rate coefficients k are usually approximated by the Arrhenius-Kooji formula [23]

$$k(T) = \alpha \left(\frac{T}{300}\right)^{\beta} \exp(-\frac{\gamma}{T})\,\mathrm{cm^3 s^{-1}}. \tag{2.1}$$

In the case of diatomic molecules, a *typical* rate coefficient of

$$\alpha_{\mathrm{DR}} = 2 \times 10^{-7} \left(\frac{300}{T}\right)^{1/2} \mathrm{cm^3 s^{-1}}. \tag{2.2}$$

is assumed. However, the DR rate coefficients of some investigated diatomic molecular species showed significant deviations from these assumed values. As an example, in the case of CF^+ [24] the measured rate coefficient was a factor of four lower compared to the *typical* rate coefficient.

2.1.1 The Case of SH^+

The gas-phase chemistry of sulfur-bearing molecules in interstellar media has been studied for more than 40 years [25]. SH^+ is one of the most fundamental molecules of the sulfur based chemistry, which has been identified as a potential probe for comets, photodissociation regions, shocked interstellar gas, diffuse molecular clouds [26] and later also for X-ray dominated regions [27]. After several attempted sighting between 1988 and 1991 [28–30], SH^+ could be successfully observed for the first time towards the galactic center within the APEX survey 2008 [31]. Since then, it could be detected with the Herschel space observatory in other environments, such as protostar disc outflows, star forming regions and photodissociation regions [9,10,32,33].

In the following, some of the most important formation and destruction reactions of SH^+ are discussed, which determine the characteristic chemistry of this molecular ion. Sulfur is ionized by the interstellar radiation field

$$\mathrm{S} + h\nu \rightarrow \mathrm{S^+} + e \tag{2.3}$$

and in dilute clouds it is mostly present in form of S^+ ions [25]. Since proton transfer reactions are often barrierless, they are feasible ion-destruction and formation processes [34]. However, the most obvious formation of SH^+ via the most abundant

H_2 molecule

$$S^+ + H_2 \rightarrow SH^+ + H \tag{2.4}$$

is endothermic by 0.84 eV in contrast to most other elements. This reaction requires an additional energy source in interstellar media with temperatures typically being below 100 K. Both Millar et al. [35] and Pineau des Forets et al. [36] proposed in 1986 that SH^+ could be efficiently formed in shocked diffuse clouds and turbulences. In dense clouds with large abundances of H_3^+, the formation via proton transfer seems feasiable [25]

$$S + H_3^+ \rightarrow SH^+ + H_2. \tag{2.5}$$

In 2008, Abel et al. [27] proposed an alternative formation via

$$S^{2+} + H_2 \rightarrow SH^+ + H^+. \tag{2.6}$$

Considering the ionization energy of about 23 eV from S^+ to S^{2+}, this pathway seems to be possible only in X-ray dominated environments. Interestingly, the destruction of SH^+ via proton transfer with H_2

$$SH^+ + H_2 \rightarrow SH_2^+ + H \tag{2.7}$$

is also endothermic [25]. In environments with low fractional ionization SH^+ is primarily destroyed in reaction with neutral species as [25]

$$SH^+ + O \rightarrow SO^+ + H \tag{2.8}$$
$$SH^+ + O \rightarrow S^+ + OH \tag{2.9}$$
$$SH^+ + N \rightarrow SN^+ + H \tag{2.10}$$
$$SH^+ + N \rightarrow S^+ + NH \tag{2.11}$$

which also link the chemical network of sulfur-bearing molecules with those of oxygen-, nitrogen-, and carbon-bearing molecules. In environments with large ionization degree and accordingly large electron densities, the destruction of SH^+ may be dominated by exothermic DR [25]

$$SH^+ + e^- \rightarrow S + H \tag{2.12}$$

which is considered with a reaction rate coefficient typically 2 to 3 orders of magnitude larger than other processes at low collision energies [16].

Despite their highly endothermic direct formation via proton transfer from the atomic cations (see Eq. 2.4), both CH^+ and SH^+ have been observed in surprisingly large quantities [9, 37, 38], which indicates local reservoirs of energy exceeding by

far that provided by UV-photons [39]. The large difference in endothermicity of these formations routes leads to a strong effective temperature dependency of their abundance ratio $n(SH^+)/n(CH^+)$ [22]. For this reason, this ratio is used as a tracer for turbulent dissipation regions. [9, 22, 40]

The relevant astrochemical networks of sulfur- and carbon-bearing molecules have been recently described in detail by Neufeld et al. [16]. In trying to model the astrochemical network, the predicted abundances of SH^+ were about a factor of four [10] and even an order of magnitude lower [9] compared to those observed. As a possible explanation for this discrepancy, an incomplete description of the dynamics in such shock waves or turbulent dissipation regions was suggested [9]. However, underestimated formation or overestimated destruction rate coefficient may also contribute.

Regarding the destruction rate of SH^+ via dissociative recombination, preliminary results of theoretical investigations on dissociative recombination of SH^+ were recently published by Kashinski et al. [41, 42]. Their calculated rate coefficient is almost two orders of magnitude below the typically assumed rate coefficient (see Eq. 2.2). At the time of the presented work, no other experimental work on dissociative recombination of SH^+ is known. For these reasons, SH^+ was experimentally investigated in this work.

2.2 Fragmentation Mechanisms induced by Low-Energy Electrons

Molecular structures and processes are usually described by means of *potential energy surfaces*. The basic concept is briefly introduced at the beginning of this section before the most important fragmentation mechanisms of molecular ions, induced by low-energy electron collisions, are described. The DR process is explained in more detail as it is the focus of this work. Comprehensive reviews on the more recent DR research were given by Florescu-Mitchell and Mitchell in 2006 [6], and by Larsson and Orel in 2008 [4].

2.2.1 Potential Energy Surfaces

Potential energy surfaces (PES) describe the potential energy between the constituents of a molecule depending on their geometry. Those are usually obtained by solving the Schrödinger equation with the adiabatic *Born-Oppenheimer* approximation [43]. Here, the nuclei of a molecule are considered stationary as the much lighter electrons may react instantaneously to any nuclear motion. Under this assumption, the solution can be separated into electronic and nuclear motions. The electronic wave function is then determined for a static molecule as a function of its geometrical parameters, e.g., bond lengths or angles. The solutions are electronic eigenenergies which, in a next step, describe the nuclear motion depending on the nuclear configuration of the molecule. In case of diatomic molecules, these hypersurfaces simplify to one-dimensional potential energy curves (PEC) as a function of the internuclear distance.

A minimum of a PES gives the geometrical equilibrium distance(s) of a molecular state while vibrational motions of the nuclei are described by oscillation around this minimum. Binary molecular reactions with electrons or photons can be understood as propagations within the corresponding PES landscape. The geometry parameters, that change during the reaction, are also referred to as *reaction coordinates*. Fragmentation processes of molecules typically proceed along repulsive PES.

The Born-Oppenheimer approximation delivers reasonable results for non-degenerate electronic states, which are well separated in energy. This approximation breaks down when PES of the same total symmetry lie energetically close to each other. For molecular energies where such crossings or near-crossings of the different PES occur, the electronic and nuclear motions become coupled. In this case, the nuclear motion can no longer be assumed to be determined by the PES of a single electronic state.

In diatomic molecules, adiabatic potential curves of states with the same symmetry are not allowed to cross according to the *non-crossing rule* formulated by von Neumann and Wigner [44]. The crossings of diabatic potential curves are converted to avoided crossings in the adiabatic limit. In the multidimensional case of PES crossing may occur as conical intersections.

2.2.2 Overview of Fragmentation Mechanisms

Binary collisions of molecular ions with free electrons can lead to internal excitations, ionization, neutralization, dissociation or even some combined processes. Especially recombinations of low-energy electrons with molecular cations can lead to different kinds of fragmentation processes with either neutral or charged products, which can also be excited. After a brief description of such collision processes, the most important dissociation processes induced by recombinations of low-energy electrons are introduced for the simple case of diatomic cations AB^+.

In collisions of molecular ions with electrons, unstable neutral complexes can be formed, which are also referred to as (electronic) *resonance* states. Those can be either repulsive or bound and also ro-vibrationally excited. The capture of electrons into large, highly excited orbits leads to so-called *Rydberg* states. However, such bound states can still couple to crossing repulsive states. Unstable neutral complexes that consist of ro-vibrationally excited bound states can also be destroyed by reverse capture, i.e., *autoionization*, where an electron is re-emitted. Such a collision is called *inelastic*, if the electron is emitted with less kinetic energy and the ion is internally excited. If the collision already starts from ro-vibrationally excited states, the electron can also be re-emitted with even higher kinetic energies, which is referred to as a *superelastic* collision. If the metastable neutral complex converts by quantum mechanical coupling to a repulsive state, the molecule dissociates into several neutral fragments. This transition of the complex from a bound to a repulsive state is referred to as *predissociation*.

The various fragmentation processes induced by electron-ion collision are classified as follows: **Dissociative Recombination (DR)** is a fragmentation process where an electron is captured by a molecular ion forming an excited neutral complex which ultimately dissociates via a doubly excited repulsive state AB^{**} into neutral fragments

$$\mathrm{AB}^+ + e^- \xrightarrow[\mathrm{AB}^*]{} \mathrm{AB}^{**} \rightarrow \mathrm{A} + \mathrm{B} \tag{2.13}$$

The molecular ion can be either promoted directly into this doubly excited repulsive state or, before, into a (singly) excited Rydberg state AB^*, which then couples to a repulsive state. These *direct* and *indirect* pathways are described in detail in Section 2.2.3.

If the kinetic energy of the incident electron is sufficient to promote the molecular ion AB^+ into its vibrational continuum, the system can also dissociate via **dissociative excitation (DE)** with neutral and ionic fragments

$$\mathrm{AB}^+ + e^- \xrightarrow[\mathrm{AB}^*]{} \begin{cases} \mathrm{A}^+ + \mathrm{B} + e^- \\ \mathrm{A} + \mathrm{B}^+ + e^- \end{cases} . \tag{2.14}$$

Again, such a dissociation can either proceed *directly* or *indirectly* via autoionization of an intermediate excited state AB^*. In the latter case, the charge distribution among the fragments is determined by the internal structure of AB^*.

At even higher collision energies ionization of both product fragments becomes possible

$$AB^+ + e^- \longrightarrow A^+ + B^+ + 2e^- \tag{2.15}$$

which is referred to as **dissociative ionization (DI)**. Also this process can proceed resonantly via an intermediate state and a subsequent autoionization.

In some cases, the intermediate neutral states may even have, at low energies, dissociation channels which lead to pairs of both positive and negative fragments

$$AB^+ + e^- \longrightarrow AB^* \longrightarrow \begin{cases} A^+ + B^- \\ A^- + B^+ \end{cases} . \tag{2.16}$$

This process is referred to as **ion-pair Formation (IPF)** or in some cases as *resonant ion-pair formation (RIP)*.

2.2.3 Dissociative Recombination

Dissociative recombination, as introduced in the previous Section, has typically different pathways, which can be distinguished as *direct* and *indirect* DR as well as DR via *core-excited* Rydberg states and *direct predissociation*. In the following paragraphs, these different types are described in more detail and depicted schematically by means of potential energy curves in the Figures 2.1 and 2.2. At the end of this section, the possible DR pathways are discussed for the concrete case of SH^+, which was investigated in this work. All the different types of DR can be described also for polyatomic molecular ions by a generalized form of the reaction equation 2.13 as

$$M^+(n,\{v\},J) + e^-(E_e) \xrightarrow[M^*]{} M^{**} \longrightarrow \sum_i F_i^{(*)} + \sum_i E_{\mathrm{KER},i}. \tag{2.17}$$

The molecular ion M^+ in the internal state $(n,\{v\},J)$[1] recombining with an electron of kinetic energy E_e can form, possibly via a excited neutral complex M^*, a repulsive state M^{**}. This repulsive state dissociates into several neutral, potentially internally excited, atomic or molecular fragments $F_i^{(*)}$. The different pathways are explained in the following paragraphs. The energy excess of such a reaction can be released in form of the kinetic energies $E_{\mathrm{KER},i}$ or partly stored as internal excitations of the reaction products $F_i^{(*)}$. These kinetic energy releases (KER) are characteristic quantities, which depend both on the structure of the molecule and the dynamic propagation into different pathways along the potential energy surfaces. The relative

[1] The electronic and rotational states are denoted by n and J, respectively. $\{v\}$ describes the various vibrational quantum numbers of the polyatomic molecular ion M^+.

abundances of these product states are referred to as *product state branching ratios*. In case of polyatomic ions, there are typically several different dissociation channels with different combinations of fragmentation products.

Direct Process

The *direct* DR process, proposed by Bates and Massey in 1947 [45, 46], requires a neutral repulsive state crossing the ionic ground state, as schematically illustrated in Figure 2.1a. The incident electron with the kinetic energy E_e excites a valence electron of the molecular ion and is captured, according to the Franck-Condon principle, into a doubly-excited repulsive state of the neutral complex M**. As this intermediate complex propagates along the repulsive potential surface, its potential energy is transformed into kinetic energy of its constituents, which leads to a stretch of the chemical bond. The complex can autoionize until it passed all crossing of the potential energy in the repulsive state becomes lower then all bound state PES of

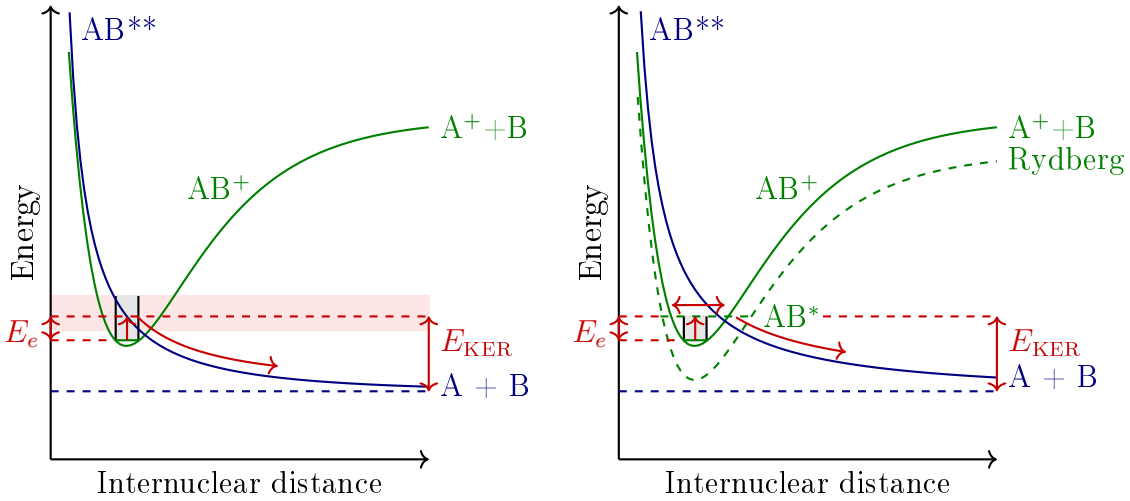

(a) direct **(b)** indirect

Figure 2.1: Schematic representation of the *direct* and *indirect* dissociative recombination processes. The ground state of the molecular ion AB^+ (green) is crossed by a repulsive resonant state AB** (blue) of the ion. The arrows indicate the process propagations and relevant energies.
(a) *Direct process*: The incident electron is captured within the Franck-Condon region (gray bar) into a resonant state from which the system dissociates along the repulsive potential.
(b) *Indirect process*: The incident electron is first captured into a vibrationally excited AB Rydberg state (dashed) of the series converging to the ion ground state. By coupling to the repulsive state the system can predissociate also outside the Franck-Condon region (gray).

the ion. The general equation of this process is

$$\mathrm{M}^+(n,\{v\},J) + e^-(E_e) \longrightarrow \mathrm{M}^{**} \longrightarrow \sum_i \mathrm{F}_i^{(*)} + E_{\mathrm{KER}} \tag{2.18}$$

which simplifies in the diatomic case to

$$\mathrm{AB}(v,J) + e^-(E_e) \longrightarrow \mathrm{AB}^{**} \longrightarrow \mathrm{A}^{(*)} + \mathrm{B}^{(*)} + E_{\mathrm{KER}}. \tag{2.19}$$

In direct DR, the incident electron is captured via a vertical, purely electronic transition within the Franck-Condon region of its vibrational level into the steeply decreasing PES of M^{**} with transition energies which vary smoothly with the internuclear distance. The projection of the Franck-Condon region onto the energy axis (see Fig. 2.1a) determines the dependence of the direct recombination cross-section on the electron energy E_e. If the Franck-Condon region lies at large electron energies, then a peak occurs. If the Franck-Condon region is close to zero electron energies this leads to a characteristic E^{-1} behavior of the DR cross section (see also Section 4.3.3).

In 1950, Bates [46] predicted a rate coefficient for direct DR of about $10^{-7}\,\mathrm{cm}^{-3}\mathrm{s}^{-1}$ at temperatures of 250 K, which was still too low compared to the experimental data. In 1968, Bardsley [47] proposed another important, the *indirect*, pathway.

Indirect Process

In the indirect DR process, the incident electron is first resonantly captured into an intermediate state as illustrated in Figure 2.1b. Each state of a molecular cation marks the endpoint of a Rydberg series of neutral bound states. Therefore, vibrationally excited Rydberg states M^* are accessible close above the ground state of the cation. The incident electron can be resonantly captured in a Rydberg state if its energy matches the transition energy into the discrete level of such a bound state. During this capture process, the electron directly excites the molecular ion core rotationally or vibrationally. Subsequently, the Rydberg state can be predissociated, analog to the direct case, by coupling to a crossing doubly excited repulsive state M^{**}. This coupling is then also possible outside the Franck-Condon region of the molecular ion. The general equation for this process is

$$\mathrm{M}^+ + e^-(E_e) \longrightarrow \mathrm{M}^* \longrightarrow \mathrm{M}^{**} \longrightarrow \sum_i \mathrm{F}_i^{(*)} + E_{\mathrm{KER}} \tag{2.20}$$

which simplifies in the diatomic case to

$$\mathrm{AB}^+(v,J) + e^-(E_e) \longrightarrow \mathrm{AB}^* \longrightarrow \mathrm{AB}^{**} \longrightarrow \mathrm{A}^{(*)} + \mathrm{B}^{(*)} + E_{\mathrm{KER}}. \tag{2.21}$$

In this way, the *indirect* process may produce the same products as the *direct* process, which cannot be distinguished. The interference of both pathways causes sharp resonances in the energy depended total cross-section and oscillations in the distri-

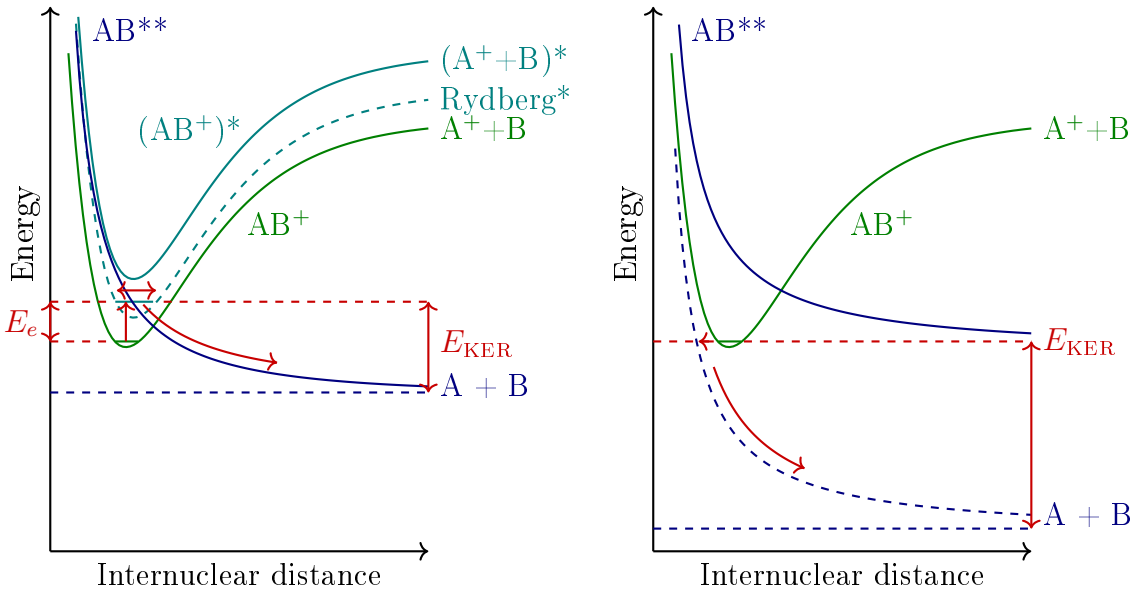

(a) core-excited resonance **(b)** direct predissociation

Figure 2.2: Schematic representation of the dissociative recombination processes via *core-excited resonances* and *direct predissociation* analog to Figure 2.1.
(a) *Core-excited resonance:* Similar to the *indirect* process, the electron is captured into a vibrationally and core-excited Rydberg state of the series converging to an electronically excited ion state (cyan) above the ground state. The system can predissociate by coupling to a crossing repulsive state.
(b) *Direct predissociation:* In case of a high-lying resonance the incident electron may couple directly, non-adiabatically to a repulsive neutral state, which lies outside the Franck-Condon region of the incident molecular ion.

bution of final states as a function of energy. Such resonances can occur especially at small impact energies, where the direct process has a smooth E^{-1} dependence.

Core-excited Resonance

Towards higher collision energies it may even possible to excite the molecule into Rydberg states corresponding to electronically excited ion states, which is illustrated in Figure 2.2. The DR via such a *core-excited* Rydberg state [4] proceeds analog to indirect DR and was first theoretically described by Guberman for DR of OH^+ [48]. Later, it has been experimentally observed for OH^+ [49] and CH^+ [50] by Amitay et al., and theoretically described for CH^+ and CD^+, showing that this process causes resonant features at higher energies in the total cross section [4].

Direct Predissociation

In some cases, DR may proceed via a direct non-adiabatic coupling into a high-lying dissociative (Rydberg) state below the ionic ground state without any initial excitation [4]. This so-called *direct predissociation*, illustrated in Figure 2.2, was first described by Guberman in the context of his DR-studies of HeH^+ [51].

3 Neutral Fragment Studies at Cooler Storage Rings

The previous chapter explained the importance of molecular ions for the gas-phase chemistry in interstellar media. The modeling of such environments, based on astrophysical observations, requires a detailed knowledge of all involved gas-phase reactions. This basically includes all interactions of atomic, molecular or cluster species in neutral or ionic form as well as electrons and photons. However, the multitude of possible interaction reactions exceeds by far the experimental capacities in the foreseeable future. Thus, the model predictions rely in many cases only on rough estimates. Therefore, experimental studies of fundamental reactions with high resolution under well defined conditions are needed to provide benchmarks for the development of the corresponding theoretical models.

In the following, heavy ion storage rings are presented as particularly powerful and successful experimental platforms for studying gas-phase reactions of molecular ions under systematically controlled conditions. The basics of synchrotron physics are described as far as needed for the work reported here, focusing on the two heavy ion storage rings of the Max Planck Institute of Nuclear Physics in Heidelberg, Germany. Subsequently, it is demonstrated how an electron cooler storage ring forms an experimental merged-beams setup which, combined with neutral fragment imaging (see Sect. 3.2), is an ideal platform for studies of electron recombination reactions of singly-charged molecular ions. Such experiments have been conducted at the former TSR (see Ch. 4) and prepared for the new CSR (see Ch. 5), which are both described in more detail in Section 3.1.4 and 3.1.5.

Gas-phase Reaction Studies

Early gas-phase reactions studies of (molecular) ions have been performed in-situ in the same plasma discharge where the ions are created. Experimental methods based on this principle, like *flowing afterglow* and later the *ion flow tube*, have been developed further since then and are still used to this day [52–55]. Despite the great progress with mass spectrometric and spectroscopic probing techniques, challenging aspects of such methods are the limited control of the purity and strong excitations of the sample. Both leads to complex ensembles which complicates the interpretation of the results.

High-resolution studies of ion reactions in the gas-phase require a good control and efficient detection of both reactants and products. In the best case, the reactants are well isolated and prepared, the reaction occurs under well controlled conditions and the products are detected with a high efficiency. The most powerful experiments have been realized with fast beams especially at cooler storage rings.

Fast-Beam Experiments

In fast-beam experiments ions are, after their creation, first accelerated to high velocities, then selected by the desired mass-to-charge ratio and finally transported to the interaction experiment. A fast ion beam can be formed by extracting ions from their source on a high potential. Higher beam energies can be achieved with appropriate acceleration facilities. Kinetic beam energies in the range from a few keV to several MeV are typically used for atomic and molecular experiments. The ion of interest with a certain mass-to-charge ratio can be selected, for example, through narrow apertures after dispersing the ion beam in a magnetic dipole field. Ion beams with high velocities can be easily guided by ion-optical elements to their interaction targets. High beam velocities favor a highly efficient detection of the reaction products at high energy resolution. Furthermore, disturbances by residual gas collisions are reduced towards higher kinetic beam energies. Extremely small collision energies can be realized in a merged-beams geometry (see Sect. 3.1.2), which is especially important for investigations of capture processes with increasing cross-sections towards lower collision energies.

Usually, ions are produced in a highly excited state. In *single-pass* experiments the time-of-flight from the source to the experiment is typically too short for the ions to radiatively decay into their ground state which makes the interpretation of the results more difficult. Given a electric dipole moment that allows spontaneous radiative decay to occur, de-excitation of the ions can be realized by simply storing them for a sufficient period of time.

3.1 Storage Ring Experiments

A fast ion beam can be stored by "bending" it on a closed orbit in a heavy ion storage ring. In combination with the experimental advantages of fast beams, storage rings offer very good experimental control of all systematics.

Magnetic Storage Rings

The technical foundation of magnetic storage rings are (strong-focusing) proton synchrotrons [56, 57] developed in the 1950s for nuclear physics research, which are, meanwhile, also well established tools for atomic and molecular physics. The ions are confined on a closed orbit by magnetic ion-optical deflectors and focusing elements. The field free straight sections between the deflectors can be used for beam manipulation and diagnostics as well as the experimental equipment. The experimental performance of these devices could be significantly improved in terms of beam lifetime and energy resolution with the introduction of phase-space cooling techniques. Besides stochastic cooling [58], laser cooling [59] and radiation damping, the most commonly used technique is electron cooling (see Sect. 3.1.3). The latter also marks the foundation of many electron-ion interaction experiments.

Several magnetic cooler storage rings used for heavy-ion atomic physics came into operation at around 1990: The TSR (1988) [60] at the Max Planck Institute

for Nuclear Physics (MPIK) in Heidelberg (Germany), the Aarhus STorage RIng in Denmark (ASTRID) (1989) [61] at ISA in Aarhus, Denmark, the Experimental Storage Ring (ESR) (1990) [62] at the Gesellschaft für Schwerionenforschung (GSI) in Darmstadt, Germany, and the CRYRING[1] (1992) [63] at the Manne Siegbahn Laboratory (MSL) in Stockholm, Sweden.

Starting with compact experiments in gas discharge cells, physics moved to higher and higher energies, building among the biggest, most complex and expensive scientific devices in the world. This is not necessary for atomic and molecular physics investigation and in the last decade there is a trend to more compact electrostatic devices.

Electrostatic Storage Rings

The concept of an electrostatic storage ring was first realized in form of the Brookhaven electron analogue [64], an electrostatic synchrotron for 1-10 MeV electrons, which was only used as a test facility between 1953 and 1957. In 1997, the first fully ELectrostatic Ion Storage ring in Aarhus (ELISA) [65, 66], Denmark, came into operation which was designed for storage of heavy ions. This 7 m long storage ring has a racetrack design with two large, originally, spherical deflectors. In 2000, this design was reimplemented with cylindrical deflectors in the form of the ESRING [67, 68] at the High Energy Accelerator Research Organization (KEK), Japan, and later even upgraded by an electron target [69]. More recently, the FLSR [70] at the University of Frankfurt, Germany, became operational. The design was even realized in a miniaturized version called Mini-ring [71] in Lyon, France.

Molecules can be easily rotationally excited even by the ambient black-body radiation at room temperature. By cooling the whole vacuum vessel to cryogenic temperatures molecular ions can be prepared in their ro-vibrational ground state for species, if they have transition dipole moment to de-excite. In addition, the vacuum pressure can be improved by several orders of magnitudes due to cryo-adsorption which leads to significantly longer storage times. The relatively compact sizes of these ELISA-type storage devices make them feasible for completely cryogenic implementations. The ELISA design was both implemented in a version operated at liquid nitrogen temperature as the room-temperature Electrostatic ion storage ring (TMU E-ring) [72] (2004) as well as in a 4 K-version as the RIken Cryogenic Electrostatic (RICE) ring [73] at RIkagaku KENkyusho (RIKEN), both located in Tokyo, Japan. Another cryogenic implementation is the Double ElectroStatic Ion Ring ExpEriment (DESIREE) [74, 75] at the MSL in Stockholm, Sweden. It consists two 8.6 m long ELISA-type rings to store ions of opposite charge with a common merged-beams section. Recently, the CSR at the MPIK in Heidelberg, Germany, was commissioned at cryogenic temperatures. The beam guiding vacuum chamber could be cooled down to about 5 K and the residual gas pressure was estimated from first experiments to reach the order of 10^{-14} mbar. In this way, the conditions in the interstellar medium are simulated. With a circumference of 35 m this is currently

[1] A ring operated together with a CRYebis electron beam ion source.

the largest fully electrostatic storage ring. It is the only cryogenic and electrostatic storage rings which will feature an electron cooler allowing experiments with phase-space cooled, low-emittance ion beams comparable to previous experiments at magnetic cooler storage rings. The CSR is described in detail in Section 3.1.5. Many of the technical concepts for realizing this electrostatic and cryogenic storage ring were developed and tested at the Cryogenic electrostatic Trap for Fast ion beams (CTF) [76].

Another advantage of fully electrostatic storage devices is that magnetic fields are avoided which can cause mixing of magnetic fine-structure states. This can, for example, change autodetachment rates and the corresponding lifetime [77] complicating the interpretation of such measurements.

3.1.1 Storage Ring Properties

In an electromagnetic field with the electric and magnetic field vectors $\vec{E}$ and $\vec{B}$ an ion with q elementary charges experiences the total force

$$\vec{F} = q(\vec{E} + \vec{v} \times \vec{B}) \tag{3.1}$$

as the sum of electric and Lorentz forces at the particle velocity $\vec{v}$. In order to confine a charged particle of mass m on a circular trajectory with radius ρ, this force has to be equal to the centripetal force

$$|\vec{F}| = F = \frac{mv^2}{\rho} \tag{3.2}$$

in the non-relativistic approximation, which is sufficient in the context of this work, as shown later. In case of purely magnetic and purely electrostatic deflection fields, respectively, the associated bending radii ρ_m and ρ_e are given by

$$\rho_m = \frac{mv}{qB} = \frac{p}{qB} \quad \text{and} \quad \rho_e = \frac{mv^2}{qE} = \frac{2E_0}{qE}. \tag{3.3}$$

In both cases, the deflecting force is perpendicular to the particle velocity so that the product of the bending field and radius is a constant of the motion proportional either to the momentum p or to the kinetic energy E_0 of the ion. These quantities characterize the ability to store a charged particle in an electromagnetic field and are referred to as *magnetic* and *electric rigidity*, respectively,

$$B\rho_m = \frac{p}{q} \quad \text{and} \quad E\rho_e = \frac{2E_0}{q}. \tag{3.4}$$

In a magnetic storage ring all ions with the same momentum and charge-state are stored at a given field strength and, accordingly, in an electrostatic storage ring ions with the same kinetic energy and charge-state. In practice, the maximum achievable electrical field strength are limited by the ion optics. For this reason, high energy

storage rings often use superconducting bending magnets.

The maximum storage velocities of magnetic and electrostatic storage rings are

$$v_{\max} = \frac{q}{m} B\rho_{\max} \quad \text{and} \quad v_{\max} = \left(\frac{q}{m} E\rho_{\max}\right)^{1/2}, \tag{3.5}$$

respectively. The electrostatic storage has a weaker q/m dependence which can be an advantage for investigations of very heavy ions. However, it remains to be noted that in both cases the maximum ion velocity decreases with increasing charge-to-mass ratio.

For ion beams of a given beam velocity, only particles with a certain mass-to-charge ratio can be stored on a stable closed orbit in a storage ring. If this ratio is altered after an interaction in an experiment the reaction products are separated from the stored beam by the following deflectors. Charged products are deflected according to their mass-to-charge ratio and can be intercepted by movable counting detectors close to the stored ion beam. Neutral products are not affected by the bending elements and can be detected with stationary detectors in the forward direction.

Beam losses in an ion storage ring are mostly caused by collisions with residual gas molecules. In order to realize sufficiently long beam lifetimes a residual-gas pressure of, typically, 10^{-10} mbar is required. The beam lifetime

$$\tau = \frac{l}{v} = \frac{1}{v n_0 \sigma} \tag{3.6}$$

is limited by the ratio of the mean free path length $l = (n_0\sigma)^{-1}$, given the residual-gas particle density n_0 and the interaction cross section σ, and the ion beam velocity v. The particle density, as a direct measure for the quality of the vacuum,

$$n_0 = \frac{p}{k_\mathrm{B} T} \tag{3.7}$$

depends on both the residual-gas pressure p and the ambient temperature T together with the Boltzmann constant k_B. In order to use the pressure as a measure for the vacuum quality for storage devices operated at different temperatures it is commonly given in room temperature equivalent (RTE) units so that it represents the same density as measured at any other temperature.

The residual-gas pressure in a vacuum system is limited by the gas desorption rates from all surfaces. By cooling the whole vacuum vessel down to cryogenic temperatures, these rates are reduced by orders of magnitudes resulting in corresponding improvements of the residual gas pressure and storage times. In this way, the conditions of interstellar media can be mimicked both in terms of ambient radiation field and particle densities (see Sect. 2.1). Long storage times are especially helpful for investigations of heavier molecular ions, which have much longer cooling times (see Sect. 3.1.3)

The rotational level spacing of molecular ions is typically in the order of a few

to tens of meV, which can be easily excited by the black-body radiation of a room-temperature environment. The typical energy of the black body radiation can be estimated with Wien's displacement law which gives the wavelength $\lambda_{\max}$ at the maximum energy density for a given temperature T

$$\lambda_{\max}(T) = \frac{2897.8\,\mu\mathrm{m\,K}}{T}. \tag{3.8}$$

For room temperature this results in a typical energy of about 130 meV. In order to enable the preparation of molecular ions, with a transition dipole moment, in their ro-vibrational ground-state the ambient temperature should not exceed about 10 K corresponding to a typical excitation energy of 5 meV.

3.1.2 Merged-Beams Technique

Since the first successful experiments in the mid 1960s [78, 79], the merged-beams technique has been well established for quantitative studies of collisional interactions between combinations of atoms, ions, electrons or photons [80] including short-lived or chemically-reactive species. This technique provides access to very low collision energies at very high energy resolution with efficient detection of reaction products at any scattering angle.

In a merged-beam experiment two fast beams are merged on a common trajectory for a finite distance of typically several tens of centimeters [80]. In this overlap geometry, very low collision energies can be realized in the center-of-mass frame by matching the velocities v_1 and v_2 of the two reactant beams in the laboratory frame. Following the interaction region, the reaction products can be effectively charge-to-mass separated from the parent beams by electromagnetic fields and, due to the high kinetic energies, detected with high efficiency. A challenging exception are reactions of two neutral species with neutral products. Moreover, it is possible to collect collision products which have been scattered under any angle, which is particularly useful for investigation of exothermic reactions such as electron capture and dissociative processes. Both the collision energies and the possible kinetic energy released are small compared to the kinetic energy of the center-of-mass system. Therefore, the reaction sphere formed by all scattering angles is kinematically compressed into a narrow cone in the forward direction. In this way, all reaction products scattered in 4π can be detected with high efficiency on a detector of compact dimensions (see also Sect. 3.2).

In a merged-beams experiment the absolute reaction cross section σ for the formation of a certain product with rate R at the relative collision velocity $v_r = |v_1 - v_2|$ can be determined as [80]

$$\sigma = \frac{R}{\Omega}\frac{v_1 v_2}{v_r}, \tag{3.9}$$

if the beam overlap Ω in the reaction volume V [80]

$$\Omega = \int J_1 J_2 dV \tag{3.10}$$

is accessible given the reactant particle fluxes J_1 and J_2. Most challenging in such experiments is the accurate determination of the beam overlap integral Ω. One specifically for storage ring experiments advantageous overlap geometry is obtained when the stored ion beam is completely immersed into a homogeneous second beam over an interaction length L_{int}. Under these conditions, the particle flux J_1 of the enveloping beam can be considered constant in the interaction region so that the reaction rate becomes independent of the overlap profile which results in

$$\Omega_{\text{mb}} = J_1 \int J_2 dV = n_1 v_1 I_2 L_{\text{int}} = n_1 v_1 N_2 v_2 \tag{3.11}$$

given the density of the first beam n_1 and the number of ions in the interaction region N_2, which is deduced from the current of the stored ion beam I_2.

The cross sections of some investigated processes have sharp onset or strongly resonant character, which is particularly the case for resonant pathways in electron capture processes like DR (see Sect. 2.2.3). With a sufficiently high energy resolution it may be possible to assign features in the energy-depended cross section to certain pathways of the investigated process. In a merged-beams experiment the energy resolution is essentially limited by the remaining relative angular and velocity spread of the two interacting beams. In practice, the so-called *rate coefficient* is measured

$$\alpha = \langle \sigma v_r \rangle = \frac{R}{n_1 N_2} \tag{3.12}$$

as a convolution of the cross section with the collision velocity vectors v_r.

Heavy ion storage rings are in particular well suited for merged-beams experiments due to their powerful preparation and manipulation capabilities of high-quality ion beams. As the ions recirculate through the interaction region with high repetition rates, a large effective ion flux can be realized from a small amount of ions. The long storage times facilitate the decay of initially highly excited states of the ions.

3.1.3 Electron Cooling and Experiments with Merged Electrons

A merged electron beam in a storage ring can be used for both effective phase-space cooling of the stored ion beam and high-resolution electron-ion collision experiments.

3.1.3.1 Electron Cooling

According to Liouville's theorem the phase-space volume, occupied by the positions and momenta of an ensemble of stored particles, cannot be reduced by conserva-

tive fields. However, for many experiments at storage rings an energetically well defined ion beam of small diameter with low divergence and small longitudinal momentum spread is desired. In a thermodynamic description this means to reduce the temperature of the stored ion beam in a co-moving frame. Several cooling techniques such as radiation damping or stochastic cooling are available [58, 59]. In particular, electron cooling, proposed by Budker in 1966 [81], is a very efficient method for phase-space cooling. It became the standard cooling technique at most medium energy (few MeV/u) storage rings and has been extended towards much higher-energetic machines [82] in the more recent past.

In an electron cooler the hot, stored ion beam is merged with a cold, intense electron beam, which completely encloses the ion beam and is typically guided by weak solenoid magnetic fields. Given the nominal ion beam energy E_0 in the storage ring, the electron beam velocity is adjusted to match the ion beam velocity by fulfilling the condition

$$E_{\mathrm{cool}} = \frac{m_e}{m_i} E_0. \tag{3.13}$$

By multiple Coulomb collisions energy is transfered from the hot ion beam to the cold electron beam. After repeated passings of the cooler the ion beam can be cooled down to almost the electron beam temperature T_e. The phase-space cooling leads to increased particle densities at smaller beam diameter and smaller divergence due to the reduced beam velocity spreads. In case of molecules, non-destructive inelastic electron scattering can occur as described in Section 2.2.2. By super-elastic collisions (SEC) this can even lead to vibrational or rotational cooling of the ions [83, 84].

The resulting ion beam temperature is finally limited by the competing intra-beam Scattering (IBS) of the ion beam, so that, in most cases, the ion beam cannot fully reach th electron beam temperature. The electron beam is continuously renewed to avoid its heating. The cooling time for an ion beam with mass m and q elementary charges by an electron beam with particle density n_e and temperature T_e behaves like [85]

$$\tau \propto \frac{m}{q^2} \frac{T_e^{3/2}}{n_e}. \tag{3.14}$$

It should be noted that electron cooling becomes more challenging for larger ion masses as longer storage times are required.

3.1.3.2 Merged-Beams Electron Experiments

Electron-ion interactions can be investigated in a merged-beams experiment for non-zero collision energies by detuning the electron beam velocity with respect to the ion beam velocity. The corresponding *detuning energy* is given by

$$E_{\mathrm{d}} = \frac{1}{2} m_e v_d^2 = \left(\sqrt{E_{\mathrm{e}}} - \sqrt{E_{\mathrm{cool}}} \right)^2 \tag{3.15}$$

for non-relativistic beam velocities in the ideal case with collision angles of $\theta = 0$, the electron energy E_e and the cooling energy E_{cool} as defined in Eq. 3.13. The relativistic form of this formula used in the analysis is given by Kieslich *et al.* [86]. The small, unavoidable merging angles in the merging and de-merging sections lead to contributions with slightly increased collision energies.

Merged-Beams Rate Coefficient

The merged-beams rate coefficient (see Eq. 3.12) is experimentally determined for different detuning energies E_{d}. Its relation to the underlying cross-section $\sigma(E)$ is expressed according to [87] as

$$\alpha\left(E_{\mathrm{d}}\right) = \int \sigma(E) v f_{\mathrm{mb}}(E, E_{\mathrm{d}}, T_{\parallel}, T_{\perp}, X) dE \tag{3.16}$$

with the center-of-mass electron-ion collision energy E and relative velocity v, respectively, and the experimental collision energy distribution f_{mb}, which considers both the electron beam energy spread, characterized by the effective temperatures $T_{\perp}$ and $T_{\parallel}$ (see below), and the experimental geometry X given for the parameter E_d varied in the experiment. The collision energy is given by $E = \frac{1}{2}\mu v^2$. The overlap geometry determines the contributions with increased collision energies in the merging and de-merging sections, which have been discussed for $T_{\perp} = T_{\parallel} = 0$ by Lampert et al. [88]. There is no analytical representation of f_{mb} known which accounts for both the velocity spread and the overlap geometry [87]. In order to extract the cross section from the measured rate coefficient, in this work a numerical method was used developed by Novotný et al. [87,89], which is also briefly described in Section 4.3.3.

Merged-Beams Energy Resolution

The energy resolution in a merged-beams experiment is determined by the velocity spreads, i.e. the variances $(\Delta v)^2$, of both involved particle beams. The velocity spreads of the electron beam can be characterized by the temperatures

$$(\Delta v_e)^2_{\perp} = \frac{2 k_{\mathrm{B}} T_{\perp}}{m_e} \quad \text{and} \quad (\Delta v_e)^2_{\parallel} = \frac{2 k_{\mathrm{B}} T_{\parallel}}{m_e}. \tag{3.17}$$

The mean collision angles can be estimated with $v_0^2 = 2E_0/m_i$ as

$$\delta_{e,x} = \sqrt{\frac{(\Delta v_e)^2_x}{v_0^2}} = \sqrt{\frac{k_{\mathrm{B}} T_x}{E_0} \frac{m_i}{m_e}} \tag{3.18}$$

For typical values found at TSR (see also Sect. 3.1.4) of the ion beam energy with $E_0 \sim 10^6\,\mathrm{eV}$ and electron temperatures with $k_{\mathrm{B}} T_{\perp} \sim 10^{-3}\,\mathrm{eV}$ and $k_{\mathrm{B}} T_{\parallel} \sim 10^{-4}\,\mathrm{eV}$ one finds

$$\delta_{e,\perp} \approx 3 \times 10^{-2} \quad \text{and} \quad \delta_{e,\parallel} \approx 10^{-3}, \tag{3.19}$$

which is large compared to typical values of cooled ion beams

$$\delta_{i,\perp} \approx 3 \times 10^{-4} \quad \text{and} \quad \delta_{i,\parallel} \approx 10^{-4}, \tag{3.20}$$

so that the contribution from the ions can be neglected. When the electron beam temperatures are converted into a collision energy spread, the result for the FWHM energy spread is [90]

$$\Delta E \approx \sqrt{\left(\ln(2) k_\mathrm{B} T_\perp\right)^2 + 16 \ln(2) k_\mathrm{B} T_\parallel E_d}. \tag{3.21}$$

For mean detuning energies $E_d \gg k_\mathrm{B} T_\perp$, the experimental energy resolution ΔE is limited by $k_\mathrm{B} T_\parallel$, and, towards lower average collision energies, it is limited by $k_\mathrm{B} T_{e,\parallel}$.

3.1.4 Test Storage Ring

The heavy-ion Test Storage Ring TSR has been operated from 1988 to 2012 at the MPIK and it is planned to continue operation at the ISOLDE facility at CERN in Geneva, Switzerland [60,91–93]. Originally designed for nuclear physics experiments, it has been used for many atomic and molecular physics experiments. In this work it was applied to study the dissociative recombination of SH^+ as reported in Chapter 4. In the following, the parts of the TSR facility relevant for the SH^+ measurements are described.

TSR Ion Production and Acceleration

At TSR a broad variety of ions could be investigated which could be provided by different combinations of ion sources and accelerators [94]. A single-stage Van-de-Graaff accelerator was used to accelerate SH^+ ions to a beam energy of 2.65 MeV. The ions were transfered to the TSR via an ~ 100 m long magnetic beam line. The vacuum pressure was gradually reduced from $\sim 10^{-7}$ mbar to $\sim 10^{-9}$ mbar along the beam line. The ions entered the TSR through a differential pumping region, leading to a pressure of $\sim 3 \times 10^{-11}$ mbar inside the TSR realized mainly with Ti sublimation and ion getter pumps [91] and bake-out up to 300 °C [95].

TSR Design

The TSR, schematically shown in Figure 3.2, is a magnetic storage ring with a closed orbit circumference of 55.4 m. In each corner the ion beam is bent by each two 45° dipole magnets with a rigidity of 1.5 Tm and focused by five quadrupole magnets and three sextupole magnets. The four straight sections between the corners have a length of 5.2 m each. The first section is used for both multi-turn beam injection

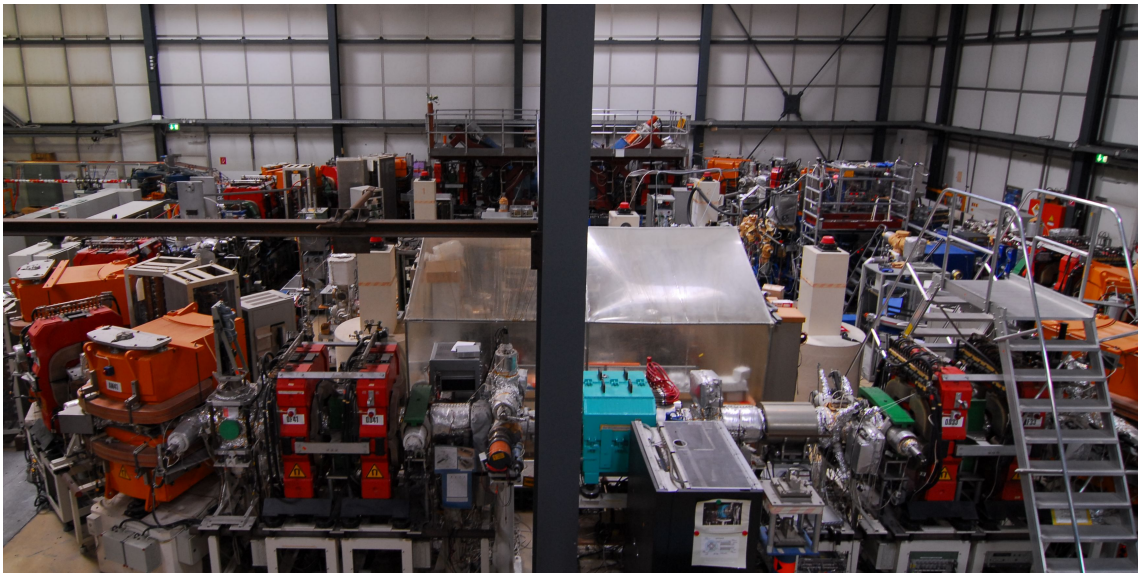

Figure 3.1: Photograph of the Test Storage Ring.

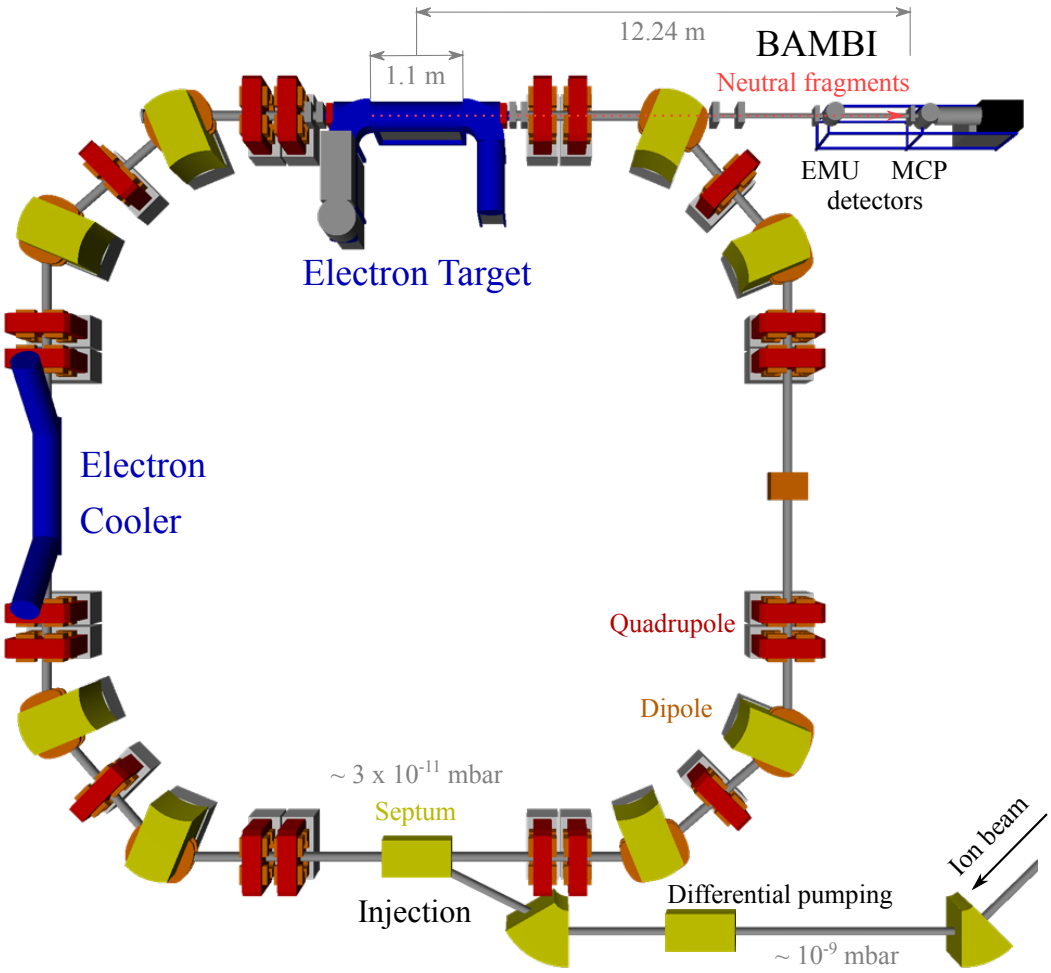

Figure 3.2: Schematic overview of TSR. After its injection, the ion beam is confined on a closed orbit by dipole and quadrupole bending and focussing magnets. Both the electron Cooler and Target can be used for phase-space cooling of the stored ion beam and as targets for merged-beams experiments. The Beamline for Advanced Molecular Breakup Investigation (BAMBI) houses the detectors for the neutral reaction products.

and extraction and another section is used for several beam diagnostics devices. In the two remaining sections TSR employed as a unique feature two merged electron beam devices which can both be utilized at the same time for cooling of the stored ion beam and merged-beams experiments. According to their usual usage they are referred to as *Cooler* [96] and *Target* [97]. In the corner sections behind each cooler the products are separated from the stored ion beam and can be detected by several different particle detectors.

TSR Electron Cooler and Target

Since 2003, the TSR featured two electron coolers. The original electron *Cooler* [98] could provide intense electron beam from a thermionic emitter cathode of about 1 A with an energy spread of about 0.11 eV or 1100 K, respectively. Its electron beam was guided by solenoid magnetic fields on the straight sections and was merged with the ion beam by toroid magnetic fields from an angle of 45°. The interaction regions of both Cooler and Target have a length of about 1.5 m in the 5.2 m-long straight section. This leaves space for additional experimental equipment and avoid disturbances from the dipole bending magnets. As the electron and ion beam are no yet perfectly aligned in the toroidal merging sections, the effective overlap length is slightly shorter.

The second device, installed in 2007, was specifically designed for high-resolution measurements. Its liquid nitrogen cooled photocathode could provide electron beams with much lower energy spread and the superconducting gun coils allow much higher magnetic expansion factors. For this reason, it was primarily used for the experiments and accordingly referred to as electron *Target*. Furthermore, the cooling force is proportional to the electron temperature. The associated cooling time is given in Equation 3.14. This makes cooling of heavier molecular species only possible with the electron *Target* [60, 99]. However, the maximum electron current of the Target was limited to $\sim 1\,\mathrm{mA}$ [100]. For this reason the Cooler was still used for either additional phase-space cooling or measurements with low ion beam currents or processes with very low reaction rates. Both devices used adiabatic expansion by which the transversal electron temperature can be decreased by a factor ranging from 1 to 30 for the *Cooler* and up to more than 100 for the *Target* [60, 99, 101]. However, this decreases also the electron beam density.

For the measurements of SH^+, reported in Chapter. 4, the Cooler was not used as its electron temperature was too high to effectively cool such a heavy ion beam (compare Eq. 3.14). The Target was used with an expansion factor of 20, which offers a good compromise of electron density and energy resolution (see Sect. 3.1.3.2). Based on previous experiments [87] with this expansion factor, the electron beam velocity spreads were assumed with

$$\begin{aligned} k_\mathrm{B}T_\perp &= (1.65 \pm 0.35)\,\mathrm{meV}, \text{ and} \\ k_\mathrm{B}T_\parallel &= 25^{+45}_{-5}\,\mu\mathrm{eV}. \end{aligned} \tag{3.22}$$

TSR Detectors

At the electron Cooler and Target various electron-ion interaction processes could be studied producing different products which were separated by the deflection magnets in the corners following the experiments. Charged products were deflected according to their mass-to-charge ratio and could be detected with movable counting detectors [102] close to the stored ion beam. Positively charged ions were studied in experiments investigating ionization or dielectronic recombination [103]. The DR process produces neutral fragments which are not deflected in the bending magnets and propagated downstream the electron Target along the Beamline for Advanced

Molecular Breakup Investigations (BAMBI) [104] which is equipped with various detector systems which can all be used for DR investigations. The detectors in this beamline were protected by a beam shutter against high particle fluxes, e.g., during injection and synchrotron acceleration. For the merged-beams DR rate coefficient measurements of SH^+, a $10 \times 10\text{cm}^2$ surface barrier detector was used [104]. Fragment momentum imaging measurements (see Sect. 3.2) were carried out by two different detector systems: First, a 78 mm Micro-Channel Plate (MCP) detector with fast phosphor screen anode (P47) at a distance of 12.24 m with a high position resolution [105]. Second, an Energy-sensitive MUlti strip detector system (EMU) at a distance of 9.41 with worse position resolution [106, 107]. In this work, the MCP detector was used.

The reaction studies carried out at the successful TSR shall be expanded towards heavier molecular and cluster systems. On one hand, the electron cooling of heavier ions requires, according to Eq. 3.14, longer beam lifetimes. On the other hand, one likes to investigate molecular ions in an environment mimicking the harsh conditions found in interstellar media with temperatures typically below 100 K and particle densities of at best $10^6\,\text{cm}^3$ [12]. Both these criteria could be realized in an improved way in the CSR described in the following section.

3.1.5 Cryogenic Storage Ring

The Cryogenic Storage Ring CSR, shown in Figure 3.3 will serve in the future as platform for further storage ring experiments at the Max Planck Institute for Nuclear Physics in Heidelberg, Germany. The CSR is an electrostatic storage ring which can be operated at temperatures ranging from room temperature down to cryogenic temperatures of about 5 K at residual gas pressures below 10^{-13} mbar (RTE) (see Sect. 3.1.1). The electric rigidity of about 600 kV of the bending electrodes allows storage of heavy charged particles with energies up to 300 keV per unit charge q, which is considerably lower than the MeV energies at TSR. Its electrostatic design makes it well suited for investigations of heavy molecular or cluster systems. Until now, CSR is the worldwide largest fully electrostatic and cryogenic ion beam storage device. In addition, it features an electron cooler allowing phase-space cooling of the stored ions and merged-beam experiments with electron beams analog to its predecessor TSR.

CSR Ion Production and Acceleration

The beam energies of up to 300 keV/q do not necessarily require larger acceleration facilities and can be realized by extracting ions from a high-voltage platform at air. The high-voltage platform of CSR provides enough space to accommodate multiple different ion sources. The experimental program of CSR includes investigations of atomic, molecular and cluster ions with both positive and negative charge. Depend-

Figure 3.3: Photograph of the Cryogenic Storage Ring just before the first commissioning at room-temperature in spring 2014. The outer isolation vacuum chamber is still open. The beam-guiding chamber is wrapped in copper. The isolation vacuum chamber was closed before the storage operation.

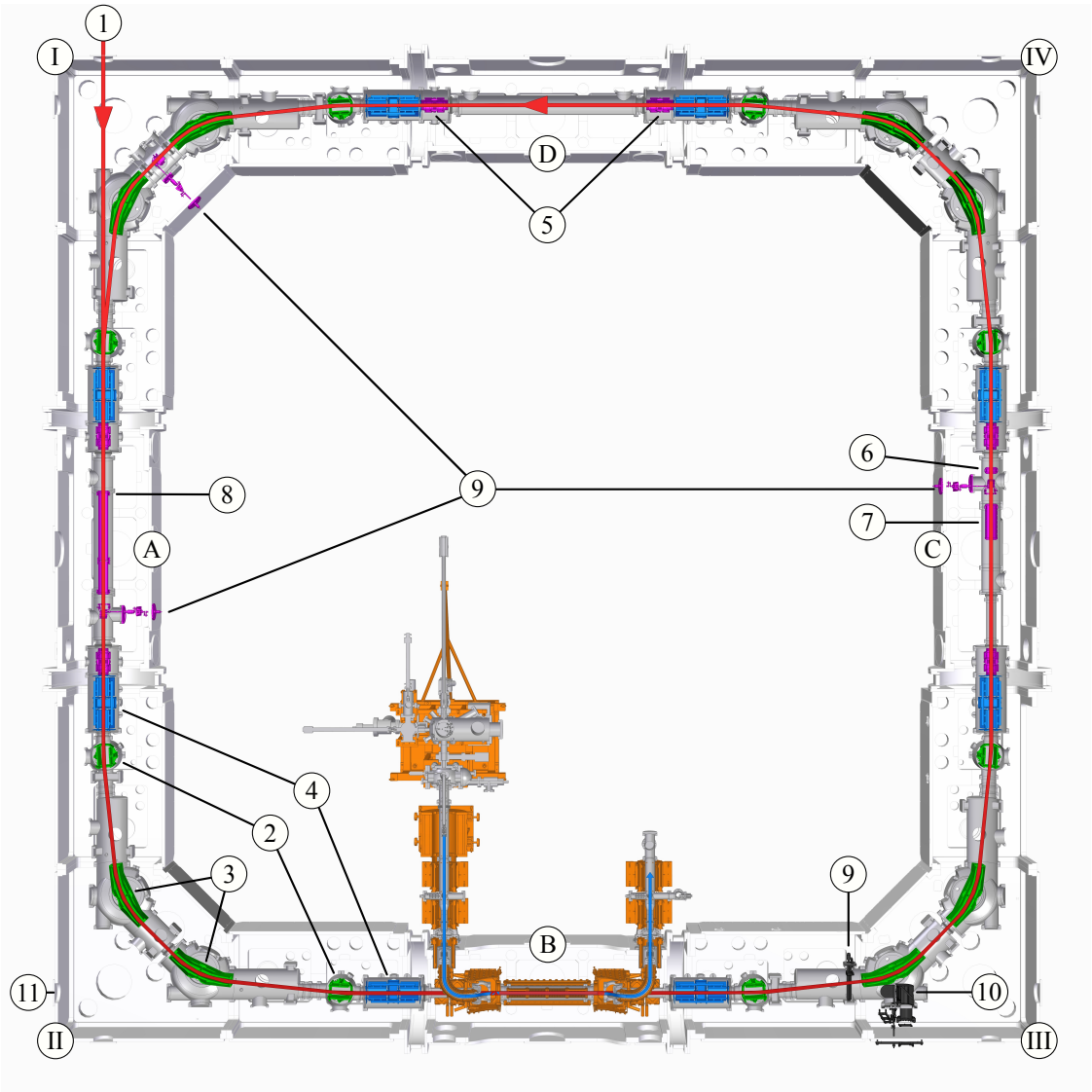

Figure 3.4: Overview model of CSR. After an ion beam (red) is injected into the CSR (1) it its confined on a closed orbit with electrostatic 6° (2) and 39° (3) deflector electrodes (green) and quadrupole doubletts focusing elements (blue) (4) in each corner. CSR features a variety of beam diagnostic devices (magenta) such as several pick-up electrodes for position (5), current (6) and Schottky-noise (7) measurements, three beam-viewers (9), and a RF-electrode (8) for bunching. Merged-beams experiments will be performed at an electron cooler (orange) in section (B) with detectors (black) for charged (9) and neutral (10) reaction products in corner (III). A ultraviolet (UV) light emitting diode (LED) (11) was installed in corner (II) for tests of the detectors even without stored ion beam. In the future, further linear sections will be equipped with a merged-beams experiment with neutral atomic beams in section (A) and a reaction microscope in section (D).

ing on the application different ion sources are used. Many systems can be ionized with a Penning ion source. Negative ions can be well produced with a Metal-Ion Sputter ion Source (MISS) source, positive ions with an Electron Cyclotron Resoncance (ECR) ion source, large biomolecular ions with an electrospray ionization (ESI) source, metal ion cluster clusters with a Laser VAPorization (LVAP) source. A 22-pole Radio-Frequency Quadrupole (RFQ) trap will allow the accumulation and internal-state cooling with buffer gas of the ions before they are injected into CSR. Most of these ion sources will be installed using a beam distribution station which is currently being developed.

CSR Design

Figure 3.4 shows an overview model of the vacuum chambers and electrodes of the CSR. The ring lattice has a quadratic four-fold symmetric layout with an ion beam orbit circumference of 35 m. In each corner a group of four electrodes bend the ion beam in total by 90°. The approximately 2.4 m-long straight sections between the corners have no ion-optical elements. This space is used for experimental instrumentation and ion beam diagnostics.

The CSR is an experimental platform for various reactions studies investigating the interaction dynamics of charged particles with photons, electrons and neutral particles. In order to separate the charged and neutral reaction products from the stored ion beam, the bending electrodes are divided into a mirror symmetric arrangement with each one 6° dipole deflectors at the end and two 39° dipole deflectors around the center of each corner. The ion beam is focused by two sets of quadrupole doublets before and after the array of bending electrodes. Charged products with an either altered mass or charge are deflected with respect to the closed orbit of the stored ion beam. They can be intercepted right next to the stored ion beam by movable detectors after the bending electrodes [108]. This way each bending electrode acts as a product mass-to-charge spectrometer. Neutral products are separated from the stored ion beam after the first 6° deflector.

For an ion beam injection one of the 6° electrodes is switched off. Before the first injected ions make a full revolution the same electrode is quickly switch on again. In this way, a long ion bunch is stored in the ring. After a few seconds storage time the injected bunch disperses into a continuous stored beam due to its intrinsic velocity spread, The first straight section after the injection corner houses a 1 m-long cylindrical electrode coaxial with the stored beam which can either be used for re-bunching of the stored ion beam by applying a radio-frequency with an appropriate amplitude modulation or for synchrotron acceleration and deceleration. This electrode also encloses the main interaction region of future atom-ion experiments.

The different beam diagnostic devices of CSR are distributed over the entire ring [109,110]. All straight sections, except the one reserved for the future electron cooler, have two pairs of capacitive position pick-up electrodes at the beginning and the end right before and after the quadrupole doublets. The diagnostic sections contain an ion current pick-up electrode and a Schottky-noise pick-up electrode.

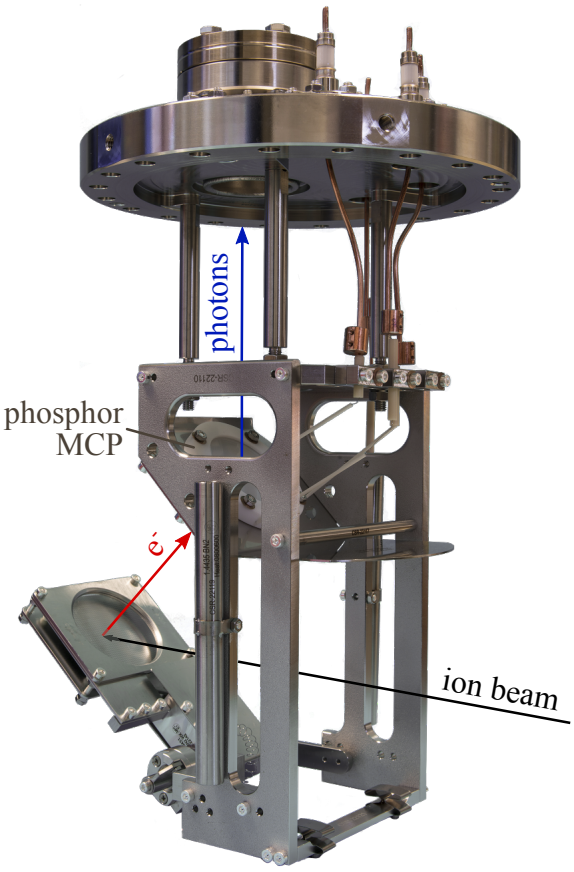

Figure 3.5: Photograph of beam profile monitor of CSR with schematic trajectories. The ion beam passes under an angle of 45° through a grid onto an aluminum plate on high potential. The released secondary electrons are accelerated trough the grid on ground potential towards an MCP with phosphor screen which is observed from outside of CSR's cryostat.

CSR Beam Profile Monitors

The spatial profile of the injected ion beam can be measured destructively at three different positions, marked 9 in Figure 3.4, during the first revolution by so-called *beam profile monitors*, which are also referred to as *first-turn diagnostics*. Those have been implemented for CSR within the scope of this work. The design is based on the beam diagnostics system developed for the REX-ISOLDE facility at CERN, Geneva, Switzerland [111, 112]. A first prototype for CSR was developed by T. Sieber [113] and tested at the CSR prototype CTF [76]. The first results of the beam profile monitors of CSR are reported in [109].

Two beam profile monitors are placed at ion-optically equivalent positions at the end of the first linear section (A) after the injection corner (I) and the opposite diagnostics section (C), respectively. The third beam profile monitor is placed in the injection corner in between the 39°-electrode where the beam has almost completed

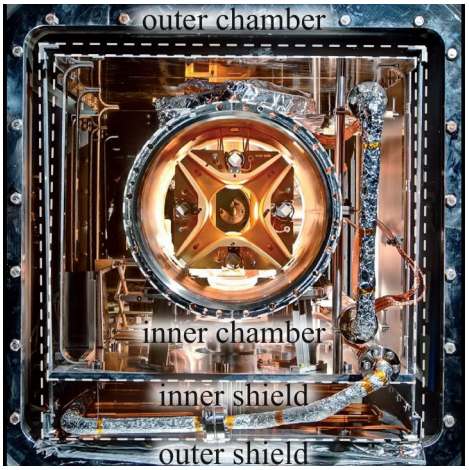

Figure 3.6: Thermal layers of CSR. In this picture, not all shield parts are assembled. The different layers are indicated by white dashed lines. The inner beam-guiding vacuum chamber is enclosed by an outer isolation vacuum chamber and is, in addition, encapsulated in two nested thermal radiation shields wrapped in multi-layer insulation. The inner chamber is mounted via titanium posts on the base plate of the inner thermal shield which in turn rests via titanium posts on the bottom of the outer chamber. The outer thermal shield is mounted via thin Inconel wires from the bottom of the base plate of the inner shield.

its first turn.

Each beam profile monitor has an aluminum converter plate that can be moved into the ion beam orbit. The ion beam produces secondary electrons on the converter plate which are accelerated towards a stationary MCP with phosphor screen anode, which is observed from outside of CSR's cryostat. The detection unit is a commercial solution (BOS-40 by Beam Imaging Solutions). Both the converter plate and the MCP are inclined by 45° with respect to the ion beam. This twofold projection under a 45° angle enables a direct, undistorted imaging of the beam profile.

The converter plate is being moved by a rotational mechanics, which is used for all movable components at CSR (see Section 5.2.3.3). The drive chain can be mechanically and, thus, thermally decoupled at several places to prevent any heat input. When the converter plate is retracted from the ion beam, its momentum is absorbed by titanium springs. The original design of the prototype converter plate holder was changed as it did not allow the specified acceleration voltage of up to −5 kV. The aluminum converter plate is mounted in a sandwich of stainless steal plates separated by ceramic pearls. The tungsten grid is fixed with a copper ring between two stainless steel plates with an according aperture for the ion beam.

CSR Vacuum and Cryostat System

In order to realize cryogenic ambient temperatures below 10 K the structure of CSR follows the design of a typical cryostat as shown in Figure 3.6 [114–116] which has been developed and tested at CSR's prototype facility CTF before [76, 117]. The beam-guiding ultra-high vacuum tube is enclosed by an isolation vacuum chamber, which prevents convection for a better thermal isolation. In addition, the inner chamber is encapsulated in two nested layers of infra-red radiation screens which were estimated in advance to be cooled down to 40 K and 80 K, respectively. In addition the outer shield is wrapped in multi-layer insulation by Ruag Space GmbH [118], which consists of multiple layers of highly reflective aluminum foil thermally

insulated by a thin fleece of glass fiber. The cutting pattern of this insulation was design in this work.

The inner chamber contains electrostatic ion optics and can be cooled down below 10 K through a superfluid helium circuit. In order to maintain the electrode adjustment in cold operation the electrodes are supported individually directly on the concrete foundation and are mechanically decoupled from the chambers via bellow tubes.

A particular challenge of CSR is that it can be both operated at room and cryogenic temperatures. In order to achieve sufficient UHV conditions (10^{-11} mbar) at room temperature, the inner beam pipe together with all beam-facing equipment is bakeable to 250 °C. However, the multi-layer insulation cannot withstand such high temperatures. During bake-outs, the temperature of the outer radiation shield is kept well below 100 °C with a water cooling system. At room temperature, the beam-guiding chamber is pumped by non-evaporative getter pumps (NEG), ion-getter and charcoal cryo-pumps. At cryogenic operation, these are supported by cryo-condensation pumps, cooled down to 2 K in order to bind hydrogen, reducing the vacuum pressure to better than 10^{-13} mbar RTE.

CSR has a non-magnetic design in order to avoid disturbances of the rather slow stored ion beams by stray or remnant magnetic fields, which could cause high beam losses or even inhibit a beam storage. Ion-optical simulations of CSR by M. Grieser have shown that a beam storage could be inhibited even by the earth magnetic field in the extreme case of light protons at the minimum beam energy of 20 keV [119]. For a future optional field correction all remnant magnetic fields should be avoided. For these reasons, all parts close to the ion beam orbit are specified to have a very low magnetic permeability of $\mu_r \leq 1.01$.

CSR Experiments

CSR is designed to combine the benefits of a low-energy, cryogenic molecular ion beam trap with those of a proven heavy ion storage ring. Consequently, the field-free, so-called *experimental* sections occupy a significant part of the CSR beam line. Already in the design phase, several target experiments have been conceived [120]. They include facility for fast ion-neutral collisions backed by a reaction microscope (ReMi), a collinear target beam line for slow ion-neutral collisions [121], as well as a merged electron-ion target and cooler section [110].

The newly developed electron-cooler is scheduled to be installed in CSR beginning of 2016. It will enable both phase-space cooling of the stored ion beam and merged-beams electron-ion experiments. A simplified model is shown in Figure 3.7 The Cooler will employ the photocathode from the TSR electron Cooler (see also Sect. 3.1.4 and [85]), including its magnetic expansion, which can provide very cold electron beams with kinetic energies down to 1 eV [122]. At a maximum ion storage energy of 300 keV this allows phase-space cooling of ion beams with masses up to 160 u [120] in a merged-beams interaction region with a length of about 1 m.

Apart from this, the new cooler is a complete redesign both regarding the merging

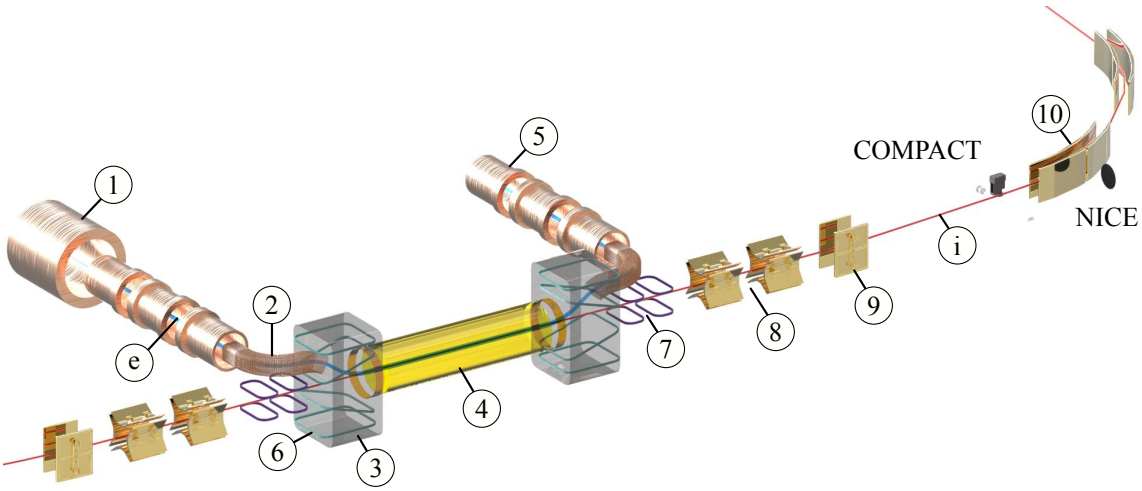

Figure 3.7: Simplified model of the CSR electron cooler showing only the beam guiding elements. In the future electron cooler the stored ion beam (i) is merged with a cold electron beam (e) by a combination of solenoid (1-5) and dipole fields (6). The deflection of the ion beam trajectory is compensated by additional dipole correction magnets (7) preceding and following the interaction section between the focussing quadrupoles (8). Reaction products are separated from the stored ion beam by the 6° and 39° deflectors (9,10). Charged products are detected with the movable COMPACT, neutral products with the static NICE detector.

and de-merging of the electron beam with the ion beam in cryogenic environment inside CSR as well as the transition from the electron emitting and collecting parts at room-temperature. The much lower storage velocities at CSR compared to TSR lead to relatively larger non-linear disturbances of the stored ion beam trajectory by the toroidal merging and de-merging fields [123].

As the electron cooler could not be finalized on time for the first cryogenic operation, a laser experiment was installed in the straight section marked (B) in Figure 3.4 for the first experiments [124]. This will be removed again when the electron cooler is installed. Meanwhile, it is planned to still use a laser in this section. It will be shoot in via adjacent ports behind the 6° deflectors originally foreseen for further detectors for changed products.

For these first experiments, a pulsed Optical Parametric Oscillator (OPO) laser (EKSPLA NT 342B with SH/SF generator) was used, covering a wavelength range from 192 nm to 2600 nm with repetition rates of up to 20 Hz and specified pulse energies of up to 30 mJ in the visible and 6 mJ in the UV range. The laser could be either shot in across the stored beam or at a grazing angle of about 3.4° for an elongated beam overlap of about 2.2 m. During the first beamtime, neutralization of stored ions by electron capture from the remaining residual gas was very unlikely given its very low gas density. In order to determine the ion storage time in CSR

photodetachment of negative ion species was observed. For this a cw-HeNe laser (632.8 nm) was coupled into section (B) using the same path as intended for the OPO Laser. It was possible to switch between both lasers with a flip mirror.

Furthermore, a merged-beams experiment for the interaction study of neutral atoms with the stored ions [121] will be installed in 2016. This experiment is located in the straight section following the injection. The atom beams are produced by photodetachment of a parent anionic ion beam, produced on a second platform with energies up to 60 keV, with an intense infrared laser.

CSR Detectors

At the commissioning in 2014 and the first cryogenic operation in 2015, two different detector systems were installed inside CSR in the corner section downstream of the future electron cooler (see Fig. 3.4). Neutral product particles can be detected by an imaging detector with a diameter of 120 mm situated straight ahead at a distance of 3.8 m with respect to the center of this straight section. This detector has been developed within the scope of this work and is described in detail in Chapter 5. With regard to its purpose the detector is referred to as NICE detector, which is a acronym for Neutral particle Imaging in Cryogenic Environment (NICE). It is placed next to the 39° electrode in corner, marked 10 in Figure 3.7, and its position is marked 10 in Figure 3.4. For the detection of charged collision products, a second movables particle counter [108, 125] was installed in CSR. These products can be intersected by a movable particle counter [108] at the according position next to the stored ion beam. This detector is referred to as Cryogenic Movable PArticle ConTer (COMPACT). The particles hit a bent aluminum converter plate and produce secondary electrons. These electrons are accelerated towards a small MCP where the particle event can be detected with a efficiency of >99 % for typical energies used at CSR. The detector is situated after the first 6°, right before the next 39° deflector. The chambers of CSR have ports after each bending electrode already foreseen for further detectors of this type. For the next beamtime in 2016, the port directly after the first 6° will be equipped with another detector of this type, which can detect even lighter reaction products.

CSR First Beamtimes

CSR was commissioned at room temperature from March to May 2014 [109]. During this first beamtime the storage ring has been tested and characterized with its beam diagnostics and detectors (see Sect. 3.1.5 and 5.4). The CSR components developed within this work, i.e., the beam profile monitors and, in particular, the NICE detector, were first tested within this commissioning beam time. Further tests were performed after the CSR cryogenic cooldown as described below.

After the first successful operation at room-temperature the storage ring was prepared for its first cryogenic operation. This included especially the manufacturing and installation of all missing diagnostic pick-up electrodes, temperature sensors, thermal shields, and the full enclosure in Mylar superinsulation. Finally, CSR was

operated at cryogenic temperatures for the first time between March and July 2015. Several atomic, molecular and cluster ions have been investigated already in this first beamtime. Besides comparative performance measurements with Ar^+ and O^-, two first showcase experiments were performed investigating the photodetachment of OH^- [124] and the photodissociation of CH^+. Both experiments were conducted using the merged laser-ion interaction section installed in place of the future electron cooler. Hence the already installed detector array intended for future electron target measurements could be employed during these laser-experiments. The large MCP-based neutral product detector developed within this work, and described in Chaper 5, was especially useful in this first experimental run of CSR. In both the OH^- and the CH^+ experiments, the molecular rotational population density can be determined as a function of laser frequency which reflects directly the internal temperature of the stored molecular ions and indirectly the ambient photon field of the storage vessel. In this manner, CSR's capability of storing internally cold ions could be demonstrated. Several other systems have been studied, which are being analyzed, e.g., carbon and silver dimer anions as well as the Cobald clusters Co_2 and Co_3 were investigated for their autodetachment and -dissociation as well as photon induced processes.

3.2 Neutral Fragment Momentum Imaging

Fragmentation reactions lead to explosions of molecules in their center-of-mass frame. Besides the total energy-dependent reaction cross section, an important parameter of such reactions is their energy balance, especially, in the context of astrochemical networks (see Sect. 2.1). This contains information about the structure and the different reaction pathways of the molecule. The kinetic energy release (see Sect. 2.2.3), characteristic for the fragmentation, is distributed among the fragments due to the conservation of momentum according to their mass ratios. Fragmentation reactions with charged products can be investigated kinematically complete with, e.g., Velocity Map Imaging (VMI) [126] techniques or reaction microscopes [127–129]. However, reactions with neutral fragments, such as dissociative recombination (see Sect. 2.2.3), cannot be investigated with these methods. In merged-beams experiments at storage rings, the kinetic energy release can be measured with the so-called *neutral fragment momentum imaging*, or short *fragment imaging*, method [130]. In the following, the basic concept of this method is explained based on the simple case of diatomic molecules. The kinematics of such an experiment is illustrated in Figure 3.8.

The energy excess of a dissociation reaction can go partly into internal excitations of the product fragments in, possibly, excited quantum states and is partly released

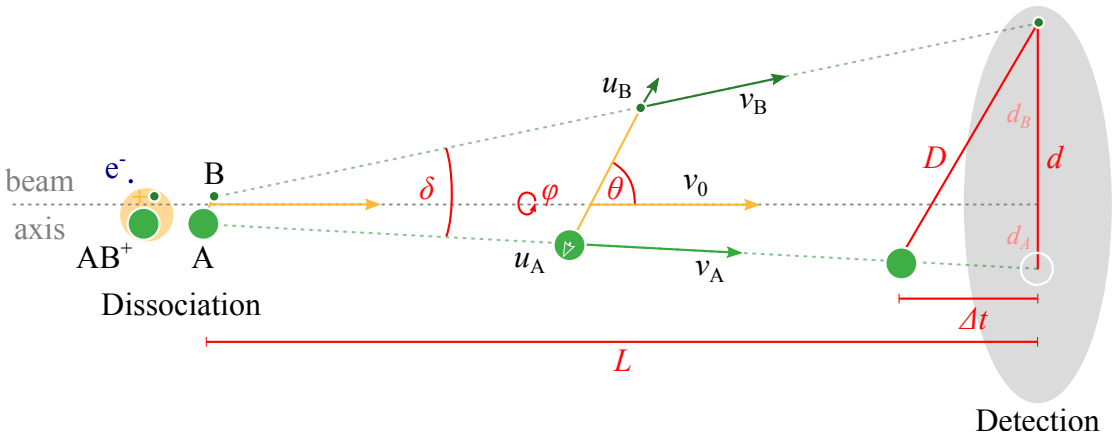

Figure 3.8: Schematic reaction kinematics of DR investigated with neutral fragment momentum imaging. The heteronuclear molecular ion AB^+ recombines with an electron and, subsequently, dissociates into two neutral fragments A and B. At the detector position, the two fragments are separated by the distance D which is proportional to $\sqrt{E_{\mathrm{KER}}}$. The momentum is partitioned amongst the fragments according to their mass ratio. The molecular ions have a random orientation in the azimuthal angle φ and the polar angle θ with respect to the beam axis. The latter determines the distance d and arrival-time-distance Δt of the two particle impacts on the detector. In reality, the distance to the detector L is much larger compared to the fragment distances D, so that d and Δt can be derived as orthogonal projections.

in form of kinetic energy E_{KER} of the product fragments. The different dissociation channels with the corresponding quantum states of the products are denoted by n. The momentum transfer leads to the relative fragment velocity

$$v_{\mathrm{r},n} = |\vec{u}_{\mathrm{A},n} - \vec{u}_{\mathrm{B},n}| = \sqrt{\frac{2\,E_{\mathrm{KER},n}}{\mu}} \tag{3.23}$$

with the reduced mass of the two fragments

$$\mu = \frac{m_{\mathrm{A}}\,m_{\mathrm{B}}}{m_{\mathrm{A}} + m_{\mathrm{B}}} = M\frac{r}{(1+r)^2} \tag{3.24}$$

with fragment masses m_{A} and m_{B}, and their mass ratio $r = {}^{m_{\mathrm{A}}}/_{m_{\mathrm{B}}}$, assuming the momentum transfer from the electron capture to be negligible. The center-of-mass of the two product fragments still propagates with the velocity of the parent ion beam

$$v_0 = \sqrt{\frac{2\,E_0}{M}} \tag{3.25}$$

which is determined by the kinetic energy E_0 and the total mass $M = m_{\mathrm{A}} + m_{\mathrm{B}}$ of the stored molecular ion beam. When the center-of-mass of the two fragments reaches the detector position at the distance L after the time-of-flight t_{TOF}, the two fragments are separated by the distance D_n. As $E_{\mathrm{KER}} \ll E_0$, the dissociation angle θ in the center-of-mass frame is kinematically compressed to the angle δ in the laboratory frame, which can be derived from the time-of-flight relations

$$t_{TOF} = \frac{L}{v_0} = \frac{D_n}{v_{\mathrm{r},n}} \tag{3.26}$$

to

$$\delta_n = \frac{D_n}{L} = \frac{v_{\mathrm{r},n}}{v_0} = \sqrt{\frac{E_{\mathrm{KER},n}}{E_0}\frac{M}{\mu}} = \sqrt{\frac{E_{\mathrm{KER},n}}{E_0}}\frac{r+1}{\sqrt{r}}. \tag{3.27}$$

The kinetic energy release of the dissociation channel n can then be determined as

$$E_{\mathrm{KER},n} = \frac{1}{2}\mu\,(\delta_n v_0)^2 = \frac{1}{2}\mu\left(\frac{D_n}{L}v_0\right)^2 \tag{3.28}$$

The molecules in the electron target are not aligned, thus, have a random orientation. In the center-of-mass frame, all relative coordinates of a dissociation with the same $E_{\mathrm{KER},n}$ then lie on a sphere of diameter D_n which transforms, in the laboratory frame, into two narrow cones of diameter $2d_{\mathrm{A}}$ and $2d_{\mathrm{B}}$ at the detector position L. This way, all fragments can be detected, independent of their break-up geometry, on an area of compact dimensions. The projection of the reaction sphere onto the plane detector can be considered orthogonal assuming the small angle approximation with $D \ll L$ and consequently $\delta \ll 1$. The dissociation angle θ (see Fig. 3.8) determines

the corresponding transversal fragment distances d and the longitudinal arrival-time-differences Δt at the detector with

$$d = D\sin(\theta) \tag{3.29}$$

$$\Delta z = D\cos(\theta) = v_0 \Delta t \tag{3.30}$$

$$\Rightarrow D = \sqrt{d^2 + \Delta z^2} = \sqrt{d^2 + v_0^2 \Delta t^2} \tag{3.31}$$

Measurable Kinetic Energy Release

As mentioned before, the kinetic energy release E_{KER} is partitioned amongst the fragments according to their mass ratio. In the case of heteronuclear diatomic molecules this results in larger relative velocities of the lighter fragments and, accordingly, larger dissociation cones at the detector position. If both fragments shall be detected, the maximum kinetic energy release that can be measured, decreases with larger mass ratios as the dissociation cone of the light fragments increase beyond the solid angle covered by the detector. Only the heavy fragment can be detected in this case. Going to more complex polyatomic molecular ions means on one hand, typically, a higher parent molecule mass which leads to lower ion beam velocities and, accordingly, larger dissociation cones. On the other hand, E_{KER} is partitioned amongst more fragments resulting in smaller dissociation cones. In the following, the limits for the detection of both and heavy fragments only in a diatomic fragmentation are discussed for TSR and CSR given their geometrical and energetic constrains.

The fragment distance of a diatomic molecule projected onto the detector surface is, as depicted in Figure 3.8, the sum of the distances of both product fragments $d = d_{\mathrm{A}} + d_{\mathrm{B}}$ with respect to the center-of-mass. With the momentum balance $d_{\mathrm{A}} m_{\mathrm{A}} = d_{\mathrm{B}} m_{\mathrm{B}}$ the distance of the heavier fragment A to the center-of-mass can be expressed as

$$d_{\mathrm{A}} = \frac{d}{1 + \frac{m_{\mathrm{A}}}{m_{\mathrm{B}}}}. \tag{3.32}$$

Given a detector with diameter d_{max}, the geometrical limit for detection of only the heavier of both product fragments is

$$d_{\mathrm{max}} = 2\, d_{A,\mathrm{max}} \left(1 + \frac{m_{\mathrm{A}}}{m_{\mathrm{B}}}\right). \tag{3.33}$$

Figure 3.9 shows the maximum E_{KER} that can be measured in case of heteronuclear diatomic molecules with different mass ratios at TSR and CSR. The corresponding expressions for E_{KER} are given in the caption. This representation assumes an well-cooled, narrow stored ion beam, which is well-aligned with the detector center. With larger mass ratios of the fragments the maximum E_{KER} for which both fragments can be still detected is significantly reduced as the dissociation cone of the lighter fragment gets too large to fit onto the detector area. The size of the dissociation cones can be reduced by higher ion beam energies which in turn enables measure-

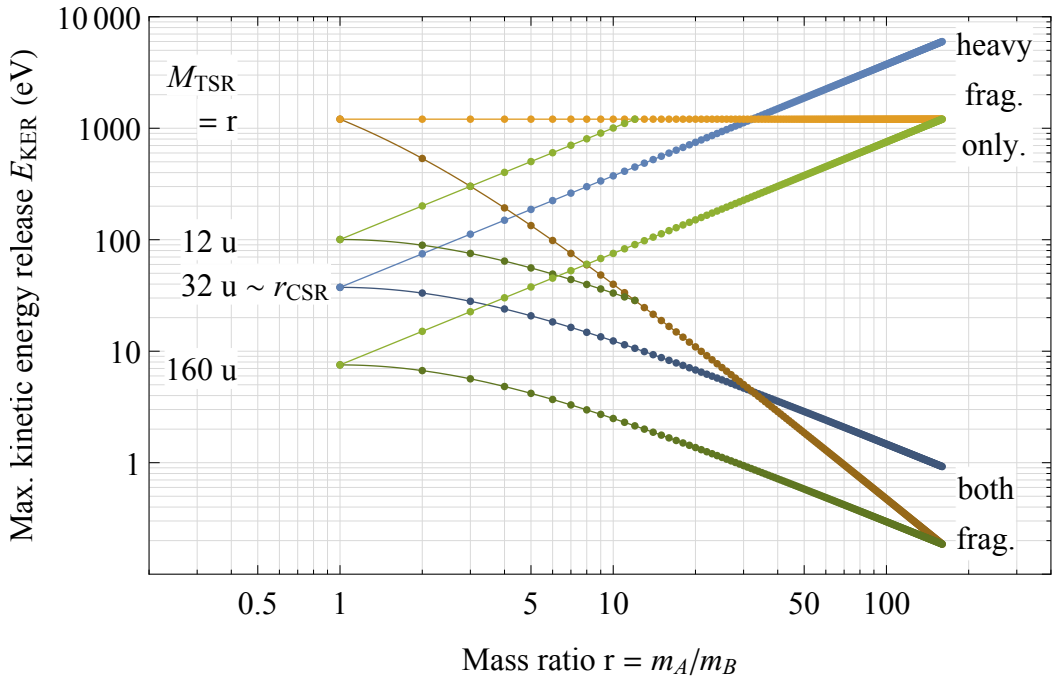

Figure 3.9: Maximum kinetic energy release E_{KER} that can be measured for diatomic heteronuclear molecules of mass M and mass ratio r at TSR (green) and CSR (blue). This is limited by the maximum possible storage energies, which are limited by the corresponding rigidities ($B\rho \sim 1.5\,\mathrm{Tm}$ and $E\rho \sim 600\,\mathrm{kV}$), and the maximum δ_{max}, which is geometrically constrained, according to Eq. 3.27, by the available detector diameter D_{max} and maximum Target distance $L_{\mathrm{max}} = L_0 + \Delta L/2$ ($\delta_{\mathrm{max}}^{\mathrm{TSR}} \sim 1/160$ and $\delta_{\mathrm{max}}^{\mathrm{CSR}} \sim 1/36$). The corresponding expressions for the maximum E_{KER}, derived from the Equations 3.28, 3.24, 3.5, and 3.33, are given in the table below for the different cases. The maximum E_{KER} is only displayed for molecular masses up to $M = 160\,\mathrm{u}$, which is the maximum mass, that can be still cooled with the electron Cooler at CSR. The extreme case of diatomic hydride molecules with $M = r$ at TSR is highlighted in orange. The maximum E_{KER} at CSR, which is highlighted in blue, behaves with mass ratio for any molecular mass M the same way as at TSR for a molecule of mass $M = 32\,\mathrm{u}$. Hence, CSR will exceed TSR's capabilities for molecular system heavier than SH^+.

Maximum E_{KER}	TSR	CSR
Both fragments	$\frac{1}{2}\frac{1}{M}\frac{r}{(r+1)^2}\left(\frac{d_{\mathrm{max}}}{L_{\mathrm{max}}}\right)^2 (q\,B\rho)^2$	$\frac{1}{2}\frac{r}{(r+1)^2}\left(\frac{d_{\mathrm{max}}}{L_{\mathrm{max}}}\right)^2 (q\,E\rho)$
Heavy fragment	$\frac{1}{8}\frac{1}{M}\quad r\quad\left(\frac{d_{\mathrm{max}}}{L_{\mathrm{max}}}\right)^2 (q\,B\rho)^2$	$\frac{1}{8}\quad r\quad\left(\frac{d_{\mathrm{max}}}{L_{\mathrm{max}}}\right)^2 (q\,E\rho)$

ments of larger kinetic energy releases. However, the maximum storage velocities are limited by the available magnetic or electric rigidity, respectively, according to Equation 3.5. Another limiting factor is the maximum dissociation angle in the laboratory frame $\delta_{\max}$ (see Eq. 3.27) for the available detector diameter $d_{\max}$ and the given maximum distance to the Target $L_{\max} = L_0 + \Delta L$, with the the distance of the detector to the center of the Target L_0 and the overlap length, which is for both TSR and CSR $\Delta L \sim 1$. The detector for the experiments at CSR has been developed in this work (see Chap. 5). A detector with 12 cm at a distance of about 3.8 m from the center of the electron target has been implemented. For the DR experiments at TSR a detector with 8 cm diameter at a distance of about about 12.2 m has been used.

In this work, the heteronuclear SH^+ ion with mass $M(SH^+) \sim 33$ u has been investigated at TSR, which is reported in Chapter 4. In this case, most of the light hydrogen fragments missed the detector, although the storage ring was operated at the highest possible storage energy. For the data analysis a new method has been developed for the determination of the product state branching ratios from the position informations of only the sulfur fragments, which is presented in Section 4.4. As shown in Figure 3.9, the maximum E_{KER} at CSR behaves with mass ratio for

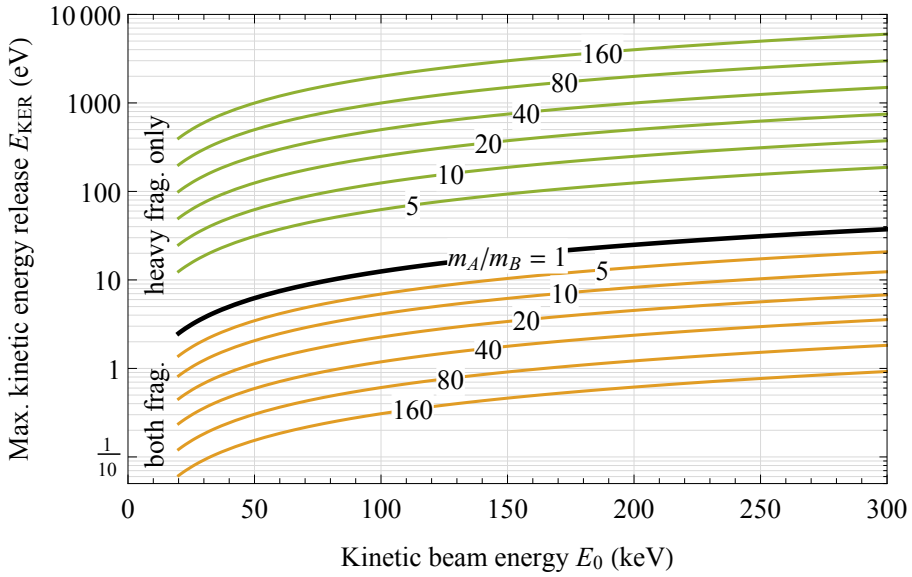

Figure 3.10: Maximum kinetic energy release which can be measured for diatomic molecules as a function of the ion beam energy for CSR. The limiting case of homonuclear molecules with a mass ratio $r = {}^{m_A}/_{m_B} = 1$ is emphasized by the black solid line. As the momentum is distributed among the fragments according to their mass ratio, the maximum measurable E_{KER} decreases if both fragments shall be detected (orange). In turn, it increases if only the heavier fragment is detected (green). In the extreme case of diatomic hydride molecules the mass ratio can be read directly as the mass of the heavier binding partner.

any molecular mass M the same way as at TSR for a molecule of mass $M = 32\,\mathrm{u}$ and will exceed TSR's capabilities for molecular system heavier than SH^+.

With regard to the future DR experiments at CSR, its maximum measurable kinetic energy release for diatomic molecules in the available ion beam energy range is depicted in Figure 3.10. For homonuclear systems the maximum E_{KER} is limited to roughly 30 eV at the maximum kinetic beam energy $E_0 = 300\,\mathrm{keV}$. The ion beam energy should be adjusted such that, preferably, the whole detector area is used in order achieve an optimal resolution of the kinetic energy release. The maximum measurable E_{KER} decreases if both fragments shall be detected and, in turn, increases if only the heavier fragment is detected.

Fragment Mass Identification

If the imaging detector does only provide position sensitivity, fragments of different masses can be identified geometrically for a well localized, cooled ion beam of narrow diameter and small divergence as the fragment distances to the center-of-mass scale with their mass ratios (see Sect. 4.4.3.1). For polyatomic systems this becomes increasingly difficult and is not viable in some cases. Here, a detection system with both position and energy sensitivity has the advantage that the fragment masses can be inferred from the detected energies as the well defined kinetic energy of a dissociating molecular ion is distributed among its fragments according to their mass ratios.

Distance Probability Distributions

The various distance probability distributions of fragment distances in a merged-beams experiment are, e.g., derived in the Theses of S. Novotny [131, 132] or by Amitay et al. [50] and are schematically depicted in Figure 3.11. In the following, only isotropic dissociations are considered.

The probability distribution of the absolute fragment distance of each dissociation channel n with dissociation angle δ_n is

$$P_n(D) = \begin{cases} \frac{1}{\delta_n \Delta L} & \text{for } \delta_n L_{\min} \leq D \leq \delta_n L_{\max} \\ 0 & \text{otherwise} \end{cases} \tag{3.34}$$

given the finite interaction length ΔL and the boundaries of the electron Target, for the distance to its center L_0,

$$\begin{aligned} L_{\min} &= L_0 - \Delta L/2 \\ L_{\max} &= L_0 + \Delta L/2 \end{aligned} \tag{3.35}$$

This requires the reconstruction of the absolute fragment distance from both the transversal and longitudinal projections, d and Δz, onto the detector. If either one of those is missing or cannot be measured correlated, they have to be consider

independently with

$$P_n(d) = \begin{cases} \frac{1}{\delta_n \Delta L}\left[\arccos\left(\frac{d}{\delta_n L_{\max}}\right) - \arccos\left(\frac{d}{\delta_n L_{\min}}\right)\right] & \text{for } 0 \le d \le \delta_n L_{\min} \\ \frac{1}{\delta_n \Delta L}\left[\arccos\left(\frac{d}{\delta_n \Delta L_{\min}}\right)\right] & \text{for } \delta_n \Delta L_{\min} < d \le \delta_n \Delta L_{\max} \\ 0 & \text{otherwise} \end{cases} \tag{3.36}$$

and for the longitudinal distance $\Delta z = v_0 \Delta t$, given the arrival-time difference Δt,

$$P_n(z) = \frac{1}{2\,\delta_n\,L} \begin{cases} \ln\left(\frac{L_{\max}}{L_{\min}}\right) & \text{for } 0 \le |\Delta z| \le \delta_n L_{\min} \\ \ln\left(\frac{\delta_n L_{\max}}{|\Delta z|}\right) & \delta_n L_{\min} \le |\Delta z| \le \delta_n L_{\max} \\ 0 & \text{otherwise.} \end{cases} \tag{3.37}$$

The kinetic energy releases of the different dissociation channels can be determined by fitting the total probability distributions

$$P(d) = \sum_n b_n P_n(d), \tag{3.38}$$

$$P(\Delta z) = \sum_n b_n P_n(\Delta z), \text{ or} \tag{3.39}$$

$$P(D) = \sum_n b_n P_n(D). \tag{3.40}$$

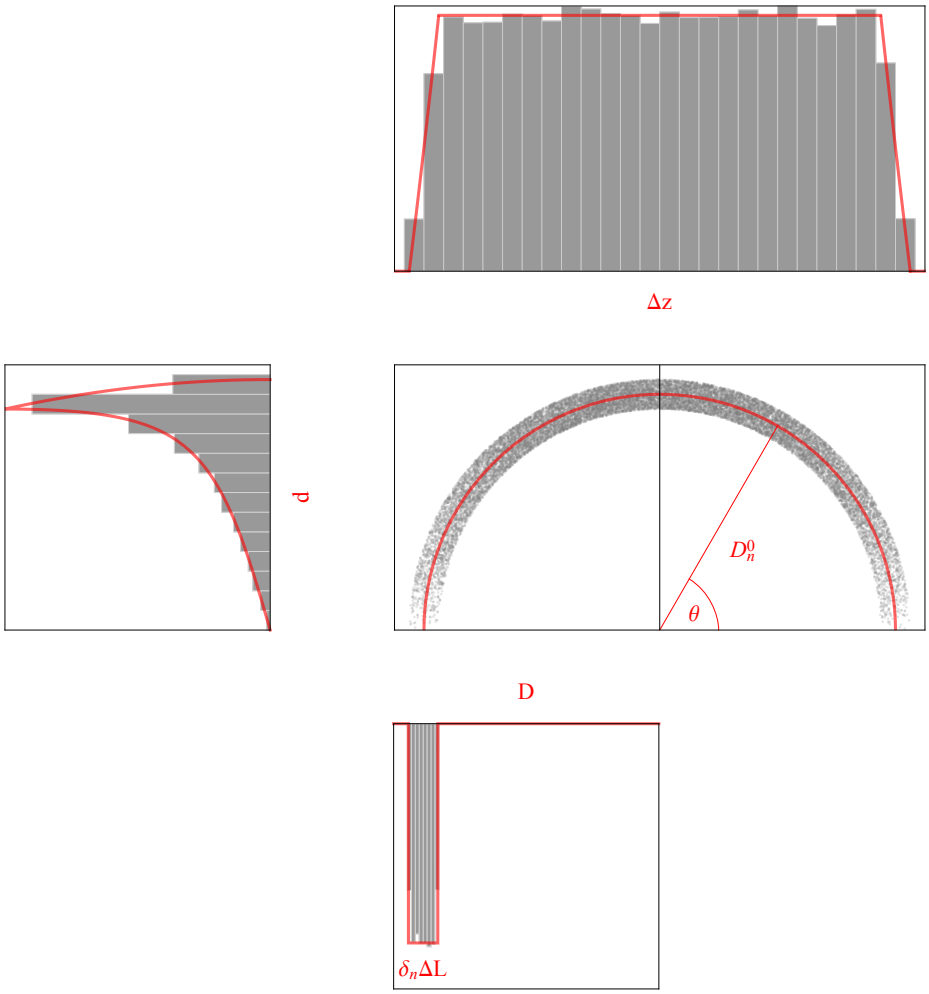

Figure 3.11: Schematic distance distributions of fragment momentum imaging. The graph in the center shows the transversal fragment distance d versus the longitudinal fragment distance Δz, which describes a half circle with radius D_n^0, corresponding to the Target center. The graphs on the top and left show the respective projections. An integration over the azimut angle θ results in the distribution of fragment distances D on the bottom. The width of this distribution is caused by the given length of the interaction region ΔL and scales with the dissociation angle δ_n. Looking at the transversal projection of the reaction sphere of dissociation fragments onto the detector, the density of events is increasing towards the edge of the sphere. The length of the interaction section ΔL leads to a superposition of reaction spheres of different sizes around D_n^0, which results in the characteristic saw-tooth shape of the transversal projection.

4 Dissociative Recombination of SH^+

Diatomic hydride molecules are among the most simple molecules in the interstellar medium. The most fundamental sulfur-bearing molecular ion *sulfanylium* SH^+ forms the basis of the interstellar sulfur chemistry. The role of SH^+ in the chemistry of interstellar media was already discussed at the beginning of Chapter 2. As mentioned before, the observed abundances of SH^+ have been underestimated in several astrophysical studies by a factor of four [10] and even by an order of magnitude [9], respectively. One of the reasons for these discrepancies could be an underestimated reaction rate for dissociative recombination of SH^+, the dominant destruction process in the presence of low-energy electron collisions (see Sect. 2.2.3).

Within the scope of this work, the first experimental investigations on dissociative recombination of SH^+ have been performed in a merged-beams experiment (see Sect. 4.2) at the TSR in Heidelberg, Germany, which is described in detail in Section 3.1.4. In two complementary measurements the merged-beams DR rate coefficient (see Sect. 4.3) and the product state branching ratios (see Sect. 4.4) have been determined.

SH^+ is one of the heaviest diatomic molecules which has ever been investigated at TSR. In addition, SH^+ has a considerably large reaction energy release of about 6.8 eV. As explained in Section 3.2, due to the momentum distribution among the two fragments with a large mass ratio and the limited kinetic beam energy at TSR most of the light hydrogen fragments missed the detector. Nevertheless, the product state branching ratios could be determined with a new analysis procedure from the obtained imaging data. In this sense, these measurements also pose as a test case in view of future DR experiments at CSR, where even heavier molecules will be investigated.

In the following Section, some properties of SH and SH^+ are discussed, which are relevant for the physical discussion of the results of the merged-beams DR rate measurements in Section 4.3.5 and the momentum imaging measurements in Section 4.4.4.

4.1 Properties of SH^+

At this point the expected DR pathways and the involved energies (see Sect. 2.2.3) of the investigated system are discussed. The reaction energy ΔE_{DR} of SH^+ DR is defined as the kinetic energy released by the dissociation from ground state SH^+ into ground state products S and H for a collision energy of 0 eV. There are multiple ways to determine this energy release. First, it was calculated via the asymptotic dissociated system $S + H^+$ with the value of the proton affinity of sulfur E_{PA} at

300 K, considering its temperature correction to 0 K, and the ionization energy of hydrogen E_I as

$$\Delta E_\mathrm{DR}(\mathrm{SH}^+) = E_\mathrm{PA}^{300\,\mathrm{K}}(S) - \frac{5}{2} k_\mathrm{B}\, 300\,\mathrm{K} - E_\mathrm{I}(\mathrm{H}) = (-6.78 \pm 0.10)\,\mathrm{eV} \tag{4.1}$$

Alternatively, the reaction energy can be calculated via the asymptotic dissociated system $\mathrm{S}^+ + \mathrm{H}$ with the dissociation energy of the $v = 0$ ground state $D_0 = D_e - {}^1\!/_2\, hc\,\omega_e$ of SH^+ and the ionization energy of sulfur as

$$\Delta E_\mathrm{DR}(\mathrm{SH}^+, \mathrm{X}^3\Sigma^-) = D_0(\mathrm{SH}^+) - E_\mathrm{I}(\mathrm{S}) = (-6.82 \pm 0.01)\,\mathrm{eV} \tag{4.2}$$

The specified uncertainty of this value is estimated from the number of significant digits of the underlying dissociation energy value D_e, which might be too low. Considering this, the two values are consistent within 0.4 eV. The reference values for these calculations are listed in Table 4.1.

For a given reaction energy, the energetically accessible product excited states can be determined. In case of SH^+, the reaction energy is sufficient to excite the sulfur products into their $^1\mathrm{D}_2$, $^1\mathrm{S}_0$ and $^5\mathrm{S}_2$ levels. However, it is not enough for an excitation to $\mathrm{H}(n = 2)$. The kinetic energy releases of the different product excited states can be determined as

$$\mathrm{KER} = -\left(\Delta E_\mathrm{DR} + E_E(S)\right). \tag{4.3}$$

The asymptotic levels of these states are depicted in the right hand part of Figure 4.1. They were calculated with respect to the ground state of SH^+ via the reaction energy of DR and the well known excitation energies E_E of sulfur from the NIST Atomic Spectra Database [133], also listed in Table 4.2, as

Potential energy curves of both the neutral SH and ionic SH^+ were calculated by Park and Sun [137] in 1992. These curves are shown in Figure 4.1 and shall

Table 4.1: Reference values for reaction energy calculations.

Parameter	Symbol	Value	Ref.
Ionization energy	$E_\mathrm{I}(\mathrm{H})$	13.598 434 005 136(12) eV	[133]
	$E_\mathrm{I}(\mathrm{S})$	10.360 01(12) eV	[134]
Proton affinity	$E_\mathrm{PA}^{300\,\mathrm{K}}(\mathrm{S})$	664.3(80) kJ/mol	[135]
		6.885(83) eV	
Dissociation energy	$D_e(\mathrm{SH}^+)$	3.70 eV$^{(*)}$	[136]
Vibrational constant	$\omega_e(\mathrm{SH}^+)$	2547.7 cm^{-1}	[136]

$^{(*)}$ Rostas et al. give a two-digit number for the dissociation energy without error estimate.

Table 4.2: Product excitation states for DR of ground state SH^+ at an electron-ion collision energy of 0 eV. The KER values of the different product states are determined with Eq. 4.3 for the reaction energies according to Eq. 4.1 ($KER^{(1)}$) and Eq. 4.2 ($KER^{(2)}$) and the sulfur excitation energies $E_E(S)$ from [134]. The product excited states with negative KER become energetically accessible, when the collision energy exceeds its absolute KER value.

Product state			$E_E(S)$	$KER^{(1)}$	$KER^{(2)}$
H	S		(eV)	(eV)	(eV)
$1s\,^2S_{1/2}$	$3s^23p^4$	$^3P_2$	0.000	6.78	6.82
$1s\,^2S_{1/2}$	$3s^23p^4$	$^3P_1$	0.049	6.73	6.77
$1s\,^2S_{1/2}$	$3s^23p^4$	$^3P_0$	0.071	6.71	6.75
$1s\,^2S_{1/2}$	$3s^23p^4$	$^1D_2$	1.145	5.63	5.67
$1s\,^2S_{1/2}$	$3s^23p^4$	$^1S_0$	2.750	4.03	4.07
$1s\,^2S_{1/2}$	$3s^23p^3(^4S^\circ)4s$	$^5S^\circ_2$	6.524	0.25	0.29
$1s\,^2S_{1/2}$	$3s^23p^3(^4S^\circ)4s$	$^3S^\circ_1$	6.860	−0.08	−0.04
$1s\,^2S_{1/2}$	$3s^23p^3(^4S^\circ)4p$	$^5P^\circ_{1,2,3}$	7.866	−1.09	−1.05
$1s\,^2S_{1/2}$	$3s^23p^3(^4S^\circ)4p$	$^3P^\circ_{0,1,2}$	8.045	−1.27	−1.23

indicate possible dissociation pathways for a first interpretation of the experimental results obtained in this work. The asymptotic energies of these potentials show significant discrepancies compared to the asymptotic values calculated according to Equation 4.1 with the values listed in Table 4.2. For the generation of the depicted curves, the numerical values of the calculated potentials, given in [137], were interpolated in second order. The zero energy in Figure 4.1 was set to the ground state level of SH^+. The vibrational ground state in the SH^+ $X\,^3\Sigma^-$ potential of Park and Sun was then put to this zero energy, shifting all other energies of their calculated curves by the same amount. In their calculation, Park and Sun were focusing on the valence orbitals of SH and considered the possible configuration interaction with higher excited neutral molecular levels only in a later step of their paper, independent of the potential curves shown. In contrast to Park and Sun, the admixture of higher excited configurations was taken into account for some of the states in the more recent calculations by Kashinski et al. [41, 42]. They show a strong interaction of the dissociating $^2\Pi$ curve of SH (see Fig. 4.1) with configurations involving $n = 4$ Rydberg states (see Fig. 6 in [41]). The associated highly excited neutral potential curves can give rise to vibrationally excited Rydberg levels driving the DR process. Also, they may serve as pathways to the highly excited $S(^5S_2)$ state, which lies only about 0.27 eV below the ionization limit of SH. Moreover, there is an excited sulfur product level ^3S only about 0.6 eV above the ionization limit of SH, which becomes energetically accessible for DR at sufficiently large collision energies. Investigations of similar systems have shown that such states often contribute as they become energetically available [139].

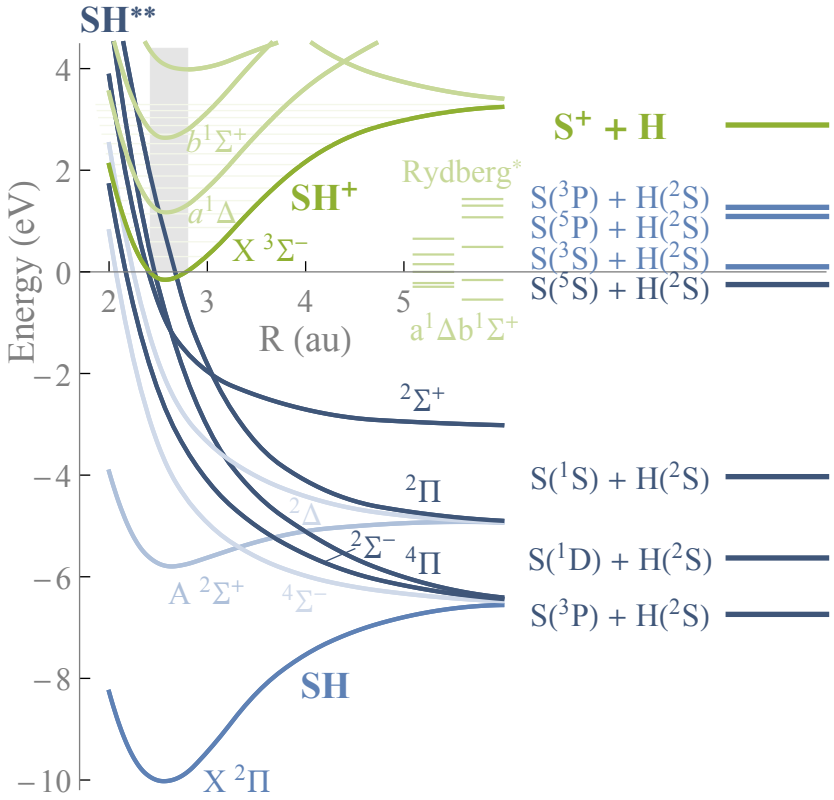

Figure 4.1: Potential energy curves of SH (green) and SH^+ (blue) by Park and Sun [137]. The numerical values of the potential curves given in that paper were interpolated in 2nd order. However, some of these values needed to be slightly adjusted in order to match the curves depicted in their paper. In addition, the vibrational levels of the $X\,^3\Sigma^-$ potential are indicated. The Frank-Condon region of the SH^+ $X^3\Sigma^-$ ground state is highlighted by a gray bar. The energy levels of SH Rydberg states, measured by Lange et al. [138], are indicated for the electronically excited $a^1\Delta$ and $b^1\Sigma^+$ states of SH^+. On the right hand side are the asymptoic energies for dissociated S and H fragments obtained by Equation 4.1 with the values listed in Table 4.2.

As shown from the approximative molecular results in Figure 4.1, the ground state of SH^+ can be expected to be crossed by both the $^2\Pi$ and $^4\Pi$ doubly-excited repulsive SH valence states which lead to the excited sulfur products $S(^1D)$ and sulfur in the ground level $S(^3P)$, respectively. In comparison, the $^2\Pi$ state has a more favorable Franck-Condon overlap, which suggest stronger direct contributions from this state. The repulsive state $^2\Sigma^+$, corresponding to the $S(^1S)$ product state, appears to have no Franck-Condon overlap, which may prevent a direct contribution from this state. An indirect dissociation via this state may be still possible with a preceding capture into a vibrationally excited Rydberg state or a direct non-adiabatic coupling. Fur-

ther indirect pathways via core-excited Rydberg state may also be possible. Some of these neutral autoionizing molecular Rydberg states were observed by Lange et al. [138] with two-photon resonance enhanced multi-photon ionization spectroscopy. The energies of bound Rydberg states of the series converging to the electronically excited $a^1\Delta$ and $b^1\Sigma^+$ states of SH^+ are also shown in Fig. 4.1. Especially, two Rydberg states converging to the $a^1\Delta$ state of SH^+ are closely above the ionization limit of SH and may facilitate DR via a capture into these core-excited Rydberg states as observed before, e.g., by Amitay et al. [49, 50].

4.2 Experiments at the Test Storage Ring

The Test Storage Ring was already introduced in Section 3.1.4. Various aspects of the experimental setup and technique have been described in detail, e.g, by Amitay et al. [50], Wolf [140], Krantz et al. [100], and Novotný et al. [87, 141]. At this point, aspects specific to the investigations of SH^+ are discussed.

4.2.1 Setup

The SH^+ ions were produced in a Penning ion source from a gas mixture of hydrogen sulfide H_2S and molecular hydrogen H_2 and accelerated in a 3 MV pelletron accelerator [94]. An SH^+ ion beam of typically 100 μA was stored in TSR at an energy of (2.649 ± 0.010) MeV and merged with a cold electron beam in the electron Target (see Sect. 3.1.4). The Target was both used for phase-space cooling of the stored ion beam (see Sect. 3.1.3) and served as a merged-beams interaction medium for the DR experiments (see Sect. 3.1.2). The Cooler was not used as its electron beam velocity spread was too high to effectively cool such a heavy ion beam (see Sect. 3.1.3). The Target was used with an expansion factor of 20, which offers a good compromise of electron density and energy resolution (see Sect. 3.1.3.2). Based on previous experiments [87] with this expansion factor, the two components of the effective collision velocity distribution were assumed with

$$\begin{aligned} k_\mathrm{B}T_\perp &= (1.65 \pm 0.35)\,\mathrm{meV}, \text{ and} \\ k_\mathrm{B}T_\parallel &= 25^{+45}_{-5}\,\mu\mathrm{eV}. \end{aligned} \tag{4.4}$$

The electron beam density was typically $n_e \approx 3 \times 10^6\,\mathrm{cm}^{-3}$.

The neutral fragments emerging from the electron-ion interaction region were detected downstream in the BAMBI beamline (see Sect. 3.1.4). Two different systems were employed for the detection of the neutral reaction products. First of all, the position sensitive MCP detector with phosphor screen anode was used as a diagnostic tool to optimize the overlap of the electron and ion beam. Later, it was used for the neutral fragment momentum imaging measurements (see Sect. 3.2) from which the branching ratios of possible product states were determined based on the measured fragment distance distribution on the detector (see Sect. 4.4). The adjustment of

the electron beam and the momentum imaging measurements were performed for zero electron-ion collision energy only. The energy-dependet merged-beams DR rate coefficient was measured with a 10×10 cm^2 energy sensitive silicon detector using a well established measuring scheme for molecular systems (see Sect. 4.3). Those results are presented in the following Section.

During the experiments, most of the light hydrogen fragments missed the detectors. There are several reasons for this (see Eq. 3.29). At the dissociation the momentum is distributed among the fragments according to their mass ratio, which is quite large in the case of SH^+ with $m_S = 31.972$ u and $m_H = 1.008$ u, respectively. In conjunction with the relative large kinetic energy releases of up to 6.8 eV this leads to very large dissociation cones of the light hydrogen fragments. In principle, it is possible to compress the dissociation cones by increasing the kinetic beam energy, however, this is limited by the rigidity of the bending magnets.

4.2.2 Internal Excitations of SH^+

The ions are produced in electronically, vibrationally, rotationally and fine-structure excited states. In TSR, the ions have been stored for about 11 s before the measurement in order to radiatively relax and thermally equilibrate with the ambient black body radiation of the storage ring enclosure at room temperature. To estimate the level population of the stored ion ensemble the various possible decay modes needed to be considered. In the following, the different contribution are discussed in detail.

A lifetime of about 1 μs was measured for the electronic transition $A\,^3\Pi \rightarrow X\,^3\Sigma^-$ by Brzozowski et al. [142]. According to Park and Sun [137] there should be two more electronic bound states, $a^1\Delta$ and $b^1\Sigma^+$, lying between the ground state $X^3\Sigma^-$ and the excited $a^3\Pi$ state. For these states no published lifetime values could be found. The lifetimes of the vibrational levels of the $X^3\Sigma^-$ ground state of SH^+ have been calculated by Senekowitsch et al. [143]. The slowest $\Delta v = 1$ transition from $v = 1 \rightarrow v = 0$ is listed with a lifetime of about 19 ms. Thus, it is expected that all ions reach their electronic and vibrational ground levels within seconds of storage.

As no publications about the radiative relaxation of the rotational levels of SH^+ could be found, this was calculated within the scope of this analysis. The temporal evolution of the rotational level population of the stored ions was estimated with a radiative relaxation model, analog to that of Amitay et al. [144], which considers both spontaneous radiative decay as well as stimulated emission and absorption by the ambient 300 K black-body radiation. The rotational radiative lifetimes of $X^3\Sigma$ were calculated analog to [144] for rotational levels ranging from $N = 0$ to $N = 14$. Since SH^+ has a non-zero total electron spin in its electronic ground state $^3\Sigma_1$ the rotational energy levels are denoted by N, corresponding to the total angular momentum except the spin. Here, since the electronic orbital angular momentum component Λ along the internuclear axis vanished, N corresponds to the quantum number of the molecular rotation. The decay rates of higher levels decay were calculated to be negligibly fast. The obtained Einstein coefficients, which corresponds

Table 4.3: Calculated rotational decay rates of $X^3\Sigma(v = 0)$ SH^+.

N	E (eV)	A (s^{-1})
0	0.0	0.0
1	0.0023	1.42×10^{-3}
2	0.0069	1.37×10^{-2}
3	0.013 75	4.94×10^{-2}
4	0.022 85	1.21×10^{-1}
5	0.034 25	2.43×10^{-1}
6	0.050 25	6.83×10^{-1}
7	0.068 55	1.03
8	0.089 15	1.475
9	0.111 95	2.03
10	0.136 95	2.72
11	0.164 35	3.54
12	0.194 05	4.5
13	0.226 05	5.67
14	0.260 35	6.976

to the inverse lifetimes, are listed in Table 4.3. The model calculation uses the dipole moments from Senekowitsch et al. [143]. Furthermore, the level energies were estimated assuming an harmonic molecular potential with $B_eN(N + 1)$ given the rotational constant B_e of 1.2 meV, also from Senekowitsch et al. [143].

The initial rotational level population was assumed to be Boltzmann distributed at a temperature of 8000 K, analog to a similar DR experiment on CF^+ [24]. The resulting temporal evolution of the rotational level populations ranging from $N = 0$ to $N = 11$ are depicted in Figure 4.2 together with the temporal evolution of the average excitation energy given by the sum of all rotational levels weighted by their population. One can see that the SH^+ molecules do not completely reach the thermal equilibrium with the 300 K ambient photon field, highlighted in red, during the measurements. After the first 11.3 s of ion storage, the model predicts a remaining average rotational level population exceeding the 300 K equilibrium by approximately 50 % at about 440 K. The excitation energy averaged over the ion population during the measurement window, from 11.3 s to 25.0 s, exceeds room temperature excitation by only 21 % corresponding to a temperature of about 360 K. This is an upper estimate, as no further pathways are considered. Omitted are spin-orbit couplings, which may provide additional pathways, or an acceleration of the rotational cooling via super-elastic ion collisions with electrons as observed before, e.g., by Shafir et al. [145].

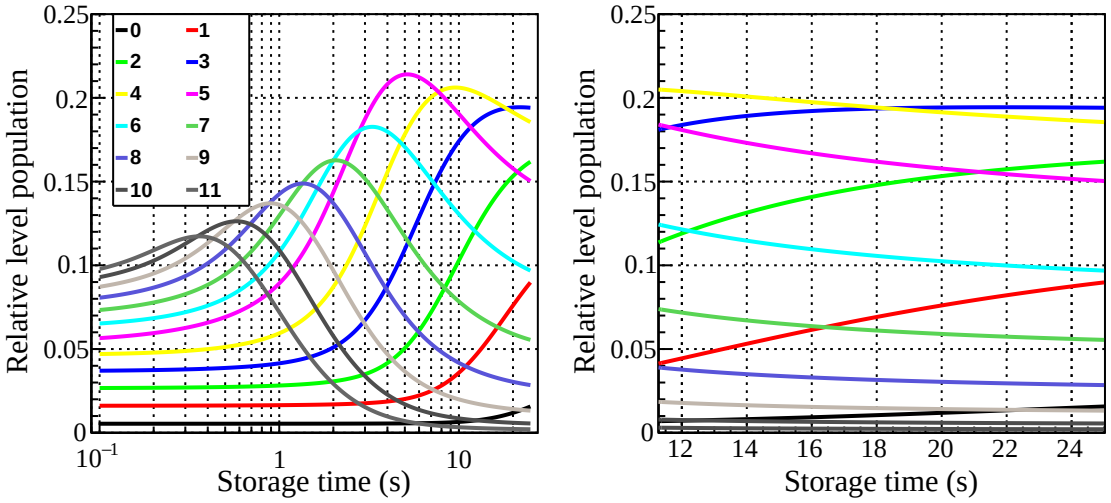

(a) Rotational level populations

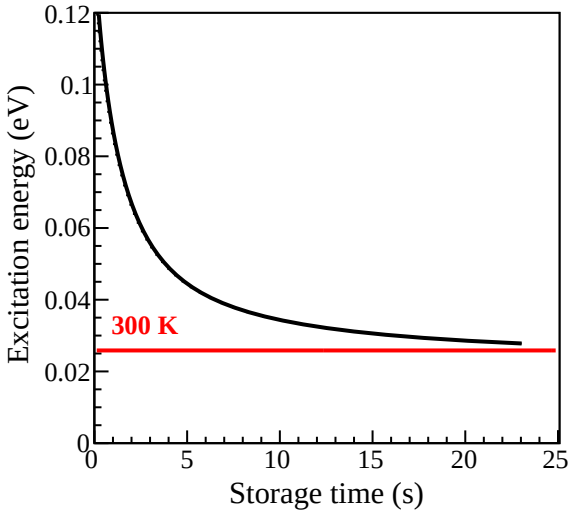

(b) Rotational excitation energy

Figure 4.2: Modeled temporal evolution of the rotational level populations (a) and the average excitation energy (b) of SH^+. The excitation energy is given by the sum of all rotational levels weighted by their population. The ion ensemble was assumed with a initial temperature of 8000 K. The level of the ambient 300 K black body radiation is indicated by a red constant line in (b).

4.3 Merged-Beams DR Rate Coefficient Measurements

According to Equation 3.12, the merged-beams DR rate coefficient can be determined from the detected count rate of neutral product fragments emerging from the interaction section in the Target normalized by the electron beam density and number of ions in the interaction section. For these measurements, the neutral fragments were detected with a 10×10 cm^2 energy sensitive silicon detector. As mentioned before, most of the light hydrogen fragments missed the detector during the measurement. Still, the heavier sulfur fragments from all DR events are confined on the detector aperture and can be counted. Various types of background occur. The events from residual gas induced processes (e.g. collision induced dissociation) can be identified by acquiring data with the electron beam being turned off. From electron-induced background events only dissociative excitation can produce neutral fragments. The channel $S^+ + H$ is not detected on the detector due a to too low kinetic energy of the H fragment. The other channel, $S + H^+$ opens only at 6.3 eV collision energy, which is above the energy range covered in this experiment. Hence, for electron-ion collision energies below 6.3 eV, DR is the only electron induced process giving rise to any neutral fragment on the detector. The DR rate can be determined from the electron-induced count rate subtracting the background from collision induced dissociation events.

The collision energies were varied in a range from 0 eV to 8 eV. The rate coefficient was determined by normalizing the background corrected rate of detected sulfur events by the electron beam density and the number of interacting ions (see Eq. 3.12). The count rate from background neutral fragment events in the residual gas, obtained when the electron beam was switched off, are subtracted before. The electron beam density was determined in a separate measurement of the electron beam current, energy and profile [103]. The number of stored ions can be inferred from the ion beam current. However, the typically store ion current in the oder of 100 nA is orders of magnitudes below the sensitivity of the current transformer of TSR [146] normally used for this purpose. To overcome this limitation, first a relative rate coefficient as a function of the electron-ion collision energy was measured by normalizing to a proxy signal for the ion beam current. In this case, the background rate was used, which originates mainly from collisions of the stored ions with the residual gas. Then, this relative rate coefficient was scaled by an absolute value measured for a single energy in a separate measurement. The investigated energy range was covered in segments of several overlapping high-resolution spectra. Next, the amplitudes of these spectra were fitted to a low-resolution overview spectrum covering the whole energy range (see Sect. 4.3.2). Finally, the spectrum was scaled by a separate measurement of the absolute rate coefficient at zero collision energy, described in the next Section.

The obtained rate coefficient was converted in two steps into a plasma rate coefficient, in order to enable the use of these experimental results for astrochemical

models. First, the DR cross-section as a function of collision energy was extracted by a deconvolution of the experimental collision energy distribution (see Sect. 4.3.3). Finally, this cross-section was convolved with a thermal Maxwell-Boltzmann distribution in order to obtain the plasma rate coefficient as function of the collisional plasma temperature (see Sect. 4.3.4). The plasma temperature reflects the collisional velocity spread in a plasma at given temperature, but not the internal excitation of the ions [87]. This conversion procedure was performed with the method developed by Novotný et al. [87], which also allows a propagation of the statistical and systematic uncertainties. The most important steps are briefly described in the according Sections 4.3.3 and 4.3.4, respectively. The results of these rate measurements are discussed in Section 4.3.5.

4.3.1 Absolute DR Rate Coefficient Measurement

The absolute rate coefficient was determined with the life-time method described in detail by Novotný et al. [147] or Kreckel et al. [148] which is based on the work of Pedersen et al. [149]. In short, the ion beam decay is measured within one injection both with the electron beam being turned on and off. Assuming an exponential decay in both cases one can extract the absolute DR rate coefficient from the inverse difference of the two decay constants.

The measurement is performed under cooling conditions for velocity matched electron and ion beams. The measured rate at zero collision energy is assumed to originate only from DR and collisions with residual gas. In case of SH^+ ion-pair formation after electron capture is energetically not accessible at zero collision energy as both channels are above the dissociation limit of SH^+. Therefore, DR is the only electron induced process introducing an ion beam decay to be considered for this rate coefficient. The absolute rate coefficient was determined for three independent runs, where the electron beam was turned off at different times. The obtained results are listed in Table 4.3b. The last run, where the on and off periods were exchanged, showed a significantly larger rate coefficient compared to the other two measurements and also did not overlap within its uncertainty. The value of the absolute merged-beams DR rate coefficient for zero collision energy is based on the weighted average of the results for the three measurements, its uncertainty as the variance of the measured values with respect to the value of the weighted average. In one separate run with the electron-beam turned on all the time it was checked that the decay is exponential within the uncertainty. Finally, the uncertainty of the electron beam density measurement needs to be included. The total uncertainty of the electron beam density was estimated to be 5 % considering the uncertainty of ion beam positions within the electron beam profile (2.7 %), the temporal evolution of the beam profiles, space charge effects and calibrations. This contribution is independent of the collision energy. Including the uncertainty for the electron beam density measurement the total uncertainty increases from 15.3 % to 15.8 %. This gives a final results of $(1.83 \pm 0.29) \times 10^{-6}\,\mathrm{cm^3 s^{-1}}$.

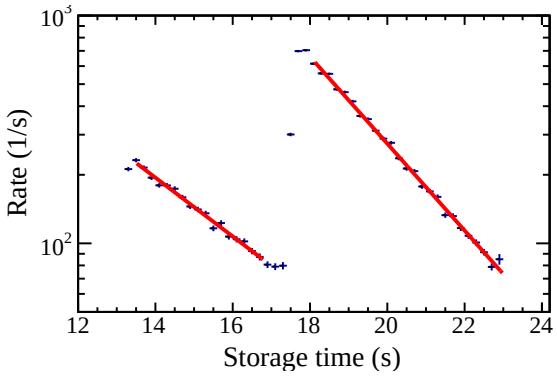

(a)

No.	Electrons on from	to	$\alpha_{\mathrm{abs}}(E_d = 0\,\mathrm{eV})$ $(10^6\,\mathrm{cm^3 s^{-1}})$
I	15 s	23 s	1.64 ± 0.13
II	18 s	23 s	1.65 ± 0.16
III	13 s	16 s	2.13 ± 0.12
Weighted average			1.83 ± 0.28

(b)

Figure 4.3: Absolute rate coefficient measurement. The lifetime of the stored beam was measured for zero collision energy. Three measurements were performed, were the electron beam was switched on and off at different times. The electron on times are listed in (b). Measurement (II) is shown in (a). The results are listed in (b).

4.3.2 Energy Dependent DR Rate Coefficient Measurement

Measurement scheme

The energy dependent DR rate coefficient was measured with a well established scheme which has been successfully used for similar DR investigations of, e.g, HCl^+ and NH^+ [87]. The injected ion beam was first pre-cooled for 9 s. After 8 s from the beam injection the mechanical shutter was opened, which takes about 1 s. In the following data acquisition phase each measurement point was measured in a repeated cycle of four different steps with different electron beam energies, which is illustrated in Figure 4.4.

In the first *cooling* step, the stored ion beam is cooled by setting the electron energy to the cooling energy (see Eq. 3.13) for matched electron and ion velocities to achieve a zero electron-ion collision energy. In the next *measurement* step, the count rate at the detector was recorded for a certain electron-ion collision energy (see Eq. 3.15) in order to obtain the merged-beam DR rate coefficient. This energy was changed with each beam injection within the investigated energy region. In the following *reference* step, the detuning energy was always set to the same value of about 1 eV. The rate measured in the reference step may be used as a proxy signal for the stored ion beam current in order to re-normalize the scans covering different energy ranges. In the last *background* step, the background rate of the detector was measured directly by turning off the electron beam.

Each *cooling* step was applied with a dwell time of 50 ms, the other steps with a dwell time of 25 ms, respectively. The power-supply of the electron cathode requires a certain time before it stabilizes. In order to ensure stable conditions during the data acquisition, an additional 5 ms were added before each step as a settling time for the voltage suppliers. At a typical ion beam lifetime with an exponential decay constant of about 3.1 s, 125 of these cycles were measured between 11.3 and 30 s after each injection.

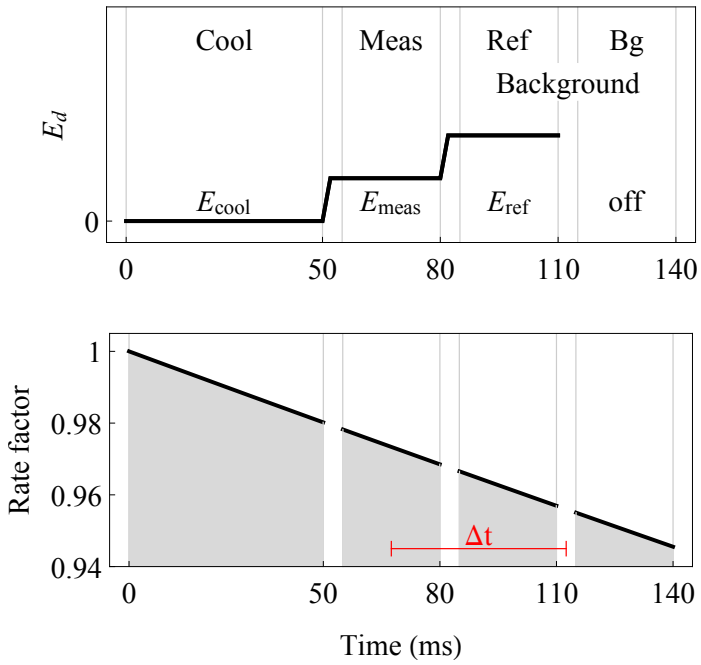

Figure 4.4: Measurement cycle scheme for energy dependent rate measurements. The upper graphs shows schematically the detuning energies during the four different steps *cool, meas, ref*, and *bg* within each measurement cycle, which is continuously repeated during the acquisition phase of each injection. In the last *bg* step, the electron beam is turned off. The measurement energy was varied between injections. The lower graph shows the relative ion beam intensity.

Analysis

The analysis was performed following an already well established approach of, e.g., Amitay et al. [50]. The whole energy spectrum (see Fig. 4.5) was measured piecewise with several high-statistics energy scans of appropriate resolution for the different energy scales and, afterwards, merged together with suitable normalizations of each scan. First, each scan was analyzed independently.

In this work, the experimental merged-beams DR rate coefficient of SH^+ was determined, based on the general Equation 3.12, according to

$$\alpha_{\mathrm{DR}} = \frac{R_{\mathrm{DR}}}{n_e N_i} \tag{4.5}$$

from the rate of detected DR events R_{DR} normalized by the electron density n_e and the number of ions in the interaction region N_i. The actually detected rate R_{meas} needs to be corrected for the background rate to obtain

$$R_{\mathrm{DR}} = R_{\mathrm{meas}} - \xi R_{\mathrm{bg}} \tag{4.6}$$

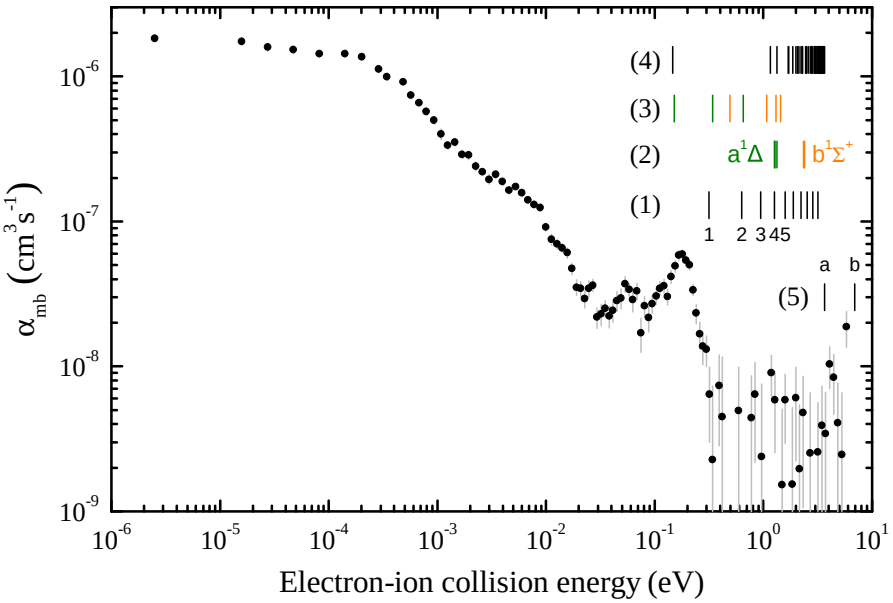

Figure 4.5: Experimental merged-beams DR rate coefficient of SH^+ with error bars indicating the the statistical uncertainty of the data. The spectrum is described in the text and discussed in Section 4.3.5. The indicated energy thresholds are
(1) vibrationally excited states of SH^+ $X^3\Sigma^-$,
(2) electronically excited $a^1\Delta$ and $b^1\Sigma^+$ states of SH^+,
(3) core-excited neutral SH Rydberg states measured by Lange et al. [138], while the colors indicate the corresponding ionic states which mark the series limit in (2),
(4) energy thresholds for excited sulfur product states,
(5) energy thresholds for (a) DE into $S^+ + H$, (b) DE into $S + H^+$.

The background is systematically measured with a relatively lower rate, as illustrated in Figure 4.4, which is accounted for by the scaling factor

$$\xi(\Delta t) = \exp\left({}^{\Delta t}/_{\tau}\right) \tag{4.7}$$

assuming a typical beam lifetime of $\tau = 3.1\,\mathrm{s}$ and the average time difference $\Delta t = 47.5\,\mathrm{ms}$ between the measurement and background steps. These values lead to a typical scaling factor of $\xi(\tau) = 1.015$.

During these measurement, the signal of the reference step showed even for long integration times the same rate as in the background step. Therefore, the reference data were used together with the electron beam off data for the background measurement

$$R_{\mathrm{bg}} = \frac{t_{\mathrm{ref}} R_{\mathrm{ref}} + t_{\mathrm{off}} R_{\mathrm{off}}}{t_{\mathrm{ref}} + t_{\mathrm{off}}} \tag{4.8}$$

given their respective measuring times.

The number of ions is determined via the ion current, which is difficult to measure. For this, the rate measured at a common reference energy may be used to

re-normalize the different energy spectra in amplitude. Another possibility is to use the measured background with electron beam turned off as a proxy signal, which is proportional to both the residual gas pressure and the ion current. This works well for measurement time periods of a single energy scan, for which the residual gas pressure can be assumed to be constant. However, the pressure may vary over longer time periods. Therefore, the energy scans are scaled to a common overview scan covering the whole investigated energy range. In each run, the relative rate coefficient as a function of collision energy are scaled by a single scaling factor to match the overall amplitude of this overview run. An improper scaling in this procedure could potentially introduce artificial structures at the joints of adjacent runs, which has been carefully checked for the obtained spectrum. Finally, the whole spectrum was scaled to match the value of $1.83 \times 10^{-6}\,\mathrm{cm^3 s^{-1}}$ for zero collision energy determined in the absolute rate measurement, described in Section 4.3.1.

Overall, the measured rate coefficient, depicted in Figure 4.5, is strongly decreasing towards higher collision energies. The spectrum also shows multiple sharp features of increasing relative magnitude towards higher energies with respect to the overall decline. For collision energies below $2 \times 10^{-4}\,\mathrm{eV}$ the rate coefficient levels off. This behavior is caused by the experimental collision velocity spread, discussed, e.g., in [87]. For the structures in the energy range from $10^{-4}\,\mathrm{eV}$ to $10^{-1}\,\mathrm{eV}$ it has been carefully checked that these are not caused by mis-matched energy spectra. In the collision energy range from $1 \times 10^{-2}\,\mathrm{eV}$ to $3 \times 10^{-1}\,\mathrm{eV}$ multiple sharp resonance structures can be observed which are strongly enhanced. For energies larger than 0.3 eV no signal above the background could be measured. The measured spectrum is further discussed regarding the possible DR pathways in Section 4.3.5.

Uncertainties

The uncertainty of the scaling of the energy dependent DR rate coefficient is mainly determined by the uncertainties of the electron density, which was already discussed in Section 4.3.1. Changes in the ion beam storage lifetime due to pressure fluctuations may also contribute, which are discussed in the following

As mentioned before, the *background* rate is always measured after the *measurement* step in the measuring cycle (see Figure 4.4), thereby, with a systematically lower rate which is account for by the scaling factor ξ given in Equation 4.7. Fluctuations in the residual gas pressure led to different ion beam lifetimes in the range from 2.5 s to 3.2 s mostly around 3.1 s. The corresponding correction factors are 1.019 and 1.015. Therefore, the uncertainty by the background subtraction is about 0.4 % of the background level. This uncertainty is negligible, especially, compared to the statistical uncertainty of the measured rate coefficient shown in Figure 4.5.

4.3.3 DR Cross-Section

The measured merged-beams DR rate coefficient α (see Eq. 3.12) is smoothed by the experimental energy resolution determined by the energy spread of the electron beam. In order to derive the cross-section σ of the investigated reaction the

experimental energy spread needs to be deconvolved. In the following the used deconvolution procedure is briefly introduced. The obtained spectrum is discussed later in Section 4.3.5.

Deconvolution Procedure

In this work, a numerical deconvolution method was applied which has been successfully used for the analysis of the similar systems HCl^+ and NH^+ [87, 139]. The method is described in detail in [87]. In contrast to the traditional methods [88, 150], it directly includes both the electron beam spread the the overlap geometry. In the following, the used numerical method is briefly introduced.

Starting from Eq. 3.16, the measured rate coefficient α is approximated by a model rate coefficient α'. The corresponding cross-section $\sigma(E_d)$ is approximated by a discrete function $\sigma'(E_d)$ with energy intervals comparable to the energy resolution ΔE at E_d as given in Eq. 4.1. The energy intervals have variable lengths adjusted according to the experimental energy resolution. The effects of both components of the electron beam velocity spread $k_\mathrm{B}T_\parallel$ and $k_\mathrm{B}T_\perp$ as well as the complete merged-beams overlap geometry X, represented by $f_\mathrm{mb}(E, E_d, T_\parallel, T_\perp, X)$, can be Monte-Carlo simulated. The computation was further accelerated by fixing the assumed electron energy spreads $k_\mathrm{B}T_\parallel$ and $k_\mathrm{B}T_\perp$ (see Eq. 3.22) as well as the merged beams geometry X as these parameters are expected to be constant during the measurements. Finally, the values of the approximating function σ' are adjusted iteratively by minimizing the χ^2 between the modeled α' and measured α.

Uncertainties

The statistical uncertainties of the measured rate coefficient α were propagated to the derived cross-section σ numerically. A set of 1000 simulated rate coefficients was created, where each energy point was randomized within its statistical uncertainty, and then deconvolved to a cross-section. The resulting distribution of σ was analyzed for its mean value and the standard deviation of values lower and higher than the mean value. These values were then used as an approximation of the propagated statistical error and are displayed as asymmetric statistical error bars in Figure 4.6.

The uncertainties introduced by the collision velocity spreads $k_\mathrm{B}T_\perp$ and $k_\mathrm{B}T_\parallel$ (see Eq. 3.22) have been investigated analog to the measurements of HCl^+ [87]. The randomized rate coefficients for the propagation of the statistical error were also evaluated for the extreme temperature values given by adding/subtracting the temperature uncertainty to its nominal value. The difference from the cross-section based on the nominal values of $k_\mathrm{B}T_\parallel$ and $k_\mathrm{B}T_\perp$ were added in quadrature and are displayed as gray error bars in Figure 4.6. According to their relative magnitude, this uncertainty is dominated by its transversal contribution.

The uncertainty of 15.8 % from the absolute scaling of α_mb (see Sect. 4.3.1) enters directly into the uncertainty of the cross-section.

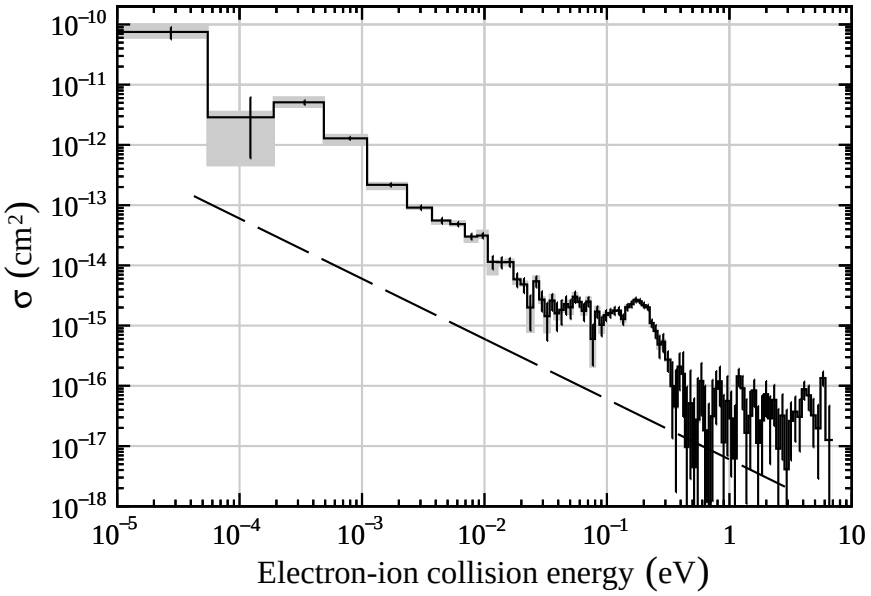

Figure 4.6: Derived DR cross-section of SH^+ (solid line histogram). The lower edge of the lowest energy bin at zero collision energy is not shown. The black error bars represent the statistical uncertainty propagated from the measured α_{mb} The gray error band shows the uncertainties from the collision velocity spreads (see Eq. 3.22). The dashed line indicates the typical cross-section $\sigma(E) \propto E^{-1}$ of the direct DR process, which is arbitraryly scaled.

4.3.4 Plasma DR Rate Coefficient

For the direct usage of the experimental results in astrophysical models, a thermal plasma rate coefficient was derived. After a astrophysical discussion, the statistical and systematic uncertainties are discussed.

Convolution

The plasma rate coefficient α_{pl} was derived from the obtained cross-section σ

$$\alpha_{\mathrm{pl}}(T) = \int_0^\infty \sigma(E) v f(E,T) dE \tag{4.9}$$

by a convolution with a thermal Maxwell-Boltzmann collision velocity distribution

$$f(E,T) = 2\sqrt{\frac{E}{\pi}} \left(\frac{1}{k_{\mathrm{B}}T}\right)^{3/2} \exp\left(-\frac{E}{k_{\mathrm{B}}T}\right) \tag{4.10}$$

as a function of the plasma temperature T, which leads to

$$\alpha_{\mathrm{pl}}(T) = \frac{4}{\sqrt{2\pi m_e}} \left(\frac{1}{k_{\mathrm{B}}T}\right)^{3/2} \int_0^\infty \sigma(E) E \exp\left(-\frac{E}{k_{\mathrm{B}}T}\right) dE. \tag{4.11}$$

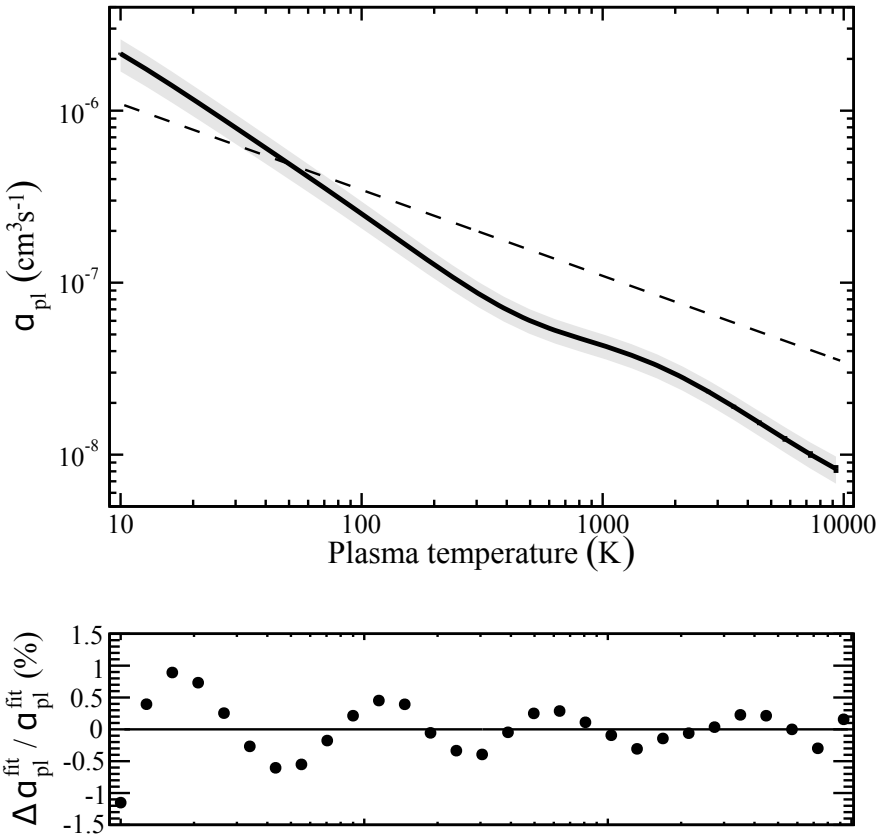

Figure 4.7: Experimentally derived DR plasma rate coefficient of SH^+ as a function of the collisional plasma temperature (full black line). The gray band indicates the total systematic error originating from the uncertainties on the absolute scaling, background subtraction, as well as in $k_B T_\perp$ and $k_B T_\parallel$. The statistical uncertainties propagated from α_{mb} are smaller than 5 % at all temperatures and the representing error bars are barley distinguishable in the plot. The relative deviations of the parameterization fit α_{pl}^{fit}, shown below, are, within about 1.2 % for all temperatures. The typically assumed DR rate coefficient for diatomic ions is indicated by a dashed line (see Eq. 2.2).

The obtained plasma rate coefficient of SH^+ is depicted in Figure 4.7 for plasma temperatures in a range from 10 K to 10 000 K. It should be noted, that the plasma temperature only represents the spread of collision velocities between electrons and ions. The internal excitation of the ions is expected to be around 360 K according to the discussion in Section 4.2.2.

Uncertainties

The statistical error of the measured rate coefficient α_{mb} was propagated to the plasma rate coefficient α_{pl} in the same way as for the cross-section σ (see Sect. 4.3.3) with a set of 1000 rate coefficient model results randomized within their statistical

uncertainty. The propagated statistical uncertainty does not exceed 5 % for all temperatures. Both uncertainties of the absolute and background scaling propagate directly to α_{pl}. The absolute scaling uncertainty of 15.8 % dominates the total uncertainty at most temperatures. The background scaling uncertainty is independent of the plasma temperature T_{pl} and is negligibly small at all displayed plasma temperatures. The contribution of the collision velocity spread is also propagated analog to the error propagation for the cross-section. Its temperature dependency can be well well approximated by $\pm 7.3 \times 10^{-6} (1\,\mathrm{K}/T_{\mathrm{pl}})^{1.3}\,\mathrm{cm^3 s^{-1}}$. The systematic uncertainties were added in quadrature for each plasma temperature T_{pl}, which results in a total systematic uncertainty of ~ 21 % at 10 K, ~ 18 % at 100 K, ~ 16 % at 1000 K, and ~ 17 % at 10 000 K, respectively.

Parameterization

Plasma rate coefficients are usually parameterized so that they can be easily used in astrochemical models and databases. Novotný et al. [87] have shown for HCl^+ that neither the commonly used two-parameter functions, e.g. from Florescu-Mitchell & Mitchell [6], nor the more general three-parameter extension, used in astrochemical databases as UMIST [151] or KIDA [23], are able to approximate the experimentally determined plasma rate coefficient better than 40 % over a temperature range from 10 K to 5000 K. A new parameterization was proposed by Novotný et al. [87] as

$$\alpha_{\mathrm{pl}}^{\mathrm{fit}}(T_{\mathrm{pl}}) = A \left(\frac{300\,\mathrm{K}}{T_{\mathrm{pl}}}\right)^{n} + B, \tag{4.12}$$

where

$$B = T_{\mathrm{pl}}^{-3/2} \sum_{i=1}^{3} c_i \exp\left(-\frac{T_i}{T_{\mathrm{pl}}}\right). \tag{4.13}$$

The first term corresponds to the usual rate coefficient energy dependency of DR also found in the typically used Arrhenius-Kooji formula (see Eq. 2.1). The other terms in B correspond to rate coefficients α_i convolved as in Eq. 4.11 from Dirac-delta shaped cross-sections $\sigma_i \propto \delta(E - k_{\mathrm{B}} T_i)$. In this way, any plasma rate coefficient can be approximated.

The experimental plasma rate coefficient of SH^+, determined in the scope of this work, was fitted with this function (4.12) for temperatures ranging from 10 K to 10 000 K. The resulting fit parameters are listed in Table 4.4. In this case, the data can be approximated better than 1.2 % over the full temperature range.

4.3.5 Discussion

In the following, the obtained experimental results are discussed with regard to the different expected DR pathways as introduced in Section 4.1.

Table 4.4: Parameters of the approximated DR plasma rate coefficient α_{pl} of SH^+ according to Equation 4.12.

Parameter	Value
A	$9.81 \times 10^{-8}\,\mathrm{cm^3 s^{-1}}$
n	9.10×10^{-1}
c_1	$-1.03 \times 10^{-4}\,\mathrm{K^{3/2} cm^3 s^{-1}}$
c_2	$3.31 \times 10^{-3}\,\mathrm{K^{3/2} cm^3 s^{-1}}$
c_3	$1.01 \times 10^{-2}\,\mathrm{K^{3/2} cm^3 s^{-1}}$
T_1	1.86×10^{2} K
T_2	2.08×10^{3} K
T_3	2.16×10^{4} K

Rate Coefficient and Cross-Section

The derived merged-beams DR rate coefficient, depicted in Figure 4.5, exhibits diverse features, which can be attributed to different pathways of the underlying dissociation process. In the figure, the known energies of involved states with respect to the $X^3\Sigma^-$ ground state of SH^+ are indicated as reference points. The depicted energy levels of vibrationally excited states mark the upper limit of a converging series of SH Rydberg states, which can be both involved in direct and indirect DR pathways. In addition, the available data on low-lying, electronically excited ionic states and the known corresponding SH Rydberg states are shown. Furthermore, the energetic thresholds for opening of product excited states are indicated.

Overall, the rate coefficient and cross-section (see Fig. 4.6) are strongly decreasing towards higher collision energies with an energy dependence of approximately $\sigma \propto E^{-1}$, which is characteristic for direct DR [4,6]. Moreover, multiple distinct features are visible which are characteristic for indirect DR pathways. In the collision energy range from 1×10^{-2} eV to 3×10^{-1} eV multiple sharp resonance structures can be observed which are strongly enhanced with respect to the overall E^{-1} dependence of direct DR. This suggests indirect pathways via vibrationally or core-excited SH Rydberg states. There is a particularly strong resonance around 0.18 eV before the rate coefficient declines to the experimental background level at about 0.3 eV. This strong decline as well as some of the resonant features can be attributed to the presence of the $v = 1$ vibrational level at about 0.32 eV [137], which marks the limit of a corresponding Rydberg series of SH states. Moreover, the strong resonance around 0.18 eV roughly coincides with a known core-excited Rydberg state of the series converging to the electronically excited $a^1\Delta$ state.

For collision energies below 2×10^{-4} eV the rate coefficient levels off. This is an expected behavior which is caused by the experimental collision velocity spread, discuss, e.g., in [87]. Beyond that, the rate coefficient shows a rather sharp knee at about 2×10^{-4} eV. The two measuring points of the derived cross-section in this energy region indicate a deviation from the overall E^{-1} dependence. This may be

caused by the presence of a low-lying state. If it is interpreted as a resonance it would be a feature of indirect DR. If it is interpreted as a resonant capture which does not lead to a dissociation of the molecule, this would lead to a drop in the cross-section. In both cases a resonant capture is involved.

Astrophysical Relevance

The derived plasma rate coefficient is enhanced by a factor of 2 at low temperatures, compared to the *typical* DR plasma rate coefficient for diatomic molecular ions, given in Eq. 2.2. However, it declines more rapidly and is lower for temperatures higher than $\sim$ 50 K. From about 500 K to 2000 K the curve is parallel due to a bump around 1000 K corresponding to the resonant structures in the measured rate coefficient around 0.1 eV. Between 500 K and 2000 K, the measured rate coefficient is a factor of about 2.5 lower than the *typical* plasma rate coefficient and deviates even more towards higher temperatures.

It may be noted, that Florescu-Mitchell and Mitchell [6] erroneously quoted in their comprehensive overview of theoretical and experimental DR investigation a rate coefficient for SH^+, which was, in fact, measured for SH_2^+ at CRYRING by Hellberg et al. [152]. This is a factor of 2 to 5 times larger than the rate coefficient measured in this work. Nevertheless, the KIDA and UMIST astrochemical databases list the *typical* rate coefficient (see Eq. 2.2) for diatomic molecules for DR of SH^+

In the context of using SH^+ as a probe for warmer astrophysical environments with temperatures larger than 50 K, our measurements suggest a reduced SH^+ destruction rate by DR compared to the case of using the *typical* plasma rate coefficient of diatomic molecules. Hence, the abundances of SH^+ predicted by the astrochemical models based on those *typical* values should be underestimated. Indeed, the investigations of Nagy et al. [10] and Godard et al. [9] show that the modeled values are a factor 4 to 10 lower than the observed SH^+ abundances. Our new results on DR of SH^+ will contribute to resolving this issue once used in the models. However, the large scale of the discrepancy suggests that also other improvements of the models are needed.

4.4 Neutral Fragment Momentum Imaging Measurement

In addition to the rate measurements, SH^+ was investigated at zero collision energy by the neutral fragment momentum imaging technique, which is described in Section 3.2. As already mentioned at the beginning of this chapter, most of the hydrogen fragments missed the detector owing to the momentum distribution among the fragments with very different masses and the limited kinetic beam energy (see Sect. 3.2). For the first time, such "incomplete" imaging data were analyzed in order to determine the product state branching ratios (see Sect. 4.4.3). Furthermore, for one highly excited product state with small kinetic energy release both fragments could be projected on the detector, so that the according kinetic energy release could be determined directly (see Sect. 4.4.2).

Measurement Scheme

For the fragment momentum imaging measurements, a different scheme as for the rate measurements was used. The data from two different runs with slightly different timings were used for this analysis. After each injection, the ion beam was cooled in the first 11 s. During this time, the shutter was closed. These data can be used to determine the MCP dark count rate. In the time period from 11.3 s to 18 s for ond, and 11.3 s to 14.3 s for the other run, the electron beam was turned off. The data from this time period are used to determine the contributions from events which do not originate from DR reactions. These are mainly reaction with the residual gas which can also occur outside the interaction region. Finally, the electron beam was set to zero collision energy in the following time period up to about 23 s in order to investigate DR reactions. In this period, the imaging data were only obtained at cooling conditions with zero collision energy.

4.4.1 Position Calibration

The phosphor screen anode of the MCP detector was observed with a CCD camera. First of all, the distances of the fragment impacts on the projected images in the camera need to be associated with the absolute dimension on the phosphor screen. A simple method is to illuminate the whole detector in order to associate the size of the projected image of the detector on the camera to its known dimensions. However, the optical imaging may introduce some higher order aberrations. A more accurate calibration was performed utilizing a mask with a regular hole pattern, which provides more reference points distributed over the whole detector area. The mask was aligned parallel a few millimeter in front of the detector. The holes of 2 mm diameter are arranged in a rectangular pattern with distances of 10 mm to their next neighbor. By associating the relative recorded positions to the known dimension of the mask pattern, a transformation matrix can be derived [132], which can even account for higher-order optical aberrations. Both the measured mask

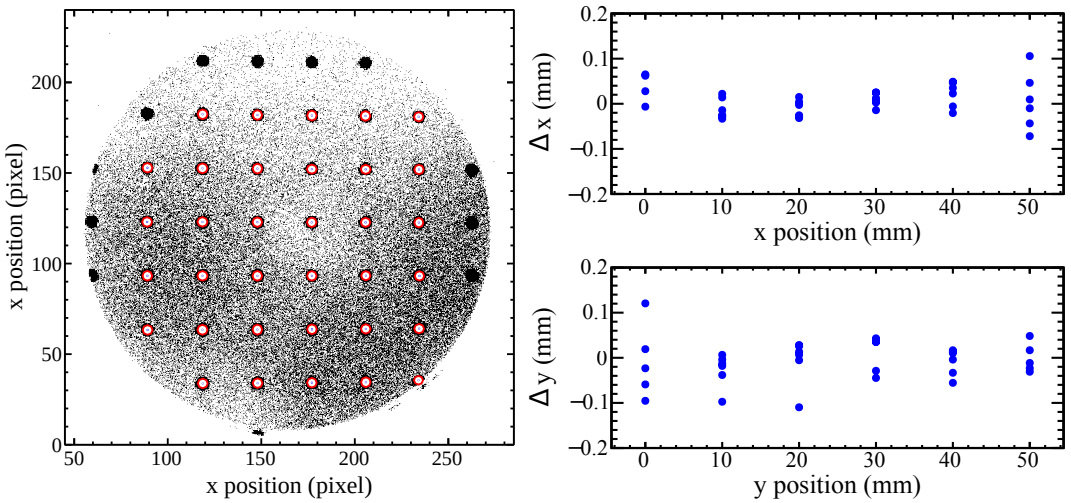

(a) Position calibration data. **(b)** Residuals of fitted spot positions.

Figure 4.8: Position calibration for the transformation from pixel positions to metric dimensions. The detector is calibrated with a regular grid pattern. (a) shows the measured mask pattern with the included points marked in red. (b) shows the deviations of the fitted spot positions from the positions calculation from the derived transformation, which are typically smaller than 0.1 mm.

pattern and the deviations from the fitted spot positions are depicted in Figure 4.8. The deviations are typically smaller than 0.1 mm.

4.4.2 Kinetic Energy Release Measurement of S($^5S_2$) Product State

The kinetic energy release of the diatomic dissociation processes can be determined from the distribution of fragment distances as described in Section 3.2. In the case of SH^+, as explained in the beginning of this chapter, most of the light hydrogen fragments missed the detector due to the limited beam energy and the momentum distribution among the fragments with very different masses. However, SH^+ is expected to have a highly excited $^5S_2$ product state with a small kinetic energy release of only about 0.25 eV (see Table 4.2). The dissociation cone of this product state was small enough in order to project both its fragments onto the detector.

The kinetic energy release was determined by a fit of the measured two-body fragment distance distribution of two-hit events with the model function given in Equation 3.36. These two-hit events are identified by a coincidence of two light spots in one camera frame. The fit needs to consider the internal excitation of the ions. A dissociation of an internally excited ion into the same final state has a kinetic energy which is larger by the excitation energy compared to the dissociation of an ion in the ground state. This leads to larger dissociation cones. Accordingly,

the population of multiple rotational levels leads to a broadening of the observed fragment distance distribution. The fit model consists of a superposition of multiple distance distributions for each rotationally excited level. The rotational level population was assumed to follow a thermal Maxwell-Boltzmann distribution. The DR cross-sections from the different rotational levels were assumed to be constant, within each product-state channel. The model calculations of the internal excitations, discussed in Section 4.2.2, predict that the ions are more rotationally excited compared to the 300 K radiation field of the enclosure at room-temperature. The mean excitation energy corresponds to a Maxwell-Boltzmann distribution with a temperature of 360 K. Overall, the population densities are still shifted towards higher rotational levels.

The graphs in Figure 4.9 show the transversal fragment distance distribution of S- and H-fragments produced by DR of SH^+. Only data from a single run were used and the distance distribution was generated without any further cut on the center-of-mass distribution. For particle distances between 0 and 25 mm on can see the characteristic sawtooth-like distribution of the $^5S_2$ product state dissociation channel. There are also contributions from the tails of the product state dissociation channels with higher kinetic energy releases. The distribution was fitted for the $^5S_2$ product state (red) with the KER as free parameter and the tails of the distance distributions of higher energetic product states were approximated by one fragment distribution with a fixed average kinetic energy release of 5.9 eV (green) as well as the branching ratios of the two considered channels. The fit was performed three times assuming different fixed mean temperatures of 0, 65 and 300 K, respectively. The results for the measured kinetic energy releases are listed in Table 4.5. The distribution can be reproduced quite well even without assuming any internal excitation (see Fig. 4.9a). The fit with a 300 K rotational excitation is significantly broadened, but cannot reproduce the peak better. The best fit result was, in fact, achieved by neglecting any rotational excitation. As the fit model assumes a constant DR rate for all rotationally excited states, this low temperature may only reflect higher rates for lower rotational levels. Super-elastic cooling by electrons could also lead to a sub-thermal level population [84].

The fits for the three different excitation temperatures result in KER-values between 0.255 and 0.276 eV. The statistical uncertainty from the fit is much lower than this KER spread. Given the limited possibilities on finding the actual internal excitation of the stored SH^+ ions, the difference of these values by about 20 meV is used as an estimate for the systematic uncertainty of the measured KER-value. Within their uncertainties, the measured KER-value agrees with both values derived from the reaction energies based on the proton affinity of sulfur (see Eq. 4.1) and the dissociation energy of SH^+ (see Eq. 4.2). With this measured KER value the reaction energy can be determined, according to Equation 4.3, as

$$\begin{aligned} \Delta E_{\mathrm{DR}} &= -\left\{\mathrm{KER}\left(\mathrm{S}\left(^5\mathrm{S}_2\right)+\mathrm{H}\left(^2\mathrm{S}_{1/2}\right)\right)+E_E\left(\mathrm{S}\left(^5\mathrm{S}_2\right)\right)\right\} \\ &= -(6.79\pm 0.02)\,\mathrm{eV}. \end{aligned} \tag{4.14}$$

Table 4.5: Results of transverse distance distribution fits in Figure 4.9. The distance distribution was fitted assuming different rotational excitation temperatures. The best result was achieved for an intermediate temperature of about 65 K. The measured kinetic energy release for the highly excited $S(^2S_2)+H(^2S_{1/2})$ product state agrees within its uncertainty with both values derived from the reaction energy of SH^+. Also, the derived branching ratio agrees well with the value determined later in Section 4.4.3.

Rotational temperature	$S(^2S_2) + H(1s)$ KER (eV)	Others Branching ratio		J_{max}	χ^2/NDF
0 K	0.276 ± 0.003	5.0 ± 0.4	95.0 ± 0.4	1	0.94
65 K	0.273 ± 0.002	5.2 ± 0.4	94.8 ± 0.4	7	0.88
300 K	0.255 ± 0.000	6.0 ± 0.8	94.0 ± 0.8	15	1.27
Result	0.27 ± 0.02	5.2 ± 0.6			

Table 4.6: KER values of DR product states of SH^+ derived from the measured KER of the $S(^5S_2)$ product state according to Eq. 4.14. All values have an uncertainty of 0.02 eV

Product state H	S		KER (eV)
$1s\,^2S_{1/2}$	$3s^2 3p^4$	$^3P_2$	6.79
$1s\,^2S_{1/2}$	$3s^2 3p^4$	$^3P_1$	6.74
$1s\,^2S_{1/2}$	$3s^2 3p^4$	$^3P_0$	6.72
$1s\,^2S_{1/2}$	$3s^2 3p^4$	$^1D_2$	5.65
$1s\,^2S_{1/2}$	$3s^2 3p^4$	$^1S_0$	4.04
$1s\,^2S_{1/2}$	$3s^2 3p^3(^4S^\circ)4s$	$^5S^\circ_2$	0.27

With this value, the kinetic energy releases of the other product excited states were derived according to Equation 4.3, which are listed in Table 4.6. We can also provide, in addition to the value by Rostas et al [136], another experimental value for the dissociation energy $D_0(SH^+, {}^3\Sigma^-)$ according to Equation 4.2 with

$$D_0(SH^+) = \Delta E_{DR} + E_I(S) = (3.57 \pm 0.02)\,\text{eV}. \tag{4.15}$$

Furthermore, the proton affinity for 0 K could be determined more precisely than the value given by Hunter and Lias [135] according to Equation 4.1 with

$$E^{0\,K}_{PA}(S) = \Delta E_{DR} + E_I(H) = (6.80 \pm 0.02)\,\text{eV}. \tag{4.16}$$

In all cases the uncertainties of the derived values are determined by the error of the measured KER value since the respective reference energies, listed in Table 4.1, are know to a much higher precision.

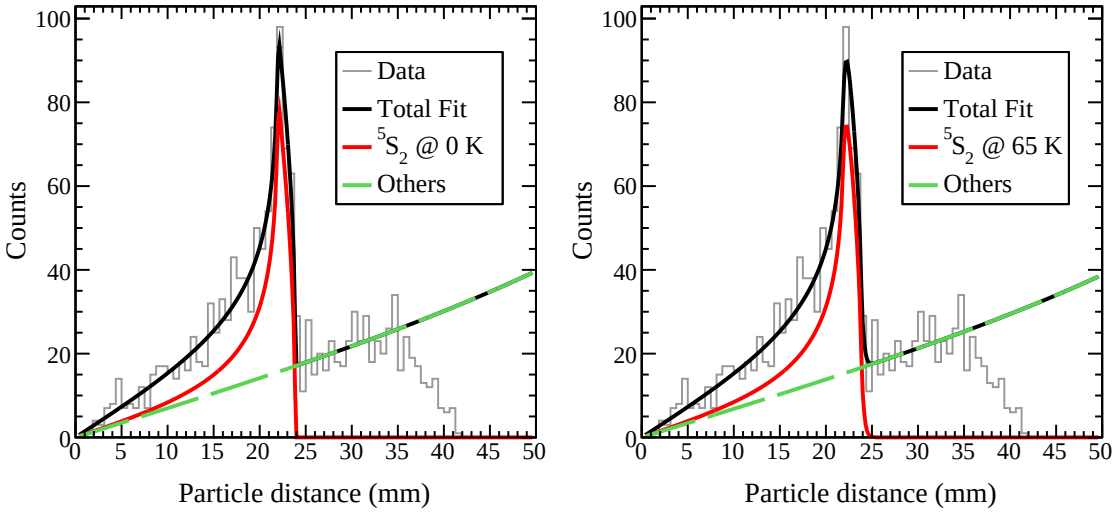

(a) 0 K

(b) 65 K

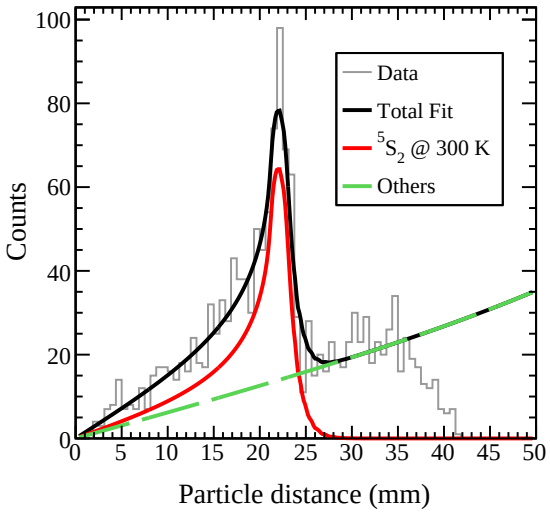

(c) 300 K

Figure 4.9: Transversal distance distribution of S- and H-fragments produced by DR of SH^+ (gray). The solid black line illustrate the sum of the fitted dissociation channels, the solid red line the contribution from the product state channel $S(^5S_2) + H(1s)$, and the dashed green line the contributions from the other product states with an approximated average KER of 5.9 eV. The fragment distribution was fitted up to 32 mm. The fits include a broadening by populations of rotationally excited levels (see Text) for temperatures of 0 K (a), 65 K (b), and 300 K (c), respectively. The fit results are listed in Table 4.5.

4.4.3 Heavy Fragment Imaging

The great advantage of fragment imaging with all fragments hitting the detector is, that the coincidence requirement of two or more fragments hitting the detector effectively suppresses background events. Furthermore, the relative fragment distances on the detector are independent of the beam profile. In the following, a new analysis approach is described to determine the product state branching ratios from the positions of only the heavy fragments in dissociation reactions of diatomic, heteronuclear molecules. This method becomes of interest when it is not possible to project all dissociation products on the detector (see Sect. 3.2) as it was the case for the investigated SH^+ ion. It requires a narrow, well-cooled ion beam and sufficiently accurate knowledge about the involved reaction energies of the investigated molecular ion.

As described in Section 3.2, the kinetic energy released in a molecular dissociation is distributed among the fragments as a consequence of the conservation of momentum according to their mass ratios. In case of dissociations of heteronuclear molecules, the heavier fragments form smaller dissociation cones, which can be more easily projected onto a detector of limited size. The distribution of distances of the heavy fragment to the global center-of-mass of the stored ion beam reflects the kinetic energy release in a similar way as the distribution of relative distances between both fragments $P_n(d)$ (see Eq. 3.36). For an ideal needle-like beam, the distances of the individual fragments d_S and d_H with respect to the center-of-mass of each dissociation is, according to Eq. 3.32, a fraction of the fragment distance d

$$P_n(d) \longrightarrow P_n^\mathrm{S}\left(d_\mathrm{S}\right) = P_n\left(\frac{d}{1+\frac{m_\mathrm{S}}{m_\mathrm{H}}}\right). \tag{4.17}$$

The beam profile as projected on the detector leads to displacements of the center-of-masses of each individual dissociation with respect to the global center-of-mass of the ion beam

$$d_\mathrm{CM}^\mathrm{S} = \sqrt{\left(x_\mathrm{S}-x_\mathrm{CM}\right)^2+\left(y_\mathrm{S}-y_\mathrm{CM}\right)^2}. \tag{4.18}$$

Conversely, the beam profile can be experimentally determined from the center-of-mass distribution $f_\mathrm{CM}(x,y)$ of those events for which all fragments are detected and unambiguously identified by their masses. As a consequence, the distribution of the different fragments distances with respect to the global center-of-mass $\widetilde{P}_n$ can be determined by the convolution

$$\widetilde{P}_n^\mathrm{S} = P_n^\mathrm{S} * f_\mathrm{CM} \tag{4.19}$$

Both, P_n^S and f_CM can be represented as two-dimensional functions with typically radial symmetry which can be easily convolved numerically. The numerical methods used for the generation of the distance-from-beam-center model distributions are described in more detail in Appendix A.1.

The shape of P_n^S can only be resolved by the convolved distribution $\widetilde{P}_n^\mathrm{S}$, if the

beam profile is significantly narrower. Therefore, a well cooled ion beam is required for this method. Using the relative amplitudes of these model distributions as free parameters, the branching ratios can be determined, analog to Equation 3.38, by fitting the measured distance-from-beam-center spectrum (see Sect. 4.4.3.3). The systematic uncertainties of this method are discussed in Section 4.4.3.4. The final results are discuss in Section 4.4.4.

4.4.3.1 Ion Beam Properties deduced from Two-Hit Events

In order to generate a distance-from-beam-center spectrum for the heavy sulfur fragments the beam profile and center needs to be known. The beam-center position and the beam-profile as projected on the detector are obtained from the center-of-mass distribution of the available two-hit events.

Fragment Mass Assignment and Beam Center Determination

In order to determine the center-of-mass of each dissociation event, the fragment masses need to be identified. An energy sensitive detector provides a direct mass sensitivity, as the well known kinetic energy of a dissociating molecular ion is distributed among the fragments according to their mass ratios. The used MCP detector does not provide a viable energy-, and thus, no direct mass-resolution (see Sect. 3.2). However, also the relative fragment distances to the center-of mass are partitioned according the their mass ratio (see Eq. 3.32). An unambiguous mass assignment is possible for a stable, narrow, well-cooled stored beam of ions with fragments of adequately different masses.

In our method for the mass assignment, the fragment coordinates of each event are permuted iteratively such that the resulting center-of-mass is closest to the global center-of-mass. The beam-center coordinates were determined by Gaussian fits of the x- and y-projections of the center-of-mass distribution (see Fig. 4.10) to $x = (28.11 \pm 0.06)\,\mathrm{mm}$ and $y = (26.62 \pm 0.01)\,\mathrm{mm}$, respectively. The beam center was displaced by about 10 mm with respect to the detector center. This leads to decreasing slopes in the distance-from-beam-center histograms for distances larger than 35 mm.

Beam Profile Determination

The knowledge of the profile of the ion beam is crucial for the generation of the modeled distance-to-beam-center distributions, which are then used to determine the product state branching ratios. The beam profile is well reflected by the center-of-mass distribution of DR events where both fragments are detected. Two corrections need to be taken into account:

1) *Non-DR contributions:* The center-of-mass distribution includes also contributions from non-DR events which may originate from reactions with the residual gas occurring outside the electron-ion interaction region. Such background events may broaden the center-of-mass distribution and should be subtracted accordingly.

These contributions were measured in a separate measurement step with the electron beam turned off.

2) *Permutational misassignments:* The center-of-mass determination relies on the correct assignment of the hydrogen and sulfur fragments to the detected fragment positions. The iterative procedure, briefly described in the previous paragraph, always prefers the heavy sulfur fragments to lie close to the beam center. The masses may be assigned incorrectly when the projected fragment distance on the detector is smaller than the displacement of the event center-of-mass with respect to the mean center-of-mass. This may occur for dissociation events with a small dissociation angle θ (see Fig. 3.8). The center-of-mass of an incorrectly assigned event lies closer to the mean center-of-mass. By this the center-of-mass distribution gets artificially narrower. Therefore, the center-of-mass data were filtered for fragment distances greater than 20 mm. For these events the risk of mis-assignments is minimal. However, for the available data no clear difference between the filtered and non-filtered data could be observed (see Fig. 4.11).

Using the radial symmetry of the experiment one can evaluate the beam profile only in the radial projection as a distribution of distances from the beam center, depicted in Figure 4.11. In contrast to a Cartesian representation, this has especially advantages for larger distances. Thereby, it is possible to perform a background subtraction despite the weak statistics.

Alternative Method for the Beam Profile Determination

According to Equation 4.19, the distance-from-beam-center distribution of one-hit events $\widetilde{P}_n(d_\mathrm{S}^\mathrm{CM})$ originates from a convolution of the distribution for an ideal needle-like beam $P_n(d_\mathrm{S})$ and the beam profile f_beam. $P_n(d_\mathrm{S})$ can be determined from two-hit data according to Equation 4.17. The beam profile f_beam can be derived by

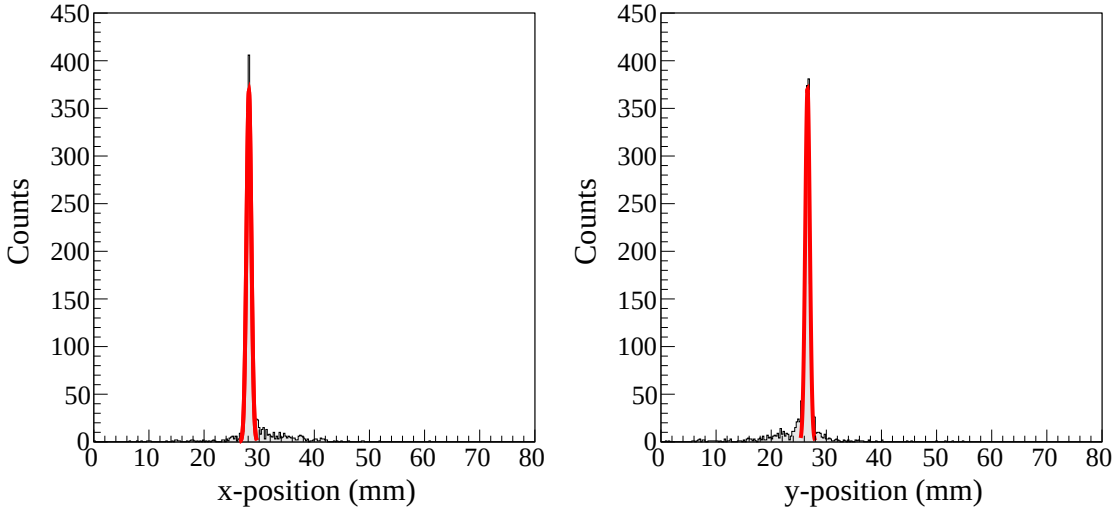

Figure 4.10: Center-of-mass distribution of two-hit events in x- and y-projection, which corresponds to the beam profile. This was fitted with a Gaussian function.

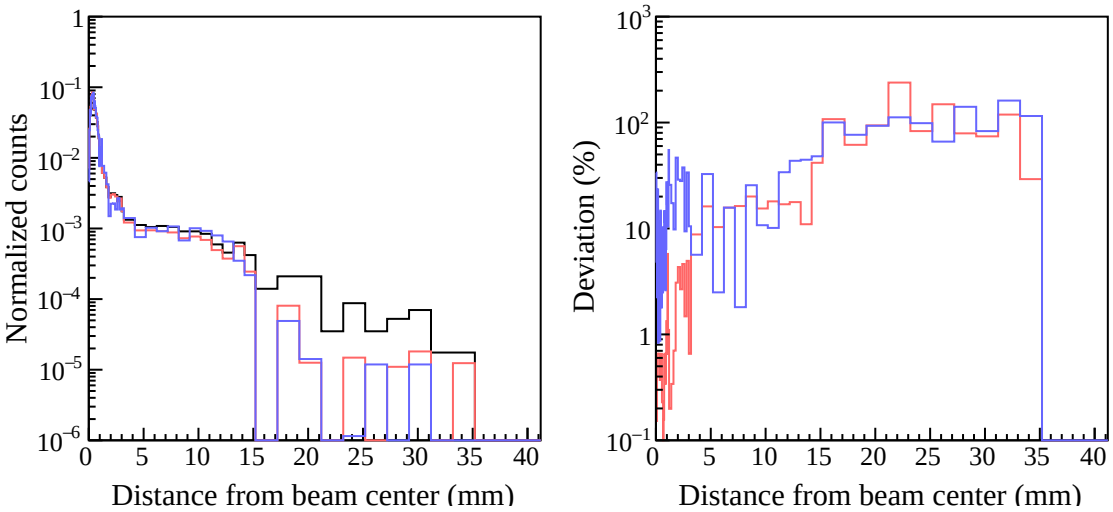

Figure 4.11: Distribution of distances from the center-of-mass for two-hit events (left graph). The unfiltered data are shown in black. The red and blue curves include both a background subtraction. The latter has an addition filter on events with large fragment distances. No clear difference can be observed between those two curves. All distributions are normalized to an integral of 1. The deviations from the unfiltered data (right) are below 20 % for the distances up to 15 mm.

an according deconvolution of these two distributions. In this case, however, the statical quality of the data was not sufficient to follow this approach.

4.4.3.2 Sulfur Fragment Distribution from One-Hit Events

The product state branching ratio of SH^+ shall be determined from the distance-from-beam-center distribution of only the heavier sulfur fragments. For this purpose the one-hit data are used as a base and corrected for other minor contributions. The corrections are applied as follows:

I subtract *MCP dark counts* from one-hit shutter-closed events scaled by their measuring time ratio,

II subtract *single hydrogen events* from two-hit events with electron-beam on,

III subtract *non-DR contributions* from one-hit events with electron-beam on, corrected for MCP dark counts, adjusted to the remainders distribution at larger distances,

IV add *sulfur events* from two-hit events with electron-beam on.

In the following paragraphs, these corrections are discussed in detail. The data for particular contributions are shown in Figure 4.12. The scaled contributions are shown in a cumulative representation in Figure 4.13. Furthermore, each step is visualized separately.

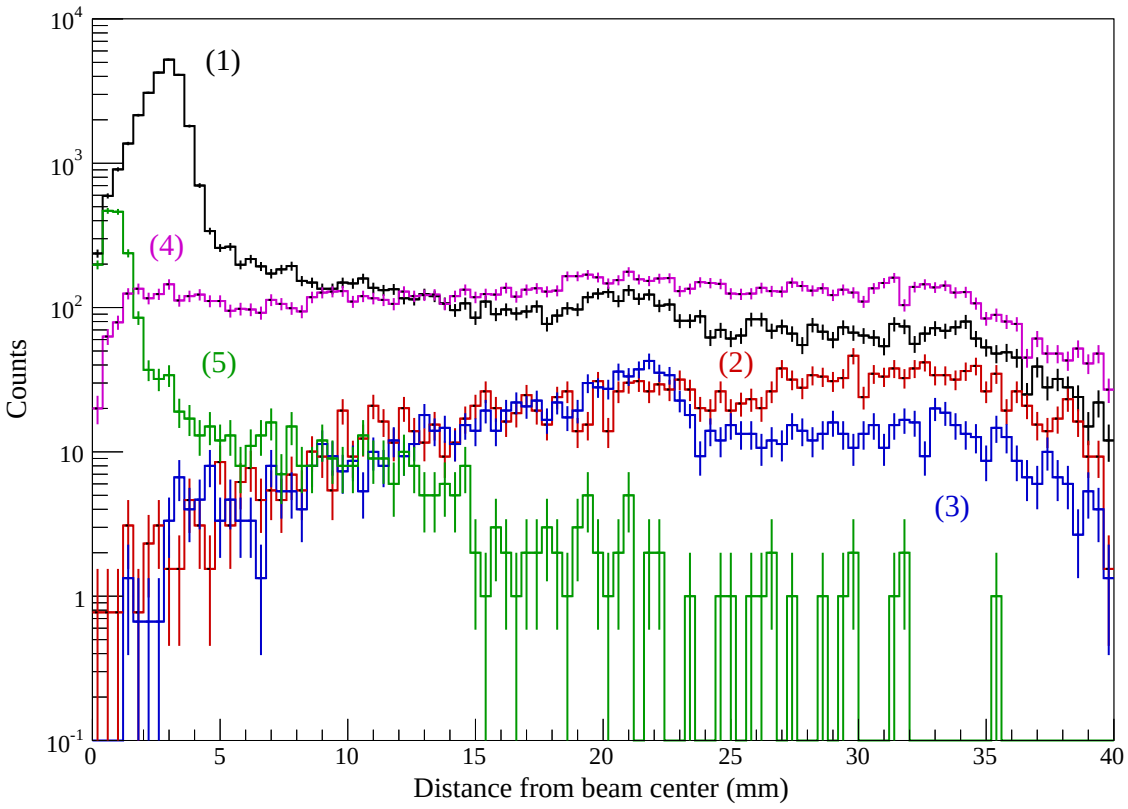

Figure 4.12:
Data of distance-from-beam-center distributions:
(1) *all* one-hit events with electron beam on,
(2) *MCP dark counts* from one-hit events with closed shutter,
(3) *single hydrogen events* from two-hit events with electron beam on,
(4) *non-DR contributions* from one-hit events with electron beam off,
(5) *single sulfur events* from two-hit events with electron beam on.
The scaled contributions are shown in Figure 4.13.

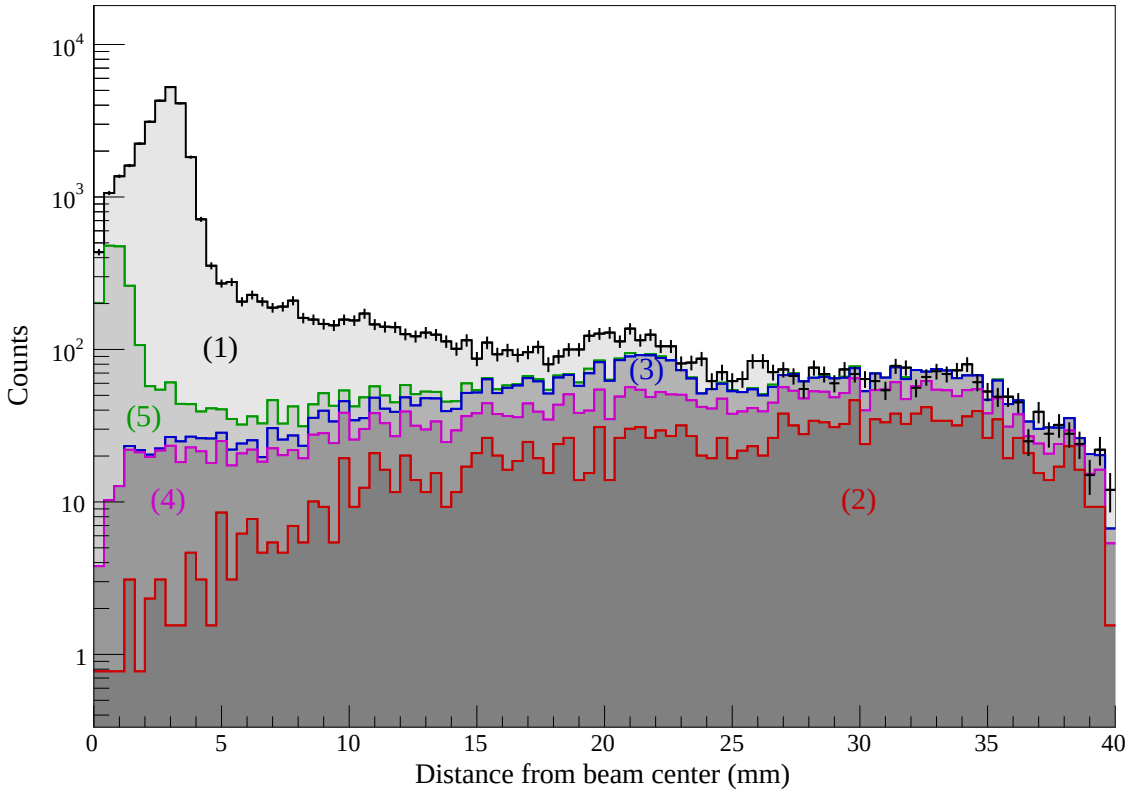

Figure 4.13:
Cumulative distance-from-beam-center distribution showing all identified contributions with appropriate scaling. In order to generate a spectrum of one-hit sulfur event only, the following corrections had to be considered:
(1) The derived distribution of sulfur fragments is extracted from the total curve, which includes the contributions from (5) and is corrected for the contributions from (2) to (4):
(2) *MCP dark counts* from one-hit beam-off data scaled by its measuring time ratio,
(3) *non-DR contributions* from one-hit electron-off data corrected for the MCP dark count rate,
(4) *single hydrogen events* from two-hit data scaled by the MCP efficiency ratio,
(5) *missing sulfur* events from two-hit data.
The fit of the resulting spectrum is shown in Figure 4.18.

MCP Dark Counts

Even if no particles hit an MCP detector one can observe a so-called *dark-count rate*, believed to originate mainly from beta-decay of ^{40}K in the bulk material of the glass substrate, which are uniformly distributed over the detector area [153]. The dark-count rate is determined in the first 11 s of each injection when the detector is still covered by a mechanical shutter. For the correction, the measured rate is scaled by the ratio of acquisition times of the shutter being closed and open. This scaling factor might be overestimated if the camera is saturated (see Sect. 4.4.3.4). This correction needs to be applied to both the DR data, with the electron beam being turned on, and the non-DR data, with the electron beam being turned off, which are both depicted Figure 4.14. The dark-count contribution increases towards larger radii as the available detector area increases linearly. Also, most of the DR signal is concentrated at the detector center so that the relative contribution of the homogeneously distributed dark counts increases towards larger radii. The comparison of the data with and without electron beam shows significantly larger contribution of dark counts for the DR data, which indicates a saturation of the camera due to the higher signal rates. The influence of this scaling factor on the result of the product state branching ratios is further discussed in Section 4.4.3.4.

Single Hydrogen Events

Although most of the hydrogen fragments missed the detector, some still hit the detector which originated either from dissociations with a sufficiently low kinetic energy release or which dissociated under a small angle with respect to the ion beam axis. On the other hand, even if both fragments hit the detector surface, some of them are not detected due to the limited open-area-ratio of sensitive channels which mainly determines the detection efficiency ε. The efficiency of the used MCPs was

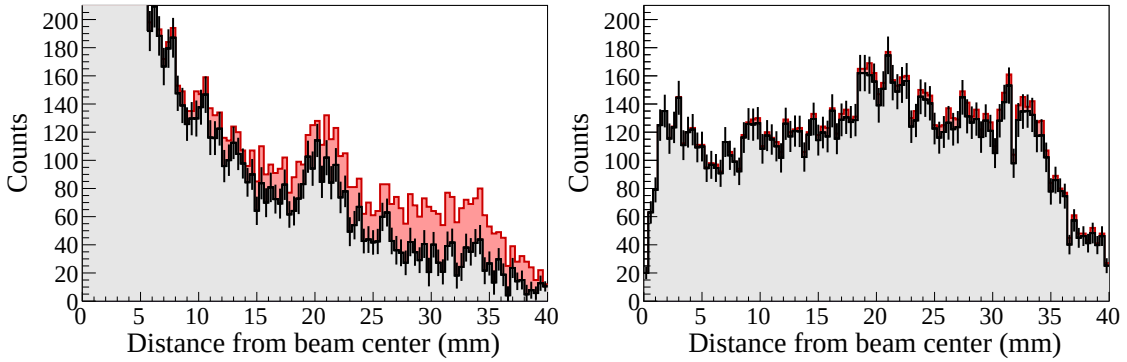

(a) Electrons on **(b)** Electrons off

Figure 4.14: Distance-from-beam-center distribution of single-hit data with correction (I) for MCP *dark counts* with the electron beam turned on (a) and off (b). The corrected data are depicted in black while the statistical errors are indicated by vertical bars. The uncorrected data are highlighted in red.

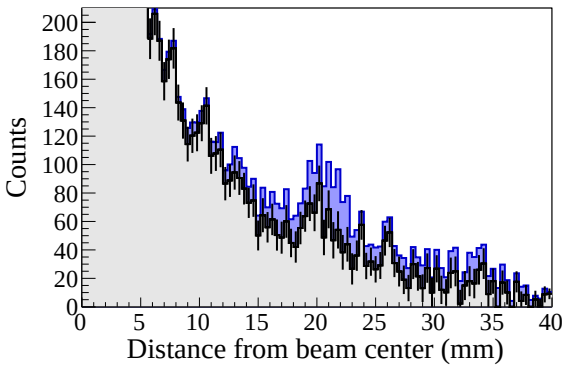

Figure 4.15: Distance-from-beam-center distribution with correction (II) for *single hydrogen events*. The data, including the corrections for dark counts (blue), were subtracted by the hydrogen fragment distribution from two-hit events scaled by the probability detecting only one of the fragments P_1 (black).

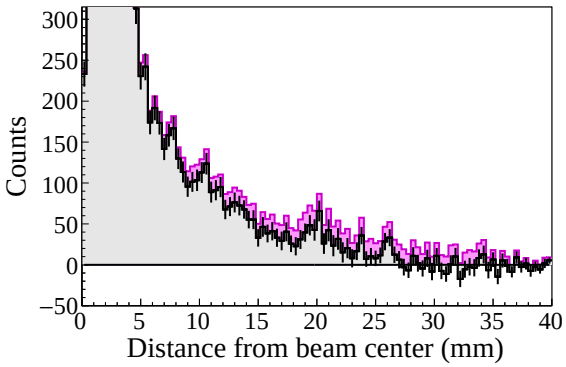

Figure 4.16: Distance-from-beam-center distribution with correction (III) for *non-DR* contributions. The non-DR contributions were determined in a separate measurements step with the electron beam turned off. Before the subtraction (magenta), the contributions were scaled such that the integral matched the spectrum between 27 and 35 mm. The final result is depicted in black.

estimated with about 60 %. The distribution of hydrogen fragments in the single-hit data was estimated by the distribution of the assigned hydrogen fragments in the two-hit data, which was scaled by the the probability of detecting only one out of two particles given a two-hit event

$$P(1|2) = \frac{\varepsilon(1-\varepsilon)}{\varepsilon^2} = 66.7\,\%. \tag{4.20}$$

The correction for single hydrogen hits is depicted in Figure 4.13 in blue. The peak structure around 20 mm is suspected to originate from the lowest energetic dissociation into the $S(^5S_2) + H(1s)$ product state. With this correction it was significantly lowered but not completely accounted for. The correction for H-only events is depicted in Figure 4.15.

Non-DR Contributions

The last considered contamination of single-hit data originate from non-DR reactions such as collisions with the residual gas, which also occur outside the electron-ion interaction region. Their contribution was determined in the measurement phase, when the electron beam is turned off and the beam shutter is open. Before these data were subtracted, their contribution was corrected for MCP dark counts rate as well. After the single-hit data were corrected for all other contributions, these data were scaled to match the amount of remaining background at larger distances in the

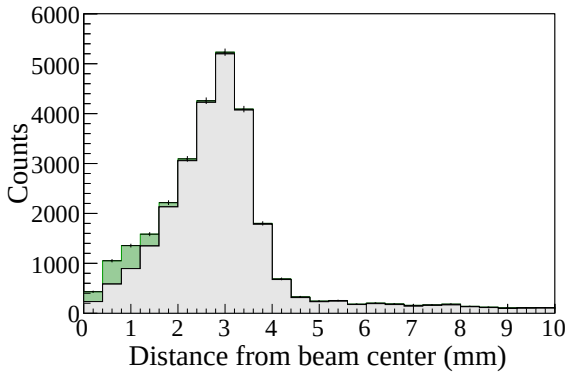

Figure 4.17: Distance-from-beam-center distribution with correction (IV) adding the missing *sulfur events* from two-hit data. The sulfur events from two-hit data are highlighted in green. The total curve is the final spectrum corresponding to DR induced S-fragments used for the determination of the product state branching ratios.

Table 4.7: Fit results for branching ratios of the different product excitation states. The systematic uncertainties were estimated from the distribution of fit result from 1000 fits, randomized within their expected uncertainty (see Sect. 4.4.3.4), the statistical uncertainty from a single fit. The assumed KER values were derived from Eq. 4.1.

Product state	KER (eV)	Branching ratios (%) (value)(stat)(sys)
$H(1s) + S\,(^5S_2)$	0.25	$4.65 \pm 0.02 \pm 0.26$
$H(1s) + S\,(^1S_0)$	4.03	$0.57 \pm 1.10 \pm 0.99$
$H(1s) + S\,(^1D_2)$	5.63	$60.77 \pm 1.90 \pm 0.50$
$H(1s) + S\,(^3P_{0-2})$	6.74	$33.73 \pm 1.90 \pm 3.54$

single-hit data, depicted in Figure 4.16. In order to determine a appropriate scaling, first, a suitable range for the matching needs to be estimated. Even the largest dissociation cone with the largest KER of about 6.8 eV has a limited diameter of about 3.6 mm and further displacements are well estimated by the center-of-mass distribution of two-hit events (see Fig. 4.11). The distribution shows a significant decrease for distances larger than 15 mm which gets even more pronounced when additional filters are applied. This sets the lower limit for the fitting range to about 20 mm. The shape of the distribution suggested a good matching in the range from 27 mm to 35 mm, which was finally used.

Sulfur Events from Two-Hit Data

Till this point, only single-hit data have been processed. Missing are sulfur events from two-hit data, which can be added directly without any scaling. Their contribution is depicted in Figure 4.17. The resulting spectrum, depicted in Figure 4.18, is used for the determination of the product state branching ratios, which is described in the next section.

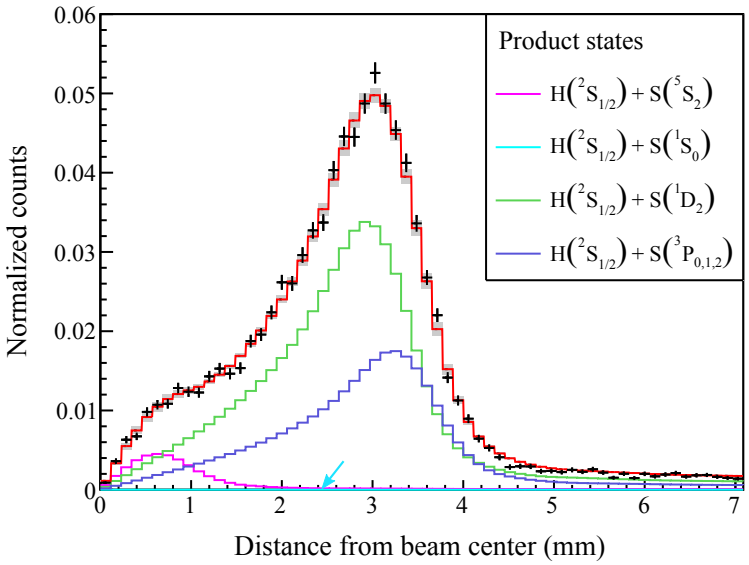

Figure 4.18: Normalized distance-from-beam-center distribution of sulfur fragments (black crosses). The fitted sum of the model distributions from different DR channels (colored lines) is highlighted in red with the 95 % confidence interval of the fit for each given bin as gray areas. The contribution of the $^1S_0$ channel is zero in this fit, while its expected peak position is marked by the cyan arrow in the Figure.

4.4.3.3 Fit Results

The distance-from-beam-center distribution were generated for all four presumed product state channels which are energetically accessible at zero electron-ion collision energy (see Table 4.2). Each of the sub-distributions was normalized to unity. In the resulting model distribution each of the sub-distributions is scaled by a free fitting parameter representing its branching ratio.

Figure 4.18 shows the fit results of the distance-from-beam-center distribution as derived in the previous Section. The data points of the distance-from-beam-center distribution are shown with their statistical error bars as black crosses. The fitted sum of the model distributions of the different DR channels is highlighted in red. The fit results with the estimated systematic errors are listed in Table 4.7.

The branching ratio of the $S(^5S_2)$ state has the smallest uncertainty as it is well separated from the other channels. The branching ratio of the $S(^1S_0)$ product state channel is found to be zero within its error bar. The KER values of the other two $S(^1D_2)$ and $S(^3P)$ product state channels differ only by about 17 %, thus display similar shapes. The fitted scaling factors are therefore strongly correlated. The experimental resolution is not sufficient to resolve the triplet splitting of dissociation into the ground state level.

Most of the data points agree with the model fit within their statistical error bars. Only very few isolated points show larger deviations, which may well be

statistical outliers. Overall, the derived sulfur fragment distance distribution can be well reproduced by the model fit. The systematic uncertainties are discussed in the following section. The obtained results are physically interpreted with regard to the different DR pathways in Section 4.4.4.

4.4.3.4 Uncertainties

The systematic uncertainties of the determined branching ratios were estimated from the distribution of fit result from 1000 fits, where both the input parameters for generating the distance-to-beam-center spectrum and the model distributions were randomized within their expected systematic uncertainty. In the following, the systematic uncertainties of the contributing parameters are discussed. The last paragraph of this Section describes the error estimation for the branching ratios including all contributions.

Camera Saturation

The camera can be operated with acquisition rates of up to about 20 frames per second which results in losses of data for DR event rates close of above this maximum rate. In addition, after each recorded event the system first needs to process the data, which leads to a dead time of about 20 ms. Because of this, not all dissociation events can be detected. That does not matter when detecting both DR fragments in the usual fragment imaging as only the fragment distances are of interest. However, in the one-fragment based method presented here, the derived distribution was also corrected for rate-depended contributions. The MCP *dark counts* are determined from the background data with closed shutter which have lower rates compare to the signal data with open shutter, and thus, are less effected by a saturation of the camera. Therefore, the scale factor of the non-DR contributions might be overestimated. Considering the signal-to-noise ratio, the dark counts of the data with electron beam were scaled in the range from 80 % to 100 % of the original value.

MCP Efficiency

The detection efficiency of an MCP is mainly limited by the surface coverage, the so-called *open-area-ratio* of the sensitive channels. For high-energy heavy particles it can be assumed that a electron avalanche is triggered by each particle hitting a sensitive channel. The detection efficiency of the employed MCP is expected to be at most 60 %. On the other hand, it may have degraded by the intense use over the years. We estimate the lower limit for the efficiency to about 50 %. This range was used in the randomized fitting routine for the propagation of the systematic uncertainties.

Kinetic Energy Release

The value of the assumed kinetic energy releases (see Eq. 4.1) has an uncertainty of 0.2 eV. For the error propagation all KER values were shifted by the same value randomized within this uncertainty.

Toroid Effects

The electron beam is merged and de-merged with and from the stored ion beam in toroidal magnetic fields. That can lead to two distorting effects of the imaging data which need to be considered:

- *Non-zero collision energies:* As the electron beam is merged and de-merged with and from the stored ion beam via toroidal fields, the angle between the ion and electron beams lead to non-zero collision energies in these regions, although the beam velocities were matched in the central interaction region. Assuming that the ion beam is not deflected by the electron beam, this can be modeled based on the known geometry of the electron beam.

- *Ion beam deflection:* If the electron and ion beams are not perfectly aligned, the ion beam can be deflected in the merging and de-merging sections, which lead to distortions of the collision angles. This effect is stronger towards cooling conditions, when the electron beam induces the largest *friction force*. If present, the cylindrical overlap symmetry, and consequently, the circular reaction profiles on the detector are distorted. No significant distortions could be observed at the measurements of SH^+.

Given the beam sizes and the relatively low kinetic electron beam energy of about 43 eV, the maximum collision energy change in the toroids is 0.5 eV. The contribution of the toroidal distortions to the total rate coefficient was estimated by a convolution of the modeled collision energies in the toroid section with the measured rate coefficient. At zero collision energy this leads to a change of only about 1 %. The contributions to the distance distributions of the sulfur fragments were estimated for the worst-case scenario: All products are assumed to dissociate with the maximum possible KER of 6.8 eV, so that the products are detected at the largest possible distances. Under these assumption, less than 1×10^{-5} of the sulfur fragments appear at distances larger than 4 mm from the center-of-mass for a given event. This effect is negligible compared to the other contributions and not considered for the total systematic uncertainty.

Estimation of Systematic Error

In order to propagate of the uncertainties of the previously discussed parameters to the uncertainties of the derived branching ratios, these parameters were randomized within their expected uncertainty ranges and the fit was executed many times for each set of parameters. The distribution of fit results was then analyzed for its mean squared error as an estimate for the propagated systematic uncertainty.

For each KER-value, 100 different convolved model distance distributions were generated. Each of those distributions were fitted with 10 different randomized MCP efficiencies and dark count scales, as those parameters can be easily varied.

The values of the mean branching ratios and their standard deviations for the different fits are given in table 4.7. The fit stability and the correlation of fit param-

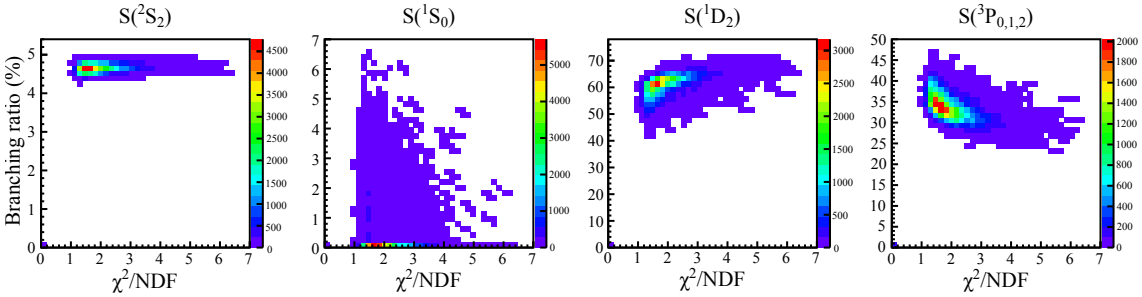

Figure 4.19: In order to estimate the uncertainty of the fit procedure, all parameters were randomized within their expected uncertainty. The two-dimensional histograms show the distribution of the resulting branching ratios against the χ^2/NDF-value (number of degrees of freedom) as a quality parameter for the fit.

eters are illustrated in Figure 4.19. The fitted branching ratios are displayed versus χ^2/NDF (number of degrees of freedom) as an measure for the fit quality.

The branching ratio of the low-KER S(^{5}S$_2$) channel is defined best as its events mainly originate from the almost background free two-hit data and is well separated from the other dissociation channels. The branching ratio of the second DR channel S(^{1}S$_0$) is compatible with zero within its error bar. The other two DR channels S(^{1}D$_2$) and S(^{3}P) are strongly correlated. Nevertheless, their values only scatter by a few percent within the range of the randomly varied parameters.

4.4.4 Discussion

Kinetic Energy Release

The small kinetic energy release of the DR product channel with the highly excited S(^{5}S$_2$) state could be measured directly from two-hit events, as both sulfur and hydrogen fragments from this product state could be projected onto the detector. The obtained value of $(0.27 \pm 0.02)\,\mathrm{eV}$ is consistent with the values derived from available reaction and atomic structure data (see Table 4.2). From this value, the kinetic energy releases of the other product states could be derived including the DR reaction energy ΔE_{DR} of SH^+. Moreover, a more precise value of the proton affinity compared to the value listed by Hunter and Lias [135] could be determined as well as another experimentally consistent value for the dissociation energy of the $v = 0$ ground state $D_0(SH^+, {}^3\Sigma^-)$ compared to the value by Rostas et al. [136]. Furthermore, the fit of the fragment distribution provides a branching ratio of this state of about 5.2 %.

Product State Branching Ratios

The SH^+ DR product state branching ratios, derived from the neutral fragment imaging measurements, agree well with the qualitative expectations from the potential energy curves by Park and Sun [137] discussed in Section 4.1. The largest contribution of about 62 % comes from the SH $^2\Pi$ state dissociating into the excited

sulfur $^1D_2$ product state with $H(^2S_{1/2})$. This was expected, as this state crosses the $X^3\Sigma^-$ ground state of SH^+ and has a favorable Franck-Condon overlap. The SH $^4\Pi$ state asymptotically leading to sulfur products in the $^3P_{0-2}$ ground levels has a significantly smaller contribution of about 33 %. According to the potential curves, this state is also crossing the $X^3\Sigma^-$ ground state of SH^+ but has a significantly smaller Franck-Condon overlap. For the SH $^2\Sigma^+$ state, leading to the sulfur $^1S_0$ product state, only a minor contribution was expected as it crosses the potential of SH^+ outside the Franck-Condon region and, in fact, the measured branching ratio is compatible with zero within its uncertainty. The highly excited $^5S_2$ product state close to the dissociation limit was measured with a distinctive contribution of 4.7 % using the new heavy-fragment imaging method. This is consistent with the value of (5.2 ± 0.6) % determined from the fit of the fragment distances from two-fragment imaging.

4.5 Outlook on Future DR Experiments at CSR

Merged-beams DR experiments in Heidelberg will be continued at the CSR storage ring. In comparison to the DR experiments performed at TSR, at CSR even heavier and more complex molecules will be investigated at significantly lower kinetic beam energies up to 300 keV. These molecules can have even larger mass ratios which lead to a similar situation as for the presented SH^+ investigation, where most light fragments missed the detector. Therefore, the heavy-fragment imaging technique developed in this work will be crucial for future investigations at CSR.

Within the scope of this work a position sensitive MCP-based detector has been developed for the CSR, which is described in the next chapter. This will enable investigations of product state branching ratios in the same way as for SH^+. While this kind of detector is not energy sensitive it is possible to assign masses geometrically in case of simple diatomic heteronuclear systems with a well cooled ion beam. In such cases, even recombination rate coefficients can be determined.

The advantages of experiments at CSR compared to TSR are foremost founded on the operation at cryogenic temperatures. On one hand this leads to vacuum condition improved by up to several orders of magnitudes, which strongly reduces background reactions with the residual gas. This enables much longer storage times which is, according to Eq. 3.14, of particular importance for the cooling of heavy systems. On the other hand, the reduced temperature of the ambient radiation field gives the possibility to store ions in their ro-vibrational ground state.

5 A Neutral-Fragment Imaging Detector for Cryogenic Environment

In this work, a detector system has been developed for the investigation of neutral products originating from reactions of molecular ions (see Sect. 2.2) in the cryogenic ultra-high vacuum environment of the CSR. Different eligible detection systems were evaluated regarding their performance and applicability considering the experimental and technical requirements of DR experiments at CSR (see Sect. 5.1). The solutions in question for the position- and time-sensitive read-out were partly simulated (see Sect. 5.1.4) with regard to the targeted experiments. The detector was designed and built (see Sect. 5.2). The key components of the realized detector system were characterized under cryogenic conditions with regard to their suitability for CSR operation (see Sect. 5.3) Finally, the detector was operated during the first two beamtimes of CSR, first at room-, later at cryogenic temperatures (see Sect. 5.4).

5.1 Concept

The detector was designed to meet the performance goals of molecular fragmentation experiments in the context of the technical requirements which originate from the operation in the harsh environment of CSR.

5.1.1 Technical Requirements

The CSR is described in detail in Section 3.1.5. Its technical requirements for the installed components stem mainly from its wide temperature range, the extremely high vacuum and the avoidance of stray or remnant magnetic fields.

The CSR operates in a temperature range from a few Kelvin to room temperature. In addition, the inner chamber and all its components must withstand bake-out temperatures of up to 250 °C in order to achieve a vacuum at the order of 10^{-11} mbar at room temperature. Thus, the choice of materials has to comply with the standard ultra high vacuum (UHV) requirements. For the mechanical design of all parts the different thermal expansion coefficients have to be considered. On one hand, the linear thermal expansion coefficients of metals are typically in the order of $\alpha \sim 10 \times 10^{-6}\,\mathrm{K}^{-1}$, which leads to linear thermal contractions in the order of $^{\Delta L}/_{L} \sim \alpha \Delta T \sim 0.1\,\%$ upon cooling from room temperature to a few Kelvin [154]. On the other hand, the values of glass and ceramics materials can be one to two orders of magnitudes lower. Especially, the different expansion coefficients of material parings

have to be taken into account. Otherwise, brittle materials like glass and ceramics can break, bolted joints can become loose and joined parts can move as a result of repeated thermal cycling.

For the parts in the isolation vacuum, interfacing the inner beam-guiding vacuum chamber at cryogenic temperatures with the outer vacuum vessel at room temperature, the heat input onto the inner chamber has to be taken in to account. While all parts inside the thermal shields have to be bakeable, the targeted vacuum pressure of only about 10^{-6} mbar permits a larger selection of materials.

As discussed in Section 3.1.5 magnetic stray fields need to be avoided at CSR as they could possibly significantly disturb the trajectories of the stored ions and charged reaction products. In the case of very light ions the earth magnetic field can prevent an ion beam storage [119]. Possible correction fields must be homogeneous over a large spatial range and should not be deformed by magnetically polarizable materials. For these reasons, all parts close to the ion beam orbit must have a very low magnetic permeability of $\mu_r \leq 1.01$.

5.1.2 Design Goals

For the investigations of electron-ion reactions at CSR, the stored ion beam will be merged with a cold electron beam over a distance of about 1 m [110]. Analog to the experiments at TSR, the diameter of the stored ion beam shall be reduced by electron cooling to below 1 mm (see also Sect. 3.1.3 and 3.1.4). The ion beam energies can be varied in the range from 20 keV to 300 keV whereas the electron-ion collision energies can be varied in a range from about 1 meV up to 1 keV. The neutral reaction products emerging from the straight merged electron-ion interaction section shall be intercepted by the detector developed within the scope of this work. In particular, the molecular fragmentation by recombination with cold electrons shall be investigated in a similar manner as in preceding experiments at TSR (see Sect. 3.1.4). Besides reaction rate measurements (see Sect. 3.1.2), a technically challenging application is the investigation of molecular fragmentation processes with the fragment momentum imaging technique, which is introduced in Section 3.2.

Geometrical Constrains

At CSR, the neutral product fragments are separated from the stored ion beam by the first 6° deflector electrode pair (see Fig 3.4 and 3.7). In principle, it would be possible to extract the neutral product fragments to a conventional room-temperature detection setup by extending the beam guiding vacuum system outside the CSR cryostat. In such a scheme the apertures facing room temperature have to be limited in size in order not to compromise the thermal stability of the beam pipe cooled down to cryogenic temperatures. This would limit the angular acceptance to only about 0.7° in case of a NW63 opening.

While the center-of-mass of the product fragments propagates with the velocity of the parent ion, the reaction spheres in the center-of-mass frame grow during the time-of-flight to the detector (see Sect. 3.2). The lower kinetic energies at CSR

Table 5.1: Maximum projected fragment distances $d_{\max}$ and arrival-time differences $\Delta t_{\max}$ at the foreseen detector position inside CSR in case of homonuclear diatomic molecules with $E_{\mathrm{KER}} = 1\,\mathrm{eV}$ for the minimum and maximum kinetic energies at which a singly charged molecular ion can be stored. The arrival-time differences scale with the velocity of the parent ion beam, which depends on the mass of the parent ion at given kinetic energy. For heteronuclear diatomic molecules both the fragment distances and arrival-time differences become larger.

Parameter	Minimum	Maximum
E_{kin}	20.0 keV	300.0 keV
$d_{\max}$	53.7 mm	13.9 mm
$\Delta t_{\max}(2\,\mathrm{u})$	38.7 ns	2.6 ns
$\Delta t_{\max}(160\,\mathrm{u})$	346.0 ns	23.0 ns

compared to experiments at TSR lead to very low ion beam velocities, especially in the case of even heavier molecules than were possible to investigate in the room-temperature storage ring. Thus, the reaction spheres grow relatively faster. As a consequence the detector should be placed closer to the interaction region in order to maximize the angular acceptance for neutral fragments.

The bending electrodes of CSR were designed such that reaction products can be efficiently separated from the ion beam. A reasonably close position for the detector is right next to the second 39° bending electrode following the 6° electrode with a distance to the center of the electron cooler of 3.8 m, where a large NW320 flange has been foreseen in advance for this detector. The available space allows the implementation of a detector with a diameter of up to 120 mm which corresponds to an opening angle of the dissociation cone of 1.8° for the center of the target. This results in an experimental limitation for the measurements of kinetic energy releases with the fragment momentum imaging technique. This is discussed for both TSR and CSR in Section 3.2. In the following, typically expected fragment and arrival-time distances on the detector in this experimental configuration are discussed.

Typical Fragment and Arrival-Time Distances on the Detector

For this estimation, the extreme case of homonuclear diatomic molecules is considered. For heteronuclear diatomic molecules both the fragment distances and arrival-time differences become larger. In the homonuclear case, the kinetic energy released at a dissociation is distributed equally among the two identical product fragments (see Eq. 3.27). Thus, the fragment distance D at the detector position is independent of the fragment masses and scales with $\sqrt{E_{\mathrm{KER}}/E_0}$. The transversal and longitudinal projection scale in the same way. Table 5.1 lists the projected fragment distances d and arrival-time differences at the foreseen detector position for a dissociation with a typical kinetic energy release of 1 eV at both the minimum and maximum ion beam energies of CSR. The largest projected fragment distances

on the detector of 53.7 mm in case of a 20 keV ion beam still fits comfortably on a detector with a diameter of 120 mm. By adjusting the beam energy the maximum arrival-time differences can be varied in the order of 10 ns to 100 ns.

5.1.3 Detector Choice

The detector for the DR reaction products should, in principle, provide as much information about the neutral final state as possible, but it still needs to be able to operate at the extreme thermal conditions inside CSR. Moreover, the kinetic beam energies at CSR are at least one order of magnitude lower compared to, e.g., previous experiments at TSR. These low particle energies effectively prohibit the use of surface-barrier diode detectors, which have previously been successfully used for storage ring experiments [106, 107, 155–157], as the penetration depths of the particles are typically too low in order to reach the detection volume. Such detectors have typically a metallic coating as electrical contact layer. As an example, the penetration depths in aluminum have been calculated with the software package SRIM (Stopping Range of Ions in Matter) [158] to be below 100 nm for 50 keV argon, below 180 nm for 40 keV carbon and below 50 nm for 2 keV hydrogen particles.

However, the cryogenic environment of CSR does provide suitable conditions for the operation of open micro-calorimeter detectors. While they are more commonly used for high-resolution X-ray spectroscopy, these kind of detectors are increasingly considered for high-resolution mass spectroscopy [159–162]. After first preparatory measurements [159] such a detector is also being developed for CSR.

For the first investigations of simple diatomic and triatomic molecular ions at CSR, an MCP-based detector [163] with position sensitive anode has been implemented in this work. This will allow, in particular, investigations with the fragment imaging technique (see Sect. 3.2) of ro-vibrationally cold ions. It has been shown that MCP-based detectors perform reasonably well under cryogenic conditions [164, 165], also with phosphor screen [166] and delay-line anodes [167]. The semi-conducting nature of the microchannel walls leads to a strong increase of the MCP resistance, which increases the recharge times of the individual channels [168] after an electron avalanche has been triggered. This may limit the maximum particle rates which can be detected with such a detector.

The readout solutions for MCP detectors can be divided into two classes, optical and electronic [169, 170]. The electron clouds emerging from the MCP are either converted into fast-decaying light spots which are then observed by a high-speed camera system, or their induced fast signal is read-out directly by an electronic system. There are hybrid systems which employ both optical and electric read-out techniques to order combine the advantages of both types of anodes [171, 172]. Simple electronic anode types, like wedge-strip and resistive anodes, provide a good position resolution from only 3 to 4 electrical channels. However, they cannot resolve multiple hits that arrive within a few ns. Advanced charge-dividing anode designs, like strip or pixel anodes, provide a very good performance [169] at the expense of a considerable complexity of the system. In the last decades, so-called delay-line

anodes enjoyed growing popularity [173]. Here, the position information is encoded into timing signals, which reduces the number of required signal lines significantly, while they are capable of detecting event rates in the order of $10^6\,\mathrm{s}^{-1}$.

The detector designed in this work will be used for all experiments at CSR involving neutral products as well as a diagnostics tool for the optimization of the beam-overlap in the electron cooler (see Sect. 3.1.5). The long cool-down and warm-up periods of each about two to three weeks place strong demands on the reliability of the detection system, which is not easily accessible. For the detection system of neutral particles at CSR, mainly two state-of-the-art designs of delay-line and phosphor screen anodes have been considered which promise a sufficient performance for DR experiment at a reasonable degree of complexity with regard to the implementation at CSR. Those two designs are briefly introduced before the final anode solution is discussed.

Phosphor Screen Anodes

A MCP detector with phosphor screen anode was for example successfully used for the DR experiments of SH^+ presented in this work (see Ch. 4). While this anode type provides a very good position resolution, it presents as a greater challenge to also measure the associated arrival times of the particle impacts. In preceding experiments at TSR, the relative arrival times of the particles were deduced from the fast intensity decay of the light spots on the phosphor screen in a quite involved set-up with two camera systems [131]. It is also possible to measure the arrival times with segmented photomultiplier tubes, provided that the particles are separated spatially such that their emitted photons are recorded by different detector segments. This method has already been successfully employed with strip-like photomultiplier anodes in several experiments [141, 174, 175]. In general, the electronic complexity of such a system tends to rise with that of the physics case under investigation, as it relies on the principle that each molecular fragment is detected by a different detector segment.

With a new read out system, developed by Urbain et al. [172], it is possible to associate the fast electronic signal, measured on a single electric line connected to the phosphor screen, to the light spots recorded by a fast camera. This system is described in more detail in Section 5.1.5.

Delay-Line Anodes

In principle, a position sensitive delay-line consists of a single wire which is wound as a large coil to form a double plane of wires. As the charged electrons, emitted by the MCP, are collected on the wire a current pulse propagate to both ends of the wire within the times t_1 and t_2. From the arrival-time difference, the position with respect to the center of the plane can be deduced according to

$$x = v_\perp(t_1 - t_2) \tag{5.1}$$

with $v_\perp$ being the effective signal velocity perpendicular to the windings of the delay-line. In this way, the position information is encoded in the delay signal $t_1 - t_2$. By adding another, crossed delay-line, one can determine the two-dimensional impact positions on the detector plane. For a given length of the delay-line wire l and the pulse propagation velocity along the wire v, the time sum of a signal pair is constant

$$l = l_1 + l_2 = v(t_1 + t_2) = \text{const.} \tag{5.2}$$

Multiple particle impacts can be distinguished by their time sum with respect to a common reference signal, e.g., from the MCP with

$$T_1 + T_2 = t_1 + t_2 - 2t_{\text{MCP}} = \text{const} \tag{5.3}$$

where T_1 and T_2 are measured with respect to the reference signal t_{MCP}. However, for this two-dimensional configuration signals may interfere on the delay-line for large particle impact rates. By adding a third redundant layer in a hexagonal structure the multi-hit performance can be significantly improved [176]. According to its hexagonal shape this type of delay-line is referred to as hexanode.

The great advantage of delay-line anodes is that they provide a high position and time resolution at a reduced complexity by encoding both the position and time information of the particles impacts in the same n-tuple of timing signals. Especially hexanode delay-lines are capable to distinguish multiple events with events rates in the order of $10^6\,\text{s}^{-1}$. A comprehensive Monte-Carlo simulation has been carried out in this work in order to investigate possible obstacles for the detection of correlated DR particle events with delay-line anodes. The results from these simulations served as a basis for the decision between the two considered anode designs. The results of these simulations are briefly discussed in Section 5.1.4

Final Anode Solution

A delay-line hexanode delivers an very good imaging performance for detecting multihit-events in the order of $10^6\,\text{s}^{-1}$. However, the Monte-Carlo simulations conducted within this work (see Sect. 5.1.2) have shown that this type of anode is not the best choice for the targeted DR experiments at CSR and a implementation would present some considerable challenges. The signal propagation times on such a delay-line are in the same order of magnitude as the the arrival-time differences of the fragments from DR reactions at CSR. This leads to signal interferences with strong event losses associated to the geometry of the hexanode, independent of the overall detected reaction rate. Furthermore, this kind of read-out requires typically seven (1 MCP, 6 hexanode) electrical signals of very high quality. Moreover, the wide temperature range may considerably stress the wound wires.

Instead, a more conservative and robust approach was chosen by using a phosphor screen read-out. In combination with the new read-out principle, developed by Urbain et al. [172], it is possible to correlate the light spots with the electrical timing signals and thus perform a three-dimension measurement of the fragment

distances in a rather economical setup. The original data acquisition system developed by Urbain et al. was also used for the first measurements at CSR, presented in Section 5.4. Another advantage of this approach is the fact that all its electronics is outside the cryostat of CSR. Therefore, it is easily accessible and can be updated with more powerful hardware in the future.

5.1.4 Delay-line Anode Simulation

A Monte-Carlo simulation of a DR experiment at CSR has been conducted in order to investigate possible issues using a MCP detector with a delay-line hexanode. The simulation program is written in C++ using ROOT libraries developed at CERN for the data analysis and presentation [177]. The different parts of the simulation are defined in separate classes. The algorithms of those classes are briefly described in Appendix A.2. The Monte-Carlo simulation is divided into four major parts:

1. generation of a *DR event* with the according fragment positions and arrival-times at the detector,
2. simulation of the *detector response* as delay-line signals for a given MCP efficiency,
3. simulation of the *electronics* with signal discrimination including dead time and signal jitter effects, and the final
4. *analysis* of the signals to reconstruct the impact positions.

The code for generating the DR events is based on a well-tested program used also for simulations of DR events at TSR [178]. In the following, the expected issues of a delay-line read-out are briefly discussed before the simulation results are presented for one representative example.

After a particle impact, two time signals are induced on the delay-line, which propagate with an effective velocity perpendicular the windings of about $0.4\,\mathrm{mm\,ns^{-1}}$ [179] in case of a hexanode delay-line for a 120 mm MCP detector. Hence, the signal propagation time across each delay-line layer is in the order of 100 ns. This time is in the same order of magnitude as the typical arrival-time difference of the product fragments estimated in Section 5.1.2. Signal interferences of multiple hits on the delay-line lead to signal losses. Some of the lost signals may be reconstructed by the time-sum criteria (see Eq. 5.3).

A typical DR experiment was simulated with an artificial diatomic homonuclear molecular ion beam with two fragments of an intermediate mass of 16 u stored at the maximum beam energy of 300 keV at CSR and assuming an electron cooled ion beam radius, similar as for similar TSR experiments, of 0.5 mm. In order to investigate the resolving power in terms of kinetic energy release, DR events with kinetic energy releases of 0.1, 0.3, 1, 3 and 10 eV were simulated. An MCP with a diameter of 120 mm and a detection efficiency of 60 % was assumed. The corresponding hexanode delay-line has a width of 160 mm in order to cover the whole MCP surface. The

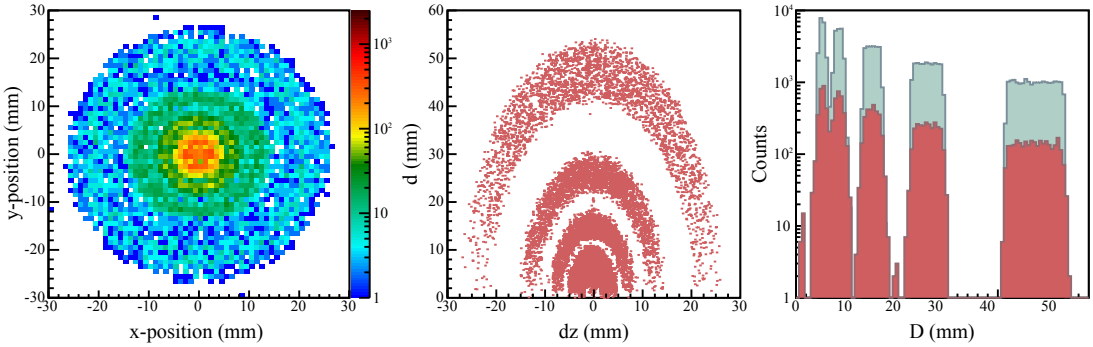

(a) MCP response

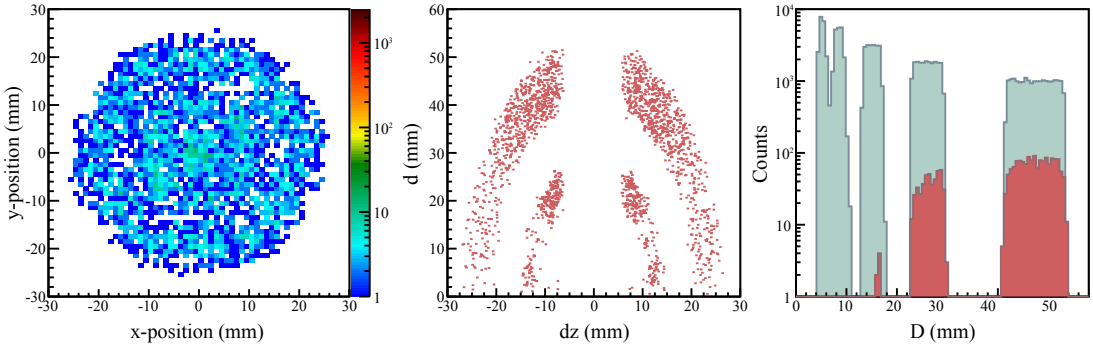

(b) Discriminated delay-line signals

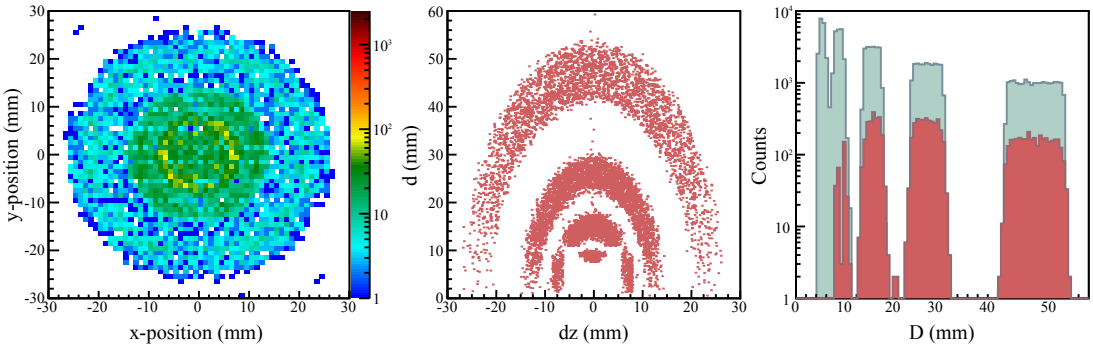

(c) Reconstructed delay-line signals

Figure 5.1: Results of Monte Carlo simulations of DR fragments detected with MCP and hexanode delay-line. The histograms in the first row show the response of the MCP, the graphs in the second row the discriminated delay-line signals, and the graphs in the third row include reconstructed events. The histograms in the first column show the two-dimensional distribution of particle impacts on the detector surface. The graphs in the second row show the transversal and longitudinal fragment distances analog to Figure 3.11. The histograms in the third row show the three-dimensional fragment distances also analog to Figure 3.11. The green histograms represent the simulated DR events, the remaining contributions including the respective steps.

spacing of the wires was assumed with 1 mm. The response of the electronics was simultated by adding a normally distributed signal jitter with a width of 0.1 ns and a signal dead time of 10 ns. This also partly accounted for the expected signal width of a few ns.

Figure 5.1 shows the results of the Monte Carlo simulations of DR events detected by an MCP with a hexanode delay-line. Figure 5.1a shows the response of the MCP considering its efficiency. Figure 5.1b shows the results deduced from discriminated delay-line signals including a 10 ns dead time and a normally distributed signal jitter with a width of 0.1 ns. For the results shown in Figure 5.1c, missing signals were reconstructed using the time-sum criteria (see Eq. 5.3). The graphs in the left column show the spatial distribution of the detected fragments. The reaction spheres projected onto the detector cover circular areas with a diameter $\propto \sqrt{KER}$. The density of these circular areas is increasing towards their respective maximum diameter. The graphs in the next two columns show the fragment distance distributions d versus Δz and the derived absolute fragment distance D analog to Figure 3.11 described by the Equations 3.34, 3.36 and 3.37.

After the simulated signal discrimination, all events with arrival-time differences smaller than 10 ns are lost. The spatial distribution exhibits 'holes' with a hexagonal pattern, which can be attributed to the geometry of the delay-line. In the correlation graph of the transversal and longitudinal fragment distances, the discriminator dead time of 10 ns manifests itself in a dead window along Δz with a width of about 12 mm. Furthermore, stronger losses can be observed for dissociation angles slightly below 60° and 120°. This corresponds to the angles of the hexagonal coordinate system of the delay line, as the impact coordinates are always reconstructed from two of the three layers.

The distribution of absolute fragment distances shows a strongly decreasing response function of the detector towards lower kinetic energy releases. As a consequence KERs of 1 eV can already not be resolved anymore. It is possible to reconstruct much of the lost signal. Still, events with KER of up to 1 eV are affected. The irregular shape of the detector response in the dissociation space is difficult to address in a real experiment.

There is another disadvantage of such a delay-line anode in view of planned experiments at CSR. It is already foreseen to combine this detector with another smaller position- and energy-sensitive microcalorimeter detector for measurements of heavier neutral fragments. The necessary hole in the detector center leads to large areas covered by only two delay-line wires, which are less multi-hit capable, or even a star-shaped area in the center with only one layer, where the hit positions cannot be reconstructed (see Fig. 5.2).

Further, even more complicated delay-line designs were investigated, but they could not circumvent the fundamental issue of this anode type for detecting correlated particles events with arrival-time differences in the order of the signal propagation time on the delay-line anode with typically a few 10 ns. Moreover, an implementation at CSR would require a high-quality transmission of all electrical signals in order to achieve the simulated performance. Therefore, this anode scheme was

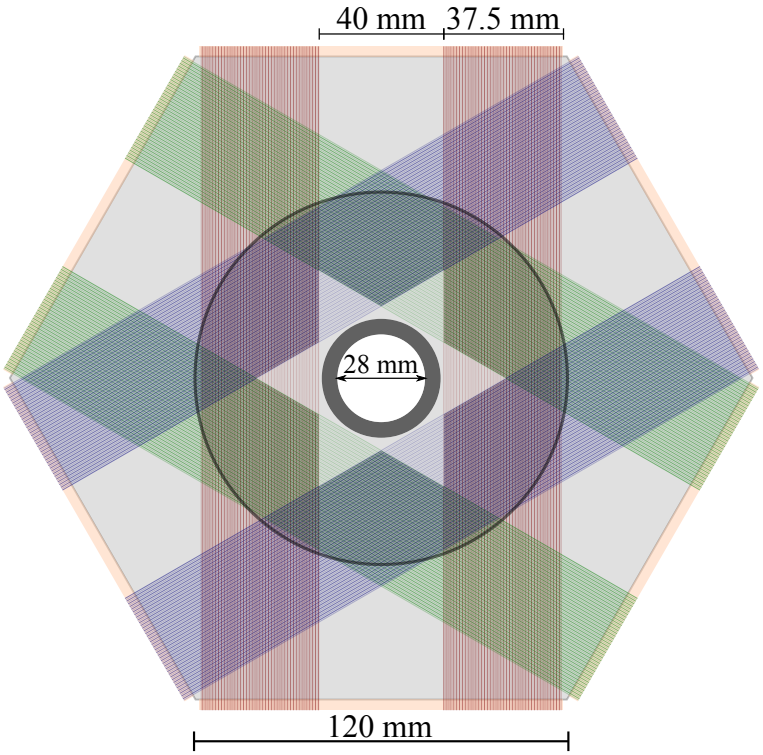

Figure 5.2: Hexanode delay-line with central hole. The three different delay-line layers are highlighted in red, green, and blue. The area covered by the MCP is indicated by the shaded circle. The brighter star-shaped area in the center is only covered by one delay-line layer and therefore not position sensitive. Only a small fraction of the detector is still covered by all three layers.

finally rejected in favor of a conservative approach using a phosphor screen anode.

5.1.5 3D Imaging with Correlated Brightness-Amplitude Assignment

An MCP-based detector with phosphor screen anode allows independent measurements of the particle impact positions by determining the positions of the light spots on the phosphor screen and their arrival-time difference from the fast electronic signals induced by the collected electron clouds on the phosphor screen anode. In order to retrieve the combined position and time information of each hit, the measured light spots and electrical pulses of all hits of a dissociation event have to be assigned to each other.

A new acquisition scheme has been developed by Urbain et. al. [172] where the time and position signal are correlated by their respective signal intensities. With regard to its operating principle this read-out scheme is also referred to as COrrelated BRightness-Amplitude (COBRA). The data acquisition system by Urbain et al. was also employed with the detector system developed in this work during the first operation tests at CSR at room temperature conditions (see Sect. 5.4).

Electron multiplication in an MCP is a cumulative effect of many secondary electron ejections from the microchannel walls. Following a quasi-Poissonian distribution [180], each ejection process yields a random number of electrons, each of which, in turn, produces more secondary electrons at the next wall collision. At high gain operation of an MCP, the total number of electrons in the avalanche converges towards an upper bound defined by space-charge screening of the accelerating potential. This results in a narrow anode pulse height distribution, which is a beneficial effect in many applications. However, when operating the MCP at low operating voltage, far from the space-charge saturation limit, the random electron multiplications accumulate freely, resulting in a broad distribution of pulse current intensities. Upon collection at the phosphor screen anode, this yields a correspondingly broad distribution of spot brightness. Under suitable conditions, the relative pulse current intensities and spot brightness intensities of an ensemble of nearly coincident particle hits onto the detector can thus be used to relate the arrival time and position coordinates of each hit. This is the essence of the COBRA 3D imaging scheme.

The great advantage of this read-out scheme is the fact that the positions and arrival times are still measured independently. In a DR experiment, the transversal and longitudinal particle distances, as projected on the detector, are correlated by the absolute distance of the fragments. The molecules have random orientations during the fragmentation. The correlation by the absolute fragment distance of the dissociation fragments results in an complementary measurement of spatial and temporal distances. The dissociation events of a diatomic molecule with large spatial separation, have a small temporal separation and vice versa. This always leads to a relatively small uncertainty of the inferred absolute fragment distances.

5.1.5.1 Spatial Correction of the Intensity Correlation

Since the COBRA scheme assigns the position and arrival-time signals by their correlated intensities, it is important to first correct those for variations which may originate from inhomogeneities in the phosphor layer or MCP gain. They may also be affected by aberrations of the optical system. In the following, a correction procedure is described which was developed for the first tests with a COBRA DAQ within the first beamtime of CSR. The results of those tests are presented in Section 5.4.

For the correlation correction only one hit events with one pulse and one spot are considered, which can be unambiguously assigned to each other. First, the detector image is subdivided in $n \times n$ rectangular segments indexed by k and l. For each detector segment (k, l) the intensity correlation of all one-hit pulse amplitudes A_1 and light spot brightnesses B_1 is fitted with the linear function

$$A_1 = a(k,l) \cdot B_1 + b(k,l). \tag{5.4}$$

The spot brightnesses of all segments are then corrected by the obtained fit parameters $a(k, l)$ and $b(k, l)$ to

$$\widetilde{B}_1 = a(k,l) \cdot B_1 + b(k,l). \tag{5.5}$$

Then, the correlation of A_1 and $\widetilde{B}_1$ follows the unity line. After all intensities have been corrected, the same acceptance condition, described in the following paragraph, can be applied to all data.

5.1.5.2 Permutation Validation

After the signal intensities have been corrected for spatially inhomogeneities of the correlation function, the position and arrival-time signals are associated by their correlated intensities. The essential part of the COBRA assignment is the algorithm for identifying the correct permutations of the multiple pulse amplitudes and light spot brightnesses. While this is already described in [172], at this point, a mathematical formulation is given. Figure 5.3 illustrates schematically the assignment algorithm for two hit events. In this graph the correlated events are distributed along the correlation axis in a band with a certain spread. All possible signal permutations are validated by a fixed acceptance threshold σ_a, to lie in this band.

For the sorting algorithm, the signals are indexed by the tupel $\{1, 2, \ldots, n\}$. Then, a single permutation of this index order is the bijective correspondence

$$\pi : \{1, 2, \ldots, n\} \to \{1, 2, \ldots, n\} \tag{5.6}$$

which assigns each natural number between 1 and n a number in the same domain. In the tupel notation the permutation function is represented by

$$\pi = (\pi(1), \pi(2), \ldots, \pi(n)). \tag{5.7}$$

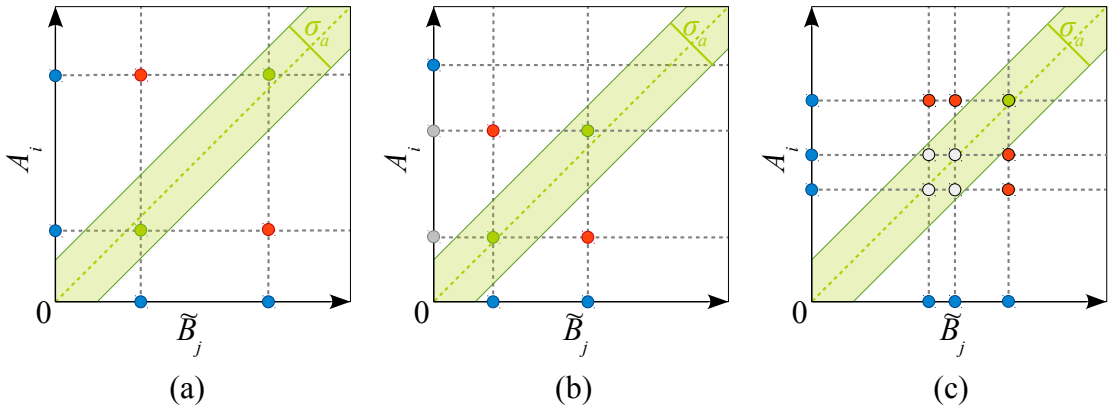

Figure 5.3: Schematic illustration of the COBRA permutation validation and reconstruction of recorded pulse amplitudes A_i and light spot brightnesses B_j. One hit events show a correlation of the signal intensities of both the electrical pulse heights and the light spot brightnesses. Multi-hit events are validated based on the acceptance threshold σ_a determined from correlated distribution of one-hit events. The blue points are the measured multi-hit pulse and light spot signal intensities. The possible permutations are validated (green) or rejected (red) via the acceptance threshold σ_a shown in (a). The reconstruction shown in (b) is explained in the text. An ambiguous three particle event is illustrated in (c).

Each application of π gives a new distinctive tupel. An $n!$-fold application leads to the original tupel. For each permutation $\pi^j \in \Pi = \{\pi^j : j \in \{1, 2, .., n!\}\}$ the correlation spread σ_{π^j} can be defined as the largest distance of all pulse and spot intensity pairs $\left(A_i, \widetilde{B}_{\pi^j(i)}\right)$ from the correlation diagonal

$$\sigma_{\pi^j} = \max_{i=1,\ldots,n} \frac{\left|A_i - \widetilde{B}_{\pi^j(i)}\right|}{\sqrt{2}} \tag{5.8}$$

For a fixed acceptance level σ_a, the number of accepted permutations can be defined as

$$n_\mathrm{a} = \sum_{\pi^j \in \Pi} \Theta\left(\sigma_\mathrm{a} - \sigma_{\pi^j}\right) \tag{5.9}$$

with the heaviside function

$$\Theta(x) = \begin{cases} 0 : x < 0 \\ 1 : x \geq 0 \end{cases} \quad \text{with } x \in \mathbb{R}. \tag{5.10}$$

Only one of all the permutations is correct. This permutation may be rejected by the threshold criteria or more than one permutation is accepted which leads to

ambiguities. In Figure 5.3, the accepted permutations are highlighted in green, the rejected permutations in red. The events can be classified by the number of accepted permutations

$$\begin{aligned} n_\mathrm{a} &= 0 \quad \text{as } \textit{invalid}, \\ n_\mathrm{a} &= 1 \quad \text{as } \textit{valid}, \text{ or} \\ n_\mathrm{a} &> 1 \quad \text{as } \textit{ambiguous}. \end{aligned}$$

This can be used to characterize the performance of the COBRA assignment. This is also discussed for the experimental results obtained during the first beamtime of CSR described in Section 5.4.1. Some effects may disturb the event validation and reconstruction: For signals of similar intensities, may be more than one permutations is accepted which introduces ambiguities in the assignment. Therefore, this method works best for very different signal intensities from a broad MCP pulse height distribution. Such an ambiguous case is illustrated in Figure 5.3c for a three-hit event. The method also does not work directly for overlapping signals. However, in some cases those signals can be reconstructed, as described in the following paragraph.

5.1.5.3 Event Reconstruction

In the case of overlapping signals, the total number of recognized pulses and spots does not agree anymore, as illustrated in Figure 5.3b. This may occur for pulses close in time and spots close in space. Then, the superimposed signal is observed with the combined intensity of both signals. This case can be identified, when the number of signals in both channels differ by one and the difference of the total intensities in both channels is smaller then the acceptance threshold

$$\left| \sum_{i=1}^{n_p} A_i - \sum_{i=1}^{n_p} B_i \right| < \sigma_\mathrm{a}. \tag{5.11}$$

Assuming that the pulse and spot intensity signals are correlated, one can split up the sum signal into two signals with the same intensity ratio as measured on the other channel. This is a very strong condition as any signal spread is neglected and, therefore, may require a lower acceptance threshold. The events with those artificial signals can be validated as described before.

5.2 Realization of the Detector Hardware

In this Section, the realized detector system is described in detail, which considered all the conceptual aspects discussed before. With regard to its purpose, the system is referred to as NICE detector which is an acronym for Neutral particle Imaging in Cryogenic Environment. The layered design of the CSR cryostat imposes a natural subdivision of the detector system into three groups characterized by their function and temperature regime. These are

1. the *cryogenic particle sensor* inside the beam-guiding chamber of CSR at cryogenic temperatures of a few Kelvin,

2. the *interfacing components* in the isolation vacuum of CSR between the inner and outer chamber at a few tens of Kelvin, and

3. the *readout electronics* outside the cryostat of CSR at room temperature.

Figure 5.4 shows a cutaway model of the whole detector systems inside CSR. The particle sensor is a cryo-compatible implementation of an MCP detector with phosphor screen anode, which is observed from outside the cryostat. The optical path extends across all temperature regimes and is briefly described in Section 5.2.1, before the three functional groups are discussed independently.

All interfacing components had to be design for a sufficiently low heat transfer from the room temperature side towards the cryogenic beam-guiding chamber of CSR. Furthermore, a heating of the particle sensor has been implemented.

Heat Transfer

The cryostat design of CSR with an isolation vacuum prevents a convective heat transfer. For the optical observation of the detector, apertures in the thermal shields are required. Here, the radiative heat transfer needs to be considered. A body with temperature T and surface area A emits radiation at a power of [181]

$$\dot{Q}_{\mathrm{em}} = \epsilon(T) A \sigma T^4. \tag{5.12}$$

where $\sigma = 5.6704 \times 10^{-8}\,\mathrm{W/m^2K^4}$ is the Stefan-Boltzmann constant. The emissivity $\epsilon(T)$ is a material specific property for a, so-called, gray body, which describes the ratio of the radiated heat flow with respect to a black body, which completely absorbs all radiation. For example, the typical emissivity of glass is well above 0.9 while that of technical metal surfaces can be also in the order of 0.01. Further emissivity values are listed, e.g., in [182]. The radiative heat transfer between two bodies is discussed for a simple case, which is a good approximation for the estimations at CSR. The body shall be placed in a surroundings of temperature T_{S} which behaves as a black body. The medium between the body and the surroundings shall be transparent for radiation. In turn, the gray body absorbs the heat $\dot{Q}_{\mathrm{abs}}$ from its surroundings with temperature T_{S} analogous to Equation 5.12. This results in a net flow of heat

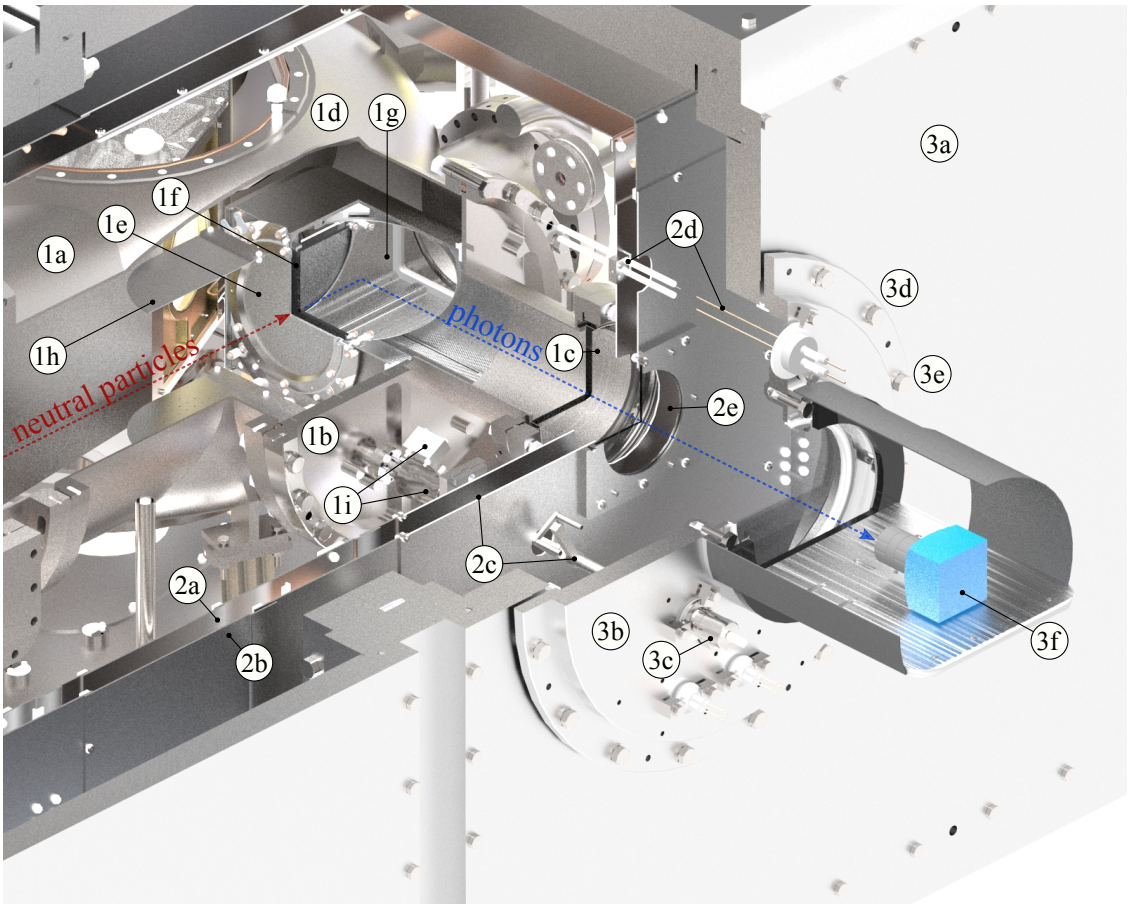

Figure 5.4: Cutaway model of the NICE detection system inside the CSR. The cryogenic beam-guiding vacuum chamber (1a) is enclosed by another isolation vacuum chamber (3a) at room temperature. In addition, there are an inner (2a) and outer thermal shield (2b). The outer shield is wrapped in multi-layer superinsulation (not shown) and has a water cooling to protect the foil during the bake-out.
All components of the cryogenic particle sensor are mounted on the inner mounting flange (1b). The detector housing (1d) both capsules the light path and provides the mounting structure for the sensitive components. Neutral particles, as indicated by the red, dotted line, hit the MCP (1e). The released electron clouds produces light spots on the phosphor screen (1f). They can be observed with a high-speed camera (3f) outside CSR's cryostat at a 90° angle via a Al-mirror (1g) through a large cryo-compatible view-port (1c) on the inner chamber, a sapphire infrared-filter on the outer thermal shield (2e) and a standard view-port (3e) on the outer detector flange (3b). The electronic signal from the phosphor screen anode is guided via a bare stainless steel wire through the shields (2d) to a decoupling box (3d) on the outer detector flange.
The MCP can be either covered by a beam-shutter or a calibration mask (1h). The model shows the mechanics of the lower calibration mask. The flaps are mounted directly on the axis of bellow-sealed rotary feed-throughs (1i), which can be moved via an intermediate drive (2c), thermally anchored on the 40-K stage, with a standard rotary feed-through (3c) mounted on the outer detector flange.

between the body and its surroundings of

$$\dot{Q} = \dot{Q}_{\mathrm{em}} - \dot{Q}_{\mathrm{abs}} = \epsilon(T) A \sigma \left(T^4 - T_{\mathrm{S}}^4\right). \tag{5.13}$$

For all interfacing components connecting different temperatures regimes, the heat conductance needs to be considered. For isotropic substances, the heat flux vector is always perpendicular to the isothermal surface [181]. The heat flow $d\dot{Q}$ through a surface element dA with its normal vector $\mathbf{n}$ is [181]

$$d\dot{Q} = -\lambda(T) \nabla T \mathbf{n} dA \tag{5.14}$$

where $\lambda(T)$ is the thermal conductivity, which may also be temperature dependent. For a long cylinder of length l with constant cross section A, this simplifies to

$$\dot{Q} = \frac{A}{l} \int_{T_1}^{T_2} \lambda(T) dT \tag{5.15}$$

where T_1 and T_2 are the temperatures on both ends.

5.2.1 Optical Design

The phosphor screen is observed by a high-speed camera system from outside the cryostat of CSR. This requires an optical path through all thermal layers of CSR. In order to fully exploit the available camera optics and to be able to combine different optical read-out solutions the optical path was optimized for a 50x50 mm beam-splitter right outside the outer view-port. Figure 5.5 shows a schematic ray tracing diagram which was used to determine the necessary aperture dimensions. The openings in the thermal shields were thermally closed by a infrared-filter made out of sapphire glass. Sapphire has a very high thermal conductivity coefficient and a transmission of more than 85 % in a spectral range from about 0.3 μm to 5 μm [183]. The according calculations, as presented in Sect. 5.2.3.1, suggested that a direct observation with relatively large transparent openings in the different thermal layers of CSR is feasible. Therefore, the use of a magnifying optics was not necessary. This way additional distortions and possible misalignments due to CSR's thermal cycles could be avoided.

It is already foreseen to combine the realized NICE detector later with an additional, smaller position- and energy-sensitive detection system behind the NICE detector. This will be especially useful for the study of heavy polyatomic molecular ions. A microcalorimeter-based detector system is in development [159]. For this reason the phosphor screen is observed from a 90° angle leaving the space behind the NICE detector free.

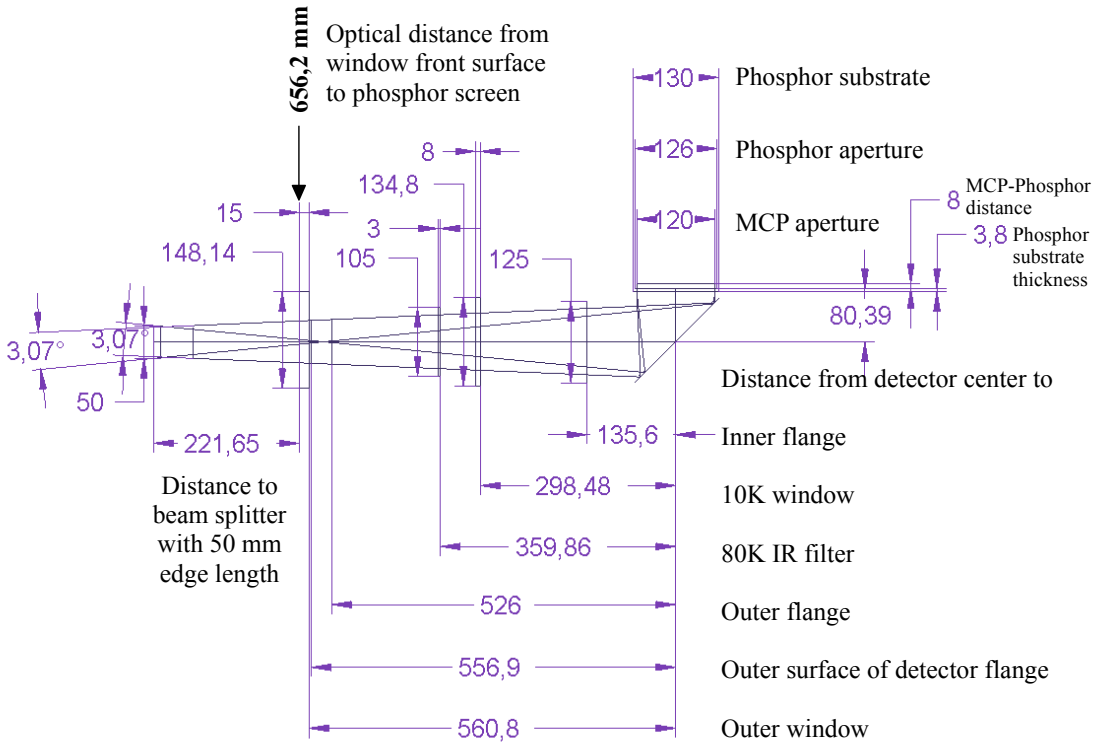

Figure 5.5: Ray tracing diagram of the optical system of the NICE detector. The dimensions of the apertures were chosen so that the light can be collected by a 50×50 optical beam splitter independent of the following camera systems. This aperture covers a solid angle of about 3° for the observation of the phosphor screen. The dimensions and positions of the different optical apertures are also listed in Table 5.2. The light from the phosphor screen (1) is reflected by an Al-mirror (2) (see Sect. 5.2.2.5), passing through a cryogenic view-port on the experimental vacuum chamber (3) (see Sect. 5.2.2.6), a sapphire IR-filter on the inner thermal shield (4) (see Sect. 5.2.3.1) before it exits CSR's cryostat through a outer view-port (5).

5.2.2 Cryogenic Particle Sensor

The heart of the detection system is the sensitive particle sensor inside the inner chamber of CSR cooled to cryogenic temperatures. Figure 5.6 shows a picture and a model of the fully assembled sensor unit as it was finally installed at CSR. All components are mounted on lateral NW320 flange with a Helicoflex® sealing. The particle sensor consists of an MCP with an position-sensitive phosphor screen anode. The electrons emerging from the MCP are converted into fast decaying light spots, which can be observed with a high speed camera. The electrons induce also small current pulses on the conductive layer of the phosphor screen, which are used as arrival-time signals of the impinging particles. The MCP unit with its heating module (see also Fig. 5.7) is mounted on the front side of the detector housing

Table 5.2: Dimensions and positions of the different optical apertures with respect to the phosphor screen. The values are taken from the construction model and may slightly differ by a few mm from the real values.

Element	Distance (mm)	Size (mm)	Thickness (mm)	Material
MCP	−8	120		
Phosphor screen	0	126	3.8	Borofloat 33
Mirror center	80	128	15	Aluminium
Extension tube	216	125		
Cyrogenic view-port	379	135	8	Borosilicate
Outer shield (IR-filter)	440	105	3	Sapphire
Outer view-port	656	148	15	Borosilicate

which encloses the optical system inside the experimental vacuum. The MCP can be covered either by a beam shutter or a calibration mask. The components are discussed in detail in the following paragraphs.

All vacuum interfacing components mounted on the NW320 flange had to successfully undergo a thermal cycling procedure, described in Section 5.3), for three times before they were installed. At CSR, almost exclusively Helicoflex® sealings are used on the inner chamber which are explicitly specified for the wide temperature range. Despite this, only conflat (CF) sealed feed-throughs and view-ports were used on the mounting flange of the NICE detector. Conflat sealings with smaller diameters are known to work at cryogenic setups and such 'standard' vacuum components are more readily available. Given the technical boundary conditions, as described in 5.1.1, only materials listed in Table 5.3 were used for the components in the extremely high vacuum (XHV) vacuum inside CSR.

The particle sensor can be tested at CSR with photons from a UV LED (SETi UVTOP 240) mounted at the opposite side of the CSR straight section for the purpose of detector tests [108] (see Fig 3.4, (11)). This is very useful for the position calibration with the mask.

5.2.2.1 Housing

The housing of the detector has several functional purposes. It serves as

1. a *mounting* and *alignment* structure for MCP, phosphor screen and mirror,
2. *positioning* of the detector in space with good alignment with respect to the ion beam axis,
3. *thermal anchor* on the beam-guiding vacuum chamber,
4. *electrical shielding* of the open high-voltage potential of the nearby 39°-deflector electrode, and

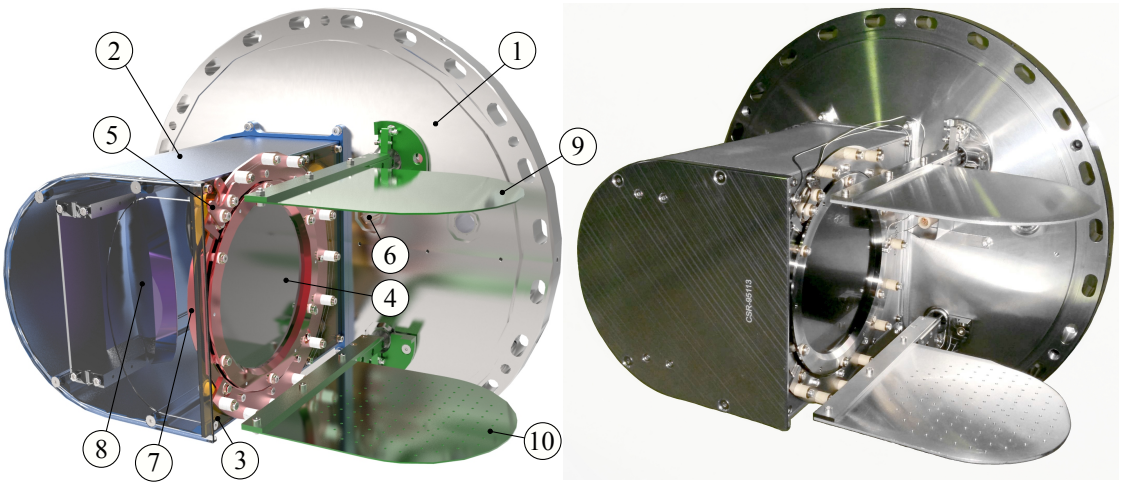

Figure 5.6: Colored model (left) and photograph (right) of the cryogenic particle sensor. All components are mounted on a NW320 flange (1) of the inner chamber. The detector housing (2) provides both an optical enclosure as well a mounting structure for all sensitive components. The MCP unit (4) with its heating element (5) is mounted together with the phosphor screen (7) from both side of a stainless steel mounting plate (3). The light from the phosphor screen is reflected by a 90°-mirror (8). The MCP can either be covered by a beam-shutter (9) or a calibration mask (10).

5. *screening* of the optical path.

The front of the housing is a 3 mm thick stainless steel (316LN) plate, on which the MCP and phosphor screen are mounted from both sides. The mounting plate can be removed independently from the housing, which makes it possible to easily store the sensitive MCP and phosphor screen separately in case of longer maintenance periods of CSR. The mounting plate is fixed on the U-shaped aluminum (EN AW-5083, AlMg4.5Mn0.7) back cover of the housing, which acts both as a mounting structure as well as a heat sink. Due to the different thermal expansion coefficients of stainless steel and aluminum, the front plate is fixed by five cylinder-head screws secured by CuBe spring washers. One countersunk screw in the lower left corner defines the lateral position.

The 90°-mirror is mounted on the aluminum side cover of the housing. This is installed in the final step after the electrical connection to the phosphor screen has been established. The side cover faces the high-voltage terminal of the 39°-deflector (see Fig. 3.4). For this reason, the fixing screws of the mirror holder are countersunk. The leading edge of the side cover exceeds the MCP in order to shield the high voltage. The detector housing encloses the optical read-out from stray light in the experimental chamber. In order to keep it relatively light-tight all fittings have overlapping edges.

The housing is mounted via an aluminum adapter piece on the mounting flange.

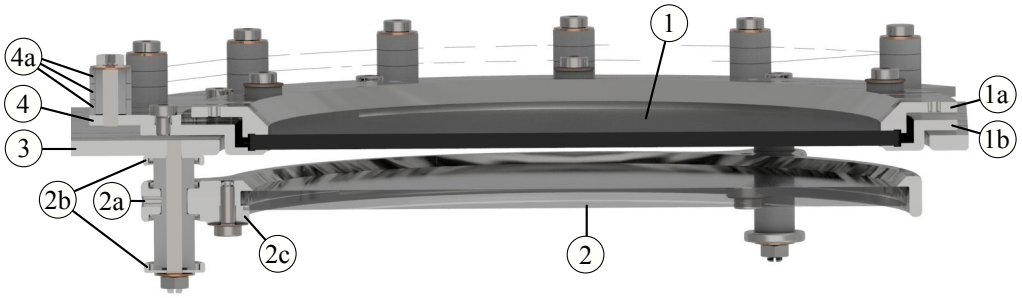

Figure 5.7: Cross section of cryogenic particle sensor unit. The MCP (1) and the phosphor screen (2) are mounted from both sides of stainless steel plate (3). The back electrode of the MCP holder (1b) is countersunk in the mounting plate. The phosphor screen holder (2a) has a slim, high-voltage proof design with according field forming end caps (2b) at its three mounting points. The MCP holder can be heated (4) via a tungsten wire, clamped between ceramic rings (4a). All screws are fastened via CuBe spring washers.

Larger misalignments of the absolute detector position can be compensated by reworking this adapter piece. In a first test assembly at room temperature the alignment of the detector center with respect to the ion beam axis was checked via a telescope from the opposite side of the CSR straight section, which was used for the alignment of the ion-optical elements. It was found that the detector center was perfectly aligned horizontally and only 2 mm lower with respect to the ion beam axis.

5.2.2.2 Microchannel Plates

A detector as large as possible is desired for the DR investigations at CSR. Given the geometrical constrains of CSR (see Sect. 5.1.2), the largest sensitive aperture size, which could be realized at the foreseen position next to the 39° bending electrode at a distance of 3.8 m from the electron target center (see Fig 3.4) was 120 mm. A thorough research showed that at that time only PHOTONIS could deliver MCPs with such a large sensitive area. MCPs of this size were only offered with a thickness of 1.5 mm and relatively large 25 µm pores to ensure the mechanical stability of the plates, while MCPs with smaller pores provide shorter pulses. For this detector two MCPs in Chevron configuration are used. The Chevron configuration effectively suppresses ion feedback [163]. The specifications of the used MCPs are listed in Appendix A.3. As a future upgrade, MCPs with tapered pores are being considered, which increase the open-area-ratio, and thus, the overall detection efficiency from typical 60 % up to about 90 % [184].

The recharging of the individual microchannels, and thus, the rate capability of the MCP depends both on the resistance of the microchannels and the detected

Table 5.3: List of materials used for the NICE detector in the inner XHV vacuum chamber.

Material	Designation	Application
Stainless steel	1.4435 BN2 (X2CrNiMo18-14-3)	Flange, mounting plate, flap mechanics, MCP & phosphor holder, screws (A4)
Aluminum	EN AW-5083 (AlMg4.5Mn0.7)	Housing, mirror, mirror holder, flaps
Copper	Cu	Feedthrough contact pins
Beryllium cooper	BeCu2	Spring washers
Alumina ceramics	Al_2O_3 99.6	Electrical isolators
Silver	Ag	Screw coating
Constantan	$Cu_{55}Ni_44Mn_1$	Heating wire
Borosilicate		Viewport

particle rates. The high resistive coating inside the channels has semi conducting properties with a negative temperature coefficient. This leads to a strong increase of the resistance towards lower temperatures. In this case, Extended-Dynamic-Range (EDR) MCPs are used, which have a lower resistance at room temperature compared to the normal type MCPs. The lower resistance leads to a faster recharging of the MCP channels. This makes a larger dynamic range of count rates accessible. However, this type of MCPs also tends to have a larger dark count rate. Kühnel et al. [167] tested the behavior of normal and EDR MCPs at cryogenic temperatures. Meanwhile, the atomic layer deposition technique is used to produce microchannels with functional films, which have more favorable conductance and secondary electron emission characteristic at cryogenic temperatures [185].

A long recharge time of the individual channels can lead to a local deterioration of the detection efficiency in the detector regions with higher particle fluxes. This might be an issue when heteronuclear molecular ions are investigated at CSR under cryogenic conditions. The heavier fragments will be concentrated on the inner part of the detector whereas the lighter fragments will distribute over a larger detector area. In such cases the reaction rates have to be chosen sufficiently low. To ensure operation at very low ambient temperatures an additional heating module has been designed, which described in the next Section. This module gives the possibility to heat the MCPs locally by a few tens of Kelvin. The supporting frame was made out of stainless steel, which provides both a certain stability and also a sufficient thermal decoupling of the connected CSR chamber, when the plate is heated. The MCPs should be removed at each longer period of CSR maintenance, when the inner vacuum chamber is vented. That is why the MCP holder was designed as a separate unit, which can be easily stored independently.

Based on the experiences of the first operation tests at CSR (see Sect. 5.4.1), the Chevron MCP stack was arranged in a configuration, which is more suitable

for the COBRA read-out. As described in Section 5.1.5, the signal assignment of the COBRA read-out technique relies on different signal intensities from a broad distribution of sufficiently large signal amplitudes. The signal intensity distribution is determined by the pulse height distribution generated by the MCP-stack, which can be controlled by its operation voltages. In general, larger amplifications and, thus, pulse heights are achieved as higher voltages are applied across an MCP. At the same time, the pulse height distribution gets more narrow as the triggered electron avalanches deplete more of the available charge in the channels. To achieve a broad pulse height distribution, the MCP stack should be operated with a voltage as low as necessary. On the other hand, both the electrical as well as the optical signal need to have a sufficient amplitude. The brightness of the light spots generated on the phosphor screen may be further amplified by higher acceleration voltages towards the phosphor screen. For the electrical pulses, this trade-off can be addressed by operating both MCPs with different gains. By operating the first MCP with a lower gain, a broad pulse height distribution can be produced, which is then further amplified by the second MCP. This can be achieved by controlling the voltage between the two plates. However, the original MCP holder design of the NICE detector does not provide this possibility. A similar effect could be achieved by arranging the two MCPs such, that the one with lower gain faces the impinging neutral particles. According to the specifications, the gain of the two MCP differ by about one order of magnitude at the same voltage (see Tab. A.1).

Moreover, the two microchannel plates are separated by a spacer ring of 0.2 mm thickness. As the two plates are not perfectly plane, the distance between the two plates is better defined which may provide a more homogeneous amplification across the plate. With a slightly larger distance, the electron cloud emerging from the first plate may distribute over several channel of the second plate. With more channels involved in the amplification process, this may lead to larger and brighter light spots on the phosphor screen.

5.2.2.3 Particle Sensor Heating

The heating module is based on resistive Constantan wire. The wire has a length of an about 0.9 m and a diameter of about 0.1 mm, resulting in a resistance of about 55 Ω, which is largely independent of the temperature.

The effect of the heating on the resistance of the MCP was investigated in a cryogenic test described in Section 5.3. It could be shown that by using this heating, the MCP temperature can be elevated by several tens of Kelvin higher with respect to the cryogenic environment.

The heating module has a horseshoe shaped mounting plate which can be screwed to the MCP holder ring of the rear MCP electrode. The holder is made out the same stainless steel material as the the MCP holder to avoid any difference in thermal expansion. Starting at the upper left end the Constantan wire is wound around the detector circumference back and forth in one loop. The wire is point welded at each end to stainless steel plates which act as a connection terminal. The wire

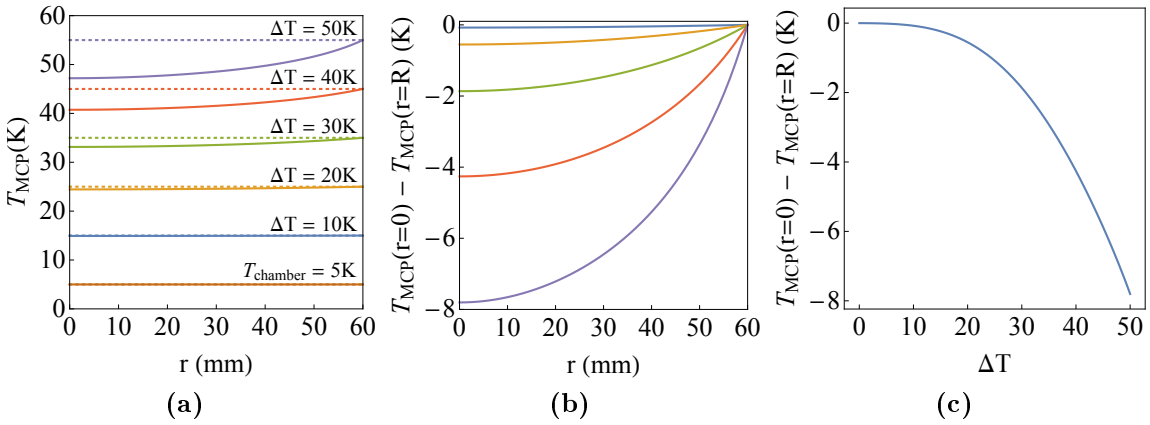

Figure 5.8:
(a) Calculated MCP temperature profiles for different elevated temperatures $\Delta T = T(R) - T_{\text{chamber}}$,
(b) Calculated MCP temperature profiles with respect to heater temperature $T(R)$,
(c) Calculated temperature difference over MCP for different elevated temperatures.

is stretched around posts of screws in the mounting plate isolated by thin ceramic tubes.

The temperature profile over the MCP surface was estimated with an according heat flow calculation. As the heating module extends over about 80 % of the circumference, one can formulate the heat flow trough and the cylindrical isothermal surfaces, using Equation 5.13 and 5.12,

$$0 = \quad 2\pi(r+dr)h\ \lambda\frac{dT(r+dr)}{dr} \quad \text{(ingoing conductive heat flow)} \tag{5.16}$$

$$-2\pi r \qquad h\ \lambda\frac{dT(r)}{dr} \quad \text{(outgoing conductive heat flow)} \tag{5.17}$$

$$-2\pi r dr \qquad \epsilon\sigma\left(T(r)^4 - T_{\text{ch}}^4\right) \quad \text{(effective radiative heat loss).} \tag{5.18}$$

The MCP temperature $T(r)$ is assumed to be elevated with respect to the chamber temperature T_{chamber}. With the approximations $\frac{dT(r+dr)}{dr} \rightarrow \frac{dT(r)}{dr} + \frac{d^2T(r)}{dr}$ and, subsequently, $dr + r \rightarrow r$ one obtains

$$r\epsilon\sigma\left(T(r)^4 - T_{\text{ch}}^4\right) = h\lambda\left(\frac{dT(r)}{dr} + r\frac{d^2T(r)}{dr}\right) \tag{5.19}$$

This differential equation was solved with Mathematica with the boundary conditions

$$\frac{dT(r)}{dr} = 0 \quad \text{and} \quad T(R) = T_{\text{heating}} \tag{5.20}$$

which leads to

$$T(r) = T_{\text{heating}} - \frac{\epsilon\sigma}{4h\lambda}(R^2 - r^2)\left(T^4(r) - T_{\text{chamber}}^4\right) \tag{5.21}$$

This results can be solved recursively. First, $T(r)$ is calculated with $T(r)^4 \rightarrow T_{\text{heat}}^4$ which is then propagated recursively. After about 10 iterations the solution stabilizes. The standard value for the thermal conductance $\lambda = 1.1 \times 10^{-2}\,\text{W/m/K}$ [186] of MCP lead-glass was taken. The resulting temperature profiles are shown in Figure 5.8 for different temperatures of the heating.

5.2.2.4 Phosphor Screen

The phosphor screen was provided by German Imaging Detector Solutions (GIDS). As phosphorescent material, P47 (Y_2SiO_5:Ce) was used which has a fast decay time of about 120 ns to 0.1 % of its peak intensity [187]. The phosphor material is often deposited on top of a conductive indium tin oxide (ITO) layer Due to the semiconducting properties of this material, the behavior at cryogenic temperatures is uncertain. Instead, the conductive layer is provided by a 50 nm-thin aluminum coating, which also acts as an reflective layer and improves the yield of photons detected by the camera. This imposes an additional energy threshold on the electron clouds from the MCP to penetrate the aluminum layer. On the other hand, the photon yield is strongly enhanced with higher electron energies. For this reason the phosphor screen holder was designed, and later also successfully tested, to hold high voltages up to 10 kV. The optical aperture of the phosphor screen holder is 6 mm larger that of the MCP holder in order to avoid distortions of the electrical field on the conical edges. The substrate as a diameter of 130 mm. The proximity to the high voltage terminal of the 39° electrode imposed strong spatial constraints. Therefore, the design of the holder had to be minimized (see Fig. 5.7).

5.2.2.5 Mirror

The thermal cycles of CSR result in a significant thermal shrinking and expansion. In case of the mirror, this might effect its alignment and could possibly cause deformations of the reflective surface. First, a glass mirror was taken into consideration but rejected due to the different thermal expansion coefficients of glass and the reflective coating. Instead, a full metal mirror made out of UHV-grade Aluminum (EN AW-5083, AlMg4.5Mn0.7) was realized. The bulk was manufactured in the local mechanical workshop. Then, the reflective surface was machined by LT Ultra Precision Technology via a special diamond milling procedure. The surface is specified with a shape accuracy of less than 3.0 µm and a roughness of less than 10 nm. Such a surface has good broad band reflection properties. In order to avoid deformations of the reflective surface the bulk material has a thickness of 15 mm. In addition, the mounting points on the top and bottom of the mirror were milled to small wings so that deformations of the holder do not stress the bulk material. The mirror holder is mounted on the side cover of the detector housing and horizontally positioned via a fitting joint.

5.2.2.6 Cryogenic Viewport

The optical design, described in Section 5.2, requires a large view-port on the inner chamber (see Fig. 5.4, 1c). The mounting flange of the cryogenic particle sensor was extended by an NW125 tube. This solution offers more space on the flange, in particular, for the high voltage feed-through of the phosphor screen anode. The tube extends the inner chamber up to the inner thermal shield reducing the necessary aperture of the view-port.

The bake-out temperatures at CSR of about 250 °C narrowed down the possible choice of glass materials to borosilicate and sapphire. View-ports, explicitly specified for cryogenic temperatures, were not available in the required size. Promising candidates were tested with the thermal circling procedure described in Section 5.3.

The optical design (see Sect. 5.2.1) requires a view-port aperture of up to 80 mm. In principle, a NW100 view-port offers a sufficiently large optical aperture, but the glass may be uneven at its welded glass-metal joint. In order to avoid optical aberration a larger NW150 view-port was chosen and successfully implemented.

5.2.2.7 Beam Shutter and Calibration Mask

The cryogenic particle sensor can be covered by two different flaps, either a beam shutter or calibration mask. The beam shutter is a 2 mm thick aluminum plate covering the whole MCP surface when it is turned in front of the detector. In addition, a calibration mask can be moved in front of the particle sensor, which enables a more precise position calibration of the camera system against distances on the detector analogous to the previous measurements at TSR (see Sect. 4.4.1). The mask has a rectangular grid pattern of 1 mm holes with distances of 10 mm to the neighboring holes (see Fig. 5.9). The pattern has three holes in between as reference points for the picture orientation. The mask can be projected onto the detector either by illumination with neutral particles or by a UV LED installed at the opposite site of CSR (see Fig. 3.4, (11)). The advantage of a calibration with photons is, that the divergence of the photon beam is well known and can be accounted for in the calibration. The drive mechanics for both the shutter and the mask is explained in Section 5.2.3.3. Both flaps are directly mounted on the axis of commercial rotary feed-throughs (Agilent Technologies L6691301 on CF16 flange). The rotation axis of the shutter is on top of the detector, the axis of the mask on the bottom. The mask is positioned closer to the MCP in order to minimize deviations of the mask image on the detector due to beam divergence. The distance of the mask to the MCP surface is (28.9 ± 0.8) mm. The distance of the beam-shutter to the MCP surface is about 45 mm.

5.2.3 Isolation Vacuum Components

The layered cryostat design of CSR requires that all parts in the beam-guiding chamber at cryogenic temperatures must be interfaced or connected to the room

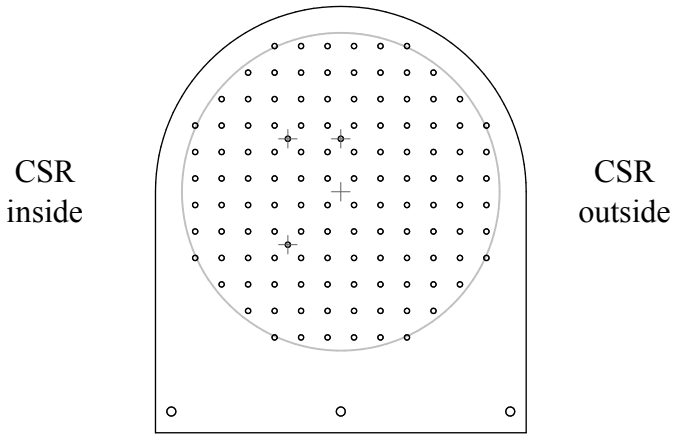

Figure 5.9: Drawing of mask pattern as observed from outside the cryostat of CSR. The MCP size is indicated by a gray circle. The orientation holes as well as the MCP center are highlighted by crosses.

temperature outer cryostat. Here, especially the thermal input on the inner chamber had to be considered. A maximum heat input power of about 100 mW has been estimated for the chamber of this detector. The main interfacing components are all electrical connections, the windows and openings for the detector as well as the flap drive mechanics. These components will be discuss in detail in the following sections.

5.2.3.1 Infrared Filter

The optical read-out scheme (see Sect. 5.2.1) requires on the one hand an optical transparency for the wavelengths emitted by the phosphor screen. On the other hand, the experimental chamber has to be shielded effectively from the infrared radiation from the warm room-temperature parts. An optical filter does not only have to absorb infrared photons, it needs to have a sufficient heat conductance to dissipate the radiated power. Sapphire has a sufficient optical transparency in the desired wavelength region around 400 nm (see Sect. 5.2.2.4) of about 85 % [183] as well as a very high thermal conductivity. The thermal conductivity of sapphire rises steeply from a few $10\,\mathrm{W\,m^{-1}\,K^{-1}}$ at room temperature to values in the order several $10^4\,\mathrm{W\,cm^{-1}\,K^{-1}}$ around 40 K (see Fig 3.15 in [154]). For an upper estimate the filter is assumed as a black body with emissivity of 1. An assumed shield temperature of 40 K results in a effective radiative heat transfer (see Eq. 5.13) onto the filter surface of 4 W. Comparing these numbers, there is no significant warm up of the filter glass to be expected.

The aperture in the inner thermal shield is not covered by any filter. For the calculation of the heat balance this hole is considered as a black-body radiator at a temperature of the outer thermal shield of about 80 K. This leads to a heat transfer of 20 mW compared to 1.3 mW of the originally foreseen 40 K-shield. The filter

was placed on the outer thermal shield, as the radiative heat input from the room temperature chamber on the outer shield is higher than the heat input from the inner shield on the inner chamber. The spectral transmission of sapphire [188] is increasing from about 30 µm. Integrating the transmission spectrum one finds, that the transmitted power is of an acceptable magnitude of 7.6 mW. Then the upper limit for the radiative heat transfer sums up to about 28 mW.

5.2.3.2 Electrical Connections

The NICE detector requires a limited number of electrical connections which cause a certain heat flux from the outer chamber at room-temperature onto the connected parts inside the cryostat of CSR. There are several high-voltage lines for the phosphor screen anode and the two MCP electrodes and two low-voltage lines each for the MCP heating and the sliding contact connection of the flap drive axis on the inner shield (see. Sect. 5.2.3.3). In order to minimize the heat flux on the inner beam-guiding chamber, all cables, except for the phosphor anode and detector ground, were thermally anchored on the inner radiation shield, which was estimated with pessimistic value of 40 K. The cables were interfaced to the vacuum systems with copper feed-throughs. The feed-through-pins on the experimental chamber were connected with screw terminals made out of high-purity copper and fixed with set screws.

Table 5.4: Heat flux onto inner chamber of CSR by electrical connections at about 10 K and the inner thermal shield at about 40 K. The heat flux was calculated for each wire according to Eq. 5.15. T_2 is the assumed temperature of the next thermal thermal anchoring point. The heat transfer coefficient of stainless steel was approximated with the parameterized data from [189], the coefficient of Manganin with the tabulated data from [190]. The coefficient of silver was approximated by the similar coefficient of Cu50 [191].

Connection	Material	No.	∅ (mm)	Length (cm)	T_2 (K)	Heat load (mW)
Thermal load on experimental chamber at about 10 K						$\Sigma = 16.4$
Phosphor anode	Stainless steel	1x	1.20	62	300	5.5
Detector ground	Stainless steel	1x	1.20	62	300	5.5
MCP high-voltage	Manganin	2x	0.25	70	40	0.009
MCP heating	Silver	2x	0.25	70	40	2.7
Thermal load on inner thermal shield at about 40 K						$\Sigma = 10.4$
MCP high-voltage	Manganin	2x	0.25	210	300	0.1
MCP heating	Silver	2x	0.25	210	300	2.8
Drive pick-up	Silver	2x	0.25	260	300	2.3

The electrical high voltage connection of the phosphor screen anode is also used as a signal line for fast current pulses induced by the electron clouds from the MCP on the phosphor screen anode. These signals are capacitively decoupled outside the cryostat (see Sect. 5.2.4.1). The connection was realized with a short, rigid stainless steel wire with a sufficiently low thermal conductance, which lead to an acceptable heat flux onto the inner chamber (see Table 5.4). The wire is not shielded. On one hand this would have been difficult to realize in a defined way given the high voltage of up to 10 kV. On the other hand, a shielding would induce an additional capacity, which would broaden the signal. However, this way the impedance of the signal line is not well defined which may lead to signal reflections. Another stainless steel wire, connected to the inner chamber, was guided in parallel to the signal wire. After the shield insets are mounted these wires can be connected from outside through the opening of the viewport. The high-voltage connections for the MCP electrodes are provided by Kapton-insulated Manganin wires from Allectra specified up to 6 kV and for cryogenic applications. For the low-voltage lines of the MCP heating and drive pick-up PEEK-insulated (poly ether ether ketone) silver wires were used. These are the same cables also used for the thermo-sensors of CSR.

The heat flux towards the inner beam-guiding chamber was was calculated for all connections with Equation 5.15. The results and the cable dimensions are listed in Table 5.4. The total heat flux of all cables onto the inner chamber was calculated to be less than 17 mW. The total heat flux on the inner radiation shield, where all cables, except the anode connection, were thermally anchored, was calculated to be less than 11 mW which is negligible compared to the high cooling power on the inner thermal shield.

5.2.3.3 Flap Drive Mechanics

As described in Section 5.2.2.7, the detector can be either covered by a beam shutter, in order to protect the sensitive MCP from too high beam intensities, or a mask for a precise position calibration. The drive mechanics, apart from the parts in the inner chamber, of both the shutter and mask flaps are the same as used to move the beam profile monitors [109] and the movable counting detector COMPACT [108] of CSR. It is divided into three parts thermally anchored at different temperature stages to minimize the thermal input on the experimental chamber. First, the flaps inside the experimental vacuum are directly mounted on the axis of the rotary feed-through. The second axis going through both the inner and outer thermal shield is thermally anchored on the ground plate of the inner shield at about 40 K. The third axis is mounted directly on the rotary feed-through on the outer flange, via which the mechanics is moved from the outside.

The axis on the inner shield has a fork on each end which surround bars on the two corresponding rotary feed-throughs at the inner and outer vacuum chamber. The forks consists of round tubes made out of stainless steel to minimize the cross-section and hence the heat conductance. The two forks are mounted on opposite sides so that the axis is balanced in every position. The axis is guided in a sliding

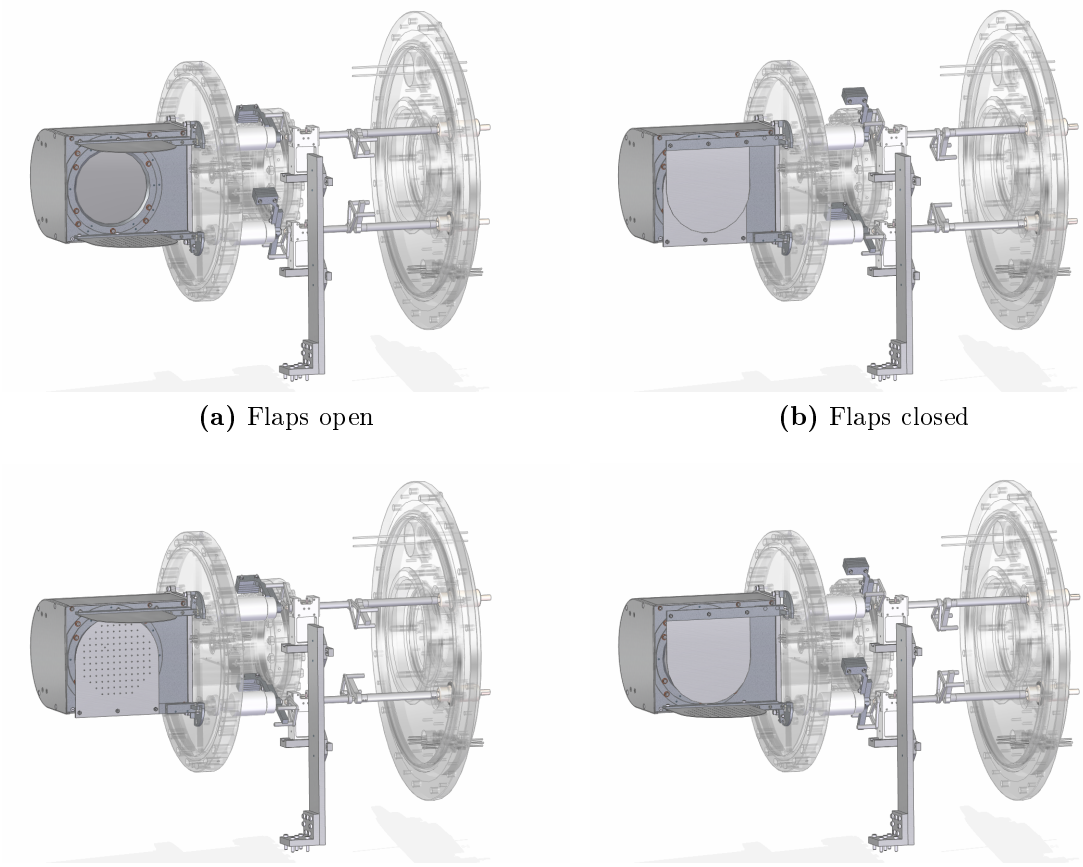

(a) Flaps open

(b) Flaps closed

(c) Mask closed

(d) Shutter closed

Figure 5.10: Mechanics of NICE beam shutter and calibration mask.

bearings made from PEEK (poly ether ether ketone). This way the axis is electrically decoupled. An additional sliding-contact in form of a titanium sheet metal stripe is spanned across the axis. This gives the possibility to check if this axis is contacted to the grounded inner or outer axis.

Inside the experimental vacuum are mechanical stops which define the two end positions for each flap, which can be fine adjusted by set screws. The flap sheets are mounted slightly off-center. The resulting imbalance is even amplified by counter weights attached to the bar on the other side of the rotary feed-through. They are mounted under an angle so that they holds each flap for both end positions in place. This way the flaps only have to be moved over the point of balance. After that they fall to the other end position by themselves. As an example, figures A.2 illustrate schematically the procedures to close the beam shutter. In the start and end positions the fork drive can be mechanically decoupled and, therefore, prevent any conductive heat flow. As the fork drive is thermally anchored on the inner radiation shield, there is no additional radiative heat transfer onto the inner chamber.

5.2.4 Read-out Electronics

The first measurements with the NICE detector, described in Section 5.4, were performed during the first beamtime of CSR with the COBRA data acquisition system by Urbain et al., which is briefly described in Section 5.2.4.2. The system is reimplemented at CSR with more recent hardware. In the following, the electronic decoupling for the fast signals for the phosphor screen is described.

5.2.4.1 Electronic Signal Decoupling Circuit

The aluminum coated phosphor screen is utilized as a large collector anode for the electron clouds emerging from the MCP. On the one hand the anode has to be provided with a static high voltage of up to 10 kV. On the other hand the short current pulses shall be decoupled from the high voltage as a timing signal of the particles hitting the detector. The decoupling circuit is illustrated in Fig. 5.11. The circuit can be divided into four functional groups: A *decoupling box* which interfaces the *signal source* with the *high voltage source* and the *signal amplifier*.

The signals are ns-short current pulses. They are induced by electron clouds emerged from the MCP collected on the phosphor screen anode. The geometry of the phosphor screen and the coplanar arrangement with the MCP at a distance of 8 mm. At the outer feed-through pin a capacity of about 84 pF has been measured, which is one of the limiting factors of the obtained signal width.

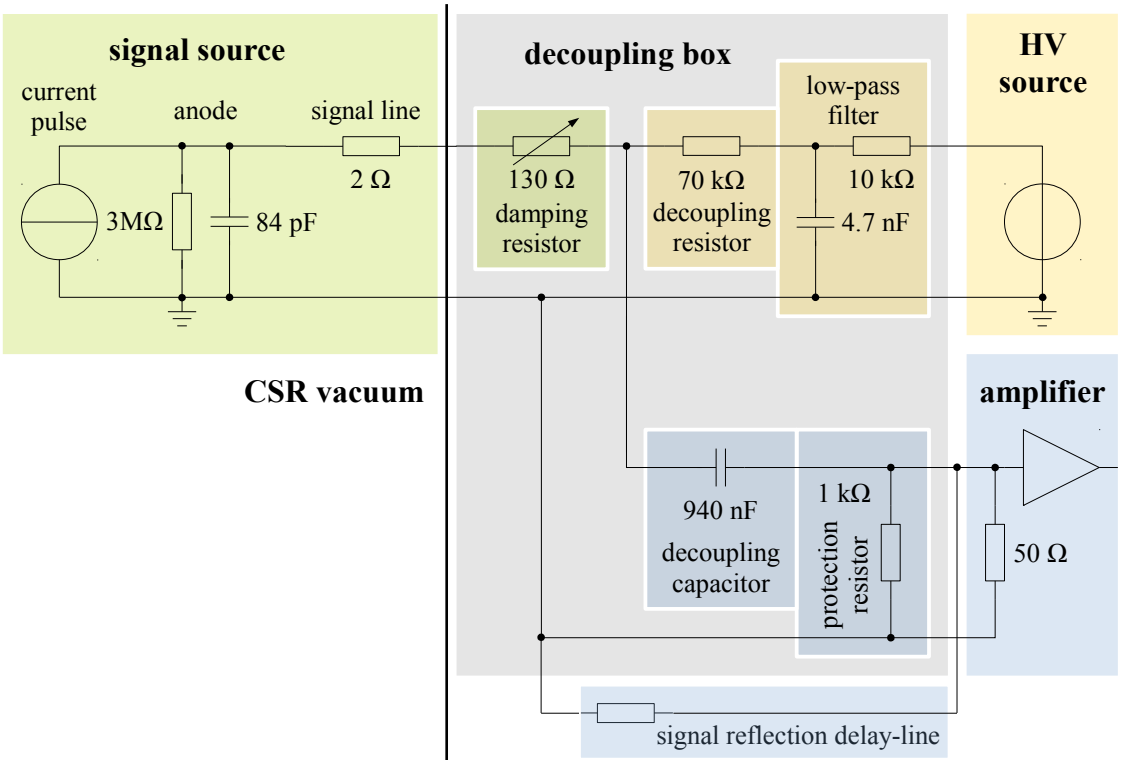

Figure 5.11: Schematic phosphor anode signal and high-voltage decoupling circuit.

The signal line was realized as a direct and as short as possible connection between the inner and outer vacuum chamber. As described in the previous section the wire is made out of stainless steel which has a relatively high thermal resistance limiting the conductive heat input. The wire is interfaced with standard CF copper pin-feed-throughs.

The decoupling of the static high voltage and the fast current pulses is realized in a decoupling box, which is mounted directly on top of the feed-through of the outer chamber. It interfaces the signal source with the HV source and the signal amplifier. This way all components are easily accessible. The high voltage is provided by a 15 kV power supply from ISEG. In the decoupling box high frequency noises from the power supply are filter by a low-pass filter with a cut-off frequency of about 20 kHz. The decoupling resistor ensures, that the fast current pulses are collected by the decoupling capacitor. An additional protection resistor of 1 kΩ makes sure that the capacity is always properly grounded to avoid damages of the amplifier when it is connected. Finally, the signal is fed into a Stanford Research SR445 fast preamplifier with an input impedance of optionally 50 Ω of 500 Ω. This amplifiers has four stages from which the first two with a total gain of 25 are used. The input impedance was set to 500 Ω as the signal line is not specifically designed for 50 Ω and this way larger pulses can be obtained. It is has a gain of 25 with low-noise and a rise time of less than 1 ns. Furthermore, the signal connection to the pre-amplifier is split. An additional *delay-line* cable terminated by a near-short is used to destructively interfere reflected signals with an inverted and delayed version of the first pulse at the input of the signal amplifier. In this way, signal reflections can be reduced and shorter pulses can be achieved.

An additional adjustable resistor is used to damp signal reflections between the decoupling capacitor and the possible connection points in the signal source. It also changes the wave impedance of the signal source (green) which should be matched for a good signal transmission.

In addition, a ground wire is guided in parallel to the signal wire from the inner chamber to the decoupling box. It is fixed on the mounting of the wire support on the extension tube of the mounting detector flange. The shielding of the high voltage line is connected to the ground of the decoupling circuit. Also, the ground in the decoupling circuit can be connected to the box housing, which is attached to the outer flange. In order to avoid further ground loops a floating power supply is used for the preamplifier.

5.2.4.2 COBRA Data Aquisition System

The COBRA data aquisition system (DAQ) by Xavier Urbain [172] consists essentially of two independent data acquisitions, which are controlled by a field programmable gate array (FPGA) electronics. The phosphor screen is observed by a high speed camera *Microtron EoSens CL* with 1280x1024 pixel of 14x14μm size and 8 bit resolution. It operates internally with a frame rate of about 10 kHz. The *Full Camera Link* interface has a bandwidth of 5.44 Gbit/s [192] which practically

limits the acquisition rate to about at 500 Hz at full resolution and about 2.5 kHz at a reduced resolution of 512x512 pixel. The electrical signal is digitized by an Aquiris DP110 PCI-card with a sampling rate of 1 Ghz and 8 bit resolution. The frame grabber of the camera and the digitizer card are both placed in the same data acquisition PC. Both systems run independently at the same time and buffer all their data. In the original DAQ, the signal line is split. Besides the connection to the digitizer, the other branch is fed into a discriminating NIM logics. The generated trigger signal is processed by an FPGA circuit to trigger the read-out of both data acquisition systems. The images from the camera are analyzed online. Only the essential data are stored, which are mainly the center-of-mass position and the integrated intensity. For each pulse the area, amplitude, time position and five sampling points are stored: The point with the largest amplitude together with its two neighboring points as well as the two smallest sampling values on the left an right side of the peak below the predefined software threshold. The three points around the maximum are interpolated by a parabola in order to determine the timing signal with an accuracy below the sampling time. In addition, the pulse area is determined as the sum of all sampling values above the software threshold. In this way, the amount of stored data is reduced.

5.3 Tests and Characterizations

The temperatures in CSR range from a few Kelvin at cryogenic operation to 250 °C at bake-out, which place strong demands on the design of all components, especially those installed inside or at the beam-guiding vacuum chamber. Material pairings with different thermal expansion coefficients cause significant mechanical stress in this wide temperature range. For this reason all critical components needed to be tested accordingly. Furthermore, the detector sensor module was also cooled down to cryogenic temperatures and the strongly temperature-dependent resistance of the MCPs was characterized.

All vacuum interfacing components installed at the beam-guiding vacuum chamber, which are the electrical and mechanical feed-throughs as well as the large viewport, had to successfully undergo a thermal cycling procedure for three times. In each cycle, the components were baked-out at a temperature of 260 °C and were, subsequently, immersed into liquid nitrogen at 77 K. Only components passing a final helium leak check were installed at CSR.

All movable components at CSR use the same kind of rotation mechanics, which is described in more detail in Section 5.2.3.3. This kind of mechanics is used to retract the beam profile monitors in and out the closed beam orbit, to move the COMPACT detector on its worm drive [108] and to retract the beam shutter and calibration mask of the NICE detector. The whole drive train was tested extensively in a dedicated cryogenic test setup for the COMPACT detector by K. Spruck [125].

In order to characterize the total temperature-dependent resistance of the used MCPs and to test the heating solution, the detector modules was installed in a test setup and cooled down to cryogenic temperatures before the detector was installed at CSR. The resistance-temperature dependency determined this way can be used as a calibration to infer the MCP temperature from its resistance when it is operated at cryogenic temperatures. The resistance is a very sensitive temperature indicator in this region, due to the strong non-linear temperature dependency towards cryogenic temperatures.

After the detector was installed at CSR, the resistance has been measured again for different temperatures during the first cool down of CSR in March 2015. The results of both measurements are presented in the following. Furthermore, the setup and the procedures of the first cryogenic tests are described in detail, which were performed before the components were installed for the first cool down of CSR. The MCPs were not yet operated with high voltage during the first tests as the vacuum pressure was not sufficiently low.

Cryogenic Test Setup

The temperature-dependent resistance of the used MCPs was characterized in a dedicated cryogenic setup, which was originally designed by S. Vogel for tests of the cryogenic amplifiers of CSR's beam diagnostics [110]. Figure 5.12 shows a model of the setup. The setup contains a dual stage pressurized helium cold-head whose inner stage cools down to about 20 K. The experimental platform is attached to the

second, coldest stage of the setup, while the first cold-head stage cools a protective radiation shield to about 35 K. Given the spatial constrains, the mounting construction for the MCP holder has been designed in a way that it mimicked the properties of the original stainless steel mounting plate (see Sect. 5.2.2). The copper mounting plate on the top of the cold head was adapted by an aluminum plate with a sufficiently large diameter to support the MCP holder on its foreseen mounting threads. The mounting construction was elevated by four aluminum blocks so that the holder could be thermally connected via the foreseen mounting threads. This construction should mimic the aluminum cover of the original detector housing which acts as a heat sink for the stainless steel mounting plate. The mounting plate was emulated by small stainless steel plates of the same thickness. The distances between the threads for the MCP holder and the aluminum block were chosen similar to the according threads on the original mounting plate.

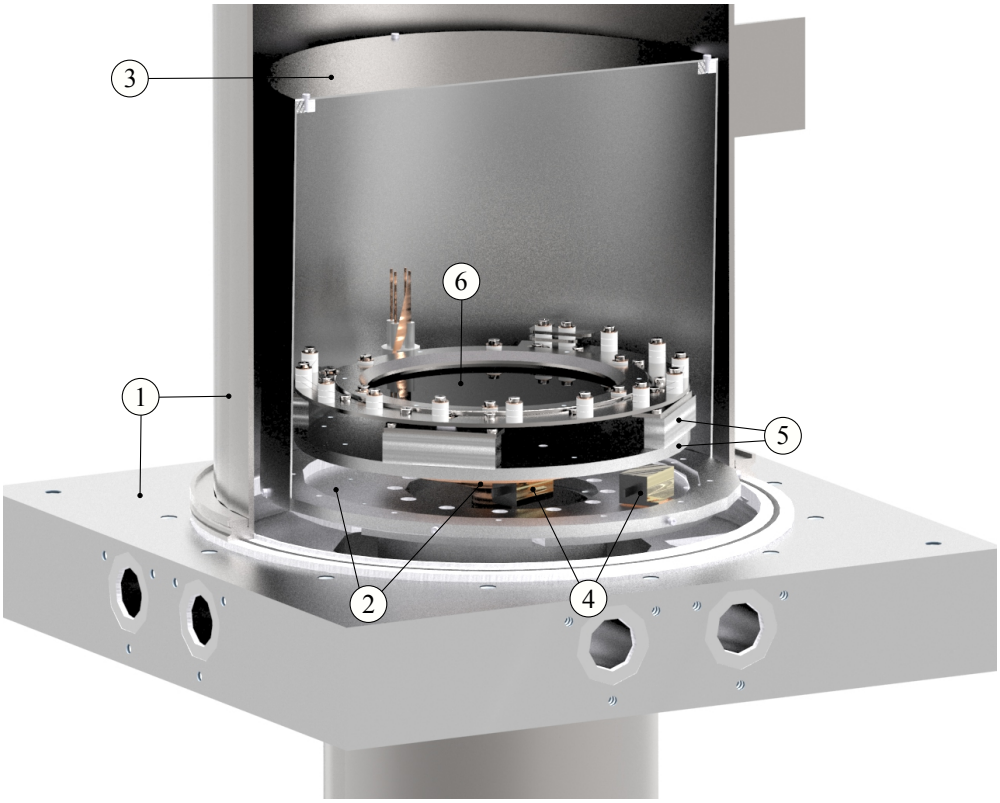

Figure 5.12: Model of the cryogenic test setup, which was originally designed for tests of the cyrogenic amplifiers installed at CSR [110]. The setup consists of a bell-shaped vacuum chamber (1) containing a dual-stage cold head (2). A thermal shield (3) is connected to the first stage of the cold-head and wrapped into several layers of Mylar insulation foil (not shown). Each thermal stage can be heated by a 20 W resistive heater (4). The second stage is adapted by a Al mounting plate (5) on which the MCP unit of the NICE detector is mounted with its heating module (6).

The MCP unit was enclosed by a thermal shield made out of aluminum sheet metal in order to achieve as low temperatures as possible. The thermal shield was covered by twenty layers of Mylar super-insulation. The vacuum pressure was directly measured in the vacuum chamber of the test setup. At room temperature a residual gas pressure of about 1×10^{-4} mbar was achieved, at the lowest temperatures of ~ 20 K it was about 3×10^{-6} mbar. The vacuum pressure inside the thermal shield may have been even higher as the inner volume was only pumped through small holes and slits in the thermal shield. Hence, a safe operation of the MCP could not be assured.

Temperature Measurements

The temperatures of several components were measured with silicon diodes and Pt1000 RTD. The silicon diodes were placed on the first and second stage of the cold head as well as on one of the small stainless steel mounting plates of the MCP holder, which is marked (3) in Figure 5.13. Unfortunately, latter silicon diode did not work properly. For this reason some additional Pt1000 temperature sensors were installed

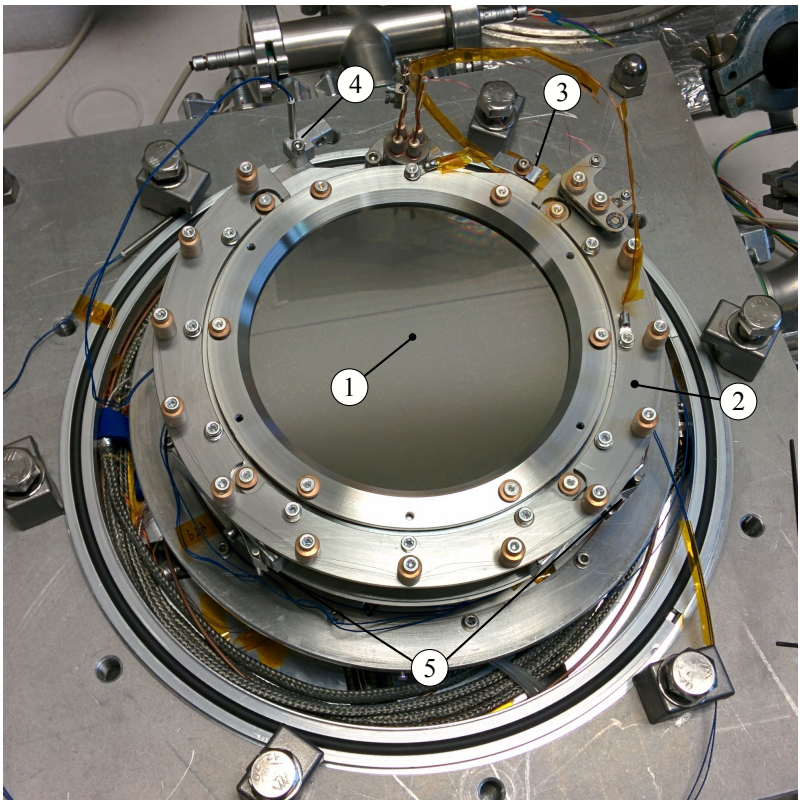

Figure 5.13: Photograph of the cryogenic test setup. The MCP unit (1) was mounted together with its heating module (2) on the cold-head. Its temperature was monitored with a silicon diode (3) and a Pt1000 resistance temperature detectors (RTD) (4) on two different a stainless steel mounting plates. Further two Pt1000 sensors were placed at aluminum mounting blocks (5).

at several positions, which are less accurate at the lowest temperatures. One of these sensors was installed on the mounting plate of the MCP holder, which is marked (4) in Figure 5.13. Two further Pt1000 sensors were placed on aluminum mounting blocks (5). Apart from this the damaged silicon diode, all temperature sensors were in reasonable agreement. The three Pt1000 sensors installed at the second cryostat stage showed typically 2 K more than the corresponding silicon diode. The largest discrepancy of 4.3 K was observed at the lowest temperature. In thermal equilibrium, the MCP temperature was determined by the mean value of the three Pt1000 sensors and the silicon diode on the second stage. The mean square error of these four sensors was taken as an estimate of the measurement uncertainty.

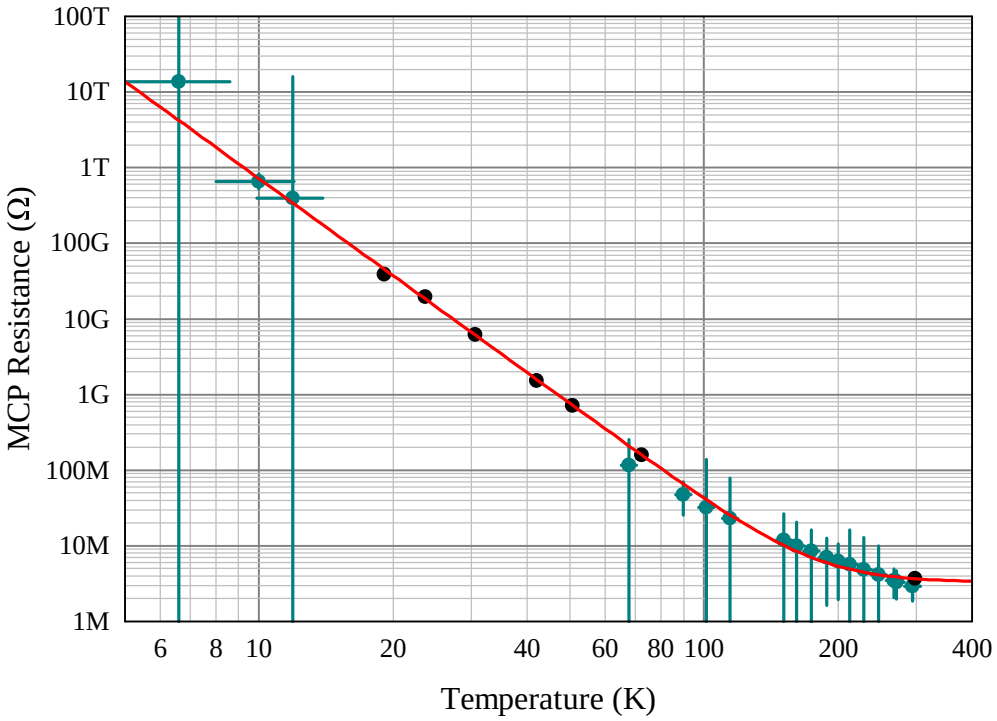

Figure 5.14: Total resistance of the MCP stack of the NICE detector measured towards cryogenic temperatures. The values of the calibration measurement (black dots) were fitted with a power function according to Equation 5.22 (red line). The measured values are also listed in Table A.3 in the Appendix. The values measured during the first cool down of CSR show a good quantitative agreement with the calibration. These values were measured on a regular basis with a measuring voltage of −100 V before the MCPs were operated at high voltage. The range was set to a value so that the resistance could be also monitored at high voltage. This is the reason for the large error bar of these values.

Resistance Measurements

The total resistance of the MCPs was measured via the bias-current across the stack at a low measuring voltage. The measuring voltage was sufficiently low to prevent triggering of electron-avalanches, which should be avoided under such vacuum conditions. The bias-current was continuously monitored with a floating nanoampere-meter by applying a measuring voltage of only −100 V to the top electrode. The back electrode was grounded via its connection to the housing.

In order to measure the temperature-dependent resistance, the whole system was thermally equilibrated at different temperatures. First, the setup was cooled down to about 20 K. Then, the system was heated up with a constant heating power using a resistive heater attached to the second stage of the refrigerator cold-head (see Fig. 5.12). Once all temperature sensors on the second stage and the monitored MCP resistance indicated a thermal equilibrium, the MCP resistance was measured with different nanoampere-meters at two different measuring voltages. Their mean value was used as an estimate for the MCP resistance. Each resistance was measured with a measuring voltage of 100 V and 250 V. Six values were measured in the range from 20 K to 70 K, which are also listed in Table A.3 in the Appendix. The resistance values obtained at the different measuring voltages differed by about 0.8 % down to 40 K and then up to 5.9 % at 20 K. The applied measuring voltage leads to a resistive power loss at the high-resistance MCPs. The electrical power loss during the permanent resistance monitoring ranged from 0.3 µW at 20 K to 2 mW at room temperature. The maximum electrical power during the absolute resistance measurements ranged from 1.7 µW at 20 K to 370 µW at 70 K.

During the cool down of the first cryogenic commissioning of CSR in 2015, the MCP resistance was again monitored on a regular basis with a floating nanoampere-meter. The cool down process extended over a time period of about three weeks so that the MCP temperature was assumed to be near thermal equilibrium with the chamber temperature. The chamber temperature was measured by a Rhodium-Iron temperature sensor. In order to avoid any heating of the MCP by the measurement, again, a measuring voltage of −100 V was used as in the previous calibration measurements. The results of both this resistance measurements and the calibration measurements are depicted in Figure 5.14. The calibration data points could be best approximated with a saturating power function

$$R(T) = a\,T^b + R_0. \tag{5.22}$$

The determined fit parameters

$$\begin{aligned} R_0 &= (3.30 \pm 0.11) \times 10^6\,\Omega \\ a &= (1.30 \pm 0.14) \times 10^{16}\,\Omega/\mathrm{K^b} \\ b &= -4.259 \pm 0.027 \end{aligned}$$

were then used to infer the MCP temperature from the inverse function

$$T = \left(\frac{R - R_0}{a} \right)^{\frac{1}{b}}. \tag{5.23}$$

The resistance values measured during the cool down of CSR show a good quantitative agreement with the calibration curve.

Active Heating

The MCP heating module, described in Section 5.2.2.3, was also tested in the cryogenic test setup after the resistance-temperature calibration measurement. The system was first thermalized at about 20 K. Then, a constant current was applied to the MCP heating module until the system thermally equilibrated again. In this way, heating powers of about 50, 200 and 400 mW were applied. These values are in the order of magnitude, what may be applied at CSR. Figure 5.15 shows the tem-

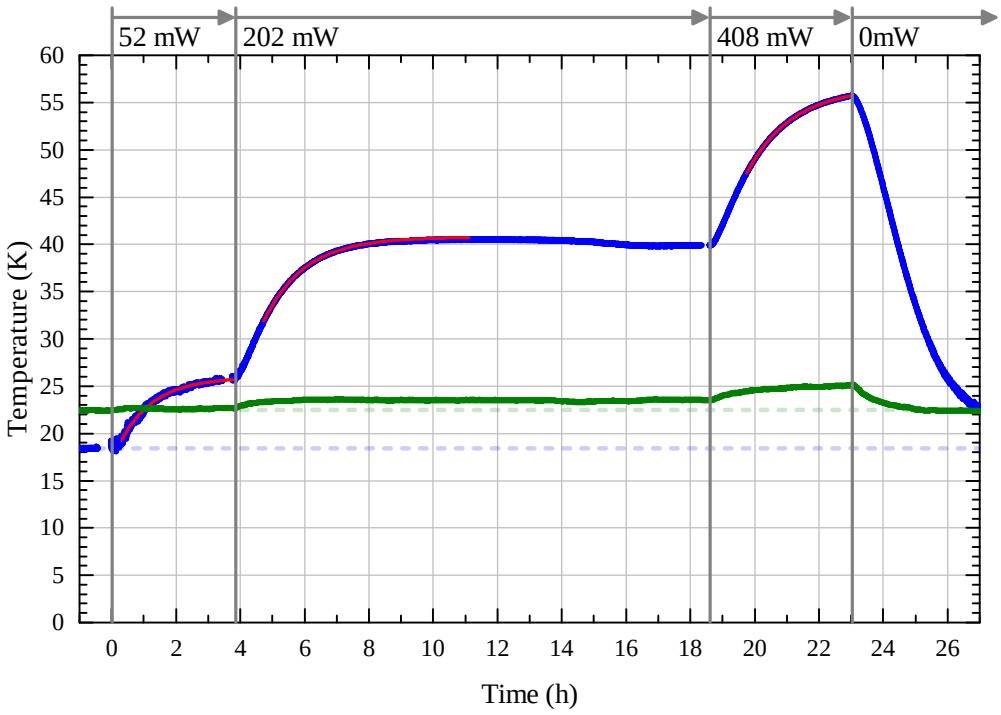

Figure 5.15: The MCP unit of the NICE detector was heated by its heating module. The temperature of the MCPs (blue) was deduced from their total resistance using the calibration measurement. The temperature gradient follows a exponential saturation curve (red). The time constants are given in table 5.5. The temperature of the nearby Pt1000 sensor (green) on the mounting plate. By applying a few 100 mW the plate could be warmed up by a few 10 K while the temperature sensors on the mounting showed only a very small increase of a few K.

Table 5.5: Results of the tests of the heating module of the NICE detector at cryogenic temperatures. For a given heating power P, the evolution of the temperature deduced from the MCP resistance (see Fig. Figure 5.15), was fitted with a exponential saturation function according to Eq. 5.24. For the first fit at 50 mW, T_0 was set to the previous equilibrium temperature. For the other two fits, this parameter was set to 0 K. From this the asymptotic temperature $T_{\mathrm{MCP}} = \Delta T + T_0$ and the warm-up with ΔT_{MCP} respect to the initial equilibrium temperature of 18.4 K were determined. Neglecting the threshold behavior, the uncertainty of the fit parameters is even lower than the given number of digits. The warm-up of a nearby Pt1000 temperature sensor is listed as ΔT_{Pt}.

P (mW)	τ (h)	T_{MCP} (K)	ΔT_{MCP} (K)	ΔT_{Pt} (K)
0	0.00	18.4	0.0	0.0
52	1.05	25.9	7.5	0.2
202	1.27	40.8	22.4	1.1
408	1.42	56.6	38.2	2.7

perature of the Pt1000 sensor closest to the detector and the temperature deduced from the MCP resistance. The temperature derived from the MCP resistance shows an about 4 K lower value under the equilibrium condition before the measurement. This may be attributed to the uncertainty of the temperature measurement which was used for the calibration. The stainless steel mounting plate provides a good thermal decoupling. Even with the highest heating power of about 400 mW the temperature of the closest temperature sensor only rose by 2.7 K, while the decrease in the MCP resistance suggests a temperature rise by almost 40 K. The rise of the MCP temperature shows an expected exponential saturation behavior, which was approximated with

$$T_{\mathrm{MCP}}(t) = \Delta T \left(1 - \exp\left(-\frac{t - t_0}{\tau}\right)\right) + T_0 \tag{5.24}$$

In Figure 5.15, the fitted temperature curves are highlighted in red. The fit results obtained for the different heating powers are listed in Table 5.5.

5.4 Operation at CSR

The NICE detector was operated in this work during the first two CSR beamtimes. The CSR was commissioned in March 2014 at room temperature conditions [109]. During this beamtime the COBRA data acquisition system of Urbain et al., introduced in Section 5.2.4.2, was used for the NICE detector read-out. The detector was tested and optimized, in particular, for a good performance regarding this read-out solution. The results of these tests are presented in the following Section 5.4.1. After the first beamtime, the detector was prepared for its foreseen operation at cryogenic temperatures (see Sect. 5.3). In the second beam time between March and July 2015, CSR operated at cryogenic temperatures. The NICE detector was first characterized regarding its performance at these temperatures (see Section 5.4.2) and then used for the various first laser experiments (see also Sect. 3.1.5). The experimental setup is described in Section 3.1.5.

5.4.1 Room-Temperature Operation

For the commissioning at room-temperature, the thermal shields, including the water cooling system, were not yet assembled. To prevent damage of the already present Mylar superinsulation foil, the beam-guiding vacuum chamber was baked at only about 120 °C. Furthermore, the NEG pumps were not yet installed. Under these circumstances, a residual gas pressure of about 10^{-7} mbar could be achieved in the inner beam-guiding vacuum chamber, which resulted in ion beam lifetimes in the order of only 1 ms [109].

The NICE detector was tested with neutral products from residual-gas collisions as neither the foreseen electron cooler nor the laser interaction experiment were yet available for this first beamtime. These tests were carried out with atomic Ar^+ and molecular N_2^+ ion beams of each 60 keV kinetic energy [109]. The first optimizations were performed with signals produced by neutral Ar atoms. Later, the dissociative electron capture reaction

$$N_2^+ + X \longrightarrow N + N + X^+ \tag{5.25}$$

was used as a source for nearly-coincident two-hit events on the detector in order to investigate and optimize its performance in combination with the COBRA read-out electronics in view of the foreseen DR experiments at CSR. Furthermore, it was possible to generate detector signals even without a stored ion beam by UV photons from the LED installed at the opposite side of this ring section (see Fig. 3.4, (11)).

Electrical Signal from Phosphor Screen Anode

The electron clouds emerging from the MCPs are accelerated towards the phosphor screen anode, where they create a fast electrical signal which is then decoupled for the high-voltage line with the circuit described in Section 5.2.4.1. This electrical signal is used as a fast arrival-time signal for the particles impinging on the NICE

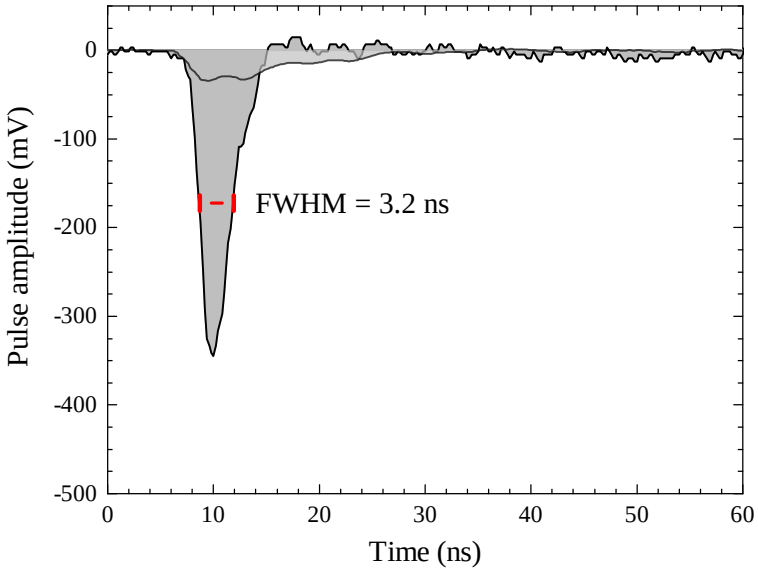

Figure 5.16: Typical pulse waveform of 25 keV neutral particle measured during the commissioning beamtime at room temperature with ORTEC VT120C amplifier. Another signal with lower amplitude is shown, which was measured without amplifier and pulse-shaping measures.

detector. A clear and narrow signal is required for measurements with ns-resolution. During the commissioning beamtime, the signal was amplified with an unipolar ORTEC VT120C fast pre-amplifier with a gain of 20 and an input impedance of 50 Ω. Figure 5.16 shows a typical pulse shape recorded for a 20 keV neutral nitrogen product fragment. The Figure shows also a second signal with lower amplitude which was measured without amplifier. The integration of this un-amplified signal delivers an estimate for the number of involved electrons of about 7×10^6.

This signal seems to consist of two superimposed pulses separated by about 3.6 ns. This is most likely caused by reflections on the signal line inside the CSR vacuum as the propagation time agrees roughly with the physical dimensions of the signal line. The second delayed pulse of the signal can be almost eliminated by a destructive interference with an inverted and delayed version of the first pulse. This was achieved by adding a short delay-line wire in front of the amplifier, which is terminated by a small adjustable resistor to ground. The amplitude of the reflected signal can be adjusted by this resistor. A resistor of about 1 Ω was used. In this way, the about 20 ns-long tail of the original pulse can be effectively reduced resulting in a clean, about 3.2 ns wide pulse. There is still a minor contribution of the second pulse visible in its tail.

During the commissioning beamtime the NICE detector was typically operated with the voltages listed in Table 5.6.

Table 5.6: Typical operation voltages during commissioning beamtime at room temperature.

MCP front	−1.95 kV to −2.4 kV
MCP back	0.0 kV
Phosphor screen anode	7.5 kV to 8.5 kV

Pulse Height Spectra

The pulse height distributions of MCP dark counts, 25-keV neutral N particles, and UV photons are depicted in Figure 5.17. The pulse height distribution of MCP dark counts, believed to originate mainly from beta-decay of ^{40}K [153], corresponds to a negative exponential distribution. Massive particles with keV-energies, however, produce a broad, almost Gaussian shaped distributions with larger pulse amplitudes. Therefore, the background can be suppressed by a threshold on low pulse amplitudes. UV photons typically produce small pulses similar to MCP dark counts, as the energy of the 245 nm-photons may only be sufficient to eject single electrons from the microchannel wall. These small pulses can only be used to a limited extent for the optimization of the decoupling circuit.

COBRA Read-Out Tests and Optimizations

Beside the obligatory optimization of the acquired signals, the basic correction and analysis procedures for the COBRA read-out, described in Section 5.1.5, were executed. These are described in the following Sections before the first acquired fragment imaging data are presented.

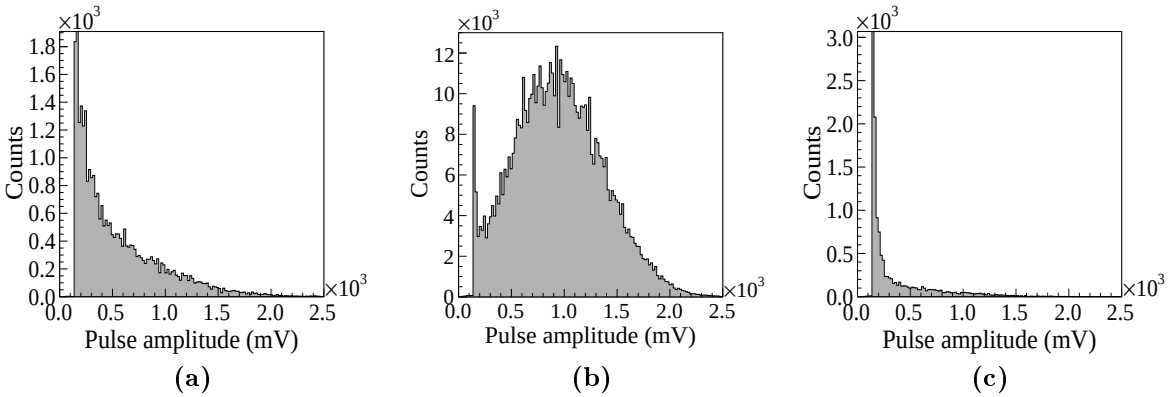

Figure 5.17: Pulse height distributions of (a) MCP dark counts, (b) 25-keV neutral N particles and MCP dark counts, (c) and UV photons with background measured with a discriminator level of 120 mV.

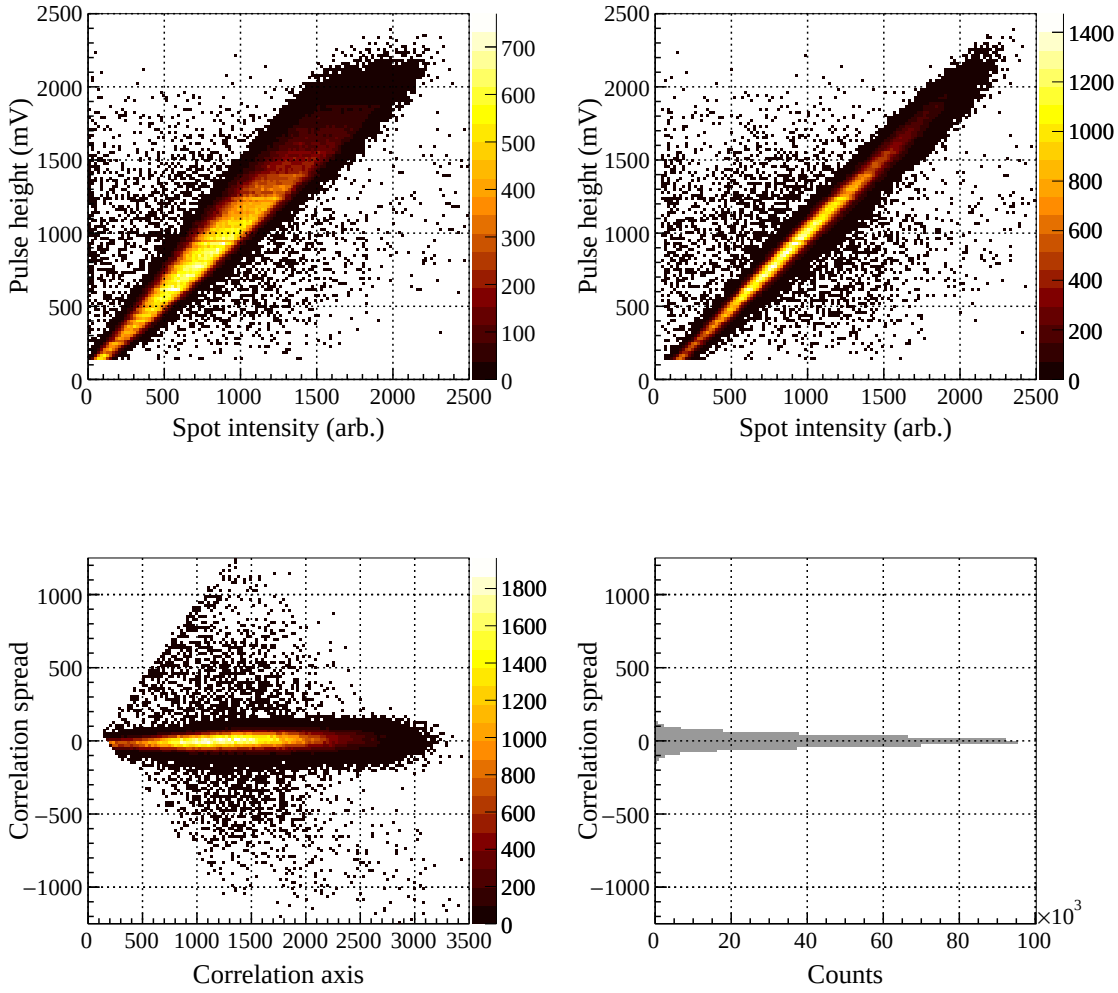

Figure 5.18: The two-dimensional histogram in the upper left panel shows the correlated signal intensity distribution of pulse heights and spot brightnesses of unambiguous one-hit events. An appropriate correction of the spot intensities, described in Section 5.1.5.1, leads to the histogram in the upper right panel. The by 45° rotated distribution in the lower left panel illustrates the intensity correlation spread which is then determined by the projection on the correlation spread axis depicted in the lower right panel.

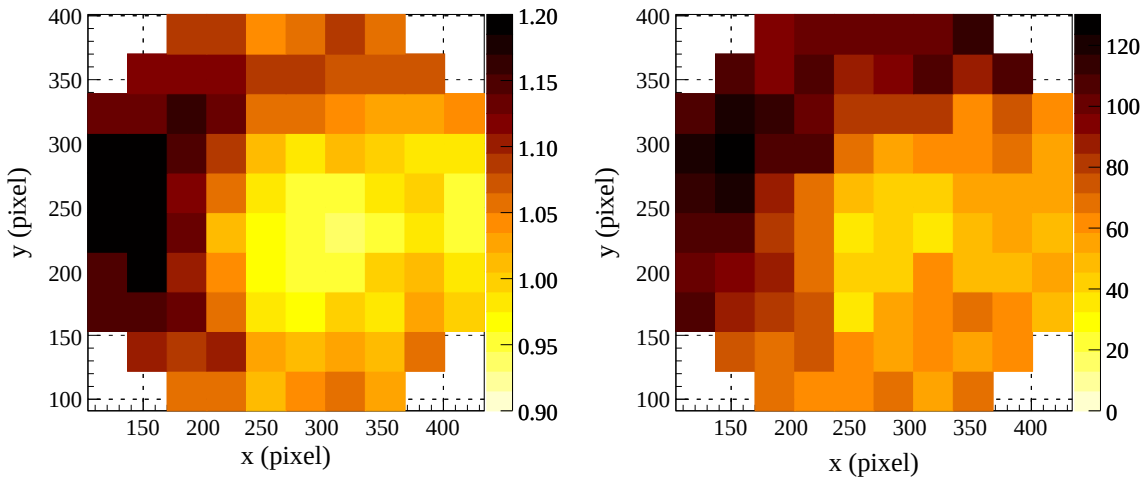

(a) Correlation fit slopes **(b)** Correlation fit offset

Figure 5.19: Correction parameters determined for the correlated one-hit intensity distributions by linear fits in each of the 10×10 segments. These are used for the correction of the intensity correlation distribution depicted in Figure 5.18.

COBRA Signal Intensity Correction

The COBRA signal assignment principle, described in Section 5.1.5.2, relies on the correlation of the electrical pulse heights and light spot brightnesses. Spatial inhomogeneities of the phosphor screen or the MCP gain can lead to variations of the signal intensity correlation across the detector surface. These variations must be first corrected according to the procedure described in Section 5.1.5.1. For the signal intensity correction, only one-hit data are considered which can be unambiguously assigned to each other. In Figure 5.18, the upper left graph shows the distribution of all correlated one-hit signal intensities of the whole detector. The slope of the signal intensity correlation appears to change across the surface which leads to a broad, asymmetrically distorted correlation distribution. For the intensity correction, the detector surface is segmented into $n \times n$ segments. For each segments the intensity correlation distribution is fitted linearly and the spot brightnesses are normalized accordingly. Figure 5.19 shows the resulting two-dimensional distribution of the correlation fit slopes and offsets for a 10×10 segmentation. The correlation fit slopes vary in a range from 0.95 to 1.24. The accordingly corrected intensity correlation distribution is depicted in the upper right graph in Figure 5.18. The spread of the signal intensity correlation distribution can be dramatically improved. Such a correction can in principle be further improved by a finer segmentation. However, at the given statistics of the presented dataset the biggest improvement is already achieved with a 5×5 segmentation. By rotating the distribution by 45°, the signal intensity correlation spread can be determined by a projection on the y-axis (see lower two histograms in Fig. 5.18). The correlation spread of the one-hit data is obtained by a fit with a normal distribution. The width of this distribution $\sigma_{1\text{hit}}$

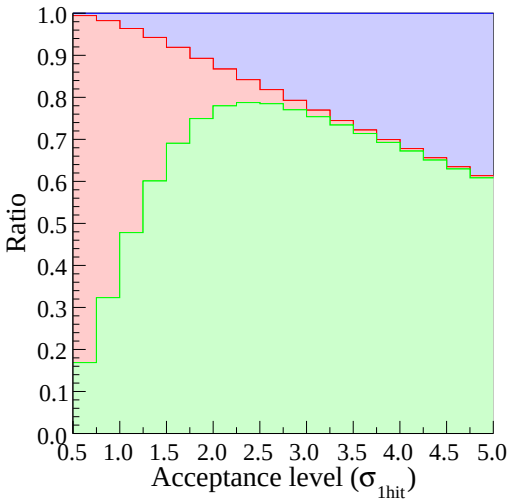

Figure 5.20: COBRA assignment performance for two hit events with different acceptance levels σ_a. The ratios of valid, invalid and ambiguous events are indicated in green, red, and blue, respectively. The highest acceptance ratio is achieved with an acceptance level of about $\sigma_a = 2.35\,\sigma_{1hit}$ corresponding to the FWHM of the correlation spread distribution. Due to signal distortions, described later, an additional filter is applied on the arrival-time differences to be larger than 30 ns.

is then used as a basis for the acceptance level for the COBRA assignment, for the identification of the valid signal permutations of pulse and spot signal intensities.

COBRA Event Validation Performance

For a multi-hit event, there are several possible permutations of pulse amplitudes and spot brightness intensities from which only one is correct. As described in Section 5.1.5.2, each permutation of the pulse and spot signal intensities is validated by its correlation spread, defined in Equation 5.8, with respect to a constant acceptance threshold σ_a. If only one signal permutation of pulse heights and spot brightnesses is accepted by the threshold criteria, the event is assumed to be correctly identified. If all possible permutations are rejected, the event is invalid. If more then one permutation passes the threshold criteria, the event is ambiguous.

In Figure 5.20, the ratios of valid, invalid and ambiguous events are shown for different acceptance levels as multiples of the measured correlation spread of one hit events described in the previous Section. The highest ratio of accepted events of almost 80 % can be achieved with an acceptance level of about $\sigma_a = 2.36\,\sigma_{1hit}$, which is about the full-width-half-maximum (FWHM) of the correlation spread. With smaller acceptance levels, more events get rejected, with higher levels the number of ambiguous cases increases. For this plot an additional filter on the arrival-time differences of two hit events was applied. The time signals for shorter arrival-times were distorted, as described later.

3D Fragment Imaging with COBRA Read-Out

As a test case for future DR experiments, dissociative electron capture reactions of N_2^+ with the residual gas molecules (see Equation 5.25) resulting in two neutral fragments have been investigated. Such reactions were used to investigate the behavior of the NICE detector system for near-coincident fragmentation events. The neutral reaction products, created within the about 4.3 m-long section between the two 6°

deflectors, were detected on the NICE detector (see Fig. 3.4, (2)). The fragment imaging results, obtained with the COBRA read-out, are depicted in Figure 5.21. The coordinates in pixels were calibrated to the outer dimensions of the detector. For this, the detector was completely illuminated with photons from the UV LED and a single picture of the detector was taken with the camera and analyzed. The upper left and lower right histogram in Figure 5.21 show the distribution of longitudinal and transversal fragment distances obtained from the measurements of the electrical pulses and light spots, respectively. The two-dimensional histogram in the lower left panel shows the correlated distribution analog to Figure 3.11. The arrival-time signal is disturbed in a region up to 30 ns, which is highlighted in red in the Figure and discussed later. The resulting distribution of fragment distances is shown in Figure 5.22 together with some expected distributions for different kinetic energy releases. Here, the distribution of undisturbed data for arrival-time differences greater than 30 ns is highlighted in green. A limitation in the arrival-

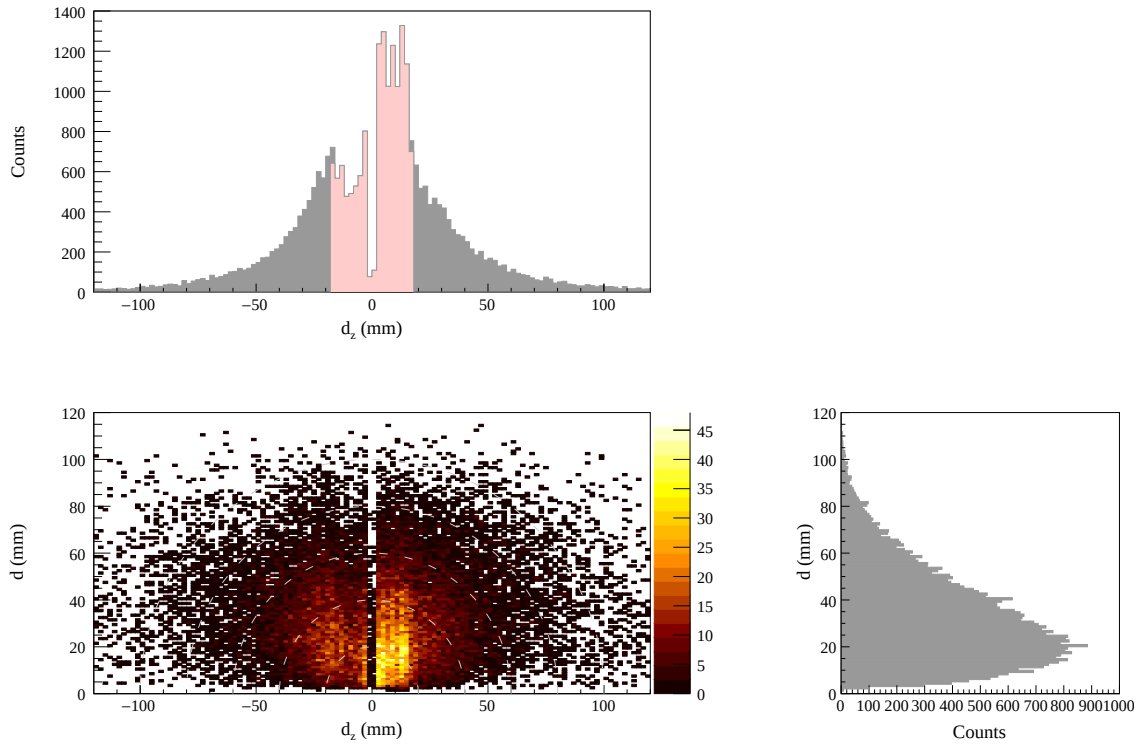

Figure 5.21: Measured distance distributions, analog to Figure 3.11, with two neutral N product fragments originating from collision induced dissociation reactions with the residual gas molecules. The upper histogram shows the distribution of longitudinal fragment distances d_z from the arrival-time measurement, the right histogram the distribution of transversal fragment distances d observed with the camera. The correlated distances are shown in the lower left panel. Critical arrival-time differences smaller than 30 ns are highlighted in red.

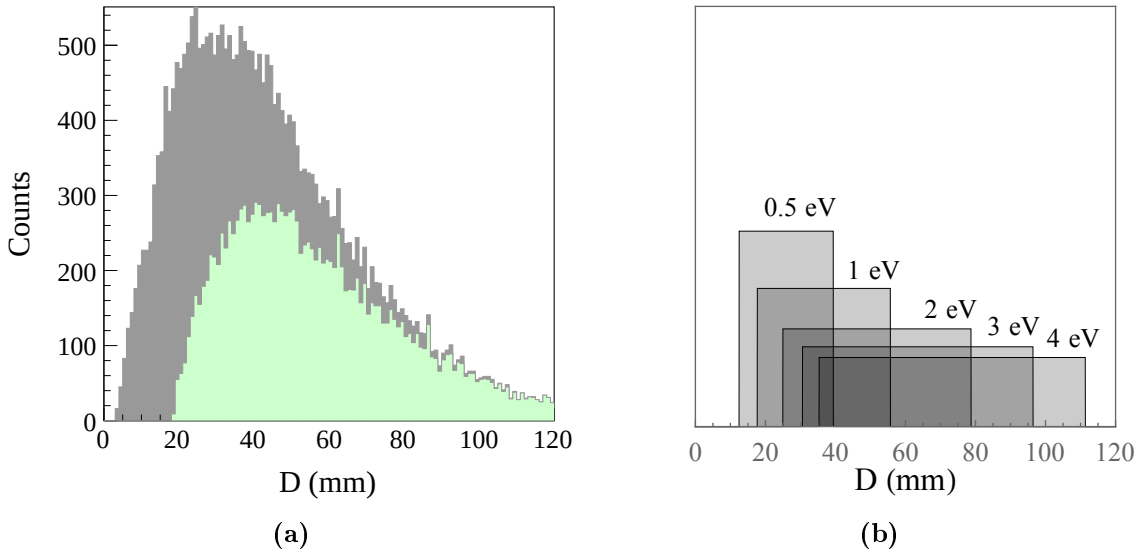

Figure 5.22: Derived absolute fragment distance distribution of the two N product fragments originating from collision induced dissociation reactions with the residual gas molecules. (a) shows the measured distribution while the green shaded histogram shows only data with uncritical arrival-time differences greater than 30 ns. (b) shows expected distributions for different kinetic energy releases, given the 4.3 m-long interaction section between the 6° deflectors.

time differences leads directly to a limitation of the kinetic energy releases that can still be resolved. In this case it is advisable to stick with the conventional two-dimensional imaging. All distributions are shown for distances in the range of the physical dimensions of the detector of 120 mm. Most of the observed fragment distances are well below this value. Therefore, it can be assumed that most of the fragments were indeed projected on the detector aperture despite the broad beam profile. The long interaction zone leads to very broad fragment distance distributions as illustrated in in Figure 5.22b. The smooth tails towards larger fragment distances in all distributions suggests a superposition of dissociations with many different kinetic energy releases. For the given detector size the maximum kinetic energy that can be fully projected on the detector for an ideally centered beam is 4.6 eV. Given the broad beam profile, this limit is further reduced accordingly and lead to losses towards larger distances.

As shown in Figure 5.21, the longitudinal fragment distance distribution seems to be disturbed for small arrival-time differences. Figure 5.23a shows a histogram of the arrival-time differences of two-hit events. The fraction of valid, invalid and ambiguous COBRA events are highlighted in green, red, and blue, respectively. The events were validated with an acceptance level of $3\,\sigma_{\mathrm{1hit}}$. For arrival-time differences smaller than 30 ns, a large fraction of events is rejected, due to disturbances of

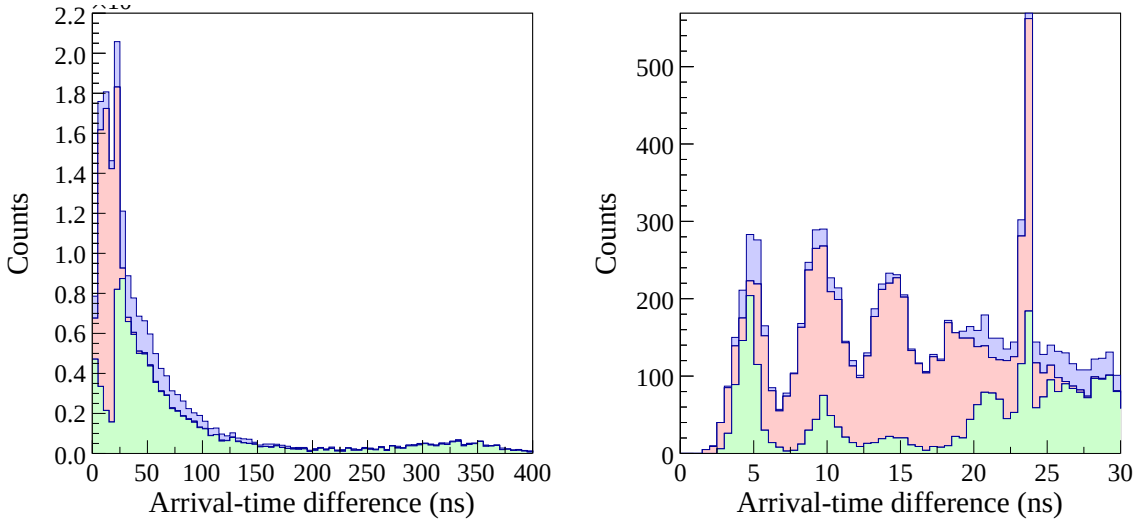

(a) **(b)**

Figure 5.23: Distribution of arrival-time difference for two-hit events within a arrival-time window of the first (a) 400 ns and of the critical (b) 30 ns. The fractions of valid, invalid and ambiguous COBRA events are highlighted in green, red and blue respectively.

the pulse amplitude of the second pulse. Figure 5.23b show the same distribution with higher resolution in this critical region. The number of detected events shows oscillatory fluctuations for different arrival-time differences with a time period of about 5 ns. This time period is similar to the delay of reflected signals observed for single pulses as discussed before. This indicates a connection to the observed reflections on the signal line observed in the pulse shapes (see Fig 5.16). The unipolar ORTEC amplifier was identified as a possible source for these observed distortions. The pulse shape was artificially shortened by the destructive interference with a delayed and inverted signal. The additional introduced signal reflection may also lead to positive signal amplitudes at the input of the amplifier which then cannot be fully amplified by the ORTEC amplifier. They may cause some of the observed signal distortions. Therefore, a linear amplifier was used for the second beamtime which is described in the following.

5.4.2 Cryogenic Operation

The CSR was first operated at cryogenic temperatures between March and Juli 2015. The beam-guiding vacuum chamber was first baked-out at about 180 °C and the NEG pumps were activated. In this way, a significantly improved residual-gas pressure of about 10^{-10} mbar compared to the first commissioning could be achieved at room temperature. The CSR was then cooled down slowly to avoid excessive temperature gradients, which could endanger the leak tightness of the vacuum system. The beam-guiding vacuum chambers reached its final temperature of ~ 5 K after about three weeks. For this beamtime, a new LabView-based data acquisition system has been implemented by O. Novotný , with similar components as the acquisition system by Urbain et al.(see Sect. 5.2.4.2). It also uses a FPGA electronics to control and synchronize all different sub-systems.

Ice Deposits on Infrared Filter

During the cool down of CSR, unfortunately, an ice deposit formed on all infrared filters of the NICE detector and the beam profile monitors. During the progression of the beamtime, these deposits accumulated further. For this reason, no imaging could be performed with the NICE detector during the first cryogenic beamtime. At the DESIREE facility [75] such deposits have been observed as well on some of the fused silica infrared filter glasses. In their case, luckily, not on the one for the detector [193]. These deposits are presumed to originate partly from water, as the pipes of the water cooling system were open in vacuum after the bake-out and may served as a water reservoir. However, even after the warm-up some residue remained on the filter which suggests also other components.

An attempt to remove the presumed water ice deposit with microwave radiation was without success. J. M. Labello estimated in his thesis about water ice deposits in cryogenic vacuum [194] the required power density for infrared desorption of a water cryo-deposit in vacuum using the 3 μm O-H stretch band of water. The estimated value of about 375 kW/cm^{-3} is far to high for a practical implementation. Moreover, the given condensation coefficient of water (see Fig. 1.15 in [194]) rises steeply to one at a partial pressure of 10^{-6} Torr and a surface temperature of about 160 K. Below this temperature any water molecule touching such a cold surface is expected to stick to it. This transition temperature may also agrees roughly with the temperature at CSR when the deposits were first recognized. No effective method could be found to remove cryo-deposits in vacuum once they appear. The only viable solution seems to be to avoid the formation of such deposits in the first place.

The holders of the infrared filters are thermally anchored on the outer radiation shield. Each filter glass surface is directly exposed to one of the few openings where probably most of the gas inclusions in the Mylar superinsulation foil are pumped. Therefore, the holder of all filters must be redesigned. The infrared filters of the DESIREE are shielded by extended tubes [193]. This may also help in our case to reduce the gas flow above the filter glass surfaces. Furthermore, the filter glasses may only be weakly thermally coupled or even decoupled from the outer radiation

shields. By keeping each filter warmer than its environment during a CSR cool down, most of the gas should preferably condense or re-sublimate first on other colder surfaces. In the end, it still needs to cool down to the temperature of the shield in order to protect the inner chamber from too high radiative heat transfer.

Electrical Signal

The unipolar ORTEC amplifier, used during the first commissioning beamtime, was identified as a possible source for disturbances of the pulse amplitudes of consecutive signals with arrival-time differences below 30 ns. These disturbances practically inhibit the COBRA signal assignment. For the second beamtime, a bipolar signal amplifier (Stanford Research SR445) was used with a bandwidth of 350 MHz. This amplifiers has four cascadable amplifier stages from which only the first two with a total gain of 25 were used. The input impedance was set to 500 Ω, as the signal line is not specifically designed for a 50 Ω impedance and this way larger pulses could be obtained. Figure 5.24 shows a typical pulse waveform, which was optimized at room temperature. The pulses are broader compared to the pulses achieved with the ORTEC setup. The pulse FWHM now agrees with the unamplified waveform in Fig. 5.16. However, even the use of this linear amplifier could not eliminate these signal disturbing effects. Some attempted changes of the signal decoupling box were also without success. Future optimizations of the signal transmission properties will require an improved impedance matching of the whole signal line in order to reduce the observed reflections. The copper feedthrough may be exchanged by stainless steel feedthroughs to avoid transitions between different material. A shielding of

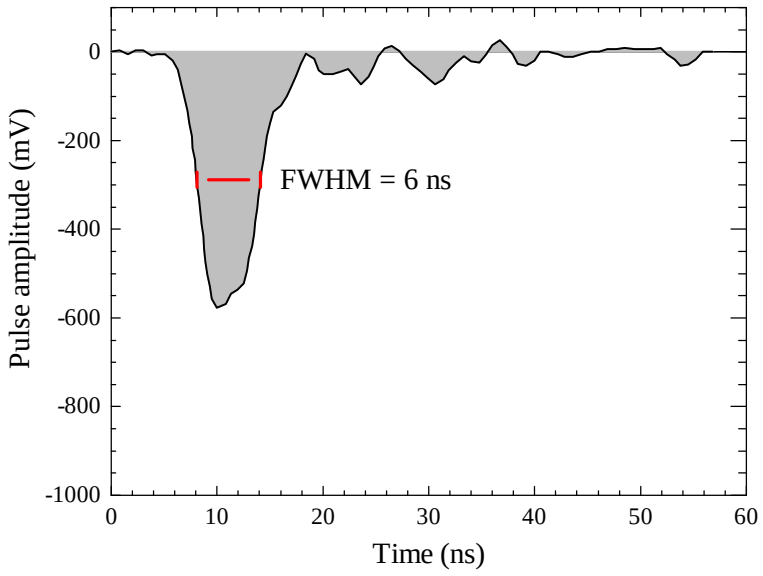

Figure 5.24: Typical pulse waveform of 25 keV neutral particle obtained during beamtime 2015 at room temperature measured with Stanford Research SR445 amplifier.

the wire may help to achieve a more defined impedance of the signal line to match with the signal amplifier. However, it is challenging to implement as it needs to allow a high voltage in the order of 10 kV and, especially, the heat flow towards the inner parts of CSR needs to be avoided.

MCP Cool Down and Heating

The resistance of the used MCPs was characterized in a temperature range of 20 to 70 K before the detector was installed at CSR. As the resistance shows a strong temperature dependence, it is possible to infer the MCP temperature from its resistance (see Sect. 5.3). During the cool down of the first cryogenic commissioning of CSR, the resistance was monitored on a regular basis and compared, with the CSR chamber temperature as a reference, to the values determined during the calibration measurement. These results are presented together with the temperature calibration in Section 5.3. As the CSR reached its final temperature after the cool down, the Rhodium-Iron temperature sensor attached to the chamber of the NICE detector showed a temperature of about 4 to 5 K. At these temperatures, the MCP resistance was in the order of a few 10 TΩ. From this resistances a temperature of about 5 K can be inferred, which is in good agreement with the temperature displayed by the Rhodium-Iron sensor attached to the according CSR chamber.

At the very lowest temperatures below 10 K, the pulses amplitudes were significantly smaller. The MCP was heated analog to the cryogenic tests, described in Section 5.3. Figure 5.25 shows the evolution of both the MCP resistance and the deduced MCP temperature in time as it is heated with a power of 48 mW starting from a temperature of about 5 K. This heating power leads to an elevated temperature

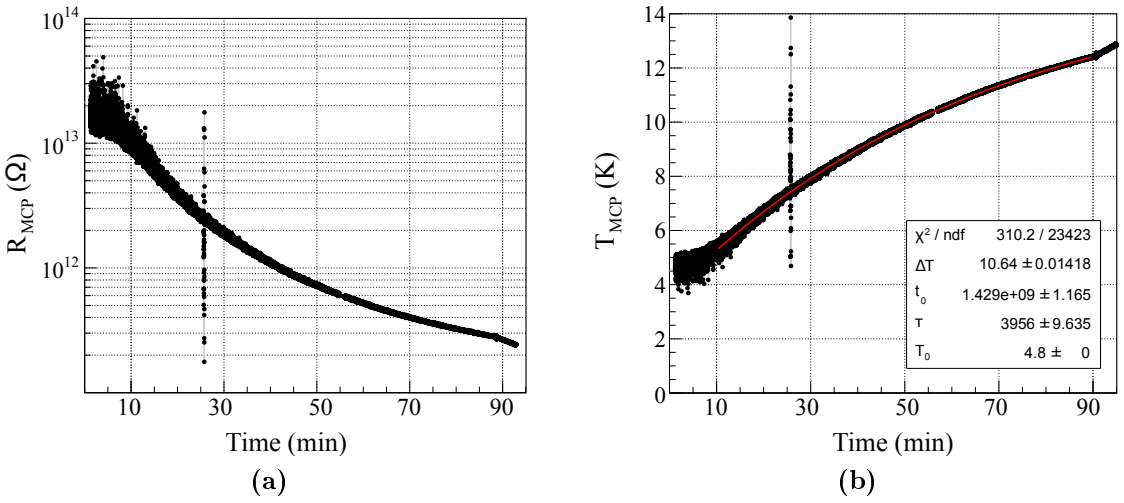

Figure 5.25: Time evolution of the MCP resistance (a) and the deduced temperature (b) while heating the MCP with a power of 48 mW starting from the coldest temperature at CSR. As the MCP temperature is increased by 10 K, the resistance decreased by about two orders of magnitude in the 100 GΩ region.

by about 10 K while the resistance was reduced by about two order of magnitude in the 100 GΩ region. The temperature evolution can be estimated with the exponential saturation function given in Equation 5.24. The resulting heating time constant of about 1.1 hours is similar to the value of 1.05 hours determined during the first cryogenic test with a heating power of 52 W starting from about 26 K.

Pulse Amplitude Spectra during Cool Down

Pulse amplitude spectra for neutral 60-keV Ar and 30-keV N particles were measured on a regular basis during the cool down of CSR. Figure 5.26 shows some of the measured pulse amplitude spectra obtained for neutral particles originating from collisions with residual gas molecules. The pulse amplitude spectra at 188 K and 101 K are from N, the others from Ar particles. The MCPs were always operated with about (1766 ± 1) kV on the front and 0 V on the back electrode. To compare their overall shape, the spectra are normalized to their total number of counts and shifted by the temperature of CSR. Given the different signal rates, the dark count contributions may vary. The pulse amplitude distributions appear to shift towards larger amplitudes at lower temperatures. At the coldest temperatures of CSR, the residual gas pressure improved so much, that no neutral particles produced by collisions with residual-gas could be detected any more on the NICE detector.

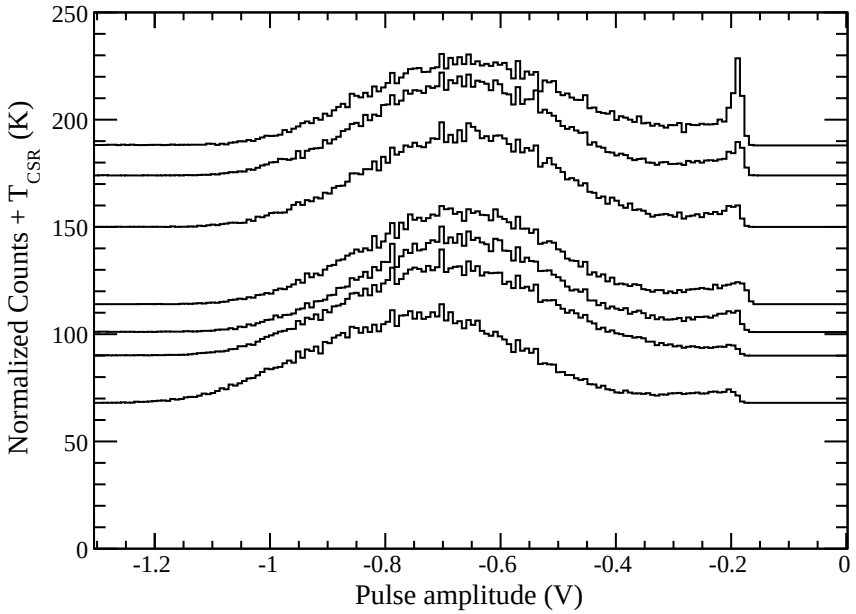

Figure 5.26: Pulse amplitude spectra measured during the cool down of CSR. The spectra at CSR temperatures of 188 K and 101 K were obtained from neutral products of a 60 keV-N_2^+ beam, the others from a 60 keV-Ar^+ ion beam. The spectra are normalized to their number of total counts in order to compare their shape as the signal rate varied between the measurements. This leads to different dark count contributions.

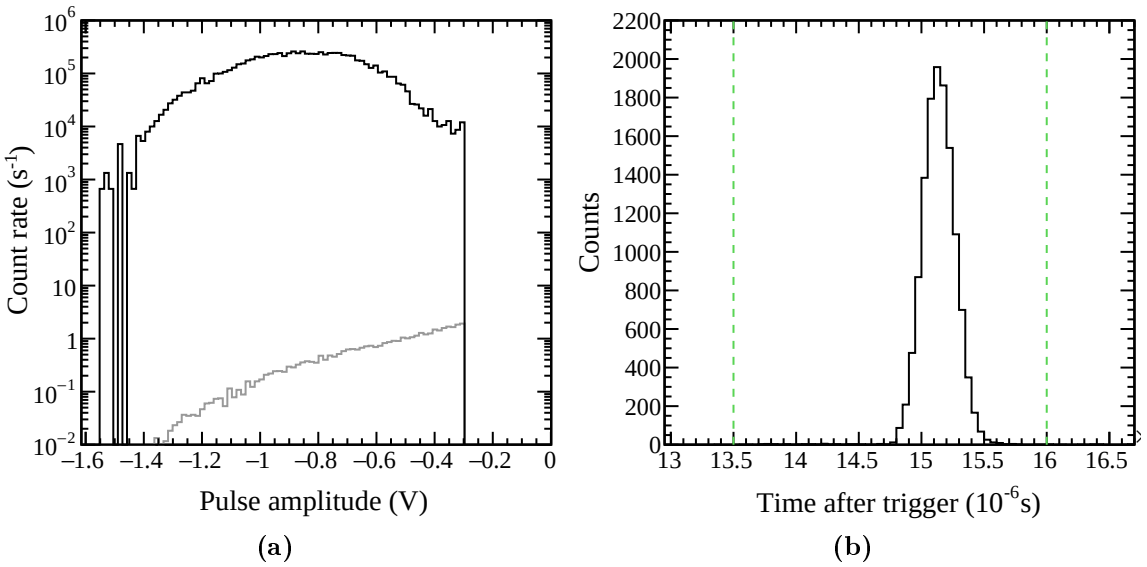

Figure 5.27: Pulse amplitude spectrum at an MCP temperature of about 30 K. The pulse amplitude spectra (a) of 60 keV OH (black line) and MCP dark counts events (gray line) could be separated by a temporal discrimination on the signal induced by the pulsed OPO laser (b, green lines).

At these temperatures neutral particles could only be observed by laser induced photodetachment or photofragmentation reactions.

Pulse Amplitude Spectra at Cryogenic Temperatures

The change of the pulse amplitude distribution with temperature of the MCPs below 60 K was investigated in a measurement series via the photodetachment signal of a stored OH^- ion beam produced with the pulsed OPO laser. The OPO laser, described in Section 3.1.5, was operated at 632.8 nm with about 500 μJ/pulse. This ion was later also investigated with the NICE detector in one of the first showcase experiments at CSR (see Sect. 3.1.5). Within the same measurement series, further comparison measurements with the COMPACT detector were performed which are described later.

For these pulse amplitude measurements, the NICE detector was first warmed up with the heating element described in Section 5.2.2.3 to an elevated temperature of about 58 K with a heating power of about 360 mW. After the MCP resistance, and thus, the MCP temperature stabilized, the heating was turn off. While the NICE detector was cooling down to the ambient temperature of the CSR chamber, the rate of neutral OH particles produced by photodetachment was measured as a function of storage time for 600 s. In the last 20 s, the ion beam was dumped to measure the detector background rate directly. After each short laser shot, the neutral products generated in the interaction region arrived at the detector in a time window of about 0.5 μs (see Fig. 5.27b). The data acquisition is triggered by the

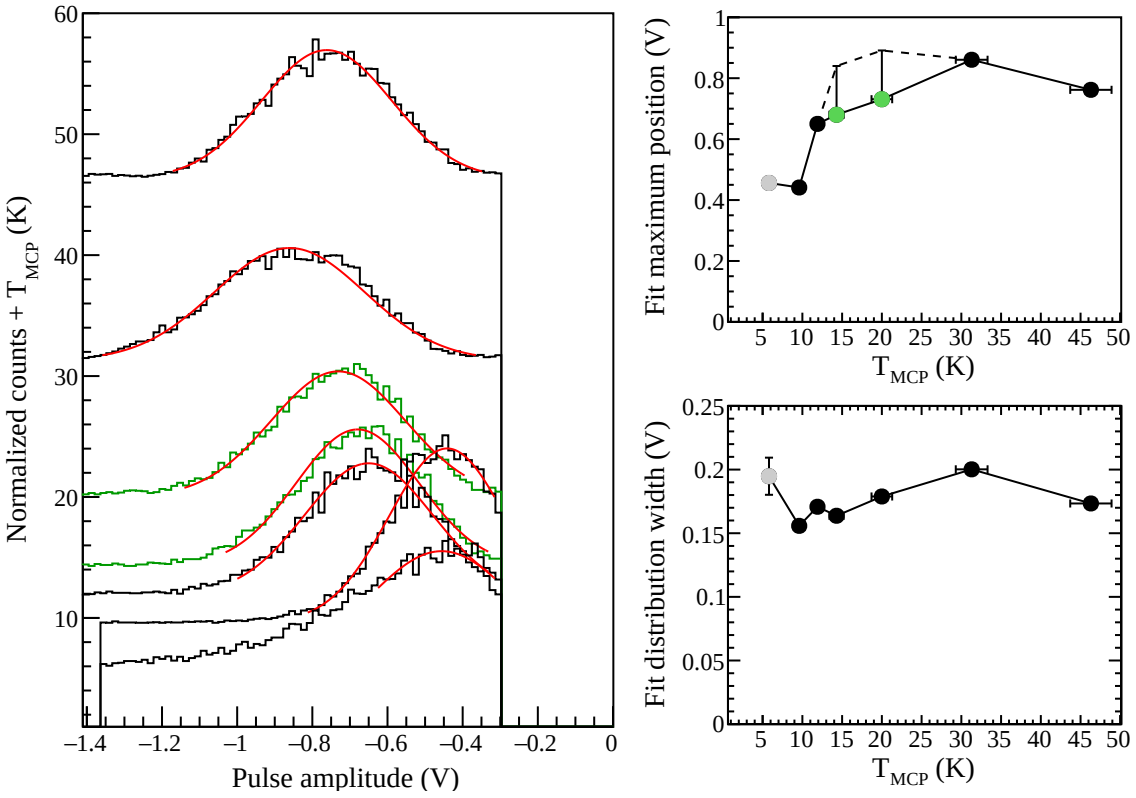

Figure 5.28: The left panels shows the pulse amplitude spectra of 60 keV OH at temperatures below 60 K measured with the pulsed OPO laser. The spectra are, analogous to Fig. 5.27, discriminated on the laser induced signal. The spectra are normalized to their total count number and shifted by the respective MCP temperature. The right panels shows the fit maximum positions and widths, from the normal distribution fits (red lines), for different MCP temperatures. The spectra at about 14 K and 20 K, highlighted in green, are measured with a reduced operation voltage, as the pulses got too large for the amplifier. The maximum positions of these measurements for the same settings were estimated from other measurements and are indicated by vertical bars. The spectrum at 6 K was measured the next day.

laser, so that it is possible to discriminate the laser induced particle signal in time. The discrimination time window was set to a range from 13.5×10^{-6} s to 16×10^{-6} s. By such a discrimination the background can be effectively suppressed by a factor of about 10^5 and signal rates even far below the dark count rate can be investigated. This is shown in Figure 5.27 with the pulse amplitude distributions of particle and MCP dark count events at an MCP temperature of about 30 K. These spectra are normalized to their acquisition time.

Figure 5.28 shows all acquired pulse amplitude spectra of particle events normalized by their total number of counts and shifted by their respective MCP temperatures inferred from the MCP resistance. In order to characterize the change of the pulse amplitude distributions, the spectra were fitted with normal distributions (red

lines in Figure 5.28). The spectrum at 6 K was measured the next day and cannot be well reproduced by the normal distribution fit. For all other distributions the statistical uncertainties of the derived maximum positions of the distributions are well below 1 %, for the distribution widths below 1.6 %. The values for the maximum positions and widths of the distributions for the different MCP temperatures are depicted in the same Figure on the right side. The spectra and data points highlighted in green were measured with a reduced MCP operation voltage of 1740 kV instead of 1767 kV, as the amplitude amplitudes, in fact, got too large for the amplifier in this temperature range. The maximum positions for the same settings were estimated from other measurements and are indicated by vertical bars. The given uncertainty of the MCP temperature is estimated from the temperature difference during each measurement inferred from the MCP resistance. Furthermore, the uncertainty of the temperature calibration is estimated with 10 %. Not included are the estimations from the temperature profile calculations in Section 5.2.2.3, as these are only based on a thermal conductivity value for room temperature. These calculations suggest for a heating to 55 K a temperature difference at the center of the MCP of 8 K. While these spectra were not measured under equilibrated thermal conditions, they agree qualitatively with other later measurements with MCP temperatures above 15 K.

While the MCP was cooling down, the widest pulse amplitude distribution was effectively achieved at around 20 K. Around 10 K, the pulse amplitude distribution rapidly shifted and deformed towards lower pulse amplitudes. This is a clear indication of charge depletion. Given the large resistance at these temperatures, the microchannels cannot be recharged fast enough. During the later experiments the NICE detector was typically heated to temperatures in the range from 20 K to 30 K.

Rate-Dependent Charge Depletion

The charge depletion of the individual microchannels depends, besides their recharging properties, on the rate of detected particles. This was, for example, observed in a lifetime measurement of OH^- with the photodetachment signal using the HeNe cw-laser (see Sect. 3.1.5) at 632.8 nm. Figure 5.29 shows the evolution of the pulse height with storage time while the MCP was heated to about 20 K. With count rates of about $700\,s^{-1}$ in the beginning, the pulse height spectrum is strongly shifted towards lower amplitudes and has its maximum around 0.4 V. With longer storage times and, accordingly, decreasing count rates the pulse amplitudes recover again. This is an indication that the available charge in the microchannels is, in the beginning, depleted to fast by consecutive particle impacts. The electrical pulses are recorded with a waveform digitizer which only records pulses with amplitudes above a certain threshold. As the pulse height spectrum is shifted below this threshold, the detected counts rates are reduced. This can be observed in this case for the measured lifetimes for storage times below about 100 s. If this behavior is characterized in more detail, it may be possible to compensate for this effect by an appropriate higher order analysis. The first experiments were performed with particle rates of only a few $100\,s^{-1}$ for which no charge depletion effects could be observed.

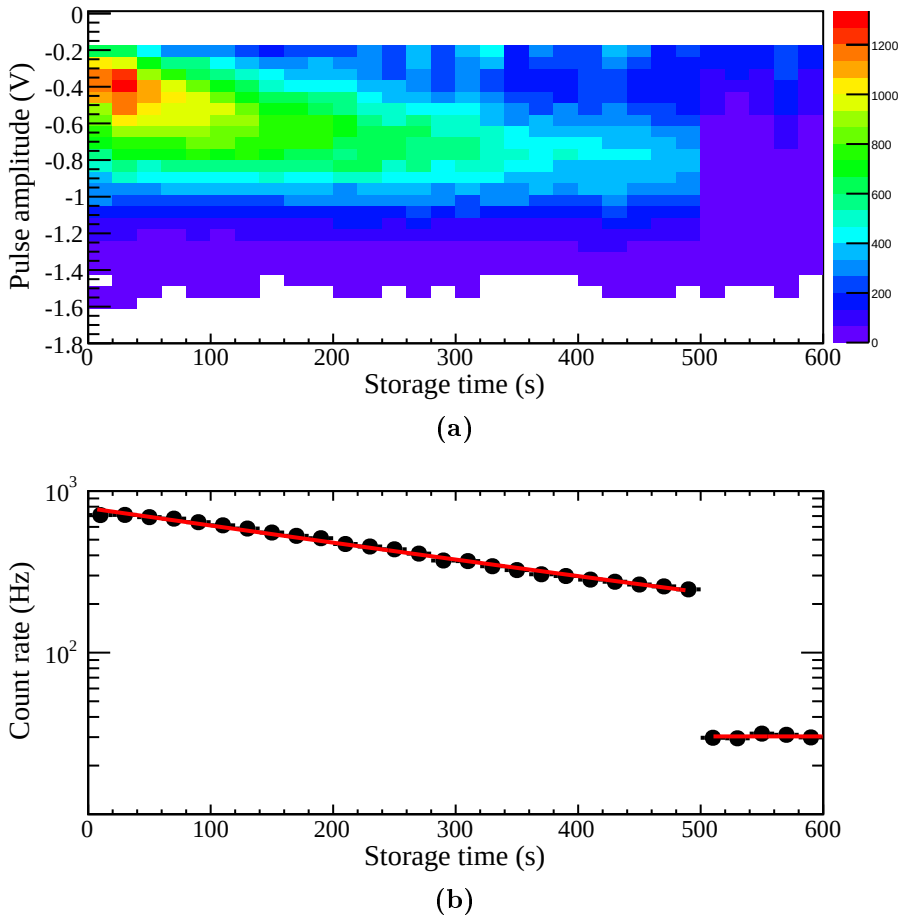

Figure 5.29: Pulse amplitude evolution (a) with storage time and, according to the beam decay, different detected count rates (b) at cryogenic temperatures. The MCP was operated at about 20 K. The beam lifetime is measured with the CW laser induced signal. At higher rates the pulse height distribution is shifted towards lower values.

Comparison Measurements with COMPACT Detector

To investigate whether the detection efficiency of the NICE detector was preserved operating at cryogenic temperatures, a comparison measurement series was performed with the COMPACT detector. The COMPACT detector is designed and tested for particle counting efficiencies of almost 100 % even under cryogenic conditions [125]. This measurement series was performed in between the previously described measurements with an OH^- beam and the OPO laser where the MCP was first heated to about 58 K and then cooled down to the ambient temperature of the CSR chamber. In this case the photodetachment signal from a HeNe cw-laser at 633 nm was used (see Sect. 3.1.5). For the comparison measurements, the COMPACT detector was positioned such that it covered half of the surface of the NICE detector. The beam-profile was measured before by detecting the rate on the COMPACT detector for different positions. The resulting beam full-width-half-

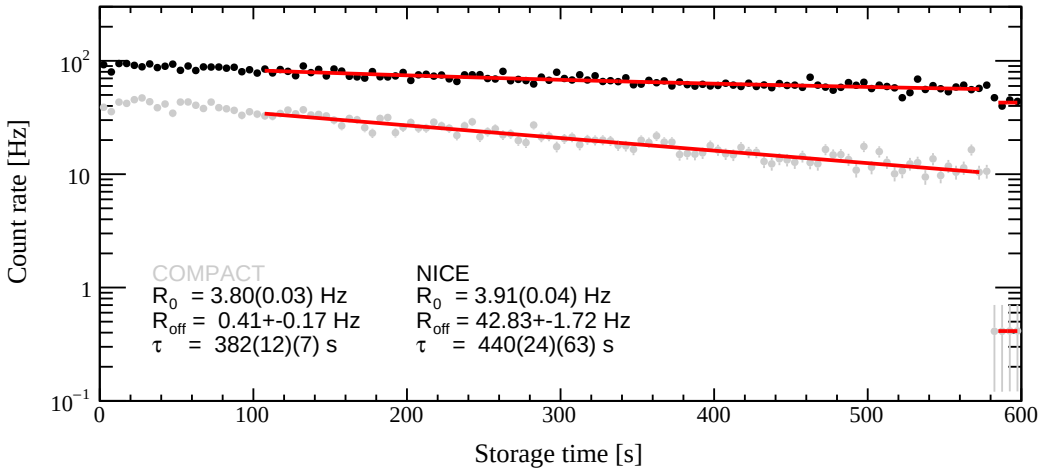

Figure 5.30: Ion beam lifetime of an OH^- beam measured with both the NICE and COMPACT detectors simultaneously. In this case, the temperature of NICE inferred from its resistance was at about 17 K. The COMPACT detector was positioned such that it covered half of the NICE detector and measured at the same time. The apparent differences in the curve slope is given by the high dark count rate of the NICE compared to COMPACT detector

maximum (FWHM) of about 20 mm corresponds to the width of the aperture of the COMPACT detector. By shifting the COMPACT by about half of the FWHM, both detectors were exposed to a comparable flux of neutral particles emerging from the laser interaction section. Although equipped with an MCP heating as well, the COMPACT detector did not exhibit any depletion effects at particle count rates below about $2000\,s^{-1}$ even at the lowest temperature of 5 K. Hence, the temperature could be kept constant during the cool down of the NICE detector.

As an example, Figure 5.30 shows the measured rate on both the NICE and COMPACT detector versus storage time. For this measurement the NICE detector had a resistance suggesting a temperature of about 17 K for which it showed among the broadest pulse height distributions. Both rates R were fitted with an exponentially decaying function

$$R = R_0 \exp\left(-\frac{t}{\tau}\right) + R_{\text{off}} \tag{5.26}$$

with a constant term for the dark count rate R_{off} measured with the ion beam turned off. The first error is the statistical error from the lifetime fit. The second error was determined from the difference of two lifetime fits where the value for the background was fixed to its minimum and maximum values including its uncertainty. Considering their respective dark count rates, both detectors showed in fact about the same particle rate and an ion beam lifetime which is consistent within its uncertainty.

Figure 5.31 shows the ratios of the averaged rates obtained during these lifetime measurement. The NICE MCPs were first heated to about 58 K. After the heating was switched off, these lifetime measurements were performed while the detector

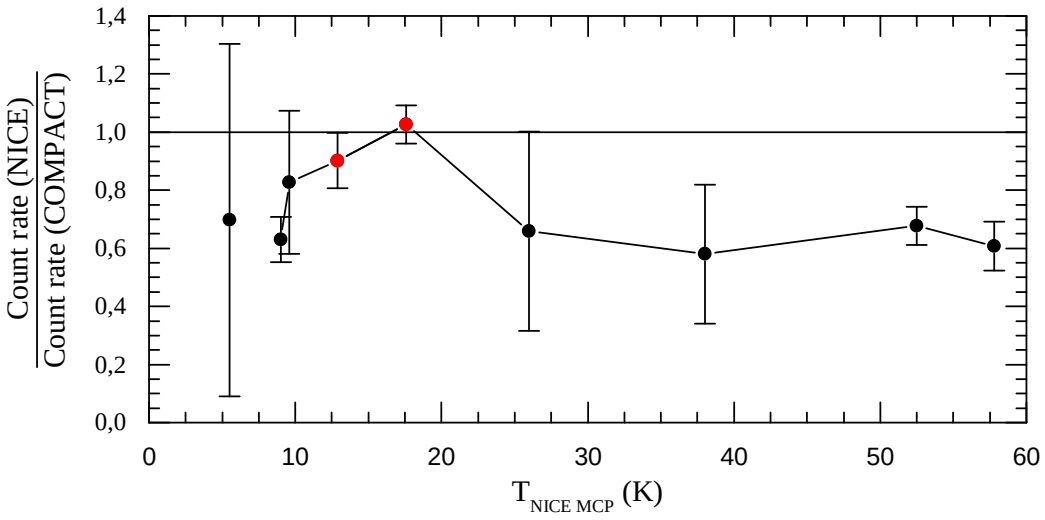

Figure 5.31: Mean rate ratio measured with the NICE and COMPACT detector, while the NICE detector was cooling down. The COMPACT detector was positioned such that it covered half of the NICE detector. The two red data points were obtained with a lower operation voltage of NICE as the pulses got too large for its signal amplifier.

was cooling down. The error bars indicate the variations of these ratios within each lifetime measurement. Analogous to the OPO measurements, the two data points at about 15 and 17 K were measured with a lower operation voltage, as the pulse height spectrum did in fact got too large for the signal amplifier. The increase of the relative detected rate for lower operation voltages with the NICE detector may be a sign of a saturation of the signal amplifier before. While one cannot derive a conclusive value for the detection efficiency from these measurements, they suggest, that the counting efficiency of the NICE MCPs is still preserved at temperatures as low as about 15 K for sufficiently low particle rates.

The advantage of the COMPACT detector for these kind of continuous lifetime measurements is its much lower dark count rate of about $0.1\,\mathrm{s}^{-1}$ compared to dark count rates in the order of a several $10\,\mathrm{s}^{-1}$ of the NICE detector. The dark count rates of MCPs are believed to originate mainly from beta-decay of ^{40}K [153] embedded in the glass substrate and, therefore, scale with the volume of the MCP. The MCPs of the COMPACT have a much smaller diameter of 18 mm compared to the NICE detector with a diameter of 120 mm Together with the much lower MCP resistance ($\sim 200\,\mathrm{G}\Omega$) this leads to a significantly larger dynamic range of the COMPACT detector.

In contrast, the anode signal line of the movable COMPACT detector is much longer and of lower quality than that of NICE. It was also not designed for near coincident particle hits and is characterized by much broader anode pulse shapes. Furthermore, its bent converter electrode leads to variations of the time-of-flight depending on the altitude of the impacts on the converter electrode. Hence the

NICE detector was much more useful in experiments on photodetachment in a pulsed laser beam, with multiple impacts of a few tens of particles on the detector in a time window of typically a few 100 ns. This allowed measurements with higher signal rates compare to COMPACT detector.

The absolute detection efficiency of MCP detectors can be measured precisely by coincidence measurements of molecular dissociation reactions with, e.g., both neutral and charged fragments similar to the more recent studies with keV-energy particles by Takahashi et al. [195] or Gaire et al. [196]. At CSR, both neutral and charged products can be detected in coincidence with the NICE and COMPACT detectors, respectively. In order to collect all charged fragments with the COMPACT detector, a more narrow ion beam is required. Such a narrow, cooled ion beam will become available at CSR once the electron cooler becomes operational.

5.5 Summary and Outlook

A multi-coincidence imaging detector for neutral reaction product particles has been developed, tested and used for the first experiments at CSR. This so-called NICE detector is an MCP based detector with phosphor screen anode which can be operated at cryogenic temperatures. It employs the new COBRA read-out which facilitates three-dimensional imaging of neutral fragmentation products.

During the first commissioning of CSR at room temperature, the NICE detector was tested and optimized for the COBRA read-out scheme. In the second cryogenic beamtime of CSR the detector was used for first fragmentation experiments. After its first cool down, the CSR reached temperatures of about 5 K. Although operation of an MCP is challenging at cryogenic temperatures, the MCPs of the NICE detector operated successfully thanks to a heating element which could be used for localized heating of the detector. Hence, the NICE detector could be used successfully as a fast counter for nearly-coincident neutral products in the first CSR beamtimes.

The shape of the pulse height distributions of the MCPs does not change significantly with temperatures down to about 15 K. In fact, the pulse height spectra tended to shift towards higher amplitudes till MCP temperatures of about 20 K. Below this temperatures the signal amplitudes degraded and were not usable any more below 10 K. This behavior indicates a strong charge depletion in the microchannels due to its high resistance at these temperatures which inhibits a recharging of the individual microchannels. Using the heating element of the MCPs, the detector was operated most of the time at elevated temperatures between 20 and 30 K without affecting the temperature of the surrounding CSR chambers to more than 2 K. Furthermore, a rate dependent charge depletion could be observed for particle rates of several $100\,\mathrm{s}^{-1}$. This limits the dynamic range of detectable particle count rates. However, in the experiment with the pulsed OPO laser it was possible to discriminate on the laser induced signal in time-of-flight, by which the background could be suppressed by a factor of 10^5 to 10^6.

First preliminary comparison measurements with the COMPACT detector indicated, that the NICE detector still has a good counting detection efficiency even at cryogenic temperatures down to 10 K.

During the cool down of CSR, the infrared filter on the outer radiation shield became opaque due to ice deposits on its surface. This will require a redesign of the filter holder for which possible constructive countermeasures have been discussed in Section 5.4.2.

The pulse shapes of the fast electrical signals decoupled from the phosphor screen high-voltage line indicated some considerable reflections on the electrical signal line. The analysis of two-hit events showed, that these kind of reflections disturbed the amplitude of consecutive pulses with arrival-time differences below 30 ns which disturbs also the COBRA event recognition in this time period. The use of a bipolar instead of a unipolar signal amplifier could not resolve this issue. Therefore, the electrical transmission properties of the signal line need to be further improved. Alternatively, the use of an optical timing read-out can be considered.

The NICE detector was already used as a fast counter of nearly-coincident neutral products for the first physical experiments at CSR with an pulsed OPO laser (see Sect. 3.1.5) and will be used for DR experiments in combination with the upcoming electron cooler.

6 Conclusion and Outlook

This work has reported on experimental studies of molecular fragmentation which have been conducted at the former Heidelberg storage ring TSR, and on preparations regarding a continuation of these experimental techniques at the new cryogenic CSR setup.

The DR process of the sulfur hydride cation SH^+ with electrons has been experimentally investigated at the TSR ion storage ring at a well-established merged-beams setup for electron-ion collision studies. In two different measurements, the merged-beams DR rate coefficient and the product state branching ratios have been determined.

In astronomical observations, the signatures of this ion are, for example, used to probe turbulences in interstellar media. However, the observed abundances have been significantly underestimated in the model calculations. In view of the astrophysical model calculations, a thermal plasma rate coefficient was derived from the rate coefficient obtained in this work. The deduced plasma rate coefficient differs from the typically assumed rate coefficient in both the amplitude and the dependence on the plasma temperature. It falls below the plasma rate coefficient used in the models at temperatures above 50 K, which is relevant for higher SH^+ abundances in ISM. Using our new data in the models will lead to a lowering of the SH^+ destruction rate and thus an increase of the modeled SH^+ abundance. This will result in an at least partial lowering of the discrepancies between observed and modeled SH^+ abundances.

Furthermore, SH^+ has been investigated with the neutral fragment momentum imaging technique at near-zero electron-ion collision energy. This measurement was complicated by the fact that most of the light hydrogen fragments missed the detector due to the large mass ratio of the constituents of this molecule and the limited ion beam energy at TSR. Only for one highly excited product state, both fragments could be detected and the according kinetic energy release could be determined directly. Based on the well known excitation energies of the product channels, the reaction energy could be derived. The obtained value agrees within its uncertainty with the derived reference values. In fact, the obtained value can be used to derive a more precise value for the proton affinity of sulfur.

As part of this work, a new method has been developed to determine the branching ratios of the different DR product excited states by the available imaging data of only the heavier fragments, in this case sulfur. Given the well-cooled ion beam, it was possible to extract a distance spectrum of only the heavier sulfur fragments with respect to the center-of-mass of the beam. This spectrum could then be fitted with the relative amplitudes of model distributions for the different product excited states to determine the branching ratios.

All these experimental results on DR of SH^+ serve as an important reference for ongoing theoretical investigations which are in a preliminary stage [41,42]. The rate coefficient predicted by theory is still almost two orders of magnitudes too low.

In the second part of this work, experimental DR studies have been prepared for the CSR ion storage ring by developing a multi-coincidence position- and time-sensitive detector for neutral reaction products. In consideration of all the technical and experimental requirements, the main challenges stemmed from the cryogenic operation temperatures and the, in comparison to TSR, much lower ion beam energies. For the first CSR experiments an MCP-based imaging detector system has been implemented. Different position read-out systems were considered and partly simulated. Finally, an MCP detector with a phosphor screen anode was implemented - the NICE detector. The COBRA read-out scheme, developed by Urbain et al. [172], is used for this detector, enabling a three-dimensional imaging of the dissociated fragments. The independent and complementary measurements of both the transversal position and longitudinal arrival-time ensure a fragment distance determination with high accuracy for all molecular orientations.

The NICE detector was tested and optimized for the COBRA read out scheme during the first commissioning of CSR at room temperature. In the second cryogenic beamtime of CSR, the detector was already used for first fragmentation experiments. After its first cool down, the CSR reached temperatures of about 5 K. Although operation of an MCP is challenging at cryogenic temperatures, the MCPs of the NICE detector operated successfully thanks to a heating element which could be used for localized heating of the detector. Hence, the NICE detector was used successfully as a fast counter for almost coincident neutral products in the first CSR beamtimes.

In the NICE detector, the electrical pulses created by the electron clouds emerging from the MCPs on the phosphor screen anode are used as a timing signal. With the realized signal decoupling circuit, short electrical pulses with a width of about 6 ns have been achieved, which already provides a good foundation. An obstacle during the first cryogenic operation was ice deposits re-sublimating on the sapphire infrared filter which prevented any imaging measurement. In view of the foreseen fragment imaging measurements, this issue will have to be solved. The appropriate constructive measures are ongoing to address this issue. A fully optical read-out scheme of the NICE detector with a fast segmented photomultiplier could be realized as a future upgrade.

In the near future, CSR will be complemented by the electron cooler required for the merged-beams DR reaction studies. In combination with the cryogenic environment this will provide unique opportunities for experiments with internally deexcited and phase-space cooled ion beams. Interestingly, the situation encountered in the TSR studies of SH^+, during which the light hydrogen fragments missed the detector aperture in most cases, will be common in future CSR experiments. Hence, the heavy-fragment imaging technique developed in this work will be crucial for future investigations at CSR. Moreover, an energy- and position-sensitive microcalorimeter detector is being developed [159]. This will be placed behind the NICE

detector, which will receive a central hole for the heavier dissociation products to reach the micro-calorimeter. This detection system will expand the capabilities of the DR studies at CSR, especially for heavier and more complex systems.

A Appendix

A.1 Numerical Methods used for Heavy Fragment Imaging

In the following, the numerical methods used for the generation of the distance-from-beam-center model distributions of the heavy fragment (see Sect. 4.4.3) are described in more detail.

A.1.1 Numerical Sampling of Model Distributions

The distance distribution P_n^{S} of, in this case, sulfur hits needs to be numerically convoluted with the measured beam profile. For this, a random sample of distances d_S distributed according to P_n^{S}) is required. This could, in principle, be generated directly by randomly sampling the inverse cumulative distribution function, also known as quantile function. Unfortunately, the expression of P_n^{S} is too complicated for a straight forward inversion. A widely used numerical approximation is the Monte Carlo integration method, which can approximate any distribution with arbitrarily high accuracy. In this case it involves the following steps:

1. Generate random radius $r \in [0, r_{\mathrm{max}}]$ with $r_{\mathrm{max}} = \frac{d}{2}$
2. Generate random probability density $p \in [0, p_{\mathrm{max}}]$ with $p_{\mathrm{max}} = P_n^{\mathrm{S}}(\delta_n L_{\mathrm{max}})$

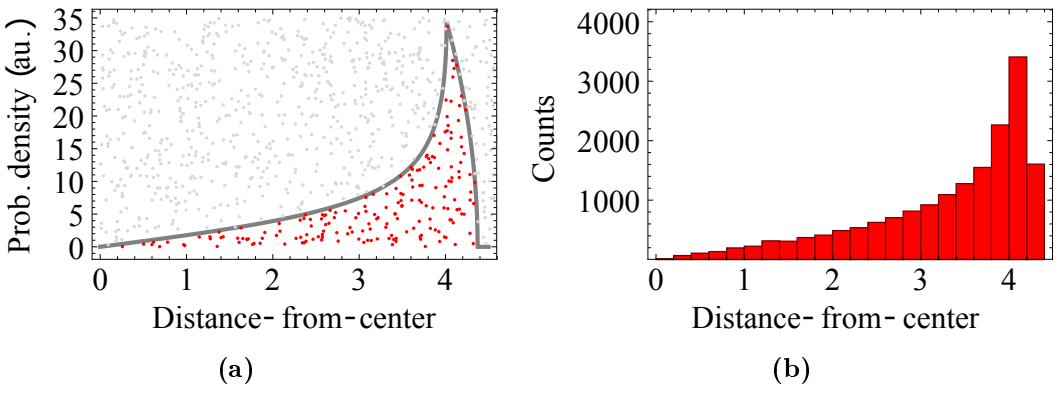

Figure A.1: Schematic illustration of Monte Carlo integration method used for the generation of a set of random numbers distributed according to $P_n(d_{\mathrm{S}})$. The Monte-Carlo selection process is shown on the left, the according histogram on the right side.

3. If $p < P_n^{\mathrm{S}}(r)$ accept r

This method is not very efficient in this case, as the distribution P_n^{S} is quite narrow and most of the generated values are rejected (see Fig. A.1). In order to optimize the computation time, the range of randomized values was set to the maximum of possibly occurring values $\delta_n L_{\max}$ according to Equation 3.27 and 3.35.

A.1.2 Numerical Convolution of the Calculated Distance Distribution with the Beam Profile

Following the definitions in Section 4.4.3, the convolution of the both two-dimensional distribution of DR distance-to-event-centers P_n^{S} and the beam center-of-mass distribution f_{cm} can be performed numerically by randomly sampling coordinates from both distributions following their probability density. The sampled values added together represent a random value of the desired convolved fragment-to-beam-center probability distribution $\widetilde{P}_n^{\mathrm{S}}$. Specifically, as the beam profile is evaluated only in the radial dimension (see Fig. A.1) one has to randomize the missing coordinate, the angle. Here an uniform distribution $\{0, \ldots, 2\pi\}$ is used. In principle, this is also true for the distance distribution. The numerical convolution was carried out as follows:

1. Get random DR hit distance d_S distributed according to the model distribution P_n^{S} (see previous section),
2. Get random distance d_{CM} from experimentally measured center-of-mass distribution f_{CM}
3. Generate random angles $\varphi_S, \varphi_{CM} \in \{0, \ldots, 2\pi\}$
4. Calculate impact coordinates on the detector with respect to the beam center

$$x_{\mathrm{CM}}^{\mathrm{S}} = d_{\mathrm{S}} \cos(\varphi_S) + d_{\mathrm{CM}} \cos(\varphi_{\mathrm{CM}})$$
$$y_{\mathrm{CM}}^{\mathrm{S}} = d_{\mathrm{S}} \sin(\varphi_S) + d_{\mathrm{CM}} \sin(\varphi_{CM})$$

5. Store convolved distance of the heavy sulfur fragment with respect to the center-of-mass of he beam in histogram

$$d_{\mathrm{CM}}^{\mathrm{S}} = \sqrt{\left(x_{\mathrm{CM}}^{S}\right)^2 + \left(y_{\mathrm{CM}}^{\mathrm{S}}\right)^2} \tag{A.1}$$

As both angles are randomized by a uniform distribution, one angle randomization is obsolete and can be skipped in the numerical implementation of this procedure.

A.2 Delay-Line Monte-Carlo Simulation Alogrithm

A Monte-Carlo simulation of a DR experiment at CSR has been conducted in order to investigate possible issues using a MCP detector with an delay-line detector. The simulation program is written in C++ facilitating the ROOT library from CERN [177]. Each logical element was described by its own class. In the following the classes are briefly described in the order of their execution.

1. `MBEvent`: Generate merged-beams event
   a) Generate random position within the merged-beams interaction section considering a Gaussian beam profile and a certain target length
   b) Calculate mean collision velocity.
   c) Generate random electron velocity in the center-of-mass frame assuming a Gaussian-distributed transversal and longitudinal velocity spread for all three degrees of freedom.
   d) Calculate collision energy
   e) Generate random isotropic molecule orientation (collision angle θ)
   f) Generate random molecule rotation (collision angle ϕ)
   g) Apply angular anisotropy
   h) Randomize the kinetic energy releases according to the branching ratios of the different dissociation channels
   i) Add rotational excitation to kinetic energy releases
   j) Add collision energy to kinetic energy releases
   k) Calculate fragment velocities
   l) Calculate fragment coordinates at the detector position
2. `MDLDetector`: Simulate detector response
   a) Remove electron clouds which miss the detector surface or are lost due to MCP efficiency
   b) Calculate attenuation of the electron cloud intensity for lower delay-line layers
   c) Hit wires
      i. Calculate time delay till both wire ends
      ii. Propagate signals by sorting them by their arrival time
3. `MDLElectronics`: Simulate detector electronics
   a) Discriminate signal by removing signals below given signal threshold
   b) Digitize signal amplitude according to 8 bit-ADC of given range

c) Remove signals within dead time t_{dead}

d) Add Gaussian signal jitter

4. `MDLAnalysis`: Analyze detector signals

a) Identify signal combinations (two different algorithms)

i. By time sum with respect to MCP signal: Test all combinations of MCP pulses and the timing signals from the wire ends A and B of all layers l. If the time sum

$$t_A^l(\cdot) + t_B^l(\cdot) - 2\left(t_{MCP}(\cdot) + t_0^l\right) - t_{sum} < \delta t \tag{A.2}$$

is within the acceptance window δt of the expected time sum save signal index values.

ii. By time sum of delay-line signals with respect to signal permutations: Test all combinations of timing signals from the wire ends of all layers.

$$[t_A^m(\cdot) + t_B^m(\cdot)] - [t_A^n(\cdot) + t_B^n(\cdot)] - 2[t_0^m - t_0^n] < \delta t \tag{A.3}$$

iii. Save only best combinations

b) (Optional) Reconstruct missing MCP signal

c) (Optional) Reconstruct missing Delay-Line signals

d) Assign signals to hits

e) Calculate hit coordinates
For the two pulses at both ends of a delay-line wire caused by a fragment hit the coordinate for one dimension perpendicular to the wire windings can be reconstructed. The coordinate can be derived from the pulse time difference Δt_e at both ends of the wire.

$$x(t_A - t_B) = x(\Delta t_e) \tag{A.4}$$

This gives the position of the fragment hit with respect to the center of the area covered by the delay-line wire. The absolute position of the hit on the wire / wire length for the signal to propagate with respect to wire end A is given by

$$l_A(\Delta t_e) = \frac{1}{2}\left(v_{signal}\Delta t_e + L\right). \tag{A.5}$$

f) Reconstruct hit positions

A.3 MCP Specifications

The two MCPs used for the NICE detector were manufactured by PHOTONIS and were retrieved by Scientific Instruments. They have the following specifications:

Table A.1: Mechanical specification of microchannel plates.

MCP	front	back
Serial number	09M0018-17	11M0023-28
Outer diameter	127 mm	
Active diameter	120 mm	
Channel diameter	25 µm	
Center to center	32 µm	
Thickness	1.5 mm	
L/D ratio	60:1	
Bias angle	8 °	
Border	rimless	
Open Area Ratio	65 %	58 %
Type	Extended Dynamic Range	

According to the specification sheet the bias current of the two microchannel plates only matches within 10 % for a high voltage applied. If the two microchannel plates are directly attached to each other, there will be a larger voltage drop over MCP 1 with the higher resistance. Although the amplifications differ by one order of magnitude for the same voltage, this uneven voltage drop should equalize the difference in amplification.

Table A.2: Electrical specification of the microchannel plates.

MCP	Voltage (kV)	Bias current (uA)	Gain
front	0.9	540	1.0×10^4
back		620	2.0×10^5
front	1.2	740	5.8×10^5
back		780	5.2×10^6

A.4 Resistance-Temperature Calibration Data

Table A.3: Measured values of temperature-resistance calibration described in Section 5.3.

P (mW)	T_{MCP} (K)	R_{MCP} (Ω)	$\frac{R(T)}{R(298\,K)}$
0	297.9 ± 1.3	$(3.67 \pm 0.02)\times10^{6}$	1
668	72.5 ± 0.3	$(1.60 \pm 0.02)\times10^{8}$	44
484	50.7 ± 1.2	$(7.15 \pm 0.06)\times10^{8}$	195
357	42.1 ± 1.7	$(1.53 \pm 0.04)\times10^{9}$	417
242	30.6 ± 0.9	$(6.19 \pm 0.01)\times10^{9}$	1687
121	23.7 ± 1.3	$(1.95 \pm 0.03)\times10^{10}$	5309
0	19.2 ± 3.7	$(3.88 \pm 0.03)\times10^{10}$	10 584

A.5 Flap Mechanics Procedures

Figure A.2 to A.5 show schematically the opening and closure procedures of the shutter and mask drive mechanics of the NICE detector. Figure A.2 contains a more elaborate description of the scheme itself.

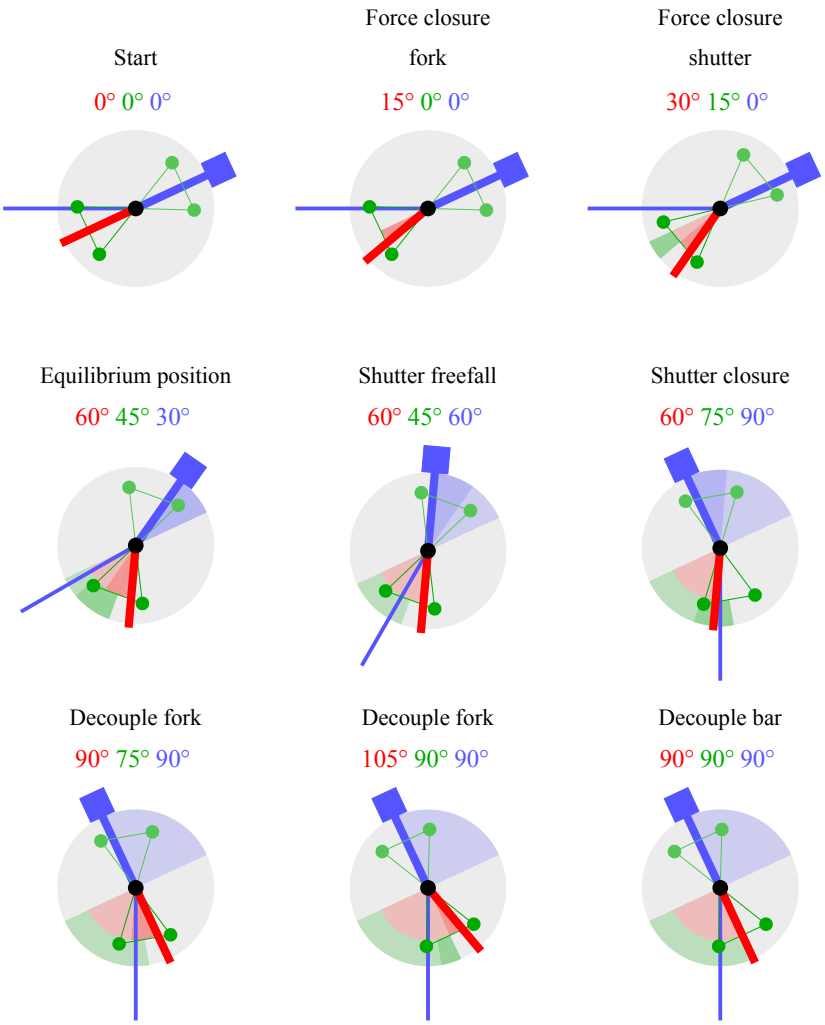

Figure A.2: Schematic illustration of shutter closure procedure. The other procedures are shown in the Appendix A.5. The shutter flap in the experimental vacuum chamber is indicated as a blue line. On the isolation vacuum side of the rotary feed-through, a bar with a counter weight is mounted, which is also highlighted in blue. The fork drive mechanics, highlighted in green, is thermally anchored on the 40 K shield. The fork is moving the inner feed-through has a lighter shade than the fork moved by the outer feed-through. The bar on the outer axis is in highlighted in red. The angles of the rotation of each element with respect to the starting position are given in the according colors on top of each diagram. In addition the angles are indicated by areas in the according colors.

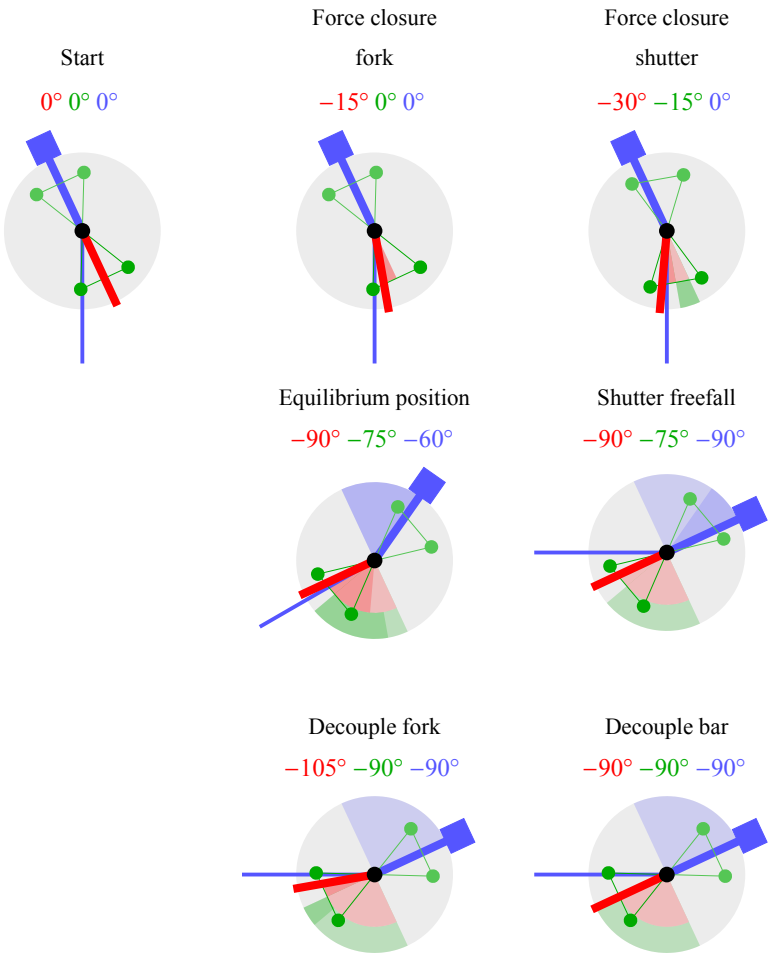

Figure A.3: Schematic illustration of shutter opening procedure, analog to Figure A.2. The shutter falls into the final position by itself over an angle of about 30°.

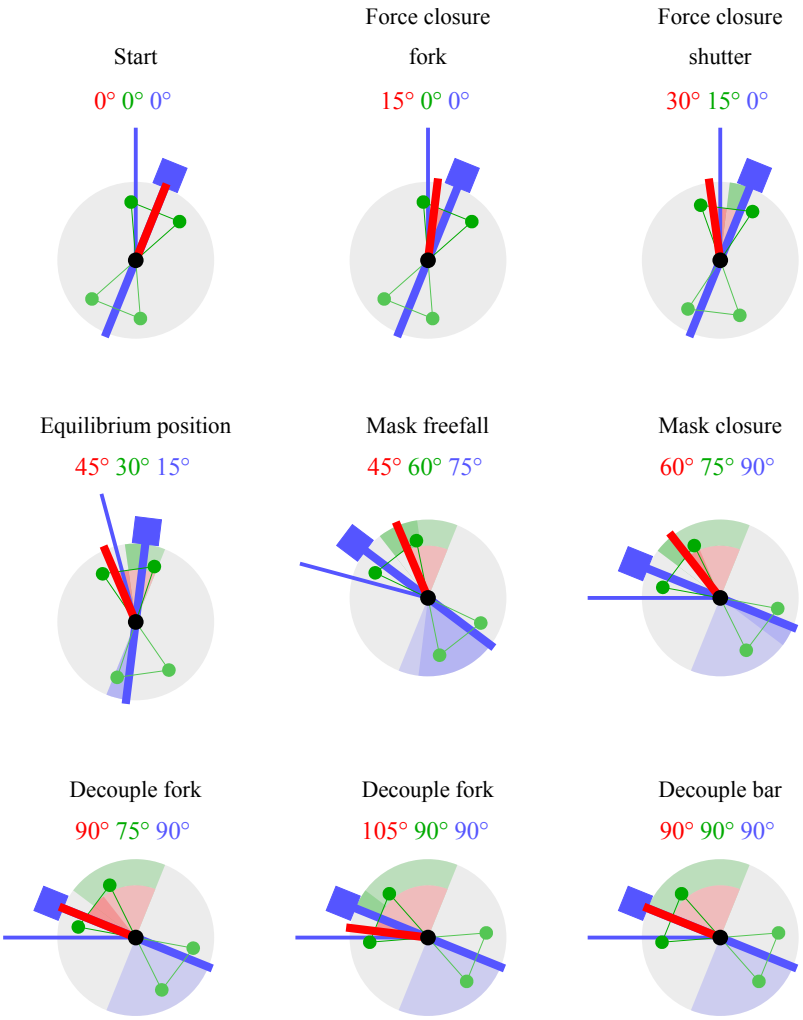

Figure A.4: Schematic illustration of mask opening procedure, analog to Figure A.2. The mask has a freefall angle of about 60°. The last 15° it can be gently put into the final position over another 15°.

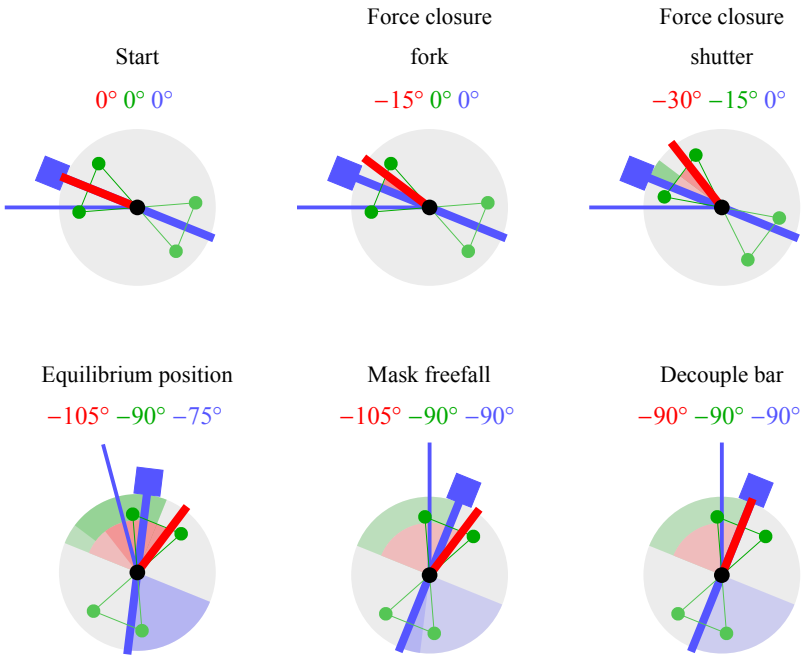

Figure A.5: Schematic illustration of mask closure procedure, analog to Figure A.2. The mask has a maximum freefall angle of about 30° between the equilibrium position and the final position.

B Lists

B.1 List of Figures

B.2 List of Tables

C Bibliography

[1] A. L. Peratt, *Physics of the Plasma Universe*. New York, NY: Springer New York, 2015. (page 11)

[2] E. Herbst and E. F. van Dishoeck, "Complex Organic Interstellar Molecules", *Annual Review of Astronomy and Astrophysics*, vol. 47, no. 1, pp. 427–480, 2009. (page 11)

[3] A. G. G. M. Tielens, "The molecular universe", *Reviews of Modern Physics*, vol. 85, pp. 1021–1081, July 2013. (page 11, 16)

[4] M. Larsson and A. E. Orel, *Dissociative Recombination of Molecular Ions*. Cambridge: Cambridge University Press, Apr. 2008. (page 11, 12, 19, 24, 74)

[5] R. D. Thomas, "When electrons meet molecular ions and what happens next: Dissociative recombination from interstellar molecular clouds to internal combustion engines", *Mass Spectrometry Reviews*, vol. 27, no. 5, pp. 485–530, 2008. (page 11)

[6] A. Florescu-Mitchell and J. Mitchell, "Dissociative recombination", *Physics Reports*, vol. 430, pp. 277–374, Aug. 2006. (page 11, 19, 73, 74, 75)

[7] L. G. Christophorou, *Electron-molecule interactions and their applications, Volume 2*. Academic Press, 1984. (page 11)

[8] I. W. M. Smith, C. S. Cockell, and S. Leach, eds., *Astrochemistry and Astrobiology*. Berlin, Heidelberg: Springer Berlin Heidelberg, 2013. (page 11, 14, 15, 16)

[9] B. Godard, E. Falgarone, M. Gerin, D. C. Lis, M. De Luca, J. H. Black, J. R. Goicoechea, J. Cernicharo, D. A. Neufeld, K. M. Menten, and M. Emprechtinger, "Comparative study of CH^+ and SH^+ absorption lines observed towards distant star-forming regions", *Astronomy and Astrophysics*, vol. 540, p. 87, Apr. 2012. (page 12, 16, 17, 18, 56, 75)

[10] Z. Nagy, F. F. S. Van der Tak, V. Ossenkopf, M. Gerin, F. Le Petit, J. Le Bourlot, J. H. Black, J. R. Goicoechea, C. Joblin, M. Röllig, and E. A. Bergin, "The chemistry of ions in the Orion Bar I. - CH^+, SH^+, and CF^+. The effect of high electron density and vibrationally excited H_2 in a warm PDR surface", *Astronomy and Astrophysics*, vol. 550, p. 96, Feb. 2013. (page 12, 16, 18, 56, 75)

[11] Govindjee, J. T. Beatty, H. Gest, J. F. Allen, and Govindjee, eds., *Discoveries in Photosynthesis*, vol. 20 of *Advances in Photosynthesis and Respiration*. Dordrecht: Springer Netherlands, 2005. (page 14)

[12] M. Gargaud, W. M. Irvine, R. Amils, H. J. J. Cleaves II, D. Pinti, J. Cernicharo Quintanilla, D. Rouan, T. Spohn, S. Tirard, and M. Viso, eds., *Encyclopedia of Astrobiology*. Springer-Verlag Berlin Heidelberg, 2 ed., 2011. (page 14, 38)

[13] A. Wootten, "The Atacama Large Millimeter Array (ALMA)", *arXiv:astro-ph/0209630*, pp. 110–118, Feb. 2003. (page 15)

[14] R. Güsten, L. Å. Nyman, P. Schilke, K. Menten, C. Cesarsky, and R. Booth, "The Atacama Pathfinder EXperiment (APEX) – a new submillimeter facility for southern skies –", *Astronomy & Astrophysics*, vol. 454, no. 2, p. 4, 2006. (page 15)

[15] D. A. Neufeld, E. Falgarone, M. Gerin, B. Godard, E. Herbst, G. Pineau des Forêts, A. I. Vasyunin, R. Güsten, H. Wiesemeyer, and O. Ricken, "Discovery of interstellar mercapto radicals (SH) with the GREAT instrument on SOFIA", *Astronomy & Astrophysics*, vol. 542, p. L6, June 2012. (page 15)

[16] D. A. Neufeld, B. Godard, M. Gerin, G. P. des Forêts, C. Bernier, E. Falgarone, U. U. Graf, R. Güsten, E. Herbst, P. Lesaffre, P. Schilke, P. Sonnentrucker, and H. Wiesemeyer, "Sulphur-bearing molecules in diffuse molecular clouds: new results from SOFIA/GREAT and the IRAM 30 m telescope", *Astronomy & Astrophysics*, vol. 577, p. A49, May 2015. (page 15, 17, 18)

[17] R. D. Gehrz, T. L. Roellig, M. W. Werner, G. G. Fazio, J. R. Houck, F. J. Low, G. H. Rieke, B. T. Soifer, D. A. Levine, and E. A. Romana, "The NASA Spitzer Space Telescope", *Review of Scientific Instruments*, vol. 78, p. 011302, Jan. 2007. (page 15)

[18] G. L. Pilbratt, J. R. Riedinger, T. Passvogel, G. Crone, D. Doyle, U. Gageur, A. M. Heras, C. Jewell, L. Metcalfe, S. Ott, and M. Schmidt, "Herschel Space Observatory: An ESA facility for far-infrared and submillimetre astronomy", *Astronomy and Astrophysics*, vol. 518, p. L1, July 2010. (page 15)

[19] H. S. P. Müller, F. Schlöder, J. Stutzki, and G. Winnewisser, "The Cologne Database for Molecular Spectroscopy, CDMS: a useful tool for astronomers and spectroscopists", *Journal of Molecular Structure*, vol. 742, pp. 215–227, May 2005. (page 15)

[20] H. S. P. Müller, C. P. Endres, J. Stutzki, and S. Schlemmer, "The CDMS view on molecular data needs of Herschel, SOFIA, and ALMA," *AIP Conference Proceedings*, vol. 1545, pp. 96–109, July 2013. (page 15)

[21] E. Habart, M. Walmsley, L. Verstraete, S. Cazaux, R. Maiolino, P. Cox, F. Boulanger, and G. P. D. Forêts, "Molecular Hydrogen", in *ISO Science Legacy* (C. Cesarsky and A. Salama, eds.), pp. 71–91, Springer Netherlands, 2005. (page 15)

[22] B. Godard, E. Falgarone, and G. Pineau des Forêts, "Chemical probes of turbulence in the diffuse medium: the TDR model", *Astronomy & Astrophysics*, vol. 570, p. A27, Oct. 2014. (page 15, 18)

[23] V. Wakelam, E. Herbst, J.-C. Loison, I. W. M. Smith, V. Chandrasekaran, B. Pavone, N. G. Adams, M.-C. Bacchus-Montabonel, A. Bergeat, K. Béroff, V. M. Bierbaum, M. Chabot, A. Dalgarno, E. F. van Dishoeck, A. Faure, W. D. Geppert, D. Gerlich, D. Galli, E. Hébrard, F. Hersant, K. M. Hickson, P. Honvault, S. J. Klippenstein, S. L. Picard, G. Nyman, P. Pernot, S. Schlemmer, F. Selsis, I. R. Sims, D. Talbi, J. Tennyson, J. Troe, R. Wester, and L. Wiesenfeld, "A KInetic Database for Astrochemistry (KIDA)", *The Astrophysical Journal Supplement Series*, vol. 199, p. 21, Mar. 2012. (page 16, 73)

[24] O. Novotný, O. Motapon, M. H. Berg, D. Bing, H. Buhr, H. Fadil, M. Grieser, J. Hoffmann, A. S. Jaroshevich, B. Jordon-Thaden, C. Krantz, M. Lange, M. Lestinsky, M. Mendes, S. Novotny, D. A. Orlov, A. Petrignani, I. F. Schneider, A. E. Orel, and A. Wolf, "Dissociative recombination of CF^+: Experiment and theory," *Journal of Physics: Conference Series*, vol. 192, p. 012021, Nov. 2009. (page 16, 62)

[25] M. Oppenheimer and A. Dalgarno, "The Chemistry of Sulfur in Interstellar Clouds", *The Astrophysical Journal*, vol. 187, pp. 231–236, Jan. 1974. (page 16, 17)

[26] M. Horani, J. Rostas, and E. Roueff, "A potential extraterrestrial species - The SH^+ molecular ion", *Astronomy and Astrophysics*, vol. 142, pp. 346–350, Jan. 1985. (page 16)

[27] N. P. Abel, S. R. Federman, and P. C. Stancil, "The Effects of Doubly Ionized Chemistry on SH^+ and S_2^+ Abundances in X-Ray-dominated Regions", *The Astrophysical Journal Letters*, vol. 675, pp. L81–L84, Mar. 2008. (page 16, 17)

[28] T. J. Millar and L. M. Hobbs, "A search for SH^+ toward Zeta Ophiuchi", *Monthly Notices of the Royal Astronomical Society*, vol. 231, pp. 953–955, Apr. 1988. (page 16)

[29] L. Magnani and J. J. Salzer, "A search for SH^+ and CH^+ in diffuse and translucent clouds", *The Astronomical Journal*, vol. 98, pp. 926–930, Sept. 1989. (page 16)

[30] L. Magnani and J. J. Salzer, "Observational limits on SH^+ in diffuse clouds and the possible detection of NI I in the ISM", *The Astronomical Journal*, vol. 101, pp. 1429–1434, Apr. 1991. (page 16)

[31] K. M. Menten, F. Wyrowski, A. Belloche, R. Güsten, L. Dedes, and H. S. P. Müller, "Submillimeter absorption from SH^+, a new widespread interstellar radical, $^{13}CH^+$ and HCl", *Astronomy and Astrophysics*, vol. 525, p. 77, Jan. 2011. (page 16)

[32] A. O. Benz, S. Bruderer, E. F. van Dishoeck, P. Stäuber, S. F. Wampfler, M. Melchior, C. Dedes, F. Wyrowski, S. D. Doty, F. van der Tak, W. Bächtold, A. Csillaghy, A. Megej, C. Monstein, M. Soldati, R. Bachiller, A. Baudry, M. Benedettini, E. Bergin, P. Bjerkeli, G. A. Blake, S. Bontemps, J. Braine, P. Caselli, J. Cernicharo, C. Codella, F. Daniel, A. M. di Giorgio, P. Dieleman, C. Dominik, P. Encrenaz, M. Fich, A. Fuente, T. Giannini, J. R. Goicoechea, T. de Graauw, F. Helmich, G. J. Herczeg, F. Herpin, M. R. Hogerheijde, T. Jacq, W. Jellema, D. Johnstone, J. K. Jørgensen, L. E. Kristensen, B. Larsson, D. Lis, R. Liseau, M. Marseille, C. McCoey, G. Melnick, D. Neufeld, B. Nisini, M. Olberg, V. Ossenkopf, B. Parise, J. C. Pearson, R. Plume, C. Risacher, J. Santiago-García, P. Saraceno, R. Schieder, R. Shipman, J. Stutzki, M. Tafalla, A. G. G. M. Tielens, T. A. van Kempen, R. Visser, and U. A. Yıldız, "Hydrides in young stellar objects: Radiation tracers in a protostar-disk-outflow system", *Astronomy and Astrophysics*, vol. 521, p. 5, 2010. (page 16)

[33] A. Zernickel, P. Schilke, A. Schmiedeke, D. C. Lis, C. L. Brogan, C. Ceccarelli, C. Comito, M. Emprechtinger, T. R. Hunter, and T. Möller, "Molecular line survey of the high-mass star-forming region NGC 6334I with Herschel/HIFI and the Submillimeter Array", *Astronomy and Astrophysics*, vol. 546, p. 87, Oct. 2012. (page 16)

[34] M. Larsson, W. D. Geppert, and G. Nyman, "Ion chemistry in space", *Reports on Progress in Physics*, vol. 75, p. 066901, June 2012. (page 16)

[35] T. J. Millar, N. G. Adams, D. Smith, W. Lindinger, and H. Villinger, "The chemistry of SH^+ in shocked interstellar gas", *Monthly Notices of the Royal Astronomical Society*, vol. 221, pp. 673–678, Aug. 1986. (page 17)

[36] G. Pineau des Forets, E. Roueff, and D. R. Flower, "Theoretical studies of interstellar molecular shocks. IV - The sulphur chemistry in diffuse clouds", *Monthly Notices of the Royal Astronomical Society*, vol. 223, pp. 743–756, Dec. 1986. (page 17)

[37] E. Falgarone, V. Ossenkopf, M. Gerin, P. Lesaffre, B. Godard, J. Pearson, S. Cabrit, C. Joblin, A. O. Benz, F. Boulanger, A. Fuente, R. Güsten, A. Harris, T. Klein, C. Kramer, S. Lord, P. Martin, J. Martin-Pintado, D. Neufeld,

T. G. Phillips, M. Röllig, R. Simon, J. Stutzki, F. van der Tak, D. Teyssier, H. Yorke, N. Erickson, M. Fich, W. Jellema, A. Marston, C. Risacher, M. Salez, and F. Schmülling, "Strong CH^+ $J = 1$–0 emission and absorption in DR21", *Astronomy and Astrophysics*, vol. 518, p. L118, July 2010. (page 17)

[38] E. Falgarone, B. Godard, J. Cernicharo, M. De Luca, M. Gerin, T. G. Phillips, J. H. Black, D. C. Lis, T. A. Bell, F. Boulanger, A. Coutens, E. Dartois, P. Encrenaz, T. Giesen, J. R. Goicoechea, P. F. Goldsmith, H. Gupta, C. Gry, P. Hennebelle, E. Herbst, P. Hily-Blant, C. Joblin, M. Kaźmierczak, R. Kołos, J. Krełowski, J. Martin-Pintado, R. Monje, B. Mookerjea, D. A. Neufeld, M. Perault, J. C. Pearson, C. Persson, R. Plume, M. Salez, M. Schmidt, P. Sonnentrucker, J. Stutzki, D. Teyssier, C. Vastel, S. Yu, K. Menten, T. R. Geballe, S. Schlemmer, R. Shipman, A. G. G. M. Tielens, S. Philipp, A. Cros, J. Zmuidzinas, L. A. Samoska, K. Klein, A. Lorenzani, R. Szczerba, I. Péron, P. Cais, P. Gaufre, A. Cros, L. Ravera, P. Morris, S. Lord, and P. Planesas, "CH^+ (1–0) and $^{13}CH^+$ (1–0) absorption lines in the direction of massive star-forming regions", *Astronomy and Astrophysics*, vol. 521, p. L15, Oct. 2010. (page 17)

[39] P. Hennebelle and E. Falgarone, "Turbulent molecular clouds", *The Astronomy and Astrophysics Review*, vol. 20, pp. 1–58, Oct. 2012. (page 18)

[40] F. Edith, G. Benjamin, G. Maryvonne, and D. L. Massimo, "CH^+ and SH^+ in the diffuse interstellar medium: Tracers of turbulent dissipation", in *AIP Conference Proceedings*, vol. 1642, pp. 321–324, AIP Publishing, Jan. 2015. (page 18)

[41] D. Kashinski, D. Talbi, and A. Hickman, "Using block diagonalization to determine dissociating autoionizing states: Application to N_2H, and the outlook for SH", *EPJ Web of Conferences*, vol. 84, p. 03003, 2015. (page 18, 58, 158)

[42] D. O. Kashinski, O. E. di Nallo, A. P. Hickman, J. Z. Mezei, I. F. Schneider, and D. Talbi, "Theoretical Studies of Dissociative Recombination of Electrons with SH^+ Ions", in *APS Division of Atomic, Molecular and Optical Physics*, p. 1149, May 2015. (page 18, 58, 158)

[43] M. Born and R. Oppenheimer, "Zur Quantentheorie der Molekeln", *Annalen der Physik*, vol. 389, pp. 457–484, Jan. 1927. (page 19)

[44] J. von Neumann and E. P. Wigner, "Über merkwürdige diskrete Eigenwerte", *Physikalische Zeitschrift*, vol. 30, pp. 465–467, 1929. (page 19)

[45] D. R. Bates and H. S. W. Massey, "The Basic Reactions in the Upper Atmosphere. II. The Theory of Recombination in the Ionized Layers", *Proceedings of the Royal Society of London A: Mathematical, Physical and Engineering Sciences*, vol. 192, pp. 1–16, Dec. 1947. (page 22)

[46] D. R. Bates, "Dissociative Recombination", *Physical Review*, vol. 78, pp. 492–493, May 1950. (page 22, 23)

[47] J. N. Bardsley, "The theory of dissociative recombination", *Journal of Physics B: Atomic and Molecular Physics*, vol. 1, p. 365, May 1968. (page 23)

[48] S. L. Guberman, "The dissociative recombination of OH^+", *The Journal of Chemical Physics*, vol. 102, pp. 1699–1704, Jan. 1995. (page 24)

[49] Z. Amitay, D. Zajfman, P. Forck, T. Heupel, M. Grieser, D. Habs, R. Repnow, D. Schwalm, A. Wolf, and S. L. Guberman, "Dissociative recombination of cold OH^+: Evidence for indirect recombination through excited core Rydberg states", *Physical Review A*, vol. 53, p. 644, Feb. 1996. (page 24, 60)

[50] Z. Amitay, D. Zajfman, P. Forck, U. Hechtfischer, B. Seidel, M. Grieser, D. Habs, R. Repnow, D. Schwalm, and A. Wolf, "Dissociative recombination of CH^+: Cross section and final states", *Physical Review A*, vol. 54, pp. 4032–4050, Nov. 1996. (page 24, 53, 60, 67)

[51] S. L. Guberman, "Dissociative recombination without a curve crossing", *Physical Review A*, vol. 49, pp. R4277–R4280, June 1994. (page 24)

[52] E. E. Ferguson, F. C. Fehsenfeld, D. B. Dunkin, A. L. Schmeltekopf, and H. I. Schjff, "Laboratory studies of helium ion loss processes of interest in the ionosphere", *Planetary and Space Science*, vol. 12, pp. 1169–1171, Dec. 1964. (page 25)

[53] E. E. Ferguson, F. C. Fehsenfeld, and A. L. Schmeltekopf, "Flowing Afterglow Measurements of Ion-Neutral Reactions", *Advances in Atomic and Molecular Physics*, vol. 5, pp. 1–56, 1969. (page 25)

[54] V. M. Bierbaum, "Go with the flow: Fifty years of innovation and ion chemistry using the flowing afterglow", *International Journal of Mass Spectrometry*, vol. 377, pp. 456–466, Feb. 2015. (page 25)

[55] D. Smith and P. Španěl, "The SIFT and FALP techniques; applications to ionic and electronic reactions studies and their evolution to the SIFT-MS and FA-MS analytical methods", *International Journal of Mass Spectrometry*, vol. 377, pp. 467–478, Feb. 2015. (page 25)

[56] E. M. McMillan, "The Synchrotron - A Proposed High Energy Particle Accelerator", *Physical Review*, vol. 68, pp. 143–144, Sept. 1945. (page 26)

[57] M. L. Oliphant, J. S. Gooden, and G. S. Hide, "The acceleration of charged particles to very high energies", *Proceedings of the Physical Society*, vol. 59, pp. 666–677, July 1947. (page 26)

[58] J. Marriner, "Stochastic cooling overview", *Nuclear Instruments and Methods in Physics Research Section A: Accelerators, Spectrometers, Detectors and Associated Equipment*, vol. 532, pp. 11–18, Oct. 2004. (page 26, 32)

[59] S. Schröder, R. Klein, N. Boos, M. Gerhard, R. Grieser, G. Huber, A. Karafillidis, M. Krieg, N. Schmidt, T. Kühl, R. Neumann, V. Balykin, M. Grieser, D. Habs, E. Jaeschke, D. Krämer, M. Kristensen, M. Music, W. Petrich, D. Schwalm, P. Sigray, M. Steck, B. Wanner, and A. Wolf, "First laser cooling of relativistic ions in a storage ring", *Physical Review Letters*, vol. 64, pp. 2901–2904, June 1990. (page 26, 32)

[60] M. Grieser, Y. A. Litvinov, R. Raabe, K. Blaum, Y. Blumenfeld, P. A. Butler, F. Wenander, P. J. Woods, M. Aliotta, A. Andreyev, A. Artemyev, D. Atanasov, T. Aumann, D. Balabanski, A. Barzakh, L. Batist, A. P. Bernardes, D. Bernhardt, J. Billowes, S. Bishop, M. Borge, I. Borzov, F. Bosch, A. J. Boston, C. Brandau, W. Catford, R. Catherall, J. Cederkäll, D. Cullen, T. Davinson, I. Dillmann, C. Dimopoulou, G. Dracoulis, C. E. Düllmann, P. Egelhof, A. Estrade, D. Fischer, K. Flanagan, L. Fraile, M. A. Fraser, S. J. Freeman, H. Geissel, J. Gerl, P. Greenlees, R. E. Grisenti, D. Habs, R. von Hahn, S. Hagmann, M. Hausmann, J. J. He, M. Heil, M. Huyse, D. Jenkins, A. Jokinen, B. Jonson, D. T. Joss, Y. Kadi, N. Kalantar-Nayestanaki, B. P. Kay, O. Kiselev, H. J. Kluge, M. Kowalska, C. Kozhuharov, S. Kreim, T. Kröll, J. Kurcewicz, M. Labiche, R. C. Lemmon, M. Lestinsky, G. Lotay, X. W. Ma, M. Marta, J. Meng, D. Mücher, I. Mukha, A. Müller, A. S. J. Murphy, G. Neyens, T. Nilsson, C. Nociforo, W. Nörtershäuser, R. D. Page, M. Pasini, N. Petridis, N. Pietralla, M. Pfützner, Z. Podolyák, P. Regan, M. W. Reed, R. Reifarth, P. Reiter, R. Repnow, K. Riisager, B. Rubio, M. S. Sanjari, D. W. Savin, C. Scheidenberger, S. Schippers, D. Schneider, R. Schuch, D. Schwalm, L. Schweikhard, D. Shubina, E. Siesling, H. Simon, J. Simpson, J. Smith, K. Sonnabend, M. Steck, T. Stora, T. Stöhlker, B. Sun, A. Surzhykov, F. Suzaki, O. Tarasov, S. Trotsenko, X. L. Tu, P. Van Duppen, C. Volpe, D. Voulot, P. M. Walker, E. Wildner, N. Winckler, D. F. A. Winters, A. Wolf, H. S. Xu, A. Yakushev, T. Yamaguchi, Y. J. Yuan, Y. H. Zhang, and K. Zuber, "Storage ring at HIE-ISOLDE: Technical design report", *The European Physical Journal Special Topics*, vol. 207, pp. 1–117, May 2012. (page 26, 35, 37)

[61] S. Moller, "ASTRID-a storage ring for ions and electrons", in , *Conference Record of the 1991 IEEE Particle Accelerator Conference, 1991. Accelerator Science and Technology*, pp. 2811–2813 vol.5, May 1991. (page 27)

[62] B. Franzke, K. Beckert, F. Bosch, H. Eickhoff, B. Franczak, A. Gruber, O. Klepper, F. Nolden, P. Raabe, H. Reich, P. Spadtke, M. Steck, and J. Struckmeier, "Heavy ion beam accumulation, cooling, and experiments at

the ESR", in *Particle Accelerator Conference, 1993., Proceedings of the 1993*, pp. 1645–1649 vol.3, May 1993. (page 27)

[63] K. Abrahamsson, G. Andler, L. Bagge, E. Beebe, P. Carlé, H. Danared, S. Egnell, K. Ehrnstén, M. Engström, C. J. Herrlander, J. Hilke, J. Jeansson, A. Källberg, S. Leontein, L. Liljeby, A. Nilsson, A. Paal, K. G. Rensfelt, U. Rosengård, A. Simonsson, A. Soltan, J. Starker, M. af Ugglas, and A. Filevich, "CRYRING — a synchrotron, cooler and storage ring", *Nuclear Instruments and Methods in Physics Research Section B: Beam Interactions with Materials and Atoms*, vol. 79, pp. 269–272, June 1993. (page 27)

[64] M. Plotkin, "The Brookhaven electron analogue, 1953–1957", tech. rep., Brookhaven National Lab., 1991. (page 27)

[65] S. P. Møller, "ELISA, and electrostatic storage ring for atomic physics", *Nuclear Instruments and Methods in Physics Research Section A: Accelerators, Spectrometers, Detectors and Associated Equipment*, vol. 394, pp. 281–286, July 1997. (page 27)

[66] S. P. Møller and U. V. Pedersen, "Small Electrostatic Storage Rings; also for Highly Charged Ions?", *Physica Scripta*, vol. 2001, p. 105, Jan. 2001. (page 27)

[67] T. Tanabe, K. Noda, and I. Watanabe, "An electrostatic storage ring for molecular science", in *Proceedings of EPAC 2000*, (Vienna, Austria), 2000. (page 27)

[68] T. Tanabe, K. Chida, K. Noda, and I. Watanabe, "An electrostatic storage ring for atomic and molecular science", *Nuclear Instruments and Methods in Physics Research Section A: Accelerators, Spectrometers, Detectors and Associated Equipment*, vol. 482, pp. 595–605, Apr. 2002. (page 27)

[69] T. Tanabe, K. Noda, and E. Syresin, "An electrostatic storage ring with a merging electron beam device at KEK", *Nuclear Instruments and Methods in Physics Research Section A: Accelerators, Spectrometers, Detectors and Associated Equipment*, vol. 532, pp. 105–110, Oct. 2004. (page 27)

[70] K. E. Stiebing, V. Alexandrov, R. Dörner, S. Enz, N. Y. Kazarinov, T. Kruppi, A. Schempp, H. Schmidt Böcking, M. Völp, P. Ziel, M. Dworak, and W. Dilfer, "FLSR – The Frankfurt low energy storage ring", *Nuclear Instruments and Methods in Physics Research Section A: Accelerators, Spectrometers, Detectors and Associated Equipment*, vol. 614, pp. 10–16, Feb. 2010. (page 27)

[71] J. Bernard, G. Montagne, R. Brédy, B. Terpend-Ordacière, A. Bourgey, M. Kerleroux, L. Chen, H. T. Schmidt, H. Cederquist, and S. Martin, "A "tabletop" electrostatic ion storage ring: Mini-Ring", *Review of Scientific Instruments*, vol. 79, p. 075109, July 2008. (page 27)

[72] S. Jinno, T. Takao, Y. Omata, A. Satou, H. Tanuma, T. Azuma, H. Shiromaru, K. Okuno, N. Kobayashi, and I. Watanabe, "TMU electrostatic ion storage ring designed for operation at liquid nitrogen temperature", *Nuclear Instruments and Methods in Physics Research Section A: Accelerators, Spectrometers, Detectors and Associated Equipment*, vol. 532, pp. 477–482, Oct. 2004. (page 27)

[73] Y. Nakano, W. Morimoto, T. Majima, J. Matsumoto, H. Tanuma, H. Shiromaru, and T. Azuma, "A cryogenic electrostatic storage ring project at RIKEN", *Journal of Physics: Conference Series*, vol. 388, p. 142027, Nov. 2012. (page 27)

[74] R. D. Thomas, H. T. Schmidt, J. Gurell, N. Haag, A. I. S. Holm, H. A. B. Johansson, G. Källersjö, M. Larsson, S. Mannervik, D. Misra, A. Orban, P. Reinhed, K.-G. Rensfelt, S. Rosén, F. Seitz, J. Weimer, H. Zettergren, G. Andler, H. Danared, S. Das, L. Liljeby, M. Björkhage, M. Blom, L. Brännholm, P. Halldén, F. Hellberg, A. Källberg, S. Leontein, P. Löfgren, B. Malm, A. Paál, A. Simonsson, and H. Cederquist, "DESIREE: a unique cryogenic electrostatic storage ring for merged ion-beams studies", *Journal of Physics: Conference Series*, vol. 300, p. 012011, July 2011. (page 27)

[75] H. T. Schmidt, R. D. Thomas, M. Gatchell, S. Rosén, P. Reinhed, P. Löfgren, L. Brännholm, M. Blom, M. Björkhage, E. Bäckström, J. D. Alexander, S. Leontein, D. Hanstorp, H. Zettergren, L. Liljeby, A. Källberg, A. Simonsson, F. Hellberg, S. Mannervik, M. Larsson, W. D. Geppert, K. G. Rensfelt, H. Danared, A. Paál, M. Masuda, P. Halldén, G. Andler, M. H. Stockett, T. Chen, G. Källersjö, J. Weimer, K. Hansen, H. Hartman, and H. Cederquist, "First storage of ion beams in the Double Electrostatic Ion-Ring Experiment: DESIREE", *Review of Scientific Instruments*, vol. 84, p. 055115, May 2013. (page 27, 144)

[76] M. Lange, M. Froese, S. Menk, J. Varju, R. Bastert, K. Blaum, J. R. C. López Urrutia, F. Fellenberger, M. Grieser, R. von Hahn, O. Heber, K.-U. Kühnel, F. Laux, D. A. Orlov, M. L. Rappaport, R. Repnow, C. D. Schröter, D. Schwalm, A. Shornikov, T. Sieber, Y. Toker, J. Ullrich, A. Wolf, and D. Zajfman, "A cryogenic electrostatic trap for long-time storage of keV ion beams", *Review of Scientific Instruments*, vol. 81, p. 055105, May 2010. (page 28, 42, 43)

[77] T. Andersen, L. H. Andersen, P. Balling, H. K. Haugen, P. Hvelplund, W. W. Smith, and K. Taulbjerg, "Metastable-ion lifetime studies utilizing a heavy-ion storage ring: Measurements on He^-", *Physical Review A*, vol. 47, pp. 890–896, Feb. 1993. (page 28)

[78] S. M. Trujillo, R. H. Neynaber, and E. W. Rothe, "Merging Beams, A Differ-

ent Approach to Collision Cross Section Measurements," *Review of Scientific Instruments*, vol. 37, pp. 1655–1661, Dec. 1966. (page 30)

[79] V. A. Belyaev, B. G. Brezhnev, and E. M. Erastov, "Measurement of the Cross Sections of Ion-atom Collisions at Low Energies by the Method of Overtaking Beams", *ZhETF Pisma Redaktsiiu*, vol. 3, p. 321, Apr. 1966. (page 30)

[80] R. A. Phaneuf, C. C. Havener, G. H. Dunn, and A. Müller, "Merged-beams experiments in atomic and molecular physics", *Reports on Progress in Physics*, vol. 62, p. 1143, July 1999. (page 30, 31)

[81] G. I. Budker and A. N. Skrinskiĭ, "Electron cooling and new possibilities in elementary particle physics", *Soviet Physics Uspekhi*, vol. 21, p. 277, Apr. 1978. (page 32)

[82] A. Burov, V. Danilov, P. Colestock, and Y. Derbenev, "Electron cooling for RHIC", *Nuclear Instruments and Methods in Physics Research Section A: Accelerators, Spectrometers, Detectors and Associated Equipment*, vol. 441, pp. 271–273, Feb. 2000. (page 32)

[83] S. Krohn, Z. Amitay, A. Baer, D. Zajfman, M. Lange, L. Knoll, J. Levin, D. Schwalm, R. Wester, and A. Wolf, "Electron-induced vibrational deexcitation of h_2^+", *Physical Review A*, vol. 62, p. 032713, Aug. 2000. (page 32)

[84] D. Schwalm, D. Shafir, S. Novotny, H. Buhr, S. Altevogt, A. Faure, M. Grieser, A. G. Harvey, O. Heber, J. Hoffmann, H. Kreckel, L. Lammich, O. Motapon, I. Nevo, H. B. Pedersen, H. Rubinstein, I. F. Schneider, J. Tennyson, F. O. W. Tamo, A. Wolf, and D. Zajfman, "Rotational Cooling of HD^+ by Superelastic Collisions with Electrons", *Journal of Physics: Conference Series*, vol. 300, p. 012006, July 2011. (page 32, 78)

[85] C. Krantz, *Intense electron beams from GaAs photocathodes as a tool for molecular and atomic physics*. PhD, Ruprecht-Karls-Universität, Heidelberg, 2009. (page 32, 44)

[86] S. Kieslich, S. Schippers, W. Shi, A. Müller, G. Gwinner, M. Schnell, A. Wolf, E. Lindroth, and M. Tokman, "Determination of the $2s$-$2p$ excitation energy of lithiumlike scandium using dielectronic recombination", *Physical Review A*, vol. 70, p. 042714, Oct. 2004. (page 33)

[87] O. Novotný, A. Becker, H. Buhr, C. Domesle, W. Geppert, M. Grieser, C. Krantz, H. Kreckel, R. Repnow, D. Schwalm, K. Spruck, J. Stützel, B. Yang, A. Wolf, and D. W. Savin, "Dissociative Recombination Measurements of HCl^+ Using an Ion Storage Ring", *The Astrophysical Journal*, vol. 777, p. 54, Nov. 2013. (page 33, 37, 60, 65, 66, 69, 70, 73, 74)

[88] A. Lampert, A. Wolf, D. Habs, J. Kenntner, G. Kilgus, D. Schwalm, M. S. Pindzola, and N. R. Badnell, "High-resolution measurement of the dielectronic recombination of fluorinelike selenium ions", *Physical Review A*, vol. 53, pp. 1413–1423, Mar. 1996. (page 33, 70)

[89] O. Novotný, A. Becker, H. Buhr, C. Domesle, W. Geppert, M. Grieser, C. Krantz, H. Kreckel, R. Repnow, D. Schwalm, K. Spruck, J. Stützel, B. Yang, A. Wolf, and D. W. Savin, "Erratum: "Dissociative Recombination Measurements of HCl+ Using an Ion Storage Ring" (2013, ApJ, 777, 54)", *The Astrophysical Journal*, vol. 810, no. 2, p. 169, 2015. (page 33)

[90] A. Müller, "Plasma rate coefficients for highly charged ion–electron collisions: new experimental access via ion storage rings", *International Journal of Mass Spectrometry*, vol. 192, pp. 9–22, Sept. 1999. (page 34)

[91] P. Baumann, M. Blum, A. Friedrich, C. Geyer, M. Grieser, B. Holzer, E. Jaeschke, D. Krämer, C. Martin, K. Matl, R. Mayer, W. Ott, B. Povh, R. Repnow, M. Steck, E. Steffens, and W. Arnold, "The Heidelberg Heavy Ion Test Storage Ring TSR", *Nuclear Instruments and Methods in Physics Research A*, vol. 268, pp. 531–537, May 1988. (page 35)

[92] E. Jaeschke, D. Kramer, G. Bisoffi, M. Blum, A. Friedrich, C. Geyer, M. Grieser, D. Habs, H. W. Heyng, B. Holzer, R. Ihde, M. Jung, K. Matl, W. Ott, B. Povh, R. Repnow, F. Schmitt, M. Steck, E. Steffens, W. Arnold, R. Neumann, and A. Noda, "The Heidelberg test storage ring for heavy ions TSR", *Proceedings of 1th European Particle Accelerator Conference (EPAC 88)*, 1988. (page 35)

[93] D. Habs, W. Baumann, J. Berger, P. Blatt, A. Faulstich, P. Krause, G. Kilgus, R. Neumann, W. Petrich, R. Stokstad, D. Schwalm, E. Szmola, K. Welti, A. Wolf, S. Zwickler, E. Jaeschke, D. Krämer, G. Bisoffi, M. Blum, A. Friedrich, C. Geyer, M. Grieser, H. W. Heyng, B. Holzer, R. Ihde, M. Jung, K. Matl, W. Ott, B. Povh, R. Repnow, M. Steck, E. Steffens, D. Dutta, T. Kühl, D. Marx, S. Schröder, M. Gerhard, R. Grieser, G. Huber, R. Klein, M. Krieg, N. Schmidt, R. Schuch, J. F. Babb, L. Spruch, W. Arnold, and A. Noda, "First experiments with the heidelberg test storage ring TSR", *Nuclear Instruments and Methods in Physics Research B*, vol. 43, pp. 390–410, Sept. 1989. (page 35)

[94] R. Repnow, "Progress and upgrading of the Heidelberg high current injector", *Pramana*, vol. 59, pp. 835–848, Nov. 2002. (page 35, 60)

[95] M. Grieser, D. Habs, R. v Hahn, C. Ellert, C. M. Kleffner, J. Liebmann, R. Repnow, D. Schwalm, E. Jaeschke, and S. Papureanu, "Recent developments at the Heidelberg Heavy Ion Cooler Storage Ring TSR", in *Proceedings of the 3rd EPAC*, (Berlin, Germany), 1992. (page 35)

[96] R. Schuch, "Atomic physics at the Heidelberg Test Storage Ring (TSR)", *Nuclear Instruments and Methods in Physics Research B*, vol. 24, pp. 11–17, Apr. 1987. (page 36)

[97] D. A. Orlov, M. Lestinsky, F. Sprenger, D. Schwalm, A. S. Terekhov, and A. Wolf, "Ultra-Cold Electron Beams for the Heidelberg TSR and CSR", *AIP Conference Proceedings*, vol. 821, pp. 478–487, Mar. 2006. (page 36)

[98] M. Steck, G. Bisoffi, M. Blum, A. Friedrich, C. Geyer, M. Grieser, B. Holzer, E. Jaeschke, M. Jung, D. Krämer, K. Matl, W. Ott, and R. Repnow, "Electron cooling of heavy ions", *Nuclear Instruments and Methods in Physics Research Section A: Accelerators, Spectrometers, Detectors and Associated Equipment*, vol. 287, pp. 324–327, Feb. 1990. (page 37)

[99] H. Danared, G. Andler, L. Bagge, C. J. Herrlander, J. Hilke, J. Jeansson, A. Källberg, A. Nilsson, A. Paál, K. G. Rensfelt, U. Rosengård, J. Starker, and M. af Ugglas, "Electron Cooling with an Ultracold Electron Beam", *Physical Review Letters*, vol. 72, pp. 3775–3778, June 1994. (page 37)

[100] C. Krantz, D. A. Orlov, J. Hoffmann, M. Lestinsky, O. Novotny, A. S. Jaroshevich, A. S. Terekhov, and A. Wolf, "An ultra cold photoelectron gun for the Heidelberg TSR target section", *Journal of Physics Conference Series*, vol. 192, p. 012025, Nov. 2009. (page 37, 60)

[101] S. Pastuszka, U. Schramm, M. Grieser, C. Broude, R. Grimm, D. Habs, J. Kenntner, H. J. Miesner, T. Schüβler, D. Schwalm, and A. Wolf, "Electron cooling and recombination experiments with an adiabatically expanded electron beam", *Nuclear Instruments and Methods in Physics Research Section A: Accelerators, Spectrometers, Detectors and Associated Equipment*, vol. 369, pp. 11–22, Jan. 1996. (page 37)

[102] K. Rinn, A. Müller, H. Eichenauer, and E. Salzborn, "Development of single-particle detectors for keV ions", *Review of Scientific Instruments*, vol. 53, pp. 829–837, June 1982. (page 37)

[103] F. Sprenger, M. Lestinsky, D. A. Orlov, D. Schwalm, and A. Wolf, "The high-resolution electron–ion collision facility at TSR", *Nuclear Instruments and Methods in Physics Research Section A: Accelerators, Spectrometers, Detectors and Associated Equipment*, vol. 532, pp. 298–302, Oct. 2004. (page 37, 64)

[104] H. Buhr, *Electron collisions and internal excitation in stored molecular ion beams*. PhD, Ruprecht-Karls Universität, Heidelberg, 2006. Zsfassung in dt. Sprache. (page 38)

[105] J. Stützel, *Fragmentation of small multi-electron molecular ions in cold electron collisions*. PhD, Ruprecht-Karls Universität, Heidelberg, 2011. Zsfassung in dt. und engl. Sprache. (page 38)

[106] H. Buhr, M. B. Mendes, O. Novotný, D. Schwalm, M. H. Berg, D. Bing, O. Heber, C. Krantz, D. A. Orlov, M. L. Rappaport, T. Sorg, J. Stützel, J. Varju, A. Wolf, and D. Zajfman, "Energy-sensitive imaging detector applied to the dissociative recombination of D_2H^+", *Physical Review A*, vol. 81, p. 062702, June 2010. (page 38, 98)

[107] M. B. Mendes, *Molecular fragmentation by recombination with cold electrons studied with a mass sensitive imaging detector*. PhD, Ruprecht-Karls Universität, Heidelberg, 2010. Zsfassung in dt. und engl. Sprache. (page 38, 98)

[108] K. Spruck, A. Becker, F. Fellenberger, M. Grieser, R. von Hahn, V. Klinkhamer, O. Novotný, S. Schippers, S. Vogel, A. Wolf, and C. Krantz, "An efficient, movable single-particle detector for use in cryogenic ultra-high vacuum environments", *Review of Scientific Instruments*, vol. 86, p. 023303, Feb. 2015. (page 41, 46, 113, 123, 128)

[109] M. Grieser, A. Becker, K. Blaum, S. George, C. Krantz, S. Vogel, A. Wolf, and R. von Hahn, "The Status of the Diagnostic System at the Cryogenic Storage Ring CSR", *Proceedings of 5th International Particle Accelerator Conference (IPAC)*, p. THPME121, July 2014. (page 41, 42, 46, 123, 135)

[110] S. Vogel, *in preparation*. PhD, Ruprecht-Karls Universität, Heidelberg, 2016. (page 41, 44, 96, 128, 129)

[111] K. Kruglov, L. Weissman, P. V. den Bergh, A. Andreyev, M. Huyse, and P. V. Duppen, "A beam diagnostic system for low-intensity radioactive beams", *Nuclear Instruments and Methods in Physics Research Section A: Accelerators, Spectrometers, Detectors and Associated Equipment*, vol. 441, pp. 595–604, Mar. 2000. (page 42)

[112] K. Kruglov, L. Weissman, P. Van den Bergh, M. Huyse, and P. Van Duppen, "A beam diagnostic system for REX-ISOLDE", *Nuclear Physics A*, vol. 701, pp. 193–198, Apr. 2002. (page 42)

[113] T. Sieber, H. Fadil, M. Grieser, R. von Hahn, and A. Wolf, "Beam Diagnostics Development for the Cryogenic Storage Ring CSR", in *Proceedings of DIPAC 2007*, (Venice, Italy), pp. 283–285, 2007. (page 42)

[114] R. von Hahn, V. Andrianarijaona, J. R. Crespo Lopez-Urrutia, H. Fadil, M. Grieser, C. Haberstroh, V. Mallinger, D. A. Orlov, H. Quack, M. Rappaport, C. D. Schroter, D. Schwalm, J. Ullrich, T. Weber, A. Wolf, and D. Zajfman, "Cryogenic Concept for the Low-energy Electrostatic Cryogenic Storage Ring (CSR) at MPI-K in Heidelberg", *AIP Conference Proceedings*, vol. 823, pp. 1187–1193, Apr. 2006. (page 43)

[115] R. von Hahn, F. Berg, K. Blaum, J. Crespo Lopez-Urrutia, F. Fellenberger, M. Froese, M. Grieser, C. Krantz, K.-U. Kühnel, M. Lange, S. Menk, F. Laux,

D. A. Orlov, R. Repnow, C. D. Schröter, A. Shornikov, T. Sieber, J. Ullrich, A. Wolf, M. Rappaport, and D. Zajfman, "The electrostatic Cryogenic Storage Ring CSR - Mechanical concept and realization", *Nuclear Instruments and Methods in Physics Research Section B: Beam Interactions with Materials and Atoms*, 2011. (page 43)

[116] F. Fellenberger, *Aufbau und Charakterisierung der ersten Ecke des kryogenen elektrostatischen Speicherrings CSR.* PhD, Ruprecht-Karls Universität, Heidelberg, 2012. (page 43)

[117] S. Menk, *A Cryogenic Trap for Fast Ion Beams.* Diploma, Ruprecht-Karls Universität, Heidelberg, 2009. (page 43)

[118] Ruag Space GmbH, "Datasheet brochure for vacuum thermal insulation", 2012. (page 43)

[119] M. Grieser, private communication, 2015. (page 44, 96)

[120] C. Krantz, F. Berg, K. Blaum, F. Fellenberger, M. Froese, M. Grieser, R. von Hahn, M. Lange, F. Laux, S. Menk, R. Repnow, A. Shornikov, and A. Wolf, "The Cryogenic Storage Ring and its application to molecular ion recombination physics", *Journal of Physics: Conference Series*, vol. 300, p. 012010, July 2011. (page 44)

[121] A. P. O'Connor, H. Bruhns, F. Grussie, T. P. Koenning, K. A. Miller, N. de Ruette, J. Stützel, D. W. Savin, X. Urbain, and H. Kreckel, "Generation of neutral atomic beams utilizing photodetachment by high power diode laser stacks", *arXiv:1509.00169 [physics]*, Sept. 2015. (page 44, 46)

[122] A. Shornikov, D. Orlov, C. Krantz, A. Jaroshevich, and A. Wolf, "Maximum intensity, transmission limited cold electron beams from GaAs photocathode in the eV and sub-eV kinetic energy range", *Physical Review Special Topics - Accelerators and Beams*, vol. 17, p. 042802, Mar. 2014. (page 44)

[123] H. Fadil, D. A. Orlov, M. Grieser, and A. Wolf, "Design of a Low Energy Electron Cooler for the Heidelberg CSR", *Proc. EPAC06*, vol. Edingburg, Scotland, pp. 1630–1632, 2006. (page 45)

[124] C. Meyer, *in preparation.* PhD, Ruprecht-Karls Universität, Heidelberg, 2017. (page 45, 47)

[125] K. Spruck, *Dielectronic Recombination Experiments with Tungsten Ions at the Test Storage Ring and Development of a Single-Particle Detector at the Cryogenic Storage Ring.* PhD, Justus Liebig University, Giessen, 2015. (page 46, 128, 151)

[126] A. T. J. B. Eppink and D. H. Parker, "Velocity map imaging of ions and electrons using electrostatic lenses: Application in photoelectron and photofragment ion imaging of molecular oxygen", *Review of Scientific Instruments*, vol. 68, pp. 3477–3484, Sept. 1997. (page 48)

[127] R. Dörner, V. Mergel, O. Jagutzki, L. Spielberger, J. Ullrich, R. Moshammer, and H. Schmidt-Böcking, "Cold Target Recoil Ion Momentum Spectroscopy: a 'momentum microscope' to view atomic collision dynamics", *Physics Reports*, vol. 330, pp. 95–192, June 2000. (page 48)

[128] J. Ullrich, R. Moshammer, A. Dorn, R. D rner, L. P. H. Schmidt, and H. Schmidt-B cking, "Recoil-ion and electron momentum spectroscopy: reaction-microscopes", *Reports on Progress in Physics*, vol. 66, pp. 1463–1545, Sept. 2003. (page 48)

[129] J. Ullrich, V. Shevelko, G. F. Drake, and G. Ecker, eds., *Many-Particle Quantum Dynamics in Atomic and Molecular Fragmentation*, vol. 35 of *Springer Series on Atomic, Optical, and Plasma Physics*. Berlin, Heidelberg: Springer Berlin Heidelberg, 2003. (page 48)

[130] D. Zajfman, Z. Amitay, C. Broude, P. Forck, B. Seidel, M. Grieser, D. Habs, D. Schwalm, and A. Wolf, "Measurement of Branching Ratios for the Dissociative Recombination of Cold HD^+ Using Fragment Imaging", *Physical Review Letters*, vol. 75, pp. 814–817, July 1995. (page 48)

[131] S. Novotny, *Fast-beam molecular fragmentation imaging using a high-speed gated camera system*. Diploma, Ruprecht-Karls Universität, Heidelberg, 2004. (page 53, 99)

[132] S. Novotny, *Fragmentation of molecular ions in slow electron collisions*. PhD, Ruprecht-Karls Universität, Heidelberg, 2008. Zsfassung in dt. Sprache. (page 53, 76)

[133] A. Kramida, Y. Ralchenko, J. Reader, and NIST ASD Team, "NIST Atomic Spectra Database (version 5.2) Available: http://physics.nist.gov/asd", online, National Institute of Standards and Technology, Gaithersburg, MD., 2014. (page 57)

[134] W. C. Martin, R. Zalubas, and A. Musgrove, "Energy Levels of Sulfur, S I Through S XVI", *Journal of Physical and Chemical Reference Data*, vol. 19, pp. 821–880, July 1990. (page 57, 58)

[135] E. P. L. Hunter and S. G. Lias, "Evaluated Gas Phase Basicities and Proton Affinities of Molecules: An Update", *Journal of Physical and Chemical Reference Data*, vol. 27, pp. 413–656, May 1998. (page 57, 79, 93)

[136] J. Rostas, M. Horani, J. Brion, D. Daumont, and J. Malicet, "Electronic spectra of the SH^+ and SD^+ molecular ions", *Molecular Physics*, vol. 52, no. 6, pp. 1431–1452, 1984. (page 57, 79, 93)

[137] J. K. Park and H. Sun, "Ab initio effective Hamiltonian calculations on the valence states of SH and SH^+", *Chemical Physics Letters*, vol. 194, pp. 485–491, July 1992. (page 57, 58, 59, 61, 74, 93)

[138] C. A. D. Lange, "Rydberg State Spectroscopy Of The SH Radical," in *The Role of Rydberg States in Spectroscopy and Photochemistry* (C. Sándorfy, ed.), no. 20 in Understanding Chemical Reactivity, pp. 457–478, Springer Netherlands, Jan. 1999. (page 59, 60, 68)

[139] O. Novotný, M. Berg, D. Bing, H. Buhr, W. Geppert, M. Grieser, F. Grussie, C. Krantz, M. B. Mendes, C. Nordhorn, R. Repnow, D. Schwalm, B. Yang, A. Wolf, and D. W. Savin, "Dissociative Recombination Measurements of NH^+ Using an Ion Storage Ring", *The Astrophysical Journal*, vol. 792, p. 132, Sept. 2014. (page 58, 70)

[140] A. Wolf, "Heavy-Ion Storage Rings", in *Atomic Physics with Heavy Ions* (H. F. Beyer and V. P. Shevelko, eds.), vol. 26 of *Springer Series on Atoms+Plasmas*, pp. 3–29, Springer Berlin Heidelberg, 1999. (page 60)

[141] O. Novotný, H. Buhr, J. Stu̇tzel, M. B. Mendes, M. H. Berg, D. Bing, M. Froese, M. Grieser, O. Heber, B. Jordon-Thaden, C. Krantz, M. Lange, M. Lestinsky, S. Novotny, S. Menk, D. A. Orlov, A. Petrignani, M. L. Rappaport, A. Shornikov, D. Schwalm, D. Zajfman, and A. Wolf, "Fragmentation Channels in Dissociative Electron Recombination with Hydronium and Other Astrophysically Important Species", *The Journal of Physical Chemistry A*, vol. 114, no. 14, pp. 4870–4874, 2010. (page 60, 99)

[142] J. Brzozowski, N. Elander, P. Erman, and M. Lyyra, "Lifetimes of Excited Levels in Some Important Ion-molecules Part I: NH^+, OH^+, and SH^+", *Physica Scripta*, vol. 10, pp. 241–243, Nov. 1974. (page 61)

[143] J. Senekowitsch, H.-J. Werner, P. Rosmus, E.-A. Reinsch, and S. V. ONeil, "Abinitio calculations of radiative transition probabilities in SH, SH^+, and SH^-", *The Journal of Chemical Physics*, vol. 83, pp. 4661–4667, Nov. 1985. (page 61, 62)

[144] Z. Amitay, D. Zajfman, and P. Forck, "Rotational and vibrational lifetime of isotopically asymmetrized homonuclear diatomic molecular ions", *Physical Review A*, vol. 50, pp. 2304–2308, Sept. 1994. (page 61)

[145] D. Shafir, S. Novotny, H. Buhr, S. Altevogt, A. Faure, M. Grieser, A. G. Harvey, O. Heber, J. Hoffmann, H. Kreckel, L. Lammich, I. Nevo, H. B. Pedersen, H. Rubinstein, I. F. Schneider, D. Schwalm, J. Tennyson, A. Wolf,

and D. Zajfman, "Rotational Cooling of HD^+ Molecular Ions by Superelastic Collisions with Electrons", *Physical Review Letters*, vol. 102, p. 223202, June 2009. (page 62)

[146] K. Unser, "A Toroidal DC Beam Current Transformer with High Resolution", *IEEE Transactions on Nuclear Science*, vol. 28, pp. 2344–2346, June 1981. (page 64)

[147] O. Novotný, N. R. Badnell, D. Bernhardt, M. Grieser, M. Hahn, C. Krantz, M. Lestinsky, A. Müller, R. Repnow, S. Schippers, A. Wolf, and D. W. Savin, "Electron-Ion Recombination of Fe XII Forming Fe XI: Laboratory Measurements and Theoretical Calculations", *The Astrophysical Journal*, vol. 753, p. 57, July 2012. (page 65)

[148] H. Kreckel, O. Novotný, K. N. Crabtree, H. Buhr, A. Petrignani, B. A. Tom, R. D. Thomas, M. H. Berg, D. Bing, M. Grieser, C. Krantz, M. Lestinsky, M. B. Mendes, C. Nordhorn, R. Repnow, J. Stützel, A. Wolf, and B. J. McCall, "High-resolution storage-ring measurements of the dissociative recombination of H_3^+ using a supersonic expansion ion source", *Physical Review A*, vol. 82, p. 042715, Oct. 2010. (page 65)

[149] H. B. Pedersen, H. Buhr, S. Altevogt, V. Andrianarijaona, H. Kreckel, L. Lammich, N. de Ruette, E. M. Staicu-Casagrande, D. Schwalm, D. Strasser, X. Urbain, D. Zajfman, and A. Wolf, "Dissociative recombination and low-energy inelastic electron collisions of the helium dimer ion", *Physical Review A*, vol. 72, p. 012712, July 2005. (page 65)

[150] J. R. Mowat, H. Danared, G. Sundström, M. Carlson, L. H. Andersen, L. Vejby-Christensen, M. Af Ugglas, and M. Larsson, "High-Resolution, Low-Energy Dissociative Recombination Spectrum of $^3HeH^+$", *Physical Review Letters*, vol. 74, pp. 50–53, Jan. 1995. (page 70)

[151] J. Woodall, M. Agúndez, A. J. Markwick-Kemper, and T. J. Millar, "The UMIST database for astrochemistry 2006", *Astronomy and Astrophysics*, vol. 466, pp. 1197–1204, May 2007. (page 73)

[152] F. Hellberg, V. Zhaunerchyk, A. Ehlerding, W. D. Geppert, M. Larsson, R. D. Thomas, M. E. Bannister, E. Bahati, C. R. Vane, F. Österdahl, P. Hlavenka, and M. Af Ugglas, "Investigating the breakup dynamics of dihydrogen sulfide ions recombining with electrons," *Journal of Chemical Physics*, vol. 122, p. 4314, June 2005. (page 75)

[153] G. W. Fraser, J. F. Pearson, and J. E. Lees, "Dark noise in microchannel plate X-ray detectors", *Nuclear Instruments and Methods in Physics Research Section A: Accelerators, Spectrometers, Detectors and Associated Equipment*, vol. 254, pp. 447–462, Feb. 1987. (page 87, 137, 153)

[154] G. Ventura and M. Perfetti, *Thermal Properties of Solids at Room and Cryogenic Temperatures*. International Cryogenics Monograph Series, Netherlands: Springer, 2014. (page 95, 121)

[155] M. J. Jensen, R. C. Bilodeau, C. P. Safvan, K. Seiersen, L. H. Andersen, H. B. Pedersen, and O. Heber, "Dissociative Recombination of H_3O^+, HD_2O^+, and D_3O^+", *The Astrophysical Journal*, vol. 543, p. 764, Nov. 2000. (page 98)

[156] S. Datz, M. Larsson, C. Stromholm, G. Sundström, V. Zengin, H. Danared, A. Källberg, and M. af Ugglas, "Dissociative recombination of H_2D^+: Cross sections, branching fractions, and isotope effects", *Physical Review A*, vol. 52, pp. 2901–2909, Oct. 1995. (page 98)

[157] L. H. Andersen, O. Heber, D. Kella, H. B. Pedersen, L. Vejby-Christensen, and D. Zajfman, "Production of Water Molecules from Dissociative Recombination of H_3O^+ with Electrons", *Physical Review Letters*, vol. 77, pp. 4891–4894, Dec. 1996. (page 98)

[158] J. F. Ziegler, M. D. Ziegler, and J. P. Biersack, "SRIM – The stopping and range of ions in matter (2010)", *Nuclear Instruments and Methods in Physics Research Section B: Beam Interactions with Materials and Atoms*, vol. 268, pp. 1818–1823, June 2010. (page 98)

[159] O. Novotný, S. Allgeier, C. Enss, A. Fleischmann, L. Gamer, D. Hengstler, S. Kempf, C. Krantz, A. Pabinger, C. Pies, D. W. Savin, D. Schwalm, and A. Wolf, "Cryogenic micro-calorimeters for mass spectrometric identification of neutral molecules and molecular fragments," *Journal of Applied Physics*, vol. 118, p. 104503, Sept. 2015. (page 98, 111, 158)

[160] M. Ohkubo, M. Ukibe, S. Shiki, K. Suzuki, K. Chiba, N. Zen, T. Kitazume, M. Koike, S. Miki, Z. Wang, M. Ejrnaes, A. Casaburi, and R. Cristiano, "Superconducting Molecule Detectors Overcoming Fundamental Limits of Conventional Mass Spectrometry", *Journal of Low Temperature Physics*, vol. 167, pp. 943–948, June 2012. (page 98)

[161] E. Leblanc, N. Coron, J. Leblanc, P. de Marcillac, J. Bouchard, and J. Plagnard, "High-energy resolution alpha spectrometry using cryogenic detectors", *Applied Radiation and Isotopes*, vol. 64, pp. 1281–1286, Oct. 2006. (page 98)

[162] M. Frank, S. E. Labov, G. Westmacott, and W. H. Benner, "Energy-sensitive cryogenic detectors for high-mass biomolecule mass spectrometry", *Mass Spectrometry Reviews*, vol. 18, pp. 155–186, Jan. 1999. (page 98)

[163] J. L. Wiza, "Microchannel plate detectors", *Nuclear Instruments and Methods*, vol. 162, no. 1–3, pp. 587–601, 1979. (page 98, 115)

[164] P. Roth and G. Fraser, "Microchannel plate resistance at cryogenic temperatures", *Nuclear Instruments and Methods in Physics Research Section A: Accelerators, Spectrometers, Detectors and Associated Equipment*, vol. 439, pp. 134–137, Jan. 2000. (page 98)

[165] J. Schecker, M. Schauer, K. Holzscheiter, and M. Holzscheiter, "The performance of a microchannel plate at cryogenic temperatures and in high magnetic fields, and the detection efficiency for low energy positive hydrogen ions", *Nuclear Instruments and Methods in Physics Research Section A: Accelerators, Spectrometers, Detectors and Associated Equipment*, vol. 320, pp. 556–561, Sept. 1992. (page 98)

[166] S. Rosén, H. T. Schmidt, P. Reinhed, D. Fischer, R. D. Thomas, H. Cederquist, L. Liljeby, L. Bagge, S. Leontein, and M. Blom, "Operating a triple stack microchannel plate-phosphor assembly for single particle counting in the 12–300 K temperature range", *Review of Scientific Instruments*, vol. 78, p. 113301, 2007. (page 98)

[167] K. U. Kühnel, C. D. Schröter, and J. Ullrich, "Operating MCP Detectors at Cryogenic Temperatures", *Proceedings of 11th European Particle Accelerator Conference (EPAC)*, p. 3 p, 2008. (page 98, 116)

[168] E. Gatti, K. Oba, and P. Rehak, "Study of the Electric Field inside Microchannel Plate Multipliers", *IEEE Transactions on Nuclear Science*, vol. 30, pp. 461–468, Feb. 1983. (page 98)

[169] J. H. Jungmann and R. M. A. Heeren, "Detection systems for mass spectrometry imaging: A perspective on novel developments with a focus on active pixel detectors", *Rapid Communications in Mass Spectrometry*, vol. 27, pp. 1–23, Jan. 2013. (page 98)

[170] J. Lapington, "A comparison of readout techniques for high-resolution imaging with microchannel plate detectors", *Nuclear Instruments and Methods in Physics Research Section A: Accelerators, Spectrometers, Detectors and Associated Equipment*, vol. 525, pp. 361–365, June 2004. (page 98)

[171] I. M. Ismail, M. Barat, J.-C. Brenot, J. A. Fayeton, V. Lepère, and Y. J. Picard, "A zero dead-time, multihit, time and position sensitive detector based on micro-channel plates", *Review of Scientific Instruments*, vol. 76, p. 043304, 2005. (page 98)

[172] X. Urbain, D. Bech, J.-P. V. Roy, M. Géléoc, S. J. Weber, A. Huetz, and Y. J. Picard, "A zero dead-time multi-particle time and position sensitive detector based on correlation between brightness and amplitude", *Review of Scientific Instruments*, vol. 86, p. 023305, Feb. 2015. (page 98, 99, 100, 105, 106, 126, 158)

[173] H. Keller, G. Klingelhöfer, and E. Kankeleit, "A position sensitive microchannelplate detector using a delay line readout anode", *Nuclear Instruments and Methods in Physics Research Section A: Accelerators, Spectrometers, Detectors and Associated Equipment*, vol. 258, pp. 221–224, Aug. 1987. (page 99)

[174] Z. Amitay and D. Zajfman, "A new type of multiparticle three-dimensional imaging detector with subnanosecond time resolution", *Review of Scientific Instruments*, vol. 68, pp. 1387–1392, Mar. 1997. (page 99)

[175] R. Thomas, S. Rosén, F. Hellberg, A. Derkatch, M. Larsson, S. Datz, R. Dixon, and W. J. van der Zande, "Investigating the three-body fragmentation dynamics of water via dissociative recombination and theoretical modeling calculations", *Physical Review A*, vol. 66, p. 032715, Sept. 2002. (page 99)

[176] O. Jagutzki, A. Cerezo, A. Czasch, R. Dorner, M. Hattas, M. Huang, V. Mergel, U. Spillmann, K. Ullmann-Pfleger, T. Weber, H. Schmidt-Bocking, and G. D. Smith, "Multiple hit readout of a microchannel plate detector with a three-layer delay-line anode", *IEEE Transactions on Nuclear Science*, vol. 49, pp. 2477– 2483, Oct. 2002. (page 100)

[177] CERN, https://root.cern.ch/, 2015. (page 101, 163)

[178] O. Novotný, private communication, 2015. (page 101)

[179] RoentDek, "MCP Delay Line Dector Manual", 2015. (page 101)

[180] G. J. Price and G. W. Fraser, "Calculation of the output charge cloud from a microchannel plate", *Nuclear Instruments and Methods in Physics Research Section A: Accelerators, Spectrometers, Detectors and Associated Equipment*, vol. 474, pp. 188–196, Dec. 2001. (page 105)

[181] H. D. Baehr and K. Stephan, *Heat and Mass Transfer*. Berlin, Heidelberg: Springer, 2011. (page 109, 111)

[182] VDI e.V., *VDI-Wärmeatlas*. Berlin, Heidelberg: Springer, 11 ed., 2013. (page 109)

[183] Dobrovinskaya, Elena, L. A. Lytvynov, and V. Pishchik, *Sapphire - Material, Manufacturing, Applications*. Micro- and Opto-Electronic Materials, Structures, and Systems, Springer, 2009. (page 111, 121)

[184] S. Matoba, R. Takahashi, C. Io, T. Koizumi, and H. Shiromaru, "Absolute Detection Efficiency of a High-Sensitivity Microchannel Plate with Tapered Pores", *Japanese Journal of Applied Physics*, vol. 50, p. 112201, 2011. (page 115)

[185] D. Gorelikov, N. Sullivan, P. de Rouffignac, H. Li, J. Narayanamoorthy, and A. S. Tremsin, "Development of atomic layer deposition-activated microchannel plates for single particle detection at cryogenic temperatures", *Journal of Vacuum Science & Technology A*, vol. 32, p. 020605, Mar. 2014. (page 116)

[186] A. Tremsin, J. Pearson, G. Fraser, W. Feller, and P. White, "Microchannel plate operation at high count rates: new results", *Nuclear Instruments and Methods in Physics Research Section A: Accelerators, Spectrometers, Detectors and Associated Equipment*, vol. 379, pp. 139–151, Sept. 1996. (page 119)

[187] German Imaging Solutions (GIDS), "Phosphor properties", 2013. (page 119)

[188] Oxfort Instruments, "Windows for Cryogenic environments", 2003. (page 122)

[189] Y. S. Touloukian and C. Y. Ho, eds., *Thermophysical Properties of Selected Aerospace Materials. Part II: Thermophysical Properties of Seven Materials.* CINDAS Purdue University, 1977. (page 122)

[190] J. Ekin, *Experimental Techniques for Low-Temperature Measurements.* National Institute of Standards and Technology, Boulder, CO, USA: Oxford University Press, Oct. 2006. (page 122)

[191] N. J. Simon, E. S. Drexler, R. P. Reed, International Copper Association., and National Institute of Standards and Technology (U.S.), *Properties of copper and copper alloys at cryogenic temperatures*, vol. 177 of *NIST Monograph.* National Institute of Standards and Technology, Boulder, CO, USA: U.S. Dept. of Commerce, 1992. (page 122)

[192] Automated Imaging Association, "Specifications of the Camera Link Interface Standard for Digital Cameras and Frame Grabbers, Version 1.1", Jan. 2004. (page 126)

[193] H. Schmidt, private communication, 2015. (page 144)

[194] J. M. Labello, *Water Ice Films in Cryogenic Vacuum Chambers.* PhD thesis, The University of Tennessee, Dec. 2011. (page 144)

[195] N. Takahashi, Y. Adachi, M. Saito, and Y. Haruyama, "Absolute detection efficiencies for keV energy atoms incident on a microchannel plate detector", *Nuclear Instruments and Methods in Physics Research Section B: Beam Interactions with Materials and Atoms*, vol. 315, pp. 51–54, Nov. 2013. (page 154)

[196] B. Gaire, A. M. Sayler, P. Q. Wang, N. G. Johnson, M. Leonard, E. Parke, K. D. Carnes, and I. Ben-Itzhak, "Determining the absolute efficiency of a delay line microchannel-plate detector using molecular dissociation", *Review of Scientific Instruments*, vol. 78, p. 024503, 2007. (page 154)

Danksagung

Abschließend möchte ich noch allen meinen großen DANK aussprechen, die zum Gelingen dieser Arbeit beigetragen haben:

Andreas Wolf für die Möglichkeit im Rahmen dieser Doktorarbeit an interessanten und herausfordernden Projekten zu arbeiten, für seine vielen wertvollen Ideen und Anregungen, sowie seiner Unterstützung bei der Fertigstellung dieser Arbeit,

Robert Moßhammer für die geduldige Begutachtung dieser Arbeit,

Claude Krantz und Oldrich Novotný, die immer ein offenes Ohr für jede meiner Fragen hatten, in jeder Hinsicht Hilfestellung geleistet und diese Arbeit gründlich Korrektur gelesen haben,

Xavier Urbain für die Bereitstellung seiner COBRA-Datenaufnahme und seiner unbezahlbaren praktischen Hilfestellung bei der Inbetriebnahme des NICE Detektors,

allen weiteren beteiligten Kollegen am MPIK für die angenehme und aufschlussreiche Zusammenarbeit, von der Konstruktion, über die Hauptwerkstatt, bis hin zu der Hahn bzw. Falkenthal Werkstatt, den tatkräfigen CSR-Technikern, sowie Dirks Last-Minute-Fertigungen und Ollis erheiternden Elektronikberatungen,

Kaija Spruck für ihre kulinarischen Bereicherungen und die Diskussionen der ganz grundlegenden Fragen,

Stephen Vogel für die Bewältigung des Arbeitsfrustes,

den übrigen Kollegen dieser Arbeitsgruppe für die angenehme Atmosphäre und entspannenden Kaffeerunden,

und schließlich meiner Familie für Ihren Rückhalt vor allem während des strapaziösen Endspurts dieser Arbeit.